“If you want to find the secrets of the universe, think in terms of energy, frequency and vibration.”

Nikola Tesla

“It doesn't matter how beautiful your theory is, it doesn't matter how smart you are. If it doesn't agree with experiment, it's wrong.”

Richard P. Feynman

Contents

CHAPTER 3

NOVEL DIRECT APPROXIMATE SOLUTION FOR THE OPTIMAL DESIGN OF TLCD SYSTEMS

Acknowledgements

I would like to first express my deepest gratitude to my tutor, Prof. Antonina Pirrotta, who provided support, encouragement and friendship throughout this experience. The confidence she placed in me, and her constant guidance, were fundamental for my growth during this path. I cannot thank her enough for the opportunities she has provided me, and for truly looking out for my best interests.

I would also like to express my profound and sincere gratitude to my external advisor, Prof. Pol D. Spanos, from Rice University (Houston, USA). During my permanence in Houston he gave me hospitality and always represented a reference point for scientific and human aspects. His invaluable suggestions were essential in my research activities and for the enhancement of this dissertation. He has set an example which I hope to emulate in my career.

I am also very grateful my co-tutor, Prof. Enrico Napoli, for his helpful suggestions and fruitful discussions, which contributed to the development of this work.

I am indebted and I extend my sincere thanks to Prof. Mario Di Paola for his valuable guidance and constructive comments. He deeply contributed in my scientific growth, and the inspiring and meaningful meetings with him permitted to develop several important topics in my research activities.

Additionally, I am pleased to acknowledge several others who contributed directly or indirectly to this research. I wish to extend my gratitude to Prof. Ioannis A. Kougioumtzoglou, for his help in the development of the last part of the dissertation. I am grateful for collaboration with Dr. Giacomo Navarra and Dr. Francesco Lo Iacono, for their support in many occasions. Their help allowed me to overcome many difficulties that I encountered. The laboratory technician, Erasmo Cataldo, is gratefully acknowledged for his help in most stages of the experiments. Thanks to my colleagues Salvo, Francesco, Gioacchino, Pietro, Emilio, Thanasis, Nazareno, Sandro, Thierry, Marco, Fabio, Giuseppe, Emma and Martina, for the discussions, cooperation and friendly moments.

I am also thankful to all Ph.D. board of advisors and to the members of the Department of Civil, Environmental, Aerospace and Materials Engineering, for giving me this opportunity.

Next, I would like to deeply thank my family, who has constantly supported me during these years. Thank you Irene, Luca, Sergio and all my nephews and nieces. I am sincerely grateful to my old and new friends: Silvia, Arezia, Anna, Nausicaa, Carolina, Marina, Rosanna, Gigi, Davide, Roberta, Norino, Emanuele and Fredrick. You have been a second family to me.

Last but not least, special thanks goes to Sara, my long lasting friend for her incessant comfort and care, Manfredi, for his constant support and encouragement since the beginning of this path, and my Mom, for having always believed in me and guided me.

To my Dad this Thesis is dedicated.

Preface

In recent years passive structural vibration control has been a flourishing research area in civil and mechanical engineering. In fact, passive control systems can be used to prevent structural elements from damage or increase human comfort due to reduced accelerations.

In this regard, several types of devices have been proposed in order to mitigate the dynamic response of different kind of structural systems. Among them, Tuned Mass Dampers are undoubtedly the most widely used vibration control devices for buildings exposed to earthquake and wind loads.

Nevertheless, Tuned Liquid Column Dampers (TLCDs) represent now an interesting alternative for some of their particular characteristics as low cost, easy installation, lack of required maintenance, and no need to add mass to the main structure. The TLCD simply consists of a U-shaped container partially filled with water. It dissipates structural vibrations by means of a combined action which involves the motion of the liquid mass within the container. Specifically, the restoring force is produced by the force of gravity acting on the liquid while the damping effect is generated by the hydrodynamic head losses which arise during the motion of the liquid inside the TLCD. For analytical investigations, this device is generally modeled as a nonlinear single-degree-of-freedom system rigidly attached to the main structure to be controlled. Its control performance principally depends on an appropriate choice of the tuning

and dissipation parameters. However since TLCD response is generally nonlinear, the determination of its optimal design parameters may be demanding.

On this base, in this work the behavior and main characteristics of this device will be investigated and its effect on the response of vibration sensitive systems will be studied, both from a theoretical and an experimental perspective.

Three main aspects will be dealt with. Firstly, an investigation on the optimal choice of TLCD parameters will be presented, with the intent of a more reliable and efficient design procedure of these devices for real damped structures. Secondly, aiming at more carefully matching experimentally obtained data, an innovative mathematical formulation for the liquid motion within the TLCD will be proposed, as well as its extension to TLCD controlled structures. Finally, the stochastic response of these devices will be developed in details resorting to a recently proposed novel technique. Specifically, results obtained from the research undertaken at the Department of Civil and Environmental Engineering at Rice University (Houston, USA) will be discussed.

In order to validate all the proposed theoretical results, numerous experimental tests have been performed in the Laboratory of Experimental Dynamics at University of Palermo, and experimental vis-à-vis numerical results will be presented for each proposed development throughout the dissertation.

Introduction

The trend towards the use of materials with higher mechanical characteristics, together with the application of modern computer methods for the design of civil engineering systems, leads to the realization of increasingly slender and vibration prone structures. For these systems, even when the level of vibration does not exceed safety criteria or causes structural failure, resulting occupant discomfort needs to be avoided.

As a consequence, a major challenge for researchers and designers in structural engineering is the study and realization of innovative devices able to mitigate and control vibrations induced by strong natural events such as earthquakes and wind excitations.

A possible method for reducing these undesired effects relates to the inclusion of passive vibration control. In this regard, the Tuned Mass Damper (TMD) undoubtedly represents one of the most widely used devices for reducing structural vibrations.

On the other hand, a novel type of passive vibration control system, namely the Tuned Liquid Column Damper (TLCD), has been recently proposed as an interesting alternative to the more common TMD. This device simply consists of a rigid U-shaped container, partially filled with water, in such a way to be tuned with the main system to which it is rigidly connected. Compared to most passive vibration control systems, including TMDs, TLCDs possess desirable characteristics, such as lower

costs, easy installation, low maintenance requirements and no need to add mass to the main structure to be controlled, which make them an ideal solution for reducing structural vibrations.

On this base, the main objective of this dissertation is to investigate the behavior and main features of these devices and their influence on the response of vibration prone systems, both from a theoretical and an experimental point of view.

To this aim, in Chapter 1 a brief introduction of some basic concepts on vibration control systems, and different types of vibration control mechanism, is outlined. Specifically, common passive control devices and seismic isolation systems will be presented in details. Further, the main aspects of TMDs are highlighted, with special emphasis to the current optimal design strategy of these systems.

In Chapter 2 the main features of TLCDs are discussed in detail. Specifically, a brief literature review in the area of TLCD is presented, and some of the existing applications of these dampers are discussed. Further, the nonlinear governing equations for the motion of the liquid inside the device, as well as of TLCD controlled structures, are derived and existing approaches in literature for the optimal design of these dampers are introduced. Finally, the chapter ends with an investigation on the control performances of TLCDs, both numerically and experimentally, and comparison with TMD device is also considered to further assess the efficiency of these systems.

Since most of the studies dealing with the optimal choice of TLCD parameters resort to an iterative procedure for the design of these systems, and direct approaches exist only for the case of undamped main

structures, in Chapter 3 an approximate direct formulation is derived to more simply evaluate TLCD parameters in case of damped main system under random loads. Even though the proposed direct approach is approximate, since based on the Statistical Linearization Technique and on some assumptions pertaining the control system, in the second part of the chapter the reliability of the proposed formulation is assessed by comparison with Monte Carlo Simulation (MCS) results based on the original nonlinear governing equations. Moreover, a parametric numerical analysis is carried out in order to investigate the effectiveness of the proposed formulation when the underlying assumptions are not fulfilled. The proposed direct approach is also used to derive the optimal TLCD design parameters, and comparison with previous methods in literature is shown. Finally, numerical results obtained with the straightforward formulation are validated through an extensive experimental campaign on a small scale SDOF shear-type model equipped with a TLCD device built in the Laboratory of Experimental Dynamics at the University of Palermo.

Although the increasing use of TLCDs for structural vibration control, recent studies have shown that currently used classical mathematical model does not always lead to an accurate description of their behavior. Specifically, for some TLCD geometrical configurations of engineering interest, the classical equation of motion may not accurately describe the real liquid motion within the device. Since several experimental results have shown an apparent sloshing effect during liquid motion in the TLCD device, in Chapter 4 the equation of motion for the TLCD liquid displacements is derived taking into account the first linear liquid

sloshing mode, through the equivalent mechanical analogy well established in literature. Further, a different mathematical formulation of the equation of motion is proposed, taking advantage of fractional operators and their properties. Specifically, since the apparent effect of sloshing is the deviation of the natural frequency from the theoretical one, a fractional differential equation of motion is proposed to model the liquid vertical displacements within the TLCD device. The latter choice is supported by the fact that the introduction a fractional derivative of order β alters simultaneously both the resonant frequency and the damping of the system. In the second part of the chapter this proposed formulation is extended to deal with structures equipped with TLCD devices. Finally it is shown, through an extensive experimental analysis, how the proposed model can accurately describe both liquid surface and structural displacements. Specifically, experimental validation of the predicted behavior is fully developed both in frequency and time domain. In this regard, it is noted that since the resulting proposed equations of motion are linear, albeit of fractional order, identification of the involved parameters is extremely simpler than the classical nonlinear formulation.

In the final Chapter 5 the stochastic analysis of TLCD systems, and TLCD controlled structures, under Gaussian white noise excitation is addressed through the promising recent technique of the Wiener Path Integral (WPI). Specifically, once the basic concepts of the WPI are introduced and its application for nonlinear SDOF and MDOF systems under Gaussian white noise is discussed, a novel formulation for an efficient evaluation of the nonstationary response PDF of such systems is proposed. Further, the utility of such an advanced tool is stressed in the

last part of the Chapter, where the case of the 2 degree-of-freedom TLCD controlled structure is considered, assessing the accuracy of the outlined procedure also with the corresponding experimentally obtained PDFs. Finally, considering the proposed fractional formulation for the motion of TLCD systems, in the last part of the chapter the WPI technique is extended to the case of linear and nonlinear systems endowed with fractional derivatives elements. Several numerical examples are presented to show the reliability of the proposed procedure, including the case of the TLCD device and the nonlinear Duffing oscillator, and comparisons with pertinent MCS data demonstrate the satisfactory degree of accuracy.

Chapter 1

Vibration control systems

1.1 Introduction

The current trend toward the use of lightweight, high strength materials, together with advanced construction techniques, have allowed the realization of buildings with increasing heights, possessing greater flexibility and lighter damping. Consequently, these structures are very sensitive to environmental excitations, such as wind and earthquakes, which cause unwanted vibrations inducing possible structural failure, occupant discomfort, and equipments malfunction. Hence the insistent demand for practical and effective devices able to reduce these vibrations.

Devices used for mitigating structural vibrations can be generally divided into separate categories based on their working principles.

Passive control devices (Fig. 1.1) are systems which do not require any external power source, imparting forces that are developed in response to the motion of the structure (Housner et al., 1997, Soong and Spencer, 2002, Soong and Dargush, 1997, Saaed et al. 2015). It follows that the total energy in the passively controlled structural system cannot be increased by the devices.

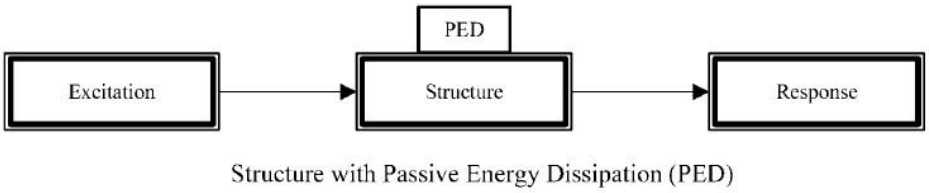

Fig. 1.1 – Scheme of structure with added Passive Energy Dissipation (PED) system (Soong and Spencer, 2002).

Active control devices (Fig. 1.2) are systems requiring external power source to drive actuators applying forces which tend to oppose the unwanted vibrations. The control force is generated depending on the feedback of the structural response. Due to the uncertainty of the power supply during extreme conditions, such systems are vulnerable to power failure, thus making passive systems generally favored over active ones.

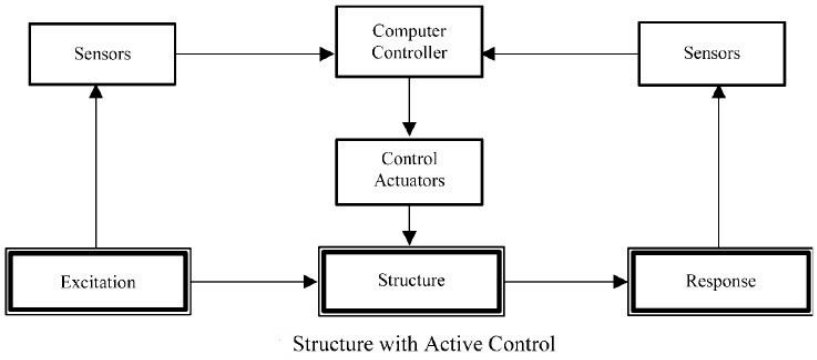

Fig. 1.2 – Scheme of structure with added Active Control system (Soong and Spencer, 2002).

Semi-active control systems (Fig. 1.3) are active control devices with energy requirements orders of magnitude less than typical active control

systems. These devices do not impart energy into the system, thus maintaining stability at all times (Symans and Constantinou, 1999).

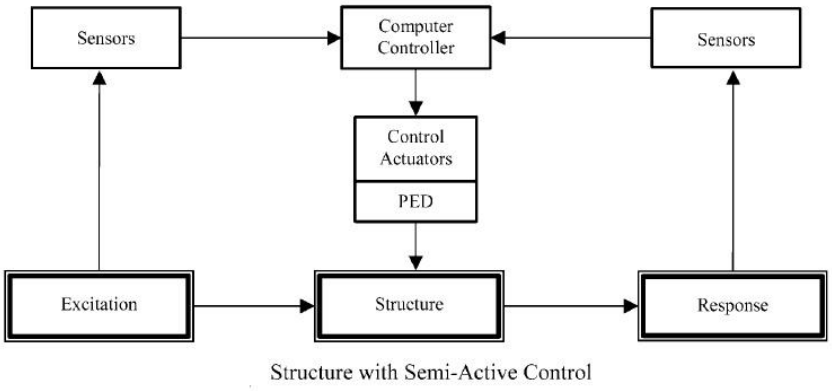

Fig. 1.3 – Scheme of structure with added Semi-active Control system (Soong and Spencer, 2002).

Finally, hybrid control devices (Fig. 1.4) employ a combination of active and passive systems or passive and semi-active systems.

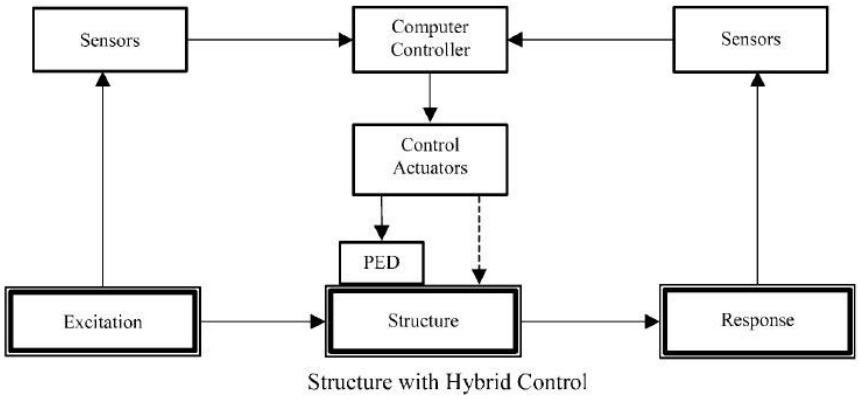

Fig. 1.4 – Scheme of structure with added Hybrid Control system (Soong and Spencer, 2002).

Due to their features, including low costs and low maintenance requirements, passive control devices are generally preferred and more commonly used to mitigate vibrations in civil structures.

In this regard, in this Chapter usual structural passive control techniques and their applications will be reviewed. Specifically, in Section 1.2 main passive control devices will be presented in details. Particular attention will be paid on seismic isolation systems, which will be described in Section 1.3. Finally the Chapter ends with a detailed analysis of a particular class of passive control systems, namely the Tuned Mass Dampers (TMDs), whose working principle is the basis for the study of Tuned Liquid Column Dampers (TLCDs), the control devices object of this dissertation.

1.2 Passive vibration control systems

Passive energy dissipation systems encompass a range of materials and devices for reducing vibrations and enhancing damping, in new as well as already existing structures.

These devices can operate on diverse principles such as frictional sliding, yielding and phase transformations in metals, deformations of viscoelastic solids or viscous fluids and the use of external mechanical systems connected to the primary structure to be controlled.

A large number of passive control systems have been developed and installed in structures for performance enhancement under wind and earthquake loads. In this regard, discussion in the remainder of this section is centered on some of the most commonly applied devices. Readers are also referenced to the many books and review papers on this topic (see e.g. Housner et al., 1997; Soong and Dargush, 1997; Constantinou et al., 1998; Kareem et al., 1999), for a thorough analysis.

1.2.1 Metallic yield dampers

One of the most effective mechanisms available for the dissipation of energy in a structure is through inelastic deformation of metals. In traditional steel structures the aseismic design relied on the plastic deformation (and post yield ductility) of structural members.

The introduction of metallic yield dampers started with the concept of utilizing separate metallic hysteretic dampers to absorb part of the external energy input to the structure. During the years a variety of such devices has been proposed, many of them using mild steel plates with triangular or hourglass shape, so that yielding spreads throughout the material.

The dissipating effect is based on the nonlinear force-displacement behavior, which typically shows hysteresis loops for energy dissipation. Many different designs and materials, such as lead and shape memory alloys, have been developed and used.

The ongoing research has resulted in the realization of several commercial products for both new and retrofit construction projects.

For instance a typical X-shaped metallic yield damper, known as ADAS (added damping and stiffness) device, is shown in Fig. 1.5.

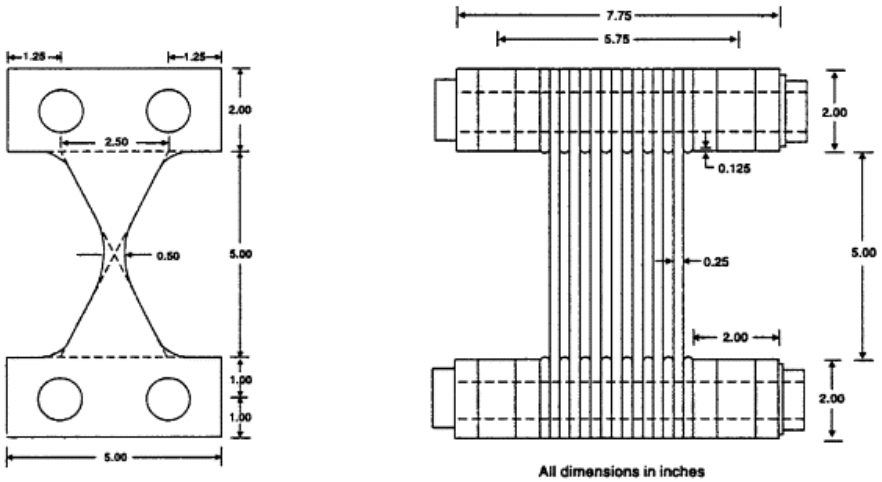

Fig. 1.5 – Example of ADAS device (Soong and Spencer, 2002).

A variation of the above mentioned device, but operating on the same principle, is the tension/compression yielding brace, also called the unbonded brace (Soong and Spencer, 2002). As shown in Fig. 1.6, it consists of a core steel plate encased in a concrete-filled steel tube, with a special coating between the core plate and concrete in order to reduce friction. The core steel plate provides stable energy dissipation by yielding under reversed axial loading, while the surrounding concrete-filled steel tube resists compression buckling.

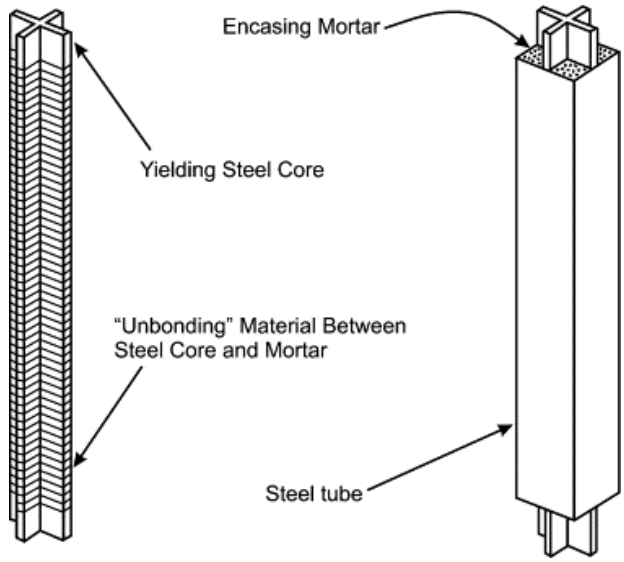

Fig. 1.5 – Example of ADAS device (Soong and Spencer, 2002).

Since their first application in New Zealand in 1980 (Skinner et al., 1980), metallic yield dampers have been employed in various countries, including a 29-storey building in Italy (Chiampi, 1991), seismic retrofit installations in USA and Mexico (Perry et al., 1993, Martinez-Romero, 1993) and a number of installations in Japan.

1.2.2 Friction dampers

Dry friction provides another excellent mechanism for energy dissipation, playing for instance an important role in automotive brakes. On this base, friction dampers use the mechanism of solid friction which develops between two sliding surfaces, to provide the desired energy dissipation.

A critical component of these systems is the sliding interface, since an improper composition of the interface layers may cause corrosion and thus an alteration of slipping properties with time. As a consequence, compatible materials must be found to ensure a constant coefficient of friction independent of environmental factors.

An example of these devices is the X-braced friction damper, shown in Fig. 1.6.

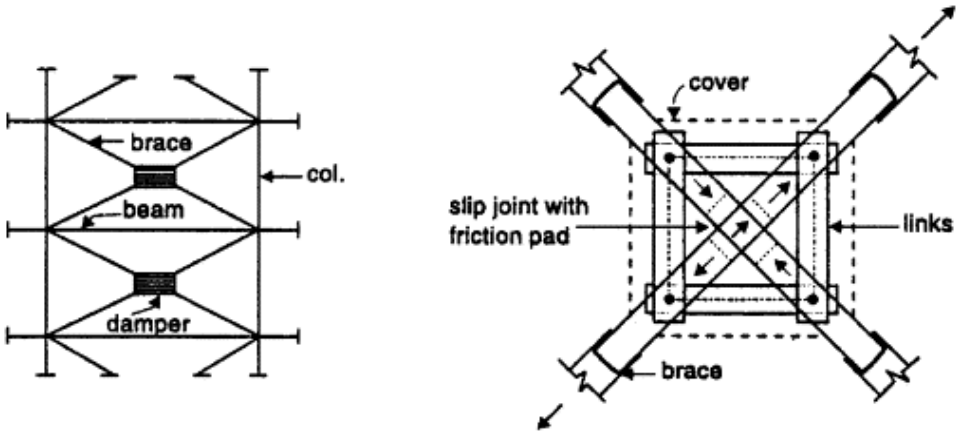

Fig. 1.6 – Example of X-braced friction damper (Soong and Spencer, 2002).

Those devices are not designed to operate during wind storms or moderate earthquakes, since maximum energy dissipation is guaranteed once slipping occurs at a predetermined optimum load before yielding occurs in primary structural members.

Test data have shown that macroscopic hysteretic models for friction dampers are usually rectangular hysteretic loop, thus similar to Coulomb friction with a constant coefficient of friction.

Friction dampers have been installed in several buildings, some as retrofits and some as new facilities, including structures in Canada and USA (Pall and Pall, 1996).

1.2.3 Viscoelastic dampers

The metallic and frictional devices described so far, are mainly intended for seismic applications. On the other hand, viscoelastic dampers can be applied in both wind and seismic protection.

Since the 50s, viscoelastic dampers have been applied as vibration absorbing materials, gaining high civil engineering relevance with the installation of about 10000 devices to reduce wind induced vibrations, in each of the Twin Towers of the World Trade Center in New York in 1969 (Samali and Kwock, 1995).

Viscoelastic materials used in these dampers are generally copolymers or glossy substances that dissipate energy through shear deformation. A typical viscoelastic damper, consisting of viscoelastic layers bonded with steel plates, is illustrated in Fig. 1.7.

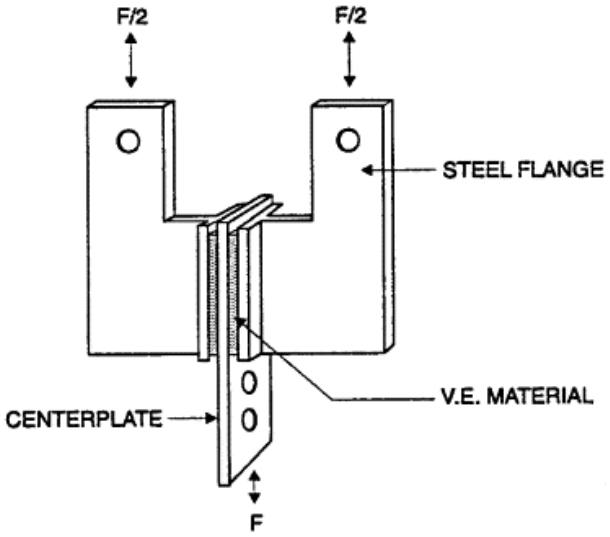

Fig. 1.7 – Typical viscoelastic damper configuration (Soong and Spencer, 2002).

When mounted in a structure, shear deformation and hence energy dissipation takes place when structural vibration induces relative motion between the steel plates.

Although originally designed for wind loading, further analytical and experimental studies have shown that viscoelastic damped structures can be very resistant against a large range of earthquake ground motion intensity levels.

Other than the World Trade Center, several buildings in USA and Taiwan (Samali and Kwock, 1995) are equipped with viscoelastic dampers to reduce wind induced vibrations, and also seismic retrofit projects have been undertaken.

1.2.4 Viscous fluid dampers

In previous sections the described passive dampers dissipated energy by inelastic deformation of solids. However, fluids can also be used effectively to achieve a desired level of passive control. One prominent example is the automotive shock absorber, where the damping effect results from the movement of a piston head with small orifices in a high viscous fluid.

On this base, many of these devices have been adapted for structural applications in civil engineering. Typical example is shown in Fig. 1.8, where the dissipation occurs by forcing a fluid, usually a compound of silicone or oil, to pass through small orifices in the piston.

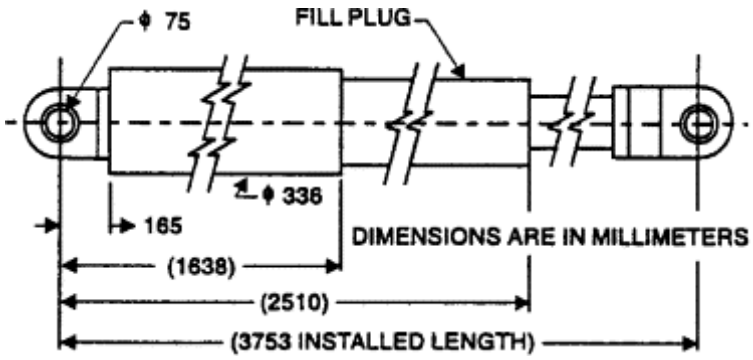

Fig. 1.8 – Scheme of viscous fluid damper (Soong and Spencer, 2002).

These damping devices are small and local components which must be integrated within the hosting structures, typically in form of braces or vertical elements connecting adjacent floor.

If the fluid is purely viscous (e.g. Newtonian), and the flow is laminar, then the output force of the damper is directly proportional to the velocity of the piston.

As far as the structural application of these devices is concerned, Housner et al. (1997) report the seismic protection of a 1000m long bridge in Italy, while in several applications they were used in combination with seismic isolation systems. For example, in 1995, viscous fluid dampers were incorporated into base isolation systems for five buildings of the San Bernardino County Medical Center (Soong and Spencer, 2002).

1.2.5 Tuned liquid dampers

Tuned liquid dampers (TLDs) are passive control devices which dissipate energy through the sloshing of liquids in a container. These devices belong to the more general class of tuned liquid vibration absorbers, which includes also the TLCDs that will be described in detail in the following Chapter.

The basic working principle relates to the application of a secondary mass in the form of a body of liquid connected to the structural system to be controlled (Fig. 1.9), and properly tuned to act as a dynamic vibration absorber. Therefore, unlike previously described passive devices, vibration energy is not immediately dissipated, but transferred to the secondary system represented by the liquid mass.

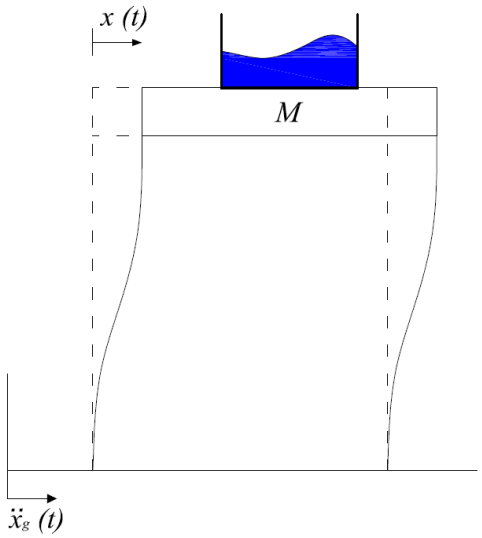

Fig. 1.9 – Tuned Liquid Damper connected to a SDOF system.

TLDs response is highly nonlinear, due to the liquid sloshing phenomenon which takes place during the motion. However the system has characteristic frequencies which can be tuned for most favorable performance, but for large oscillation amplitudes the system is rather insensitive to detuning between host and secondary structure.

Circular containers can be used for symmetric structures with the same fundamental frequencies in the principal directions, while rectangular tank are preferred for unsymmetrical structures with different fundamental frequencies along the principal axis.

One of the first structural implementation of this device was a steel frame airport tower in Nagasaki, Japan (Tamura et al., 1995), consisting of 25 cylindrical TLDs, each one being a stacked arrangement of 7 layers of water. Other relevant applications can be found in the book by Ibrahim (2005).

1.3 Seismic Isolation

The concept of seismic isolation was developed to mitigate all kinds of ground excitation but, on the other hand, this damping method does not work for other type of loads such as strong wind excitations. Clearly, this is only a minor restriction for the success of seismic isolation in earthquake prone countries, where seismic isolation is a highly appreciated concept to protect important structures. Since the isolation system is typically installed at the foundation of a structure (Fig. 1.10(a)), it is often called base isolation system.

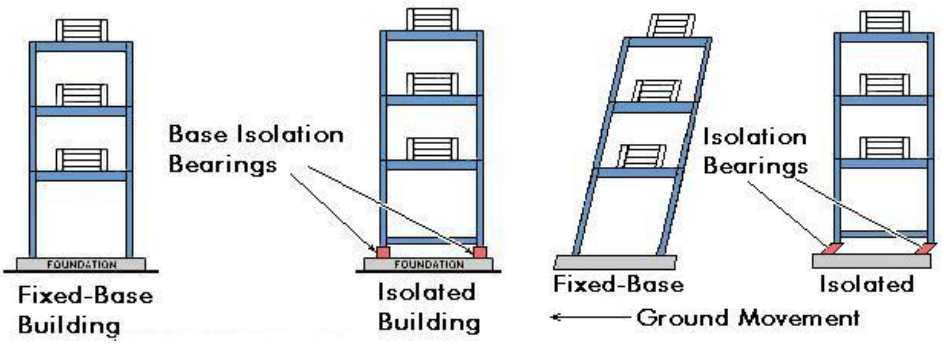

(a) (b)

Fig. 1.10 – Movement of Building with Base Isolation vs. No Base Isolation

Base isolation uncouples the building or structure from the horizontal components of the ground motion (Fig. 1.10(b)) and allows the simultaneous reduction of interstorey drifts and floor acceleration by providing the necessary flexibility. The underlying idea is to cut down the fundamental structural frequency to be much lower than both its fixed

base frequency and the predominant frequencies of the earthquake. Therefore, the isolation system deflects the seismic energy through the modified structural dynamics, rather than dissipating it. Nevertheless, a certain level of damping at the isolation level is beneficial to increase the first mode damping ratio of the structure, thus suppressing resonance at the isolation frequency.

The first ideas of base isolation date back to the beginning of the 20th century (Naeim and Kelly, 1999), but only since the development of proper high strength bearings, the concept of seismic isolation has become a practical reality. Basically, modern seismic isolation systems can be divided into two groups: cylindrical multiple-layer hard rubber (or elastomeric) bearings and rollers or sliders.

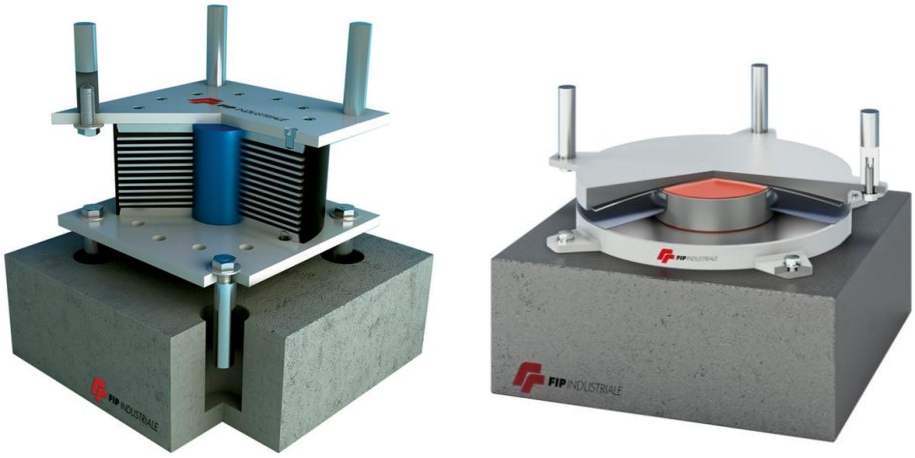

(a) (b)

Fig. 1.11 – Base isolation devices: (a) Lead Rubber Bearings; (b) Friction Isolation Pendulum.

The first one represents the most common type of base isolation systems, and it is made by vulcanization bonding of sheets of rubber to

thin steel reinforced plates (Fig. 1.11(a)). These bearings are very stiff in the vertical direction and can carry the weight of the building while remaining very flexible horizontally. Commonly lead plugs are included within the bearing, dissipating energy by yielding (Pirrotta, 1996; Pirrotta and Ibrahim, 1997).

The second type of isolation systems employs rollers or slider between the foundation and the base of the structure (Fig. 1.11(b)). The shear force transmitted to the structure across the isolation interface is limited by keeping the friction coefficient as low as possible, but at the same time sufficiently high to sustain strong winds or small earthquakes without sliding. Further, to limit displacements, high tension springs or a concave dish for the rollers are used to provide the restoring force to return the structure to its equilibrium position (Chopra, 1995; Muscolino et al., 1997).

Clearly, whichever type is used, one has to ensure that there is enough space around the structure to allow for the necessary large base displacements.

Actual implementations are numerous (Naeim and Kelly, 1999), including prestigious buildings like the San Francisco City Hall or the Los Angeles City Hall.

1.4 Tuned Mass Damper (TMD)

The purpose of incorporating a Tuned Mass Damper (TMD) in a structure is mainly the same as that discussed for all other vibration control systems: reducing the demand for energy dissipation on the primary structure under the action of external forces.

In the case of TMD this reduction is achieved by transferring the energy produced by the vibrations to the TMD itself which, in its simplest form, consists of a mass-spring-dashpot system connected to the main structure to be controlled, as shown in Fig. 1.12.

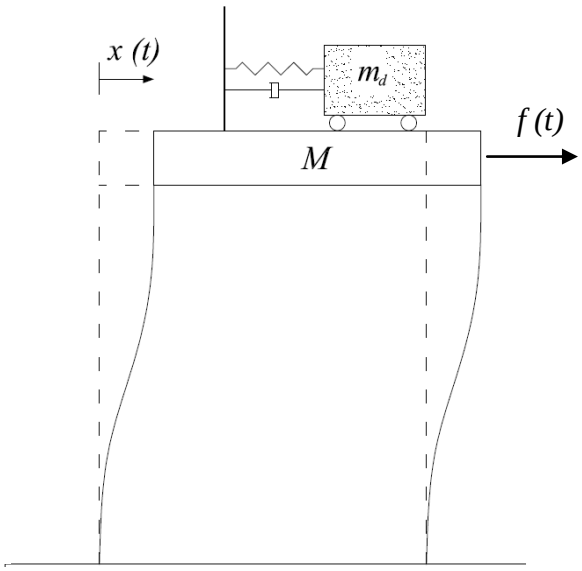

Fig. 1.12 – Tuned Mass Damper connected to a SDOF system under external excitation.

In the simple case of harmonic excitation $f(t) = f_0 \sin(\Omega t)$ and no damping in the main system, it can be demonstrated (Den Hartog, 1956) that the main mass *M* does not vibrate if the natural frequency of the absorber $\sqrt{k/m}$ is chosen to be equal to the frequency Ω of the external force $f(t)$.

It is worth noting that a number of practical considerations should be observed in the design of a TMD systems, such as the amount of added mass that can be practically placed on the top of a building. Also TMDs displacement relative to the building represents another important design parameter, since large movements are often needed for a reasonable response reduction of the building. Finally, low friction bearing surfaces are needed in sliding mass TMDs, so that the device can respond to the building movements also at low levels of excitation.

1.4.1 Literature review on TMD systems

The concept of using TMDs for structural control has its roots in the dynamic vibration absorbers invented by Frahm in 1909 (Frahm, 1909, Den Hartog, 1956).

The system devised by Frahm had however no damping, so it was only effective when the natural frequency of the absorber was very close to that of the external excitation.

In the early 50s Den Hartog (Den Hartog, 1956) considered the case of a linear undamped single-degree-of-freedom (SDOF) system,

connected to a TMD with damping, and subjected to a harmonic force. In this way he demonstrated how, if a certain level of damping was introduced into the TMD device, system response could be significantly reduced also at frequencies different from the resonance one (Fig. 1.13). The same author then derived some closed form expressions in order to determine optimal TMDs design parameters.

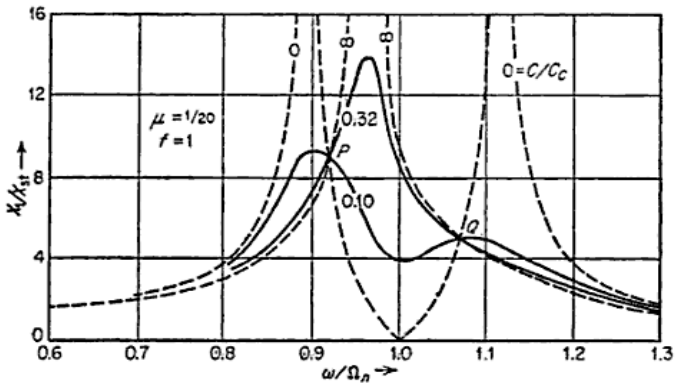

Fig. 1.13 – Displacement amplitude of the main structure for various values of the damping in the TMD (Den Hartog, 1956).

This first study was then followed by many others, among which those of Ioi and Ikeda and that those of Warburton in 1980.

Ioi and Ikeda (Ioi and Ikeda, 1978) found some correction factors for the optimal TMDs parameters assuming a modest value of viscous damping in the main structure.

Warburton and Ayorinde (Warburton and Ayorinde, 1980) analytically determined the optimal values of TMDs parameters, for various values of the ratio between the mass of the TMD and the main system, and for certain values of the damping coefficient of the structure.

Subsequently, the same author (Warburton, 1982) analyzed also the response of a SDOF structure with a TMD and subjected to either harmonic type or to a white noise base excitation. In this way he derived closed-form expressions for the optimal TMD parameters in case of undamped SDOF system.

The efficiency of this system in reducing the vibrations of structures forced by wind, as well as for the case of seismic excitation, is now well established (for example, Villaverde, 1994).

In the study of Villaverde three different structures were analyzed: a 2D 10-storey building, a 3D single-storey frame and a cable-stayed bridge (Fig. 1.14), using nine different records of seismic accelerations.

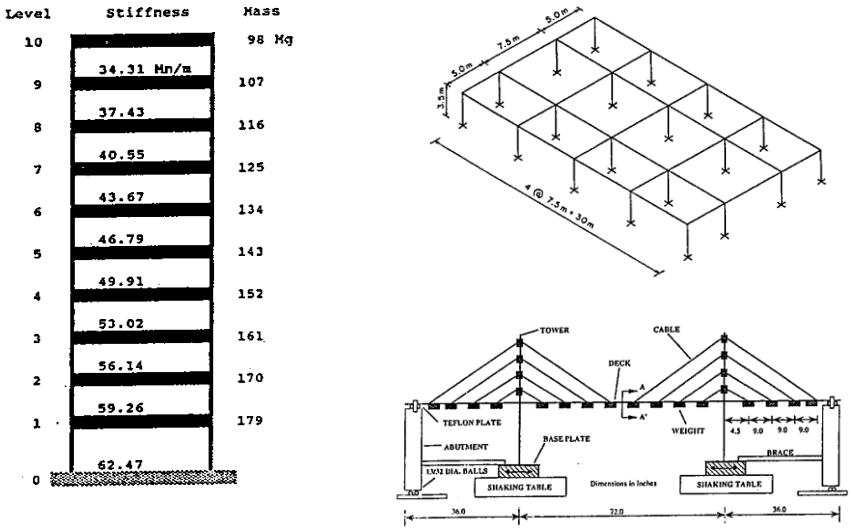

Fig. 1.14 – The three analyzed models (Villaverde, 1994).

The obtained theoretical and experimental results showed that the efficiency of the TMD in reducing the response of the same structure

during different earthquakes, or of different structures during the same earthquake, is significantly different. In fact, in some cases good performance can be achieved, while in some cases no appreciable effect can be obtained. Specifically, the damping effect was higher for base excitation frequencies close to the resonance and decreased as soon as the frequency departed from the natural frequency of the system to which the TMD was tuned.

Much of the initial research on TMDs has been focused on the restrictive assumption that a single operating frequency is in resonance with the fundamental frequency of the machine. Civil engineering structures however, are subjected to different types of environmental loads, which contain many frequency components. Thus the performance of TMD is complex, and for multi-degree-of-freedom (MDOF) systems less efficient than expected. In this regard, the response of the first mode of a structure with TMD tuned to the fundamental frequency can be greatly reduced but, in general, the higher modal response may only be marginally reduced or even amplified. To overcome this problem more than one TMD, each tuned to a different dominant frequency, can be employed.

The concept of multiple TMDs (Multiple Tuned Mass Damper, MTMD), together with the development of its optimization procedure has been proposed by Clark (1988). Since then, numerous studies have been conducted on the behavior of MTMDs connected in parallel to the main system (Xu and Igusa, 1992; Yamaguchi and Harnporchai 1993).

Having observed that the prevailing response of isolated structures is related to the contribution of the first mode only, and since TMDs can

significantly reduce the response of this mode, Palazzolo and Petti (1999) proposed to combine in a single system these two properties (Fig. 1.14).

Analytical results showed that the use of TMD in a structure with base isolation has the advantage of absorbing the energy produced by the earthquake without affecting the isolation effect, greatly reducing the displacements at the base of the main system.

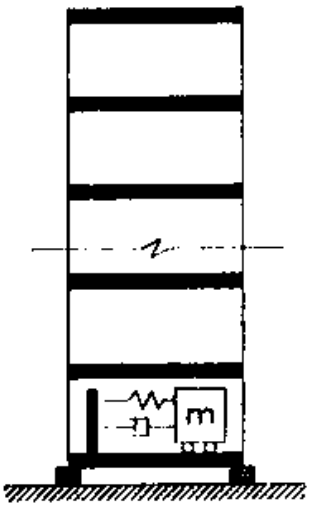

Fig. 1.15 – Base isolated structure, with TMD (Palazzolo and Petti, 1999).

Since then, numerous other studies have been conducted for the development of this vibration control system, especially as regards both different possible procedures of optimization, and for the use of such a device in combination with other modern control systems, such as active, semi-active or hybrid control (Housner et al., 1997; Spencer and Nagarajaiah, 2003. Soong and Spencer, 2002).

1.4.2 Applications of TMDs for structural control

A large number of passive vibration control systems has now been developed and installed in numerous facilities around the world. Only in North America, these devices have been applied in hundreds of new and existing buildings, and many more in bridges. Figure 1.16 shows the distribution of these buildings on the basis of the year in which the system was installed up to 2000.

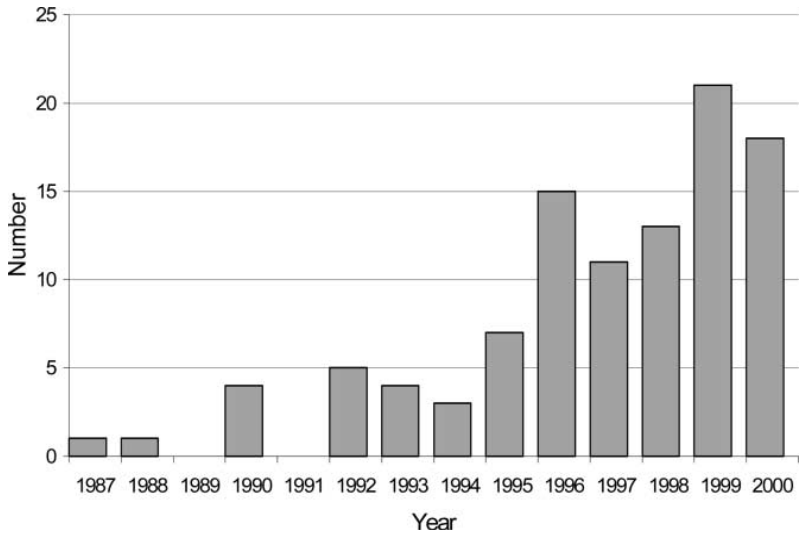

Fig. 1.16 – Application of passive control systems in North America (Soong and Spencer, 2002).

TMDs, and their variants, represent the majority of the passive control devices currently in use. These devices are not only applied to buildings, but also to chimneys, bridges and other industrial equipment in Saudi

Arabia, Pakistan, Japan, Australia, Britain, Germany, Belgium and Canada.

One of the first applications of TMDs in a building dates back to 1977, when in a 277*m* high skyscraper, the Hancock Tower in Boston (Fig. 1.17(a)), two TMDs were installed at the 58th floor of tower

(a) (b)

Fig. 1.17 – (a) Hancock Tower (Boston, USA); (b) Citicorp Center (New York, USA).

Each unit measures approximately $5.2 \times 5.2 \times 1m$ and consists of a steel container filled with lead, with a weight of 300*t*, connected to the structure with shock absorbers; with this system structural response reductions up to the 50% have been obtained.

Another of the first applications, dating back to 1978, is the Citicorp Center, a tower of 278*m* in New York (Fig. 1.17(b)). The system consists of a concrete block of 410*t* connected to the structure through a set of two spring mechanisms, installed at the 63rd floor and allowing for a reduction of the wind induced displacements up to the 40%.

Finally, a very recent and world famous TMD can be found in the Taipei Financial Center, known as Taipei 101 (Fig. 1.18), Taipei in Taiwan. The building with its 508*m* is the fourth highest in the world and includes an internal TMD pendulum weighing 660*t* (Fig. 1.19(a)), and two other, later installed, TMDs, of 4.5*t* each (Fig. 1.19(b)).

Many other applications of TMDs can be found around the world, some of them are listed in Fig. 1.20.

Fig. 1.18 – The Taipei 101 (Taipei, Taiwan).

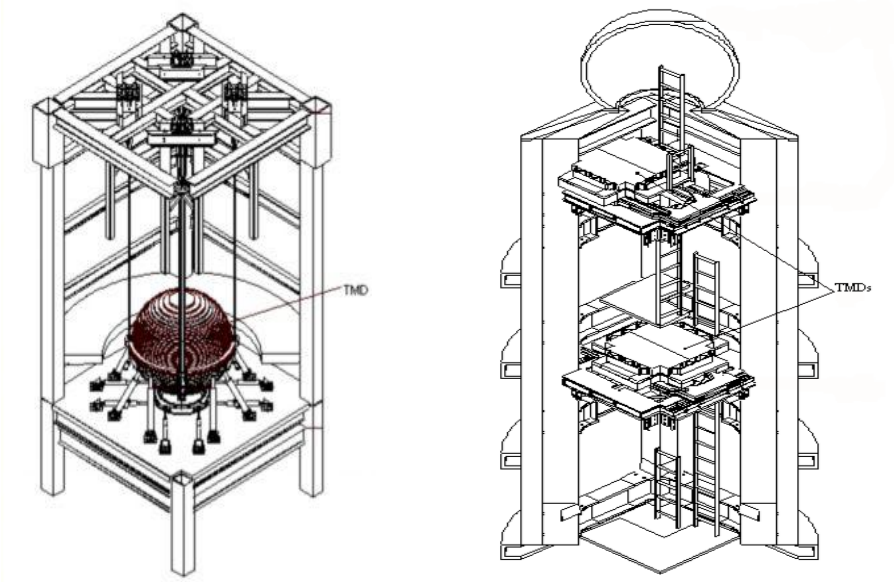

(a) (b)

Fig. 1.19 – (a) Pendulum TMD; (b) pinnacle type TMDs.

Name and type of structure	City/country	Type and number of dampers	Date of installation
CN TowerTV antenna (553 m)	Toronto, Canada	PTMD (Pen.)	1975
John Hancock Building (244 m)	Boston, USA	2 PTMDs	1977
City Corp Center (278 m)	New York, USA	PTMDs	1978
Sydney Tower (305 m)	Sydney, Australia	PTMD (Pen.)	1980
Al Khobar 2 chimney (120 m)	Saudi Arabia	PTMD	1982
Ruwais Utilities chimney	Abu Dhabi	PTMD	1982
Deutsche Bundespost cooling tower (278 m)	Nurnberg, Germany	PTMD	1982
Yanbu Cement Plant chimney (81 m)	Saudi Arabia	PTMD	1984
Hydro-Quebec wind generator	Canada	PTMD	1985
Chiba Port Tower (125m)	Chiba, Japan	2 PTMDs (SP)	1986
Pylon, Aratsu Bridge (cable-stayed)	Japan	PTMD	1987
Pylon, Yokohama Bay Bridge (cable-stayed)	Yokohama, Japan	PTMD	1988
Bin Quasim Thermal Power Station (70 m)	Pakistan	PTMD	1988
Tiwest Rutile Plant chimney (43 m)	Australia	PTMD	1989
Fukuoka Tower (151 m)	Fukuoka, Japan	PTMDs (SP)	1989
Higashiyama Sky Tower (134 m)	Nagoya, Japan	2 PTMDs	1989
Pylon, Bannaguru Bridge	Japan	PTMD	1990
Crystal Tower (157 m)	Osaka, Japan	2 PTMDs	1990
Hibikiryokuchi Sky Tower (135 m)	Kitakyushu, Japan	PTMD	1991
Huis Ten Bosch Domtoren	Nagasaki, Japan	PTMDs	1990
HKW chimney (120 m)	Frankfurt, Germany	PTMD	1992
BASF chimney (100 m)	Antwerp, Belgium	PTMD	1992
Siemens power station (70 m)	Killingholme, UK	PTMD	1992
Rokko Island P&G (117 m)	Kobe, Japan	PTMD (Pen.)	1993
Al Taweelah chimney (70 m)	Abu Dhabi	PTMD	1993
Akita Tower (112 m)	Akita, Japan	PTMD	1994
Chifley Tower (209 m)	Sydney, Australia	PTMD (Pen.)	1994
Washington National Airport Tower	Washington, D.C.,USA	PTMD	1997
Sendai AERU	Sendai, Japan	PTMD	1998
Peronas Twin Towers (452 m)	Kuala Lumpur , Malaysia	12 PTMDs	1998
Wichita Pedestrian Bridges (98 m, 74 m)	Kansas, USA	PTMD	2000
Trump World Tower (269 m)	New York, USA	PTMD	2001
Taipei 101 (508 m)	Taipei, Taiwan	3 PTMDs	2002
Dublin Spire (120 m)	Dublin, Ireland	2 PTMDs	2003
Bloomberg Tower (246 m)	New York, USA	PTMD	2005
Sakhalin1 Drilling Rig Project	Sakhalin, Russia	PTMD	2005
Grand Canyon Skywalk (20 m)	Arizona, USA	3 PTMDs	2006
Shenzhen Bridge (3,500 m, cable-stayed bridge)	Hong Kong , China	7 PTMDs	2007
Ironton-Russell Bridge (781 m)	Ironton,Ohio : Russell, Kentucky	PTMD	2008

PTMD = Passive Tuned Mass Damper, Pen = Pendulum, SP = slide-platform

Fig. 1.20 – List of buildings with TMDs (Chaiviriyawong e Prachaseree, 2009).

1.4.3 The equations of motion

Consider a shear-type single-degree-of-freedom structure (main system) subjected to a base excitation $\ddot{x}_g(t)$ (Fig. 1.21(a)), whose equation of motion can be written as

$$M\ddot{x}(t)+C\dot{x}(t)+Kx(t)=-M\ddot{x}_g(t) \tag{1.1}$$

where $x(t)$ is the relative displacement of the main system and M, C and K are the mass, damping and stiffness parameters of the main structure respectively.

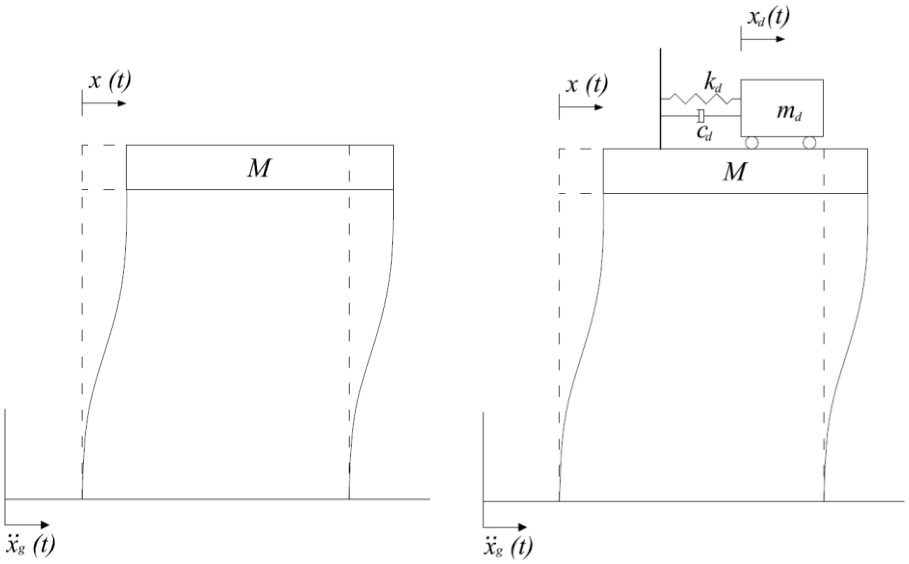

Fig. 1.21 – (a) Main system; (b) System connected to the TMD device.

Let the motion of the main system be controlled through a TMD device (Fig. 1.21(b)) possessing mass m_d, stiffness k_d and damping c_d. Clearly, because of the base acceleration, the mass *M* of the main system will be subjected to a displacement in the horizontal direction $x(t)$, and the TMD mass displacement in the horizontal direction will be $x_d(t)$.

Natural frequency and damping ratio of the main system can be defined respectively as

$$\omega_1 = \sqrt{\frac{K}{M}} \tag{1.2}$$

$$\zeta_1 = \frac{C}{2M\omega_1} \tag{1.3}$$

Analogous relations can be obtained for the TMD parameters

$$\omega_d = \sqrt{\frac{k_d}{m_d}} \tag{1.4}$$

$$\zeta_d = \frac{c_d}{2m_d\omega_d} \tag{1.5}$$

Finally the following parameters, useful for the optimal design of the TMD device, can be introduced

$$\nu_d = \frac{\omega_d}{\omega_1} \tag{1.6}$$

$$\mu_d = \frac{m_d}{M} \tag{1.7}$$

where ν_d is the so-called tuning frequency ratio and μ_d is the mass ratio.

Since the structure in Fig. 1.21(b) is a two degrees-of-freedom linear system, its equations of motion can be directly written as

$$\begin{cases} M\ddot{x}+\left(C+c_d\right)\dot{x}-c\dot{x}_d+\left(K+k_d\right)x-k_d x_d=-M\ddot{x}_g \\ m_d\ddot{x}_d-c_d\dot{x}+c_d\dot{x}_d-Kx+k_d x_d=-m_d\ddot{x}_g \end{cases} \tag{1.8}$$

Substituting Eqs. (1.4)-(1.7) into Eq. (1.8) yields the equations of motion in canonical form as

$$\begin{cases} \ddot{x}+\left(2\omega_1\zeta_1+2\mu_d\omega_d\zeta_d\right)\dot{x}-2\mu_d\omega_d\zeta_d\dot{x}_d+\left(\omega_1^2+\mu\omega_d^2\right)x_1-\mu_d\omega_d^2 x_d=-\ddot{x}_g \\ \ddot{x}_d-2\omega_d\zeta_d\dot{x}+2\omega_d\zeta_d\dot{x}_d-\omega_d^2 x+\omega_d^2 x_d=-\ddot{x}_g \end{cases} \tag{1.9}$$

If the case of a generic forcing function $f\left(t\right)$ acting directly on the main structure is considered, Eq. (1.9) can be modified as

$$\begin{cases} \ddot{x}+\left(2\omega_1\zeta_1+2\mu_d\omega_d\zeta_d\right)\dot{x}-2\mu_d\omega_d\zeta_d\dot{x}_d+\left(\omega_1^2+\mu\omega_d^2\right)x_1-\mu_d\omega_d^2 x_d=\dfrac{f\left(t\right)}{M} \\ \ddot{x}_d-2\omega_d\zeta_d\dot{x}+2\omega_d\zeta_d\dot{x}_d-\omega_d^2 x+\omega_d^2 x_d=0 \end{cases} \tag{1.10}$$

1.4.4 Optimization of the design parameters

The aim of the design of any control system for the reduction of unwanted vibrations, is to optimize the damper parameters to maximize its effectiveness. In this regard, the main TMDs parameters are certainly the frequency ω_d (Eq. (1.4)) or equivalently the frequency ratio ν_d in Eq.(1.6), and the damping ratio ζ_d in Eq. (1.5). Other parameters, such as the mass ratio μ_d, are generally obtained by practical considerations and geometrical constraints, thus their optimization is not generally considered.

One of the first studies in this direction is due to Den Hartog (1956). In his paper, the author analyzed the behavior of SDOF oscillator connected to a TMD and subjected to an external harmonic excitation $f(t) = P_0 e^{i\Omega t}$, assuming no damping in the main system $(\zeta_1 = 0)$. Then he studied the influence of damping ratio ζ_d on the dynamic magnification factor (DMF), defined as

$$DMF = \frac{x_{\max}}{x_{st}} \tag{1.11}$$

where $x_{\max}$ is the maximum response of the main system in steady state conditions, while $(x_{st} = P_0/K)$ is the static displacement produced by the maximum force $f(t) = P_0$ when applied statically to the structure.

Figure 1.22 shows a typical plot of the DMF in Eq. (1.11) as a function of the nondimesional excitation frequency $(\tilde{\beta} = \Omega/\omega_1)$ for $\nu_d = 1$ (tuned case), $\mu_d = 0.01$, and several values of the damping ratio ζ_d. As shown in this figure, without absorber damping $(\zeta_d = 0)$ the response amplitude of the combined system is infinite at two new resonant frequencies, while, exactly for $\tilde{\beta} = 1$, the response amplitude vanishes. On the hand, if the TMD damping is infinite the two masses are virtually fixed together, forming a new SDOF system with an increased mass $(M + m_d)$ and a slightly decreased resonant frequency. Therefore somewhere between these extremes there must be an optimal value of ζ_d for which the response reaches a minimum for broad band excitation.

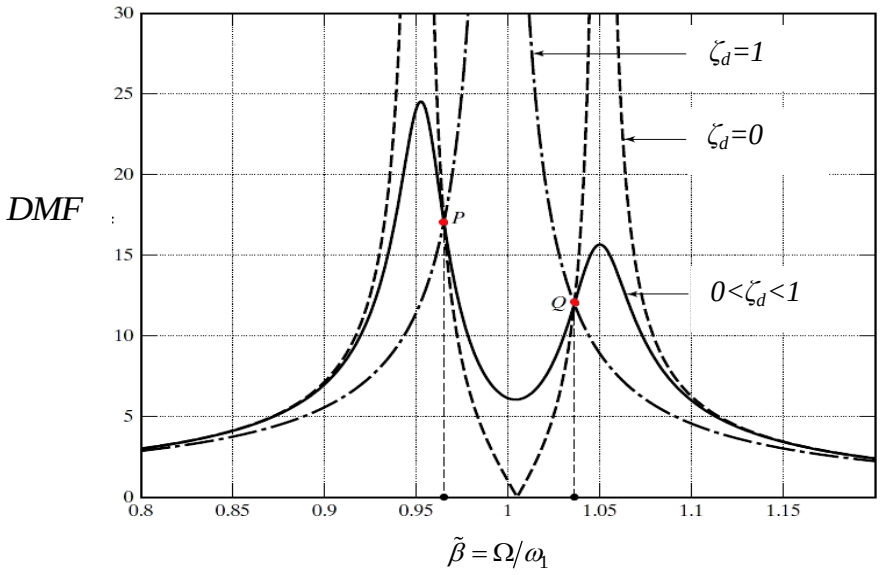

Fig. 1.22 – DMFs for various values of damping ratio ζ_d $\left(\mu_d = 0.01; \gamma_d = 1\right)$.

Figure 1.22 shows also another important phenomenon which occurs in case of an undamped main system. Specifically, for a certain value of γ_d and independently of the absorber damping ratio ζ_d, there exist two invariant points *P* and *Q* where all response curves possess the same value of the DMF. Once the mass ratio μ_d has been set, the location of such fixed points depends only on the frequency ratio ν_d, that can be varied until it reaches a value for which the minimum possible DMF is obtained for both *P* and *Q*. Therefore the objective of minimal structural response is accomplished by demanding that the invariant points have equal heights, i.e. equal DMF. This can be achieved by the correct choice of ν_d and subsequently ζ_d can be employed to adjust the response curves to pass with horizontal tangent through *P* and *Q* (Fig. 1.23).

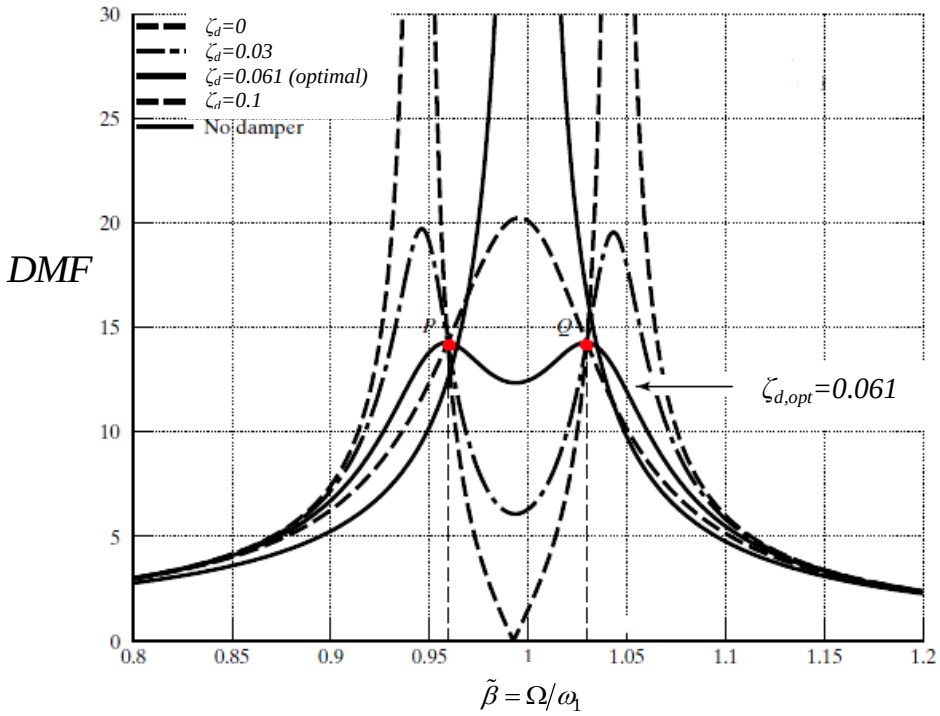

Fig. 1.23 – DMFs for optimal value of ν_d $\left(\mu_d = 0.01;\ \nu_{d,opt} = 0.987;\ \zeta_{d,opt} = 0.061\right)$.

Following this procedure, Den Hartog (1956) obtained the optimum frequency ratio and damping ratio for the undamped main system under harmonic external excitation as

$$\nu_{d,opt} = \frac{1}{1+\mu_d} \tag{1.12}$$

$$\zeta_{d,opt} = \sqrt{\frac{3\mu_d}{8(1+\mu_d)}} \tag{1.13}$$

After Den Hartog's study, many other procedures have been proposed in order to find the optimal tuning ratio and damping ratio, for undamped primary structures under different kind of loading conditions (Warburton,

1982; Rana and Soong, 1998; Hoang et al., 2008; Adam et al., 2003). Table 1.1 reports some of the optimal TMD parameters for various excitations.

Table 1.1 - Optimal TMD parameters for loading conditions of a SDOF system.

Type of excitation	**Point of application**	$\nu_{d,opt}$	$\zeta_{d,opt}$
$P_0 e^{i\Omega t}$	Structure	$\frac{1}{1+\mu_d}$	$\sqrt{\frac{3\mu_d}{8(1+\mu_d)}}$
$\Omega^2 x_g \sin(\Omega t)$	Base	$\frac{1}{1+\mu_d}$	$\sqrt{\frac{3\mu_d}{8(1+\mu_d)}}$
Stationary random noise	Structure	$\sqrt{\frac{1+\mu_d/2}{(1+\mu_d)^2}}$	$\sqrt{\frac{\mu_d(1+3\mu_d/4)}{4(1+\mu_d)(1+\mu_d/2)}}$
Stationary random noise	Base	$\sqrt{\frac{1-\mu_d/2}{(1+\mu_d)^2}}$	$\sqrt{\frac{\mu_d(1-\mu_d/4)}{4(1+\mu_d)(1-\mu_d/2)}}$

It is worth noting that when the damping ratio of the main system ζ_1 is not negligible, the fixed points *P* and *Q* are no longer uniquely determined. Therefore, numerical procedures are required to derive optimal values of TMD parameters. For instance Warburton (1982) applied a optimization criterion based on the minimization of the transfer function amplitude of the main system $R = |H(\omega)|$. In this manner, optimal values of ν_d and ζ_d can be obtained solving the following set of equations

$$\begin{cases} \dfrac{\partial R}{\partial \gamma_d} = 0 \\ \dfrac{\partial R}{\partial \zeta_d} = 0 \end{cases} \tag{1.14}$$

These equations are generally nonlinear, therefore numerical solutions are often required. In this regard, optimal values have been reported in table form by Warburton (1982), for various values of the mass ratio and main system damping ratio ζ_1, as shown in Fig. 1.24.

μ_d	ζ_1	R_{opt}	$v_{d.opt}$	$\zeta_{d.opt}$
0.01	0	10.138	0.9876	0.04981
	0.01	7.743	0.9850	0.04981
	0.02	6.205	0.9819	0.04981
	0.05	3.798	0.9704	0.04982
	0.1	2.249	0.9436	0.04982
0.03	0	6.058	0.9636	0.08566
	0.01	5.110	0.9592	0.08566
	0.02	4.424	0.9545	0.08566
	0.05	3.109	0.9380	0.08567
	0.1	2.036	0.9032	0.08569
0.1	0	3.602	0.8861	0.1527
	0.01	3.285	0.8789	0.1527
	0.02	3.014	0.8714	0.1528
	0.05	2.399	0.8468	0.1529
	0.1	1.765	0.7991	0.1531
0.2	0	2.865	0.7906	0.2097
	0.01	2.680	0.7815	0.2098
	0.02	2.516	0.7721	0.2099
	0.05	2.113	0.7421	0.2103
	0.1	1.649	0.6862	0.2112

Fig. 1.24 – Optimal TMD parameters for a damped SDOF main system (Warburton, 1982).

From this figure it is apparent that for fixed mass ratio μ_d, ζ_1 has little effects on the optimal TMD parameters. Specifically for increasing values of the structural damping ratio, the optimal tuning ratio decreases while the optimal damping ratio experiences small variations.

Chapter 2

The Tuned Liquid Column Damper

2.1 Introduction

Vibration control by means of liquid motion was proposed for the first time by Frahm, a German shipbuilder, at the end of the 19th century, when a device realized connecting two tanks filled with water (Fig. 2.1) was successfully used to reduce ship rolling motion (Den Hartog, 1956). In this regard, first studies on these devices for structural control applications are due to Kareem and Sun (1987), Modi and Welt (1987) and Fujino et al. (1988).

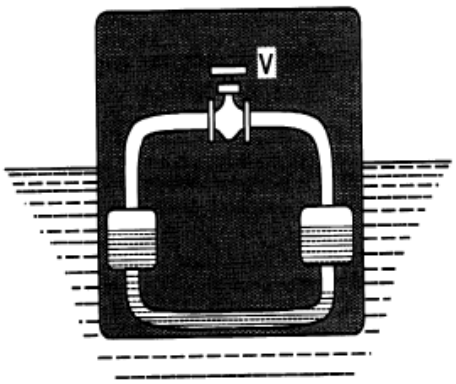

Fig. 2.1 – Frahm's anti-rolling tank (Den Hartog, 1956).

Based on these works, Sakai et al. (1989, 1991) proposed a novel type of vibration control device for the pylons of cable-stayed bridges, the so-called Tuned Liquid Column Damper (TLCD).

Unlike classical TLDs (see Section 1.2.5), which depend on the movement of the liquid (namely the sloshing) in rectangular or circular vessels to reduce structural vibrations, TLCDs dissipate vibrations through a combined action that involves the movement of mass of liquid inside a U-shaped container. Specifically, when the structure experiences vibration, its energy is transferred to the TLCD liquid. The motion of the main structure is then reduced by the TLCD through the gravitational restoring force acting on the displaced liquid, and energy dissipated by viscous interaction between the liquid and TLCD rigid wall. Clearly, if higher dissipation is needed, orifices can be included inside the TLCD container. Figure 2.2 depicts a schematic drawing of a TLCD device.

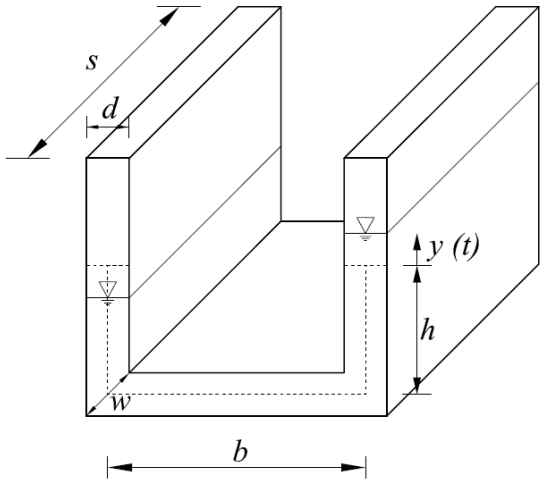

Fig. 2.2 – Tuned Liquid Column Damper.

It is worth noting that TLCDs offer some interesting advantages over other commonly used passive control devices, such as TMDs, as well as over other systems based on liquid motion, including TLDs (Ziegler, 2007). Specifically:

- Easy implementation;
- Low cost and almost no maintenance needed, because no mechanical systems are required;
- No need to add external mass to the primary structure to be controlled, since the container can be used for building water supply, unlike a TMD where the dead weight of the mass has no other functional use;
- TLCDs can take almost any shape, so that they can also be easily installed in existing structure;
- Unlike their counterpart, the TLDs, the working mechanism of TLCDs is more simple, so that a mathematical model that accurately describes the dynamic of TLCD controlled systems can be formulated;
- Damping in TLCDs can be controlled by changing orifices openings, thus even enabling to implement active control mechanism if necessary;
- TLCDs frequency can be easily changed, simply adjusting the liquid column height inside the container. This is an attractive feature, should one need to retune the damper in case of a change in the primary system frequency.

All these characteristics make TLCDs a particularly attractive passive control device and, therefore, an interesting alternative among other systems.

On this base, in this Chapter the main features of TLCDs will be discussed in detail. Specifically, in Section 2.2 a brief literature review in the area of TLCD is presented. Relevant literature is also referenced at appropriate places in later chapters of the dissertation. Some of the existing applications of these dampers, especially in civil engineering structures, are discussed in Section 2.3. Further, the governing equations for the motion of the liquid inside the device, as well as of TLCD controlled structures, are derived in Section 2.4. In Section 2.5, the existing approaches in literature for the optimal design of these dampers are discussed. Finally, in Section 2.6, control performances of TLCDs are investigated, both numerically and experimentally, and comparison with TMD device is also considered to further assess the efficiency of these systems.

2.2 Literature review on TLCD systems

As already stated, it was firstly Sakai et al. (1989) who introduced TLCDs as an effective device for reducing vibrations of civil engineering structures. In this regard, some of the earliest studies on TLCDs for the control of wind excited structures can be found in Xu et al. (1992) and Balendra et al. (1995), while the performance of TLCDs for applications to seismic excited structures was studied by Won et al. (1997) and Sadek et al. (1998).

Gao and Kwok (1997) studied the effectiveness of TLCDs in controlling structural vibration, and estimated the optimum parameters of TLCDs for maximum reduction of peak structural response to harmonic excitation. Their results showed that the mass ratio and structural damping ratio govern the optimum parameters. Related studies were conducted by Balendra et al. (1995, 1998, 1999), Chang and Hsu (1998) and Chang (1999), Yalla and Kareem (2000) and Debbarma et al. (2010). Readers are referred to Section 2.5 for a detailed analysis of relevant studies on optimum TLCD parameters evaluation.

Multiple Tuned Liquid Column Dampers (MTLCDs) with natural frequencies distributed around the natural frequency of the primary system requiring control have been studied extensively by Fujino and Sun (1993), Sadek et al (1998), Chang et al. (1998), Gao et al. (1999), and Yalla and Kareem (2000). Such systems lead to smaller sizes of TLCDs which would improve their construction, installation and

maintenance, and also offer a range of possible spatial distributions in the structure. The tuned multiple spatially distributed dampers, offer a significant advantages over a single damper since multiple dampers, when strategically located, are more effective in mitigating the motions of buildings and other structures undergoing complex motions (Bergman et al. 1989).

Experimental studies on these devices have been conducted for the first time by the same Sakai et al. (1991) verifying the performance of a TLCD installed in a small-scale model of a pylon of a cable-stayed bridge. Balendra et al. (1995) conducted tests on the TLCDs with shaking tables, to study the effect of different opening ratio of the inner orifice on the motion of the liquid. Xue et al. (2000) have presented an experimental study on the application of TLCDs for the reduction of the pitching motion of the structures and have conducted some tests to delineate the influence of the different parameters of the damper on the performance of TLCDs. More recently Colwell and Basu (2008) have considered the use of various liquids in TLCDs, testing the effect of viscosity on the properties of the control system, demonstrating that TLCDs performance deteriorates at increasing fluid viscosity.

A rather small variation of TLCDs, the so-called Liquid Column Vibration Absorbers (LCVAs), has been proposed by Hitchcock et al. (1997a), considering an intermediate horizontal tube with different cross sectional area with respect to the vertical tubes of the U-shaped container. Results showed that since the vertical and the horizontal parts of the container have different dimensions, some benefits can be obtained such as easier adjustment of the frequencies and wider range of reachable

natural frequencies. In fact, LCVA natural frequency is determined not only by the height of the liquid column but also by its geometrical configuration.

Experimental tests on such devices have been conducted by Hitchcock et al. (1997b), for LCVAs without orifices inside the tank, to determine the features affecting their characteristics. Specifically natural frequency of LCVA was found to depend also on the ratio of the cross-sectional area of the vertical columns to the cross-sectional area of the horizontal column.

One of the major disadvantages of TLCDs and LCVAs is that their control effect is unidirectional; accordingly they may be installed in structures that oscillate with a single prevalent direction, but not on structures oscillating in several directions. To overcome this problem, systems such as the Double Tuned Liquid Column Damper (DTLCD), formed by two TLCD positioned orthogonally to one another (Fig. 2.3) (Sakai et al., 1991), have also been proposed.

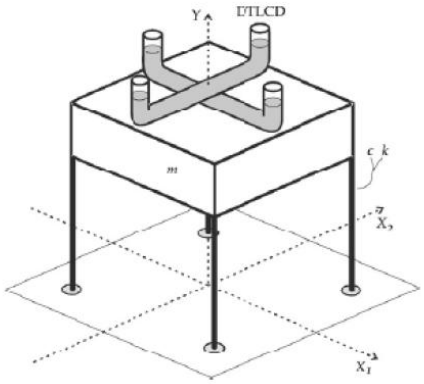

Fig. 2.3 – Double Tuned Liquid Column Damper.

Also a fluid-dynamic hybrid system, called Hybrid Tuned Liquid Column Damper (HTLCD), was developed to overcome this problem (Fig. 2.4). This system consists of a unidirectional TLCD fixed on a rotating circular platform, whose motion is controlled by an electro-mechanical device (Battista et al., 2008). This hybrid system is passive in the production of the control forces to reduce the amplitude of the oscillations, while it is of the active type in the research phase of the prevailing direction of the action.

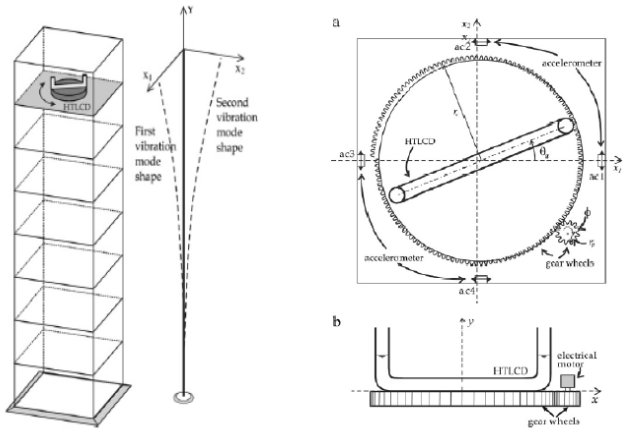

Fig. 2.4 – Hybrid Tuned Liquid Column Damper (Battista et al., 2008).

Finally, a different type of TLCD, called Pressurized Tuned Liquid Column Damper (PTCLD) (Ziegler, 2008; Hochainer, 2005; Hochainer and Ziegler, 2006), has been proposed generating a pressure inside the two air chambers sealed at both ends of a TLCD. In this way the frequency can be adjusted not only by varying the height of the liquid column, but also the pressure inside of its two air chambers.

In recent years several applications of modified TLCD devices have been studied in order to enhance the control performance. In Min et al. (2014) a two-way column/sloshing liquid damper has been proposed; in Sarkar and Gudmestad (2014) the TLCD has been coupled to a pendulum mass damper; Al-saif et al. (2011) investigate on a modified version of TLCD in which a moving ball is introduced in the horizontal part of the pipe; in Ziegler (2008) a novel design of a torsional sealed liquid column-gas damper (TLCGD) has been presented in order to enhance the efficiency in strongly asymmetric buildings.

2.3 Applications of TLCDs for structural control

Even though TMDs, and their modifications, represent the great majority of currently applied passive vibration control devices with auxiliary mass, there exist several real applications of TLCDs systems for vibration mitigation. To show the applicability of these devices, in this Section some of these examples are presented.

One of the first installations of TLCD in a building dates back to the mid-90s (Teramura and Yoshida, 1996), in the Sofitel Hotel (Tokyo, Japan), a 26 story steel building with a height of 106*m* (Fig. 2.5).

Fig. 2.5 – Sofitel Hotel (Tokyo, Japan).

This building has a large height to width ratio and it is therefore wind sensitive. For this reason a TLCD with a period adjustment equipment (LCD-PA) has been built, thus making it possible to adjust the movement of the liquid within the TLCD, as shown in Fig. 2.6.

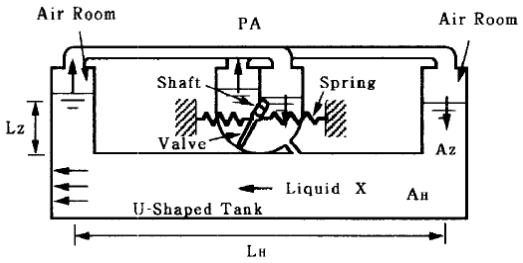

Fig. 2.6 – LCD-PA.

The device installed in the Sofitel Hotel is a bidirectional TLCD with a rectangular base, with four Period Adjustment (PA) devices, a total weight of 58*t* and a weight of the liquid only of 36*t*. The tank has a part in which the liquid is free to move horizontally, four vertical sections at each corner and four air chambers that constitute the PA, separated by dividers; the PA is housed between two vertical sections, as shown in Fig. 2.7.

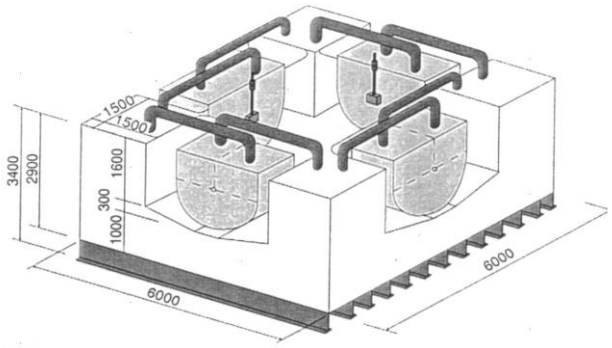

Fig. 2.7 – The built system.

It is worth noting that tests have shown that this system has effectively reduced maximum accelerations of almost 50% with respect to the uncontrolled structure.

Another interesting and more recent application of TLCDs can be found in the One Wall Centre (Vancouver, Canada) (Fig. 2.8).

Fig. 2.8 – The One Wall Centre (Vancouver, Canada).

Completed in 2001 and with a height of 150*m*, the tower contains two TLCDs at the top, each one with 230*t* of water, installed to reduce wind induced vibrations (Fig. 2.9).

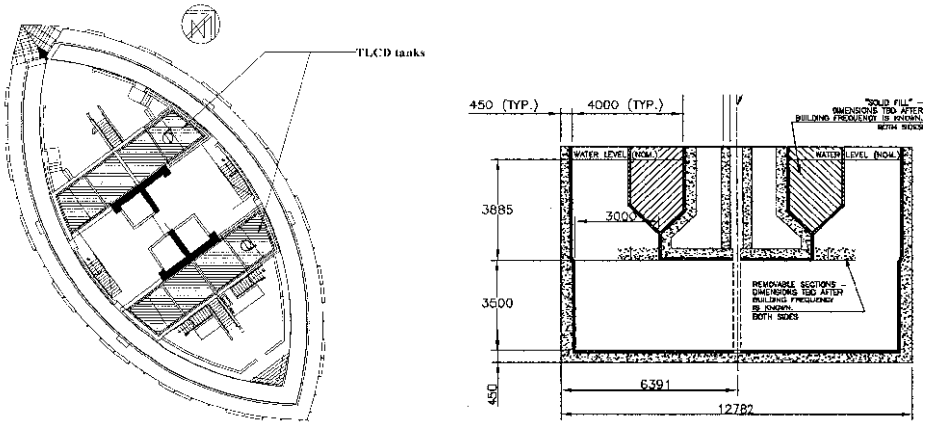

(a) (b)

Fig. 2.9 – TLCD design for One Wall Centre: (a) top floor plan; (b) cross-section of one of the TLCDs.

Examples of TLCDs controlled structures can be found also in the USA. For instance the Random House Tower (New York, USA) (Fig. 2.10) is a skyscraper completed in 2003 and with an height of 208*m*, containing two orthogonal TLCDs of 430*t* and 290*t* respectively (Fig. 2.11).

Fig. 2.10 – The Random House Tower (New York, USA).

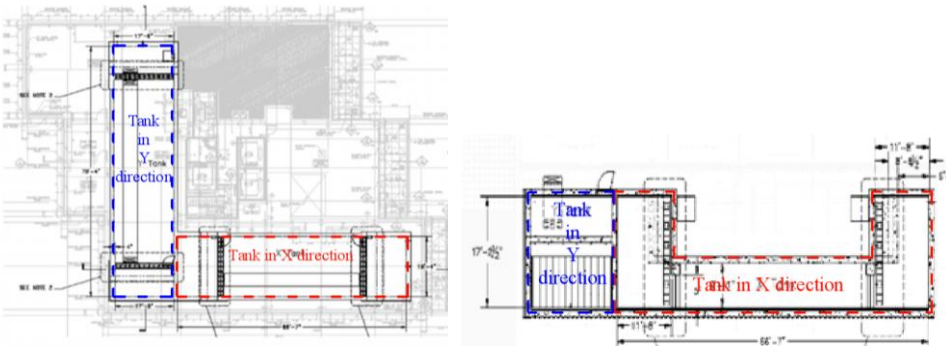

(a) (b)

Fig. 2.11 – TLCD design for the Random House Tower: (a) 50° floor plan; (b) East-West section through building top.

Another example can be found in the Comcast Center or One Pennsylvania Plaza (Philadelphia, USA). This tower, completed in 2008 and with a height of 297*m*, constitutes the world largest existing TLCD, with a mass of liquid of 1.300*t* (Fig. 2.12).

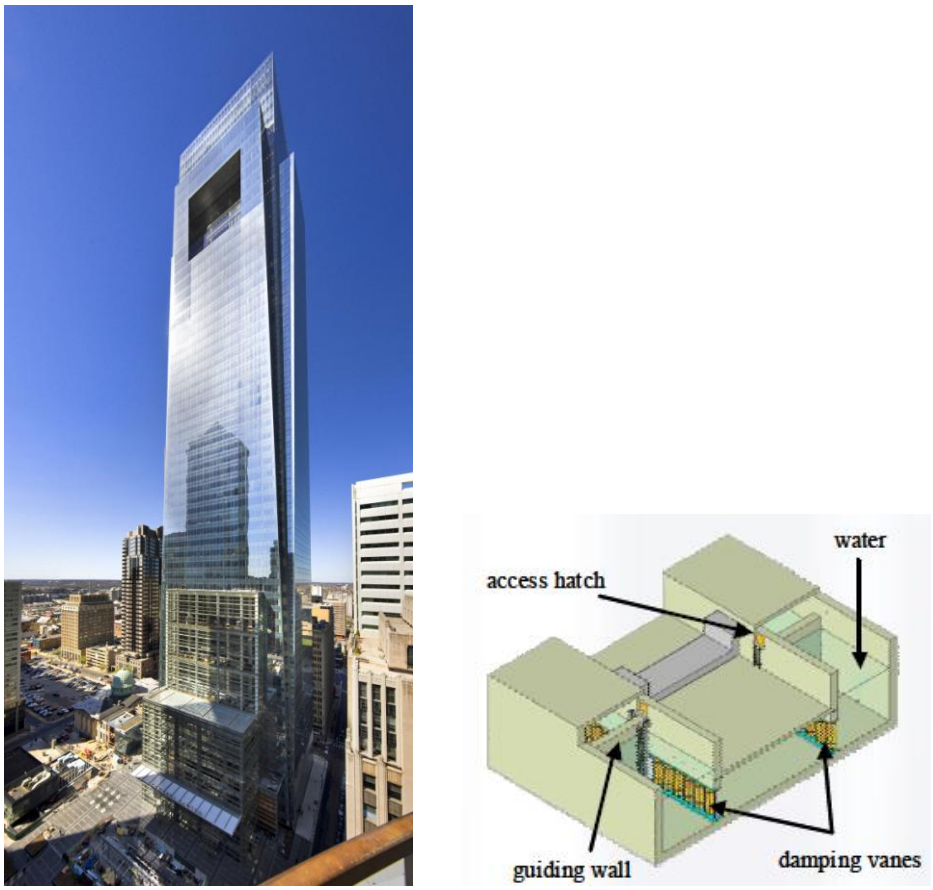

(a) (b)

Fig. 2.12 – TLCD design for the Comcast Center (Philadelphia, USA): (a) the tower; (b) 3D rendering of the TLCD tank.

In the early design stages of the project, space was allocated at the top of the building for the supplementary damping system. To optimize

lateral drift serviceability performance, the tower required supplementary damping in its most slender axis only; therefore, one large TLCD was designed instead of the more typical two orthogonal TLCD configurations. Overall structural cost savings (in millions of dollars) have been obtained by using TLCD's to achieve occupant comfort and lateral drift serviceability criteria.

Finally, it is worth mentioning that TLCDs have been planned for the proposed Millennium Tower (Tokyo, Japan), a 170-floor (840*m* high) skyscraper, designed by architect Sir Norman Foster. Due to this super-tall building exposure to typhoons, external damping sources are needed to control the wind induced vibrations. In addition to massive steel blocks at the top, there are water tanks with ducts between them. The water would provide passive resistance under normal conditions, but under high winds, the sensors trigger a pumping mechanism, changing the control mode from passive to active. Figures 2.13 and 2.14 show the rendering of the structure and the scheme of the circular TLCD concept in this tower.

Fig. 2.13 – The Millennium Tower (Tokyo, Japan).

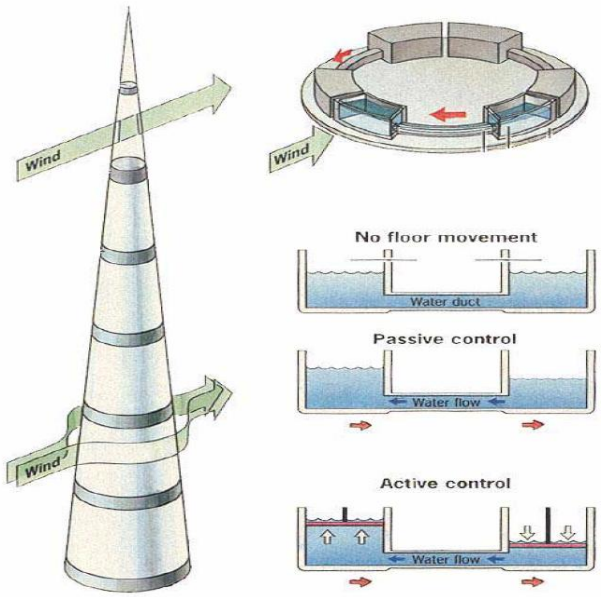

Fig. 2.14 –The Millennium Tower: passive and active TLCD concept.

2.4 The equations of motion

As shown in previous Section 1.2.5, TLCDs are passive control devices belonging to the family of Liquid Vibration Absorbers systems. Similarly to the more common TMDs, TLCD frequency needs to be appropriately tuned to the structural frequency, and TLCD damping ratio needs to be correctly chosen, in order to reach the best performance in terms of structural vibration control. Clearly, before presenting the classical procedures proposed in literature for the optimal choice of TLCDs design parameters, the classical equation of motions for the TLCD liquid displacements and TLCD controlled structures displacements have to be introduced.

In this regard, in Section 2.4.1 the equation of motion of the TLCD device only will be derived, whereas in Section 2.4.2 the motion of TLCD controlled system will be taken into account, considering the cases of base excited structures.

2.4.1 Governing equations of TLCD devices

Consider a TLCD device as shown in Fig. 2.15, excited at the base with an acceleration $\ddot{x}_g(t)$. The vertical and the horizontal column cross-sectional areas are A_v and A_h, respectively. Since the transversal dimension of the vertical columns is generally much smaller than the

horizontal length, during the motion the liquid volume inside the vertical columns is assumed to move vertically relative to the tube with an average velocity $\dot{y}(t)$. Further, from the continuity equation, the horizontal liquid velocity in the horizontal duct has an average velocity $\tilde{v}\dot{y}(t)$, where $\tilde{v}$ is the area ratio of the vertical column to the horizontal column of the TLCD, that is $(\tilde{v} = A_v / A_h)$.

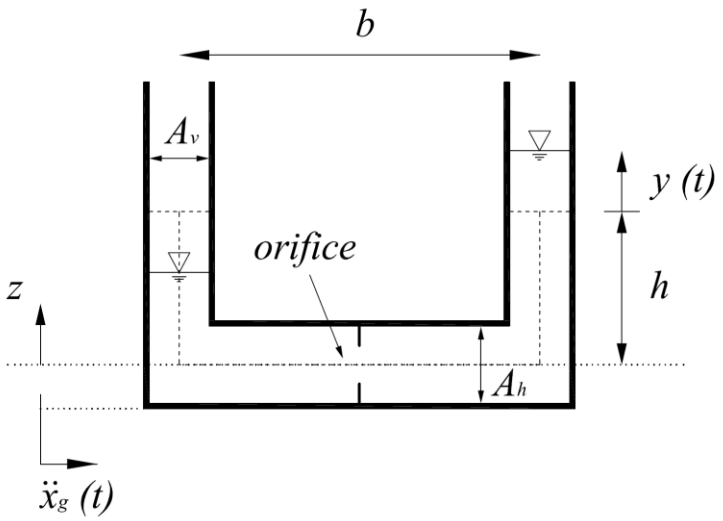

Fig. 2.15 – TLCD device.

Using the energy principles, the equation of motion of the liquid displacement $y(t)$ can be derived from the Lagrange equation

$$\frac{\partial}{\partial t}\left[\frac{\partial(T-U)}{\partial \dot{y}}\right] - \frac{\partial(T-U)}{\partial y} = Q_y \tag{2.1}$$

where T and U are the total kinetic energy and the total potential energy of the system, respectively, and Q_y is the total non-conservative force in the direction of $y(t)$, related to the head loss.

In particular, assuming unsteady and non-uniform flow (Hitchcok et al., 1997a), negligible sloshing behavior on the liquid surface and dimension of the column cross-section much smaller than the horizontal length of a TLCD (Chaiviriyawong et al., 2007), the kinetic energy T and potential energy U can be written as (Chang and Hsu, 1998)

$$T = \frac{1}{2}\int_{V_L} \rho\left(\dot{y}^2 + \dot{x}_g^2\right) dV + \frac{1}{2}\int_{V_H} \rho\left(\tilde{v}\dot{y} + \dot{x}_g\right)^2 dV + \frac{1}{2}\int_{V_R} \rho\left(\dot{y}^2 + \dot{x}_g^2\right) dV = \\ = \rho A_v h\left(\dot{y}^2 + \dot{x}_g^2\right) + \frac{1}{2}\rho A_h b\left(\tilde{v}\dot{y} + \dot{x}_g\right)^2 \tag{2.2}$$

$$U = \int_{V_L} \rho g z\, dV + \int_{V_R} \rho g z\, dV = \rho A_v g\left(h^2 + y^2\right) \tag{2.3}$$

where V_L and V_R are the volumes of the fluid in the left and right column respectively, V_H is the volume of fluid in the horizontal section of the TLCD, g is the gravitational acceleration, ρ is the density of liquid, h and b are the vertical and horizontal liquid length respectively, and z is the vertical coordinate measuring from a reference datum (see Fig. 2.15).

Substitution of Eq. (2.2) and (2.3) in Eq. (2.1) leads to the classical, and widely used equation of motion of the liquid in the TLCD (Sakai et al, 1989; Gao et al, 1999)

$$\ddot{y}(t) + \frac{1}{2}\frac{\xi}{L_e}\tilde{v}\left|\dot{y}(t)\right|\dot{y}(t) + \omega_2^2 y(t) = -\frac{b}{L_e}\ddot{x}_g(t) \tag{2.4}$$

where

$$L_e = 2h + \tilde{\nu} b \tag{2.5}$$

is defined as the effective liquid length, ξ is the head loss coefficient and

$$\omega_2 = \sqrt{\frac{2g}{L_e}} \tag{2.6}$$

is the natural frequency of liquid oscillation inside the TLCD container.

It can be observed that, if the simple case of uniform cross section $\left(\tilde{\nu} = 1\right)$ is considered, then $\left(L_e = L = 2h + b\right)$, which represents the total length of the liquid inside the TLCD.

It is worth stressing that, in order to obtain Eq. (2.4), the non-conservative force (see Sakai et al., 1989)

$$Q_y = -\frac{1}{2}\rho A_h \tilde{\nu}^2 \xi \left|\dot{y}(t)\right| \dot{y}(t) \tag{2.7}$$

has been used, which should take into account the head loss caused by the presence of an orifice inside the TLCD and the head losses caused by sharp-edged turn-elbow, the transition of the cross section in the vicinity of the elbow (Wu et al, 2005) and viscous interaction between the liquid and rigid container wall (Hitchcok et al., 1997a). Note that the absolute value of the liquid velocity which appears in Eq. (2.7), allows for the Q_y to be considered always opposed to the liquid flow.

2.4.2 Governing equations of TLCD controlled structures

Consider now a shear-type SDOF structure (main system) subjected to a base excitation $\ddot{x}_g(t)$, whose equation of motion can be written as

$$M\ddot{x}(t)+C\dot{x}(t)+Kx(t)=-M\ddot{x}_g(t) \tag{2.8}$$

where $x(t)$ is the relative displacement of the main system and M, C and K are the mass, damping and stiffness parameters of the main structure respectively.

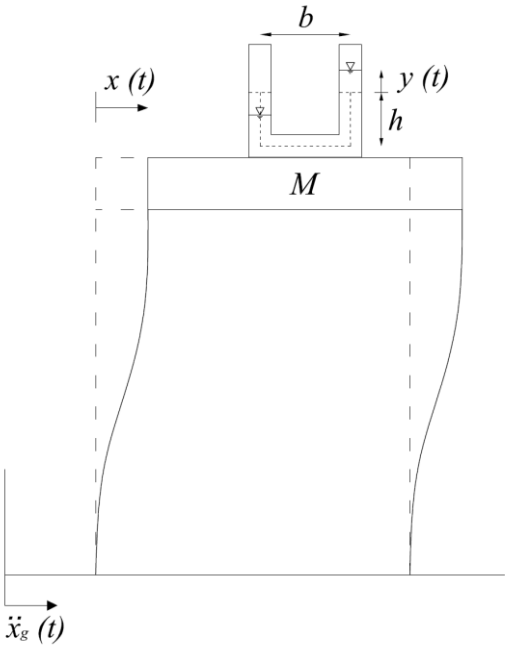

Fig. 2.16 – TLCD controlled system.

Let the motion of the main system be controlled through a TLCD device (see Fig. 2.16). Clearly, because of the base acceleration, the mass *M* of the structure will be subjected to a displacement in the horizontal direction $x(t)$, and the water level will consequently experience a displacement in the vertical direction $y(t)$. The equation of motion of this two degrees-of-freedom system can be derived through the Lagrange equations

$$\frac{d}{dt}\left[\frac{\partial(T-U)}{\partial \dot{x}}\right]-\frac{\partial(T-U)}{\partial x}=Q_x \tag{2.9}$$

$$\frac{d}{dt}\left[\frac{\partial(T-U)}{\partial \dot{y}}\right]-\frac{\partial(T-U)}{\partial y}=Q_y \tag{2.10}$$

where *T* and *U* are the total kinetic and potential energy respectively, and Q_x is the non-conservative force in the direction of $x(t)$.

As far as the potential energy *U* is concerned, it can be simply obtained as the sum of the potential energy of the liquid U_l and the potential energy of the structure U_s, given respectively as

$$U_l=\rho A_v g\int_0^{h-y} z dz+\rho A_v g\int_0^{h+y} z dz=\rho A_v g(h^2+y^2) \tag{2.11}$$

$$U_s=\frac{1}{2}Kx^2 \tag{2.12}$$

As far as the kinetic energy *T* is concerned, it can be simply obtained as the sum of the kinetic energy of the liquid T_l and the kinetic energy of the structure T_s, given respectively as

$$T_l = \frac{1}{2}\rho A_v (h-y)\left[\dot{y}^2 + \left(\dot{x}_g + \dot{x}\right)^2\right] + \frac{1}{2}\rho A_v (h+y)\left[\dot{y}^2 + \left(\dot{x}_g + \dot{x}\right)^2\right] + \frac{1}{2}\rho A_h b\left[\tilde{\nu}\dot{y} + \left(\dot{x}_g + \dot{x}\right)\right]^2 \tag{2.13}$$

$$T_s = \frac{1}{2}M(\dot{x} + \dot{x}_g)^2 = \frac{1}{2}M(\dot{x}^2 + \dot{x}_g{}^2 + 2\dot{x}\dot{x}_g) \tag{2.14}$$

Finally, assuming classical viscous damping for the structural system, the non-conservative force Q_x is given as

$$Q_x = -C\dot{x} \tag{2.15}$$

Substituting Eqs. (2.11-2.12) and (2.13-2.15) in Eqs. (2.9-2.10) and manipulating, leads to the classical equations of motion of TLCD controlled systems under a base excitation

$$M\ddot{x} + (2\rho A_v h + \rho A_h b)\ddot{x} + \rho A_h \tilde{\nu} b\,\ddot{y} + C\dot{x} + Kx = = -M\ddot{x}_g - (2\rho A_v h + \rho A_h b)\ddot{x}_g \tag{2.16}$$

$$(2\rho A_v h + \rho A_h b\tilde{\nu}^2)\ddot{y} + \rho A_h b\tilde{\nu}\ddot{x} + \frac{1}{2}\rho\xi A_h \tilde{\nu}^2 \dot{y}\left|\dot{y}\right| + 2\rho g A_v y = = -\rho A_h b\tilde{\nu}\,\ddot{x}_g \tag{2.17}$$

Rewriting yields the system

$$\begin{cases} \left(M + \rho A_v L_e\right)\ddot{x} + \rho A_h \tilde{\nu} b\,\ddot{y} + C\dot{x} + Kx = -\left(M + \rho A_v L_e\right)\ddot{x}_g \\ \rho A_h b\tilde{\nu}\ddot{x} + \rho A_v L_e \ddot{y} + \frac{1}{2}\rho\xi A_h \tilde{\nu}^2 \dot{y}\left|\dot{y}\right| + 2\rho g A_v y = -\rho A_h b\tilde{\nu}\,\ddot{x}_g \end{cases} \tag{2.18 a,b}$$

Finally, in the case in which $(\tilde{\nu} = 1)$, then

$$\begin{cases} (M+m)\ddot{x}(t) + m_h\ddot{y}(t) + C\dot{x}(t) + Kx(t) = -(M+m)\ddot{x}_g(t) \\ m_h\ddot{x}(t) + m\ddot{y}(t) + \frac{1}{2}\rho A\xi|\dot{y}(t)|\dot{y}(t) + 2\rho Agy(t) = -m_h\ddot{x}_g(t) \end{cases} \quad (2.19\text{ a,b})$$

where $(m = \rho AL)$ represents the total liquid mass in the TLCD device and $(m_h = \rho Ab)$ is the liquid mass of the horizontal portion only.

Equations (2.19) are then the equations of motion of the system that, even in the simple case in which main system behaves linearly, is a system of second-order nonlinear differential equations. In Eq. (2.19b), in particular, the second term represents the inertial force that opposes the motion with a corresponding mass of liquid equal to *m*, the damping effect is represented by the third term in which it appears the head-loss coefficient ξ; finally the last term in the first member represents the restoring force of the liquid mass, considering that the difference in piezometric level between the two liquid free surfaces is $2y(t)$. The terms $m_h\ddot{x}(t)$ and $-m_h\ddot{x}_g(t)$, represent the forces acting in opposite direction to that of the motion, when the TLCD container is subjected to an acceleration $(\ddot{x}(t) + \ddot{x}_g(t))$. These two terms imply, however, that the horizontal portion of the TLCD is always completely full of liquid.

Finally, dividing Eq. (2.19a) by M and Eq. (2.19b) by m, Eq. (2.19) can be recast in canonical form as

$$\begin{cases} (1+\mu)\ddot{x}(t) + \alpha\mu\ddot{y}(t) + 2\zeta_1\omega_1\dot{x}(t) + \omega_1^2 x(t) = -(1+\mu)\ddot{x}_g(t) \\ \alpha\ddot{x}(t) + \ddot{y}(t) + \frac{\xi}{2L}|\dot{y}(t)|\dot{y}(t) + \omega_2^2 y(t) = -\alpha\ddot{x}_g(t) \end{cases} \quad (2.20\text{ a,b})$$

where $\left(\zeta_1 = C/2M\omega_1\right)$ and $\left(\omega_1^2 = K/M\right)$ are the damping coefficient ratio and natural frequency of the main structure respectively,

$$\mu = \frac{m}{M} \tag{2.21}$$

is the mass-ratio between the liquid and the main structure, and

$$\alpha = \frac{b}{L} \tag{2.22}$$

is the ratio between the horizontal liquid length *b* and the total liquid length *L*, namely the so-called length ratio.

2.5 Optimization of the design parameters

All previous studies on TLCD indicate that highest damper control performance could be achieved only if its parameters are chosen properly. Therefore, an appropriate selection of the damper parameters should be crucial. However, due to inherent nonlinear liquid damping, a great computational effort is required to search the optimum parameters of TLCD numerically. Several studies have been then performed to determine optimal TLCD parameters.

In this regard, considering the case of harmonic excitation, interesting studies have been developed in (Shum, 2009; Wu et al., 2009, and Farshidianfar and Oliazadeh, 2009). Specifically in Shum (2009) a closed form solution scheme for explicit design formulas of TLCD parameters has been obtained for the case of undamped primary structures, by optimizing the response at the two invariant points and verified the results with those obtained from the conventional iterative method. Wu et al. (2009) introduced a closed form solution together with design tables for both uniform and non-uniform TLCDs, as quick guidelines for practical use. Further, Farshidianfar and Oliazadeh (2009), dealing with the problem of a structure connected to a TLCD and subject to a harmonic base excitation, concluded that better control performances are obtained for higher value of the mass ratio μ and higher value of the parameter α.

On the other hand, when concerned with earthquake type of loadings, these formulations may not model correctly the system behavior, leading to improper TLCD design parameters.

Dealing with earthquake ground motion, Won et al. (1996, 1997) investigated the seismic performance of TLCDs for the passive control of flexible structures using time-domain non-stationary random vibration analysis. In their works a non-stationary stochastic process with frequency and amplitude modulation is used to represent the earthquake strong motion, and a simple equivalent linearization technique is used to account for the nonlinear damping force in the TLCD. Furthermore a parametric study is conducted to investigate the effects of the mass ratio, head loss coefficient, and loading intensity on the TLCD performance. Sadek et al. (1998) investigated on the evaluation of design parameters for single and multiple-TLCDs in a deterministic framework. Wu et al. (2005) derived a design procedure for TLCDs for damped SDOF structures under a white noise type of wind excitation and white noise type of earthquake excitation (Wu and Chang, 2006) and presented the design optimum parameters numerically obtained through the minimization of the normalized response of a damped SDOF structure equipped with a TLCD. However, it is worth stressing that, in the aforementioned studies, an iterative procedure has been used, which is not practically feasible for pre-design purposes that require a straight approach.

Direct approach was firstly presented by Yalla and Kareem (2000). Using the TLCD theory and the equivalent linearization scheme, they proposed a new non-iterative procedure for explicit expressions of

optimum tuning ratio and head loss coefficient considering undamped primary structures subjected to white noise and filtered white noise excitations representing wind and seismic loadings. Similarly in Chang and Hsu (1998) the equations of motion for the liquid column vibration absorber (LCVA) are obtained and the optimal head loss coefficient is derived explicitly under the condition that the LCVA's frequency is tuned to that of the structure.

Furthermore, in Chang (1999) two sets of common formulas for the optimal properties as well as some useful design formulas for various passive absorbers, including TLCD, TMD and LCVA, have been derived in closed form for undamped primary structures, under a broad-band white noise excitation of either wind or earthquake type of loadings. Specifically, for a wind type of loading assumed as a Gaussian white noise process with power spectral density S_0, the obtained expressions are

$$\omega_{2,opt} = \omega_1 \frac{\sqrt{1+\mu-\frac{1}{2}\lambda}}{1+\mu} \tag{2.23}$$

$$\zeta_{2,opt} = \frac{1}{2}\sqrt{\frac{\lambda\left(1+\mu-\frac{1}{4}\lambda\right)}{(1+\mu)\left(1+\mu-\frac{1}{2}\lambda\right)}} \tag{2.24}$$

where $(\lambda = \mu)$ for the TMD case, while $\left(\lambda = \alpha^2\mu\right)$ for the TLCD case.

Further, for a Gaussian white noise process base excitation, the optimal parameters have been obtained as

$$\omega_{2,opt} = \omega_1 \frac{\sqrt{1+\mu-\frac{3}{2}\lambda}}{1+\mu} \tag{2.25}$$

$$\zeta_{2,opt} = \frac{1}{2}\sqrt{\frac{\mu\left(1+\mu-\frac{5}{4}\lambda\right)}{(1+\mu)\left(1+\mu-\frac{3}{2}\lambda\right)}} \tag{2.26}$$

where $\omega_{2,opt}$ is the optimal value of the TLCD frequency, while $\zeta_{2,opt}$ is given as

$$\zeta_{2,opt} = \frac{c_{eq}}{2\gamma AL\omega_2} \tag{2.27}$$

c_{eq} being the equivalent damping coefficient of the linearized counterpart of the equation of motion Eq. (2.20), according to the procedure outlined in the following Section 3.2. Note that in (Chang, 1999), an approximate formula has been reported for the structural displacement variance of the controlled system as

$$\sigma_X^2 \cong \frac{\pi G_0}{4\omega_1^3} \frac{2\zeta_1(2\mu+\lambda)+(\mu+\lambda)\sqrt{\mu\left(1-\frac{5}{4}\lambda\right)}}{2\zeta_1^2(2\mu+\lambda)+\zeta_1(\mu+2\lambda)\sqrt{\mu\left(1-\frac{5}{4}\lambda\right)}+\frac{\mu}{2}\lambda} \tag{2.28}$$

where G_0 is the one-sided white noise strength.

Recently Gosh and Basu (2007), extending the classical theory of fixed–point frequencies to undamped structure-TLCD system, proposed a new approach for optimal parameters design. In this regard, a closed form solution for the optimum tuning ratio of a TLCD attached to an

undamped structure has been obtained minimizing the maxima of the displacement transfer function of the structure. Then they justify the assumption of the existence of fixed-points for damped structural systems with attached TLCD through numerical studies.

Finally another procedure to obtain the optimum TLCD parameters has been proposed by Hochrainer (2005), based on the analogy between TLCDs and TMDs. He showed in fact that the dynamics of TLCD can be described in terms of the corresponding TMD, as shown in Fig. 2.17, as it is possible to subdivide the total liquid mass *m* in a so-called active mass m^*, which affects the dynamic behavior of the structure, and in a so-called inactive mass $\bar{m}$.

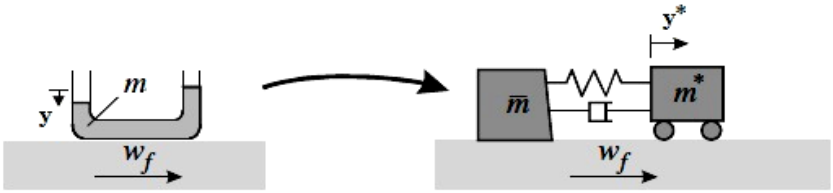

Fig. 2.17 – Analogy between the TLCD and the TMD (Hochrainer, 2005).

Specifically, he obtained

$$m^* = \alpha^2 m \tag{2.29}$$

$$\bar{m} = m - m^* = m\left(1-\alpha^2\right) \tag{2.30}$$

Consequently, once TLCD geometry has been chosen, the aforementioned analogy can be used to derive the optimal frequency value and the optimal value of the equivalent damping ratio, using the already introduced relation for the TMD design in Section 1.4.4.

2.6 Effectiveness of the control: TMD vis-à-vis TLCD device

In this Section, the control performance of the TLCD will be investigated, in comparison also to the more common TMD device.

Specifically, both numerical analysis on a benchmark structure, and experimental investigation will be performed in order to highlight the efficiency of the control of both devices and underscore the differences.

2.6.1 Numerical investigation on a benchmark structure

A flexible building modeled as a SDOF system excited at the base with a Gaussian white noise is here considered as an example to demonstrate the control performance of the TMD and TLCD. The mass, stiffness and damping coefficient of the SDOF system are assumed respectively as $M = 4.61 \cdot 10^7\ Ns^2/m$, $C = 1.04 \cdot 10^6\ Ns/m$ (corresponding to $\zeta_1 = 1\%$) and $K = 5.83 \cdot 10^7\ N/m$ (corresponding to $\omega_1 = 0.179 \cdot 2\pi\ rad/s$). These properties represented the first mode of a benchmark 75-story flexible skyscraper used in Chang (1999) and Chand and Hsu (1998) and Wu and Chang (2006).

To compare the control performances of the TMD with those of the TLCD, for various input strength G_0 and different mass ratio μ, in

Fig.2.18 the structural variance σ_X^2 for the uncontrolled system (black bold line), the TMD controlled system (continuous dot line) and TLCD controlled system (crosses), are reported. Specifically, since the system is excited by a Gaussian white noise, the structural displacement steady state variance of the uncontrolled system can be obtained in closed form as

$$\sigma_{X_0}^2 = \frac{\pi G_0}{4\zeta_1 \omega_1^3} \tag{2.31}$$

while the steady state variances of the TMD and TLCD controlled systems are obtained through Eq. (2.28) considering $(\lambda = \mu)$ and $(\lambda = \alpha^2 \mu)$ respectively. Note that in that figure, a value of $(\alpha = 0.8)$ has been used for the TLCD system.

As shown in Fig. 2.18, variances of TLCD controlled systems are always slightly higher than those of the TMD controlled systems, for every value of the mass ratio. However, for higher values of the mass ratio, differences among the two control systems decrease. Further, variances for both TLCD and TMD systems increase for greater values of the input intensity.

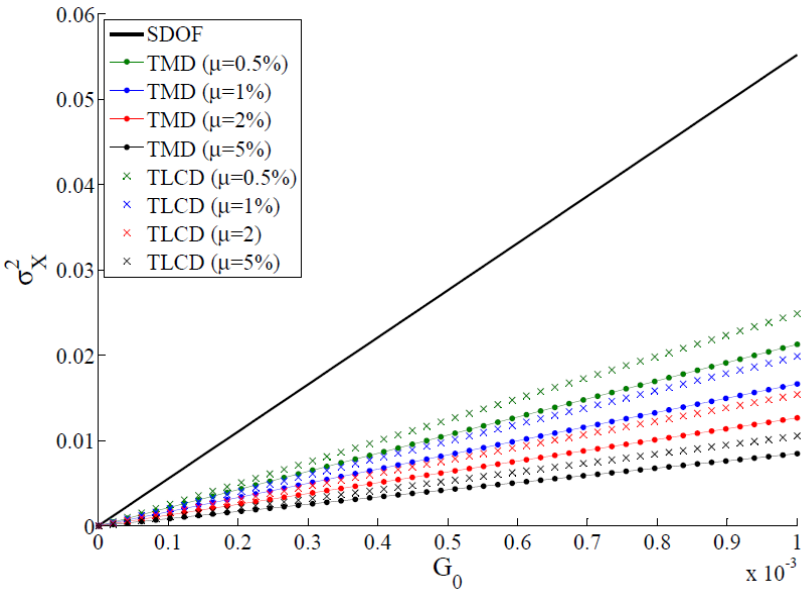

Fig. 2.18 – Structural displacement variance for TMD and TLCD controlled systems as a function of G_0: continuous black line - SDOF main system, lines with dots – TMD, crosses – TLCD with $(\alpha = 0.8)$.

Another relevant aspect is related to the variation of the control performances for different values of the length ratio α. In this regard, in Fig. 2.19 the control performance of the TMD system is compared with the one of the TLCD device, for different values of α. Specifically, in this case the control performance index ε, given by

$$\varepsilon = \frac{\sigma_X^2}{\sigma_{X_0}^2} \tag{2.32}$$

has been used, since it is independent on the input strength G_0. Note that in Eq. (2.32) σ_X^2 is the variance of the controlled system computed through Eq. (2.28), while $\sigma_{X_0}^2$ is the variance of the uncontrolled system,

given by Eq. (2.31). Clearly, the smaller the value of ε is, the higher is the control performance.

As shown in Fig. 2.19, once again higher control is reached through the TMD, regardless the value of α of the TLCD system. However, differences in the control performance between TMD and TLCD decrease for higher values of α.

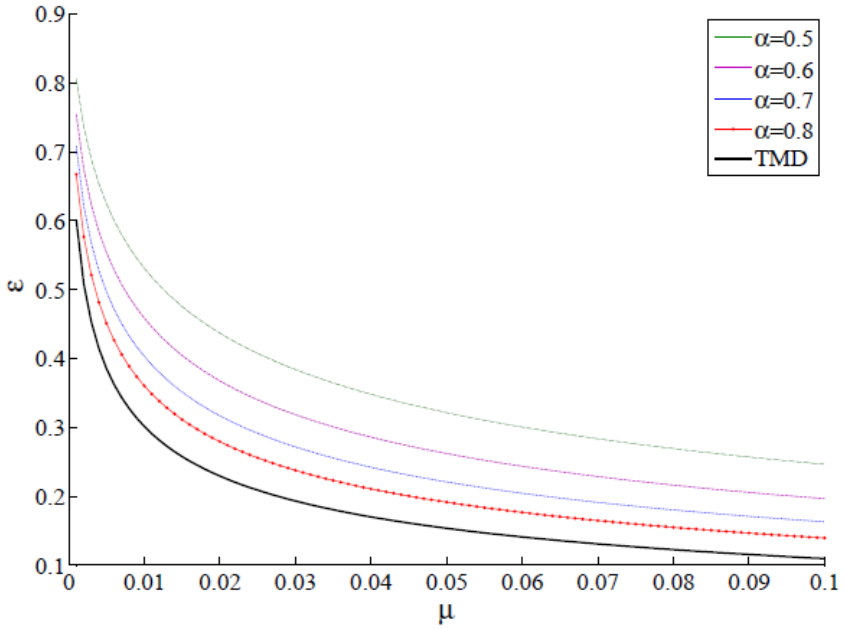

Fig. 2.19 – Control performance index for the TMD and TLCD.

From these figures, it is apparent that TMDs are more efficient in terms of control performance, in comparison with TLCDs with the same mass ratio. Note that similar results have been obtained by (Chang, 1999) for the case of wind excitation.

However, as stated in (Chang, 1999): "Although the control performance of the TMD is always better than the liquid type of mass dampers, there may well be other practical situations when the latter type is still preferred. These liquid type of mass dampers offer some unique practical advantages, such as low cost, easy adjustment, flexible installation, and almost maintenance-free which might eventually outweigh the slightly better control performance provided by the TMD".

2.6.2 Experimental investigation

Since comparisons in previous Section 2.6.1, are made purely based on the mathematical derivations in (Chang, 1999) under ideal situations where the base excitation is assumed to be broadband stationary, in this Section control performances of both TMD and TLCD control devices are experimentally compared.

In this regard, three different experimental models have been built and tested in the Laboratory of Experimental Dynamics at the University of Palermo.

The first one is a small scale SDOF shear-type frame (Fig. 2.20(a)) composed by two steel columns and two nylon rigid plates as base and floor respectively, whose dimensions are reported in Fig. 2.20(b). The total mass of the model is $\left(M = 4.481kg\right)$, of which $0.408kg$ takes into account the dead weight of the tube mass of TLCD or of the TMD connection element. Note that, considering the geometric dimensions

given in Fig. 2.20(b), the theoretical natural frequency of the aforementioned system is $\left(\omega_{1,the} = 10.605\, rad/s\right)$.

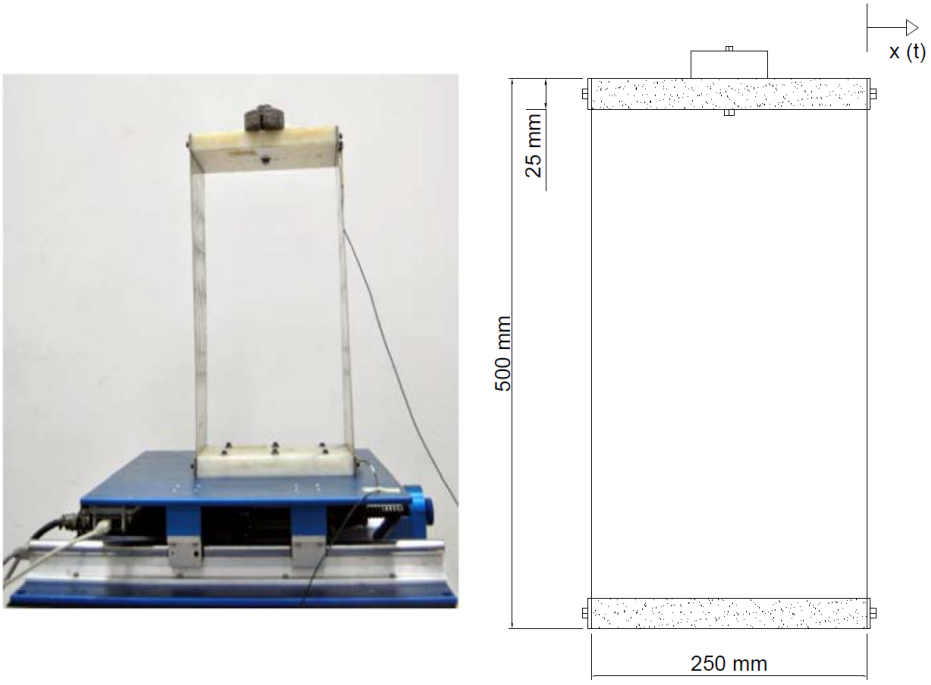

(a) (b)

Fig. 2.20 – SDOF shear-type model: (a) picture of the experimental setup; (b) dimensions.

In the second model (Fig. 2.21(a)), the U–shaped Plexiglass cylinder tube of diameter $\left(d = 0.054\, m\right)$ (see Fig. 2.21(b) for details) with a constant cross section $\left(A = 22.9\, cm^2\right)$ rigidly connected to the upper plate of the SDOF frame, has been filled with water, to create a simple TLCD control system. Water $\left(\rho = 997\, g/dm^3\right)$ has been poured to a level of $\left(h = 0.04\, m\right)$ from the centerline of the base tube, equivalent to a

total liquid quantity of $450\,ml$ and total liquid length of $(L = 0.185\,m)$, which correspond to a theoretical natural frequency, given by Eq. (2.6), of $(\omega_{2,the} = 10.29\,rad/s)$, so that the TLCD device has been correctly tuned to the frequency of the main system $\omega_{1,the}$. Further, the liquid mass is $(m = 0.422\,kg)$, corresponding to a mass ratio μ closed to 0.1.

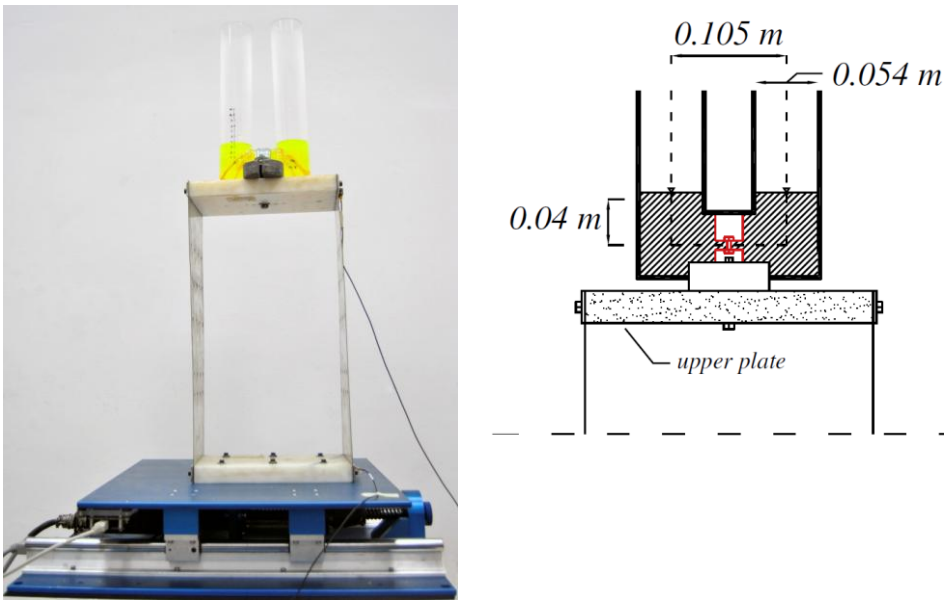

(a) (b)

Fig. 2.21 – SDOF system with TLCD: (a) picture of the experimental setup; (b) dimensions.

In the third model (Fig. 2.22(a)) a simple pendulum has been rigidly connected to the SDOF shear-type frame, so as to set up a simple TMD control system. The TMD is composed of a steel rod, whose dimensions are reported in Fig. 2.22(b), bolted to the upper floor, and a steel mass of $(m = 0.440\,kg)$ connected to the free end. The total mass of the TMD

device was almost the same of the TLCD device, so as to maintain unvaried the mass ratio of the TLCD model and of the TMD one. Further, considering the geometric dimensions given in Fig. 2.22(b), the theoretical natural frequency of the TMD device is $\left(\omega_{TMD,the} = 9.13 rad/s\right)$, so that it is correctly tuned to the theoretical frequency of the uncontrolled system, according to the procedure outlined in Section 1.4.

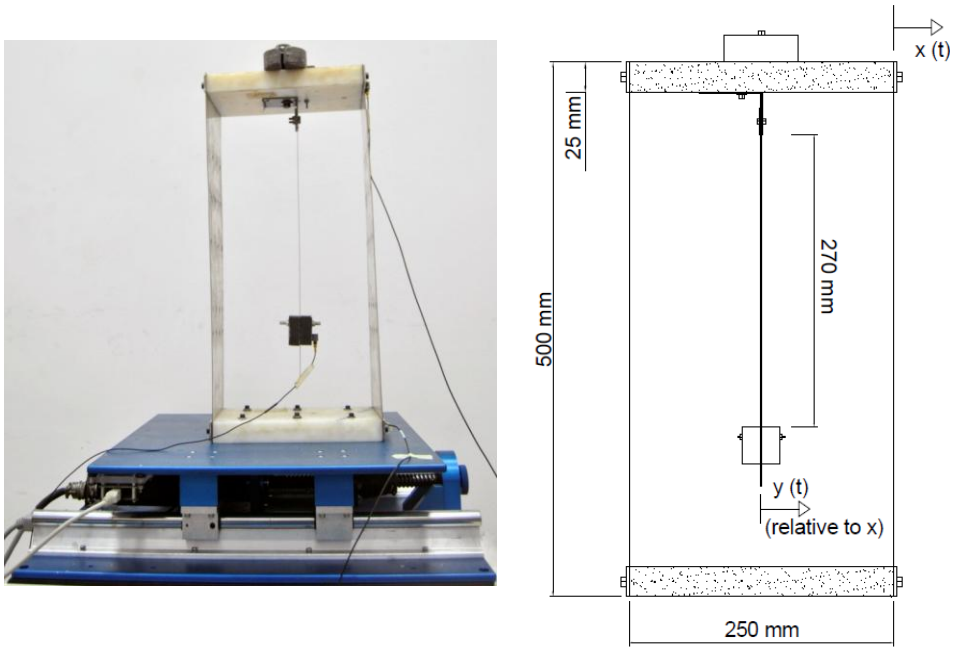

(a) (b)

Fig. 2.22 – SDOF shear-type model with TMD: (a) picture of the experimental setup; (b) dimensions.

As far as the test procedure is concerned, acceleration responses at the base, at the storey and on the TMD mass have been acquired using Miniature DeltaTron Accelerometers Bruel & Kjær – Type 4507-002

piezoelectric accelerometers. In order to condition and amplify current signals coming from accelerometers before being acquired and saved, a conditioning amplifiers, the Brüel&Kjær Nexus Range Of Conditioning Amplifier – Type 2693A014, has been used. Voltage signals have been acquired by means of a National Instruments NI-PCI-442 Analogical-Digital (A-D) Acquisition Board and then processed using a self-developed signal processing software in Labview and Matlab environment. Further, shear-type models have been mounted on a shaking table model Quanser Shake Table II that provides the ground motion. Figure 2.23 shows the schematic experimental setup, while details on the various elements of the acquisition system used for the experimental tests can be found in Appendix A.

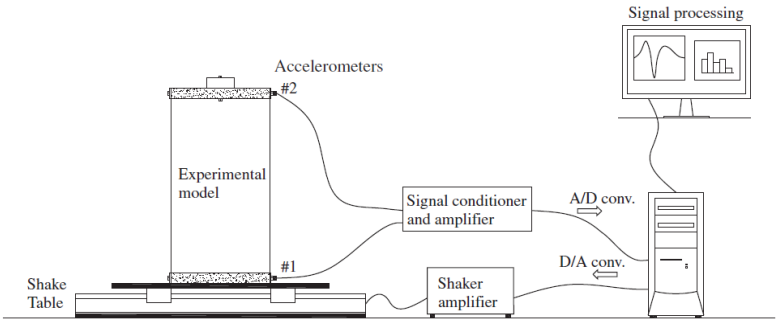

Fig. 2.23 – Acquisition system for the shake-table test.

The dynamics parameters of the uncontrolled system have been determined by exciting the structure through sweep sine tests in the frequency range: 0.1 - 4 Hz (see Fig. 2.24).

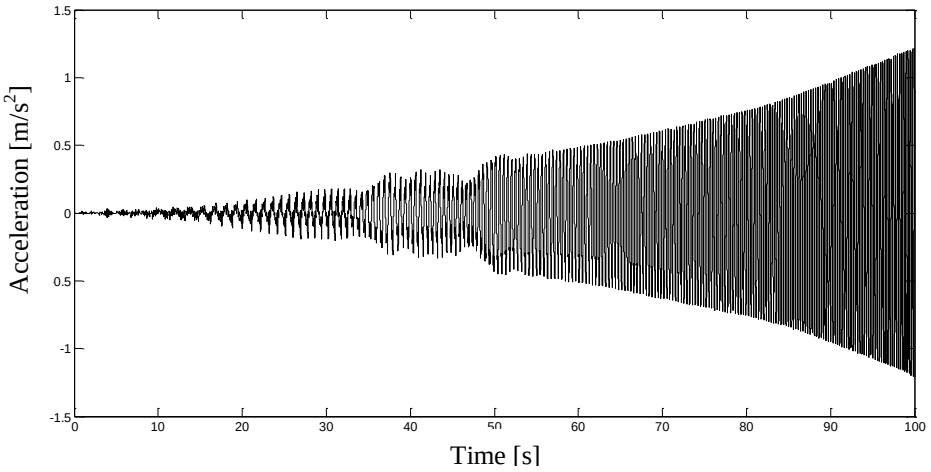

Fig. 2.24 – Recorded sweep sine base acceleration.

Four series of data were recorded and, using the acceleration signals, the mean Frequency Response Functions (FRF) was computed (see Fig.2.25). Finally, by means of the peak-picking procedure together with the half-power bandwidth method (Ewins, 1984) the natural frequency and the damping ratio of the main system have been obtained as $(\omega_1 = 10.12\, rad/s)$ $(f_1 = 1.61 Hz)$ and $(\zeta_1 = 0.009)$ respectively. Note that the experimentally obtained natural frequency is rather close to the theoretical one, given above.

All the models have been investigated under a series of different sinusoidal ground motion, to capture the main features of the control performance of TLCD and TMD.

In particular two values of the amplitude of the ground acceleration have been selected: *0.5 mm* and *1 mm*. For each amplitude, four different values of excitation frequency have been considered: $1.4\, Hz, 1.53\, Hz, 1.6\, Hz$ and 1.75 *Hz.*

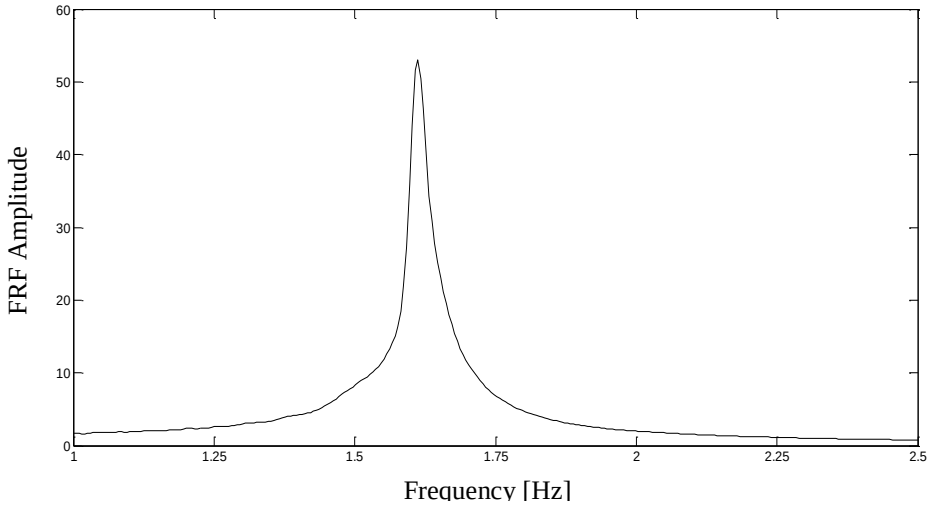

Fig. 2.25 – Experimental FRF.

Experimental results in terms of acceleration at the storey of all the three models driven by a sinusoidal ground motion at resonance, are compared in Fig. 2.26.

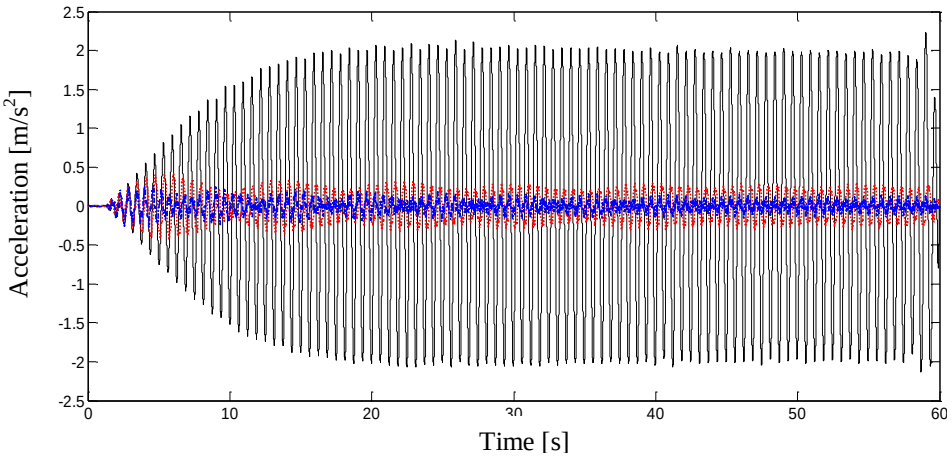

Fig. 2.26 – Experimental response acceleration for sinusoidal ground motion with amplitude *0.5mm* and frequency *1.6 Hz:* black line – uncontrolled system; red dashed line – TLCD controlled system; blue dotted line – TMD controlled system.

It is apparent that at resonance both controlled systems are very effective and this is fundamental for vibration control. In particular, for both amplitude values, the TMD allows a reduction of the main system acceleration of about the 88%, while with the TLCD reduction of the 83% is reached. Then, as expected, the control performance obtained through the TMD is just slightly superior to the TLCD one, and this justifies the growing interest on TLCD.

Experimental investigation has also shown that in some cases an amplification of the acceleration responses may be caused by the TMD and the TLCD devices if a correct choice of the damping parameters is not performed (Di Matteo et al., 2012).

For instance, considering a sinusoidal ground motion of frequency 1.4*Hz*, the TLCD causes an amplification of about 45% of the uncontrolled system acceleration (Fig. 2.27).

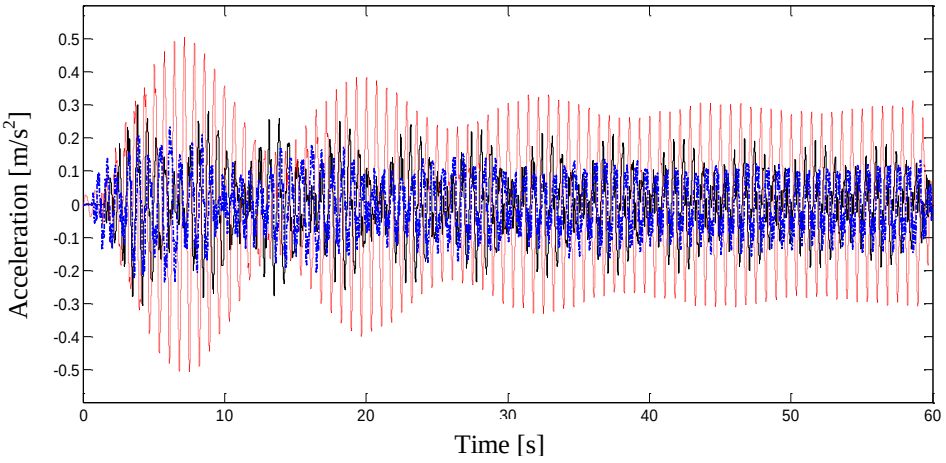

Fig. 2.27 – Experimental response acceleration for sinusoidal ground motion with amplitude *0.5mm* and frequency *1.4 Hz:* black line – uncontrolled system; red dashed line – TLCD controlled system; blue dotted line – TMD controlled system.

On the other hand, with a sinusoidal frequency of 1.75*Hz* the TMD causes an amplification of about 60% of the uncontrolled system acceleration (Fig. 2.28).

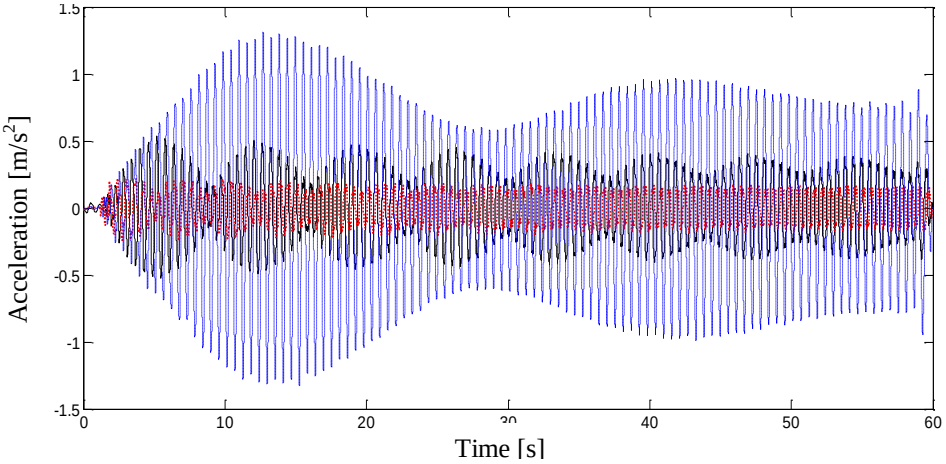

Fig. 2.28 – Experimental response acceleration for sinusoidal ground motion with amplitude *0.5mm* and frequency *1.75 Hz:* black line – uncontrolled system; red dashed line – TLCD controlled system; blue dotted line – TMD controlled system.

It is worth noting that this behavior is probably due to the non-perfect choice of values of the damping ratio for the TMD and TLCD devices. Better performances can in general be reached also at frequencies different from the resonance one, for optimal values of the damping coefficient, which however are not generally easy to obtain.

Previous considerations are reported just to describe the general behavior of both devices, but of course, the performance control is not compromised, since the maximum value of the uncontrolled acceleration is never exceeded.

Chapter 3

Novel direct approximate solution for the optimal design of TLCD systems

3.1 Introduction

Analytical and experimental studies on the control performance of TLCD in reducing structural dynamic response are widely developed in literature, as shown in previous Chapter 2. From these studies it is apparent that, like TMDs, the effectiveness of a TLCD depends on proper tuning and damping value. The determination of the optimal TLCD parameters, with respect to the main structure to be controlled, plays a key role in structural design, hence the insistent demand of performing response analysis in a quick way for pre-design purposes.

However, even assuming that the main structure behaves linearly, the response of the whole damper-structure system is nonlinear and the determination of the optimal parameters is time consuming.

In order to overcome this problem, there has been a proliferation of studies to evaluate the optimal TLCD tuning parameters by using simplified formulations, as detailed in Section 2.5.

It is worth stressing that, in the vast majority of cases, an iterative procedure has been used, which is not practically feasible for pre-design purposes, which require a straight approach.

On the other hand, as shown in Section 2.5, few studies introduce a direct approach for the evaluation of the design parameters (Yalla and Kareem, 2000; Chang and Hsu, 1998; Chang, 1999; Gosh and Basu, 2007). From all these analyses, it emerges that to facilitate the design procedure, design formulas for choosing appropriate parameters based on the optimization of stochastic responses basically assumed no damping in the structure (Yalla and Kareem, 2000; Chang and Hsu, 1998; Chang, 1999), since it has been shown that if the structure is lightly damped the influence of structural damping on design parameter values is negligible (Luft, 1979). However, in presence of structural damping, results obtained may not represent the actual optimum since damping may have a significant effect on the design parameters.

In this Chapter a straight formulation is introduced to more simply evaluate TLCD parameters and to predict the behavior of a damped main system controlled with a TLCD under random loads.

Clearly, as detailed in Section 3.3, the proposed simplified formulation is approximate since obtained through the Statistical Linearization Technique (SLT) and according to some assumptions pertaining the control effectiveness.

However, in Section 3.4 the reliability of the proposed formulation, useful for pre-design purposes, has been assessed by comparison with numerical Monte Carlo Simulation (MCS) based on the nonlinear complete system. Moreover, a parametric analysis has been carried out in

order to investigate the effectiveness of the proposed formulation when the underlying assumptions are not fulfilled and to define the parameters range of applicability.

Further, in Section 3.5 the proposed formulation has been used to derive the optimal TLCD design parameters, and comparison with previous methods in literature is shown.

Finally, in Section 3.6 numerical results obtained with the straightforward formulation are validated through an experimental campaign on a small scale SDOF shear-type model equipped with a TLCD device.

3.2 Statistical linearization of TLCD

In this Section, a brief review of the classical Statistical Linearization procedure applied to TLCD controlled systems is presented for sake of clarity. Further details on the general the Statistical Linearization Technique (SLT) can be found in (Roberts and Spanos, 1990).

Suppose that the main system equipped with a TLCD is driven by random forces like earthquake ground accelerations. Ground motion records exhibit non-stationary characteristics both in time and in frequency domain, but it is of common use to consider that earthquakes have a pseudo-stationary part that can be modeled as zero-mean Gaussian random process. In this way, it is possible to take advantage of the powerful tools of stochastic analysis, if the pseudo-stationary part of the ground motion is adequately long with respect to the natural period of the structural system and the damping is sufficient to limit the transient response.

Therefore, let the earthquake ground accelerations be modeled as a zero mean Gaussian white noise processes. It follows that the displacements of the main system and of the liquid, and their derivatives, are stochastic processes too (here denoted with capital letters). Moreover, due to the presence of the nonlinear damping term, responses are non-Gaussian processes.

According to the SLT, the original nonlinear system Eq. (2.20) is replaced by a linear equivalent one as follows:

$$\begin{cases} (1+\mu)\ddot{X}(t)+\alpha\mu\ddot{Y}(t)+2\zeta_1\omega_1\dot{X}(t)+\omega_1^2X(t)=-(1+\mu)\ddot{X}_g(t) \\ \alpha\ddot{X}(t)+\ddot{Y}(t)+2\zeta_2\omega_2\dot{Y}(t)+\omega_2^2Y(t)=-\alpha\ddot{X}_g(t) \end{cases} \tag{3.1}$$

where ζ_2 is the equivalent damping ratio, obtained minimizing the mean square with respect to ζ_2 (Spanos, 1981; Roberts and Spanos, 1990). Omitting the time dependence, for clarity sake, yields

$$\mathrm{E}\left[\left(c\left|\dot{Y}\right|\dot{Y}-2\zeta_2\omega_2\dot{Y}\right)^2\right]=\min_{\zeta_2} \tag{3.2}$$

where $\mathrm{E}[\cdot]$ means ensemble average and $(c=\xi/2L)$. Once the minimum is evaluated the equivalent damping is obtained as

$$\zeta_2=\frac{c}{2\omega_2}\frac{\mathrm{E}\left[\left|\dot{Y}\right|^3\right]}{\mathrm{E}\left[\dot{Y}^2\right]} \tag{3.3}$$

Since the system in Eq. (3.1) is linear and it is forced by a Gaussian process, the responses are Gaussian processes too and then the averages involving the velocity of the fluid $\dot{Y}$ in equation (3.3) can be written as:

$$\mathrm{E}\left[\left|\dot{Y}\right|^3\right]=\frac{1}{\sqrt{2\pi}\sigma_{\dot{Y}}}\int_{-\infty}^{\infty}\exp\left(-\frac{\dot{y}^2}{2\sigma_{\dot{Y}}^2}\right)\left|\dot{y}\right|^3d\dot{y}=2\sqrt{\frac{2}{\pi}}\sigma_{\dot{Y}}^3;\ \ \mathrm{E}\left[\dot{Y}^2\right]=\sigma_{\dot{Y}}^2 \tag{3.4}$$

As a consequence, the expression for the equivalent damping ratio becomes

$$\zeta_2=\frac{c}{\omega_2}\sqrt{\frac{2}{\pi}}\sigma_{\dot{Y}} \tag{3.5}$$

where $\sigma_{\dot{Y}}$ is the standard deviation of the velocity of the fluid. It should be noted that the expression reported in Eq. (3.5) is in total agreement with those reported in (Balendra et al., 1995; Banlendra et al., 1999).

Moreover, it should be stressed that the kind of nonlinearity exhibited by TLCDs, namely $|\dot{Y}|\dot{Y}$, can be also recast as $|\dot{Y}|^2 \operatorname{sgn}(\dot{Y})$, that belongs to the more general class of nonlinearities represented by $|\dot{Y}|^{\vartheta} \operatorname{sgn}(\dot{Y})$ when $\vartheta = 2$, $\operatorname{sgn}(\cdot)$ being the signum function.

This latter class has been investigated since several dissipating devices can be modeled in this way. For instance, by setting $\vartheta = 0$ one can obtain a pure friction device, while by choosing $0 < \vartheta < 1$ a nonlinear viscous damper is modeled (Barone et al., 2008).

The determination of an equivalent linear system for this class of devices has been performed in many different ways in literature. For example in Soong and Constantinou (1994) and Lee et al. (2004) the equivalent viscous damping ratio is obtained by equating the energy dissipated by an equivalent linear viscous damping with the energy of the nonlinear one in one cycle of vibration under harmonic forces, while in Di Paola et al. (2007 and 2008) an approach based on SLT has been proposed for the case of the viscous damper subjected to random loads for SDOF systems, and in Di Paola et al. (2009) a similar technique has been applied also for multi-degree-of-freedom (MDOF) systems.

In Di Paola et al. (2009) the equivalent viscous damping ratio for the general case of a nonlinear damping force described as $f_d = c|\dot{Y}|^{\vartheta} \operatorname{sgn}(\dot{Y})$, is found to be

$$\zeta_2 = \frac{c}{2\omega_2} \frac{2^{\frac{\vartheta+1}{2}} \Gamma\left(1+\frac{\vartheta}{2}\right)}{\sqrt{\pi}} \sigma_{\dot{Y}}^{\vartheta-1} \tag{3.6}$$

where $\Gamma(\cdot)$ is the Gamma function. Notice that relation (3.6) reduces to Eq. (3.5) for $\rho = 2$.

The use of Eq. (3.5) for design purposes is not straightforward since the standard deviation of the velocity of the fluid $\sigma_{\dot{Y}}$ is still unknown and it implicitly depends on ζ_2; then, in general, an iterative procedure is necessary as outlined in the following.

Let recast the equation of motion of the equivalent linear system Eq. (3.1) in compact form as

$$\mathbf{M}\ddot{\mathbf{Z}}(t) + \mathbf{C}_{lin}\dot{\mathbf{Z}}(t) + \mathbf{K}\mathbf{Z}(t) = -\mathbf{M}\boldsymbol{\tau}\ddot{X}_g(t) \tag{3.7}$$

where $\mathbf{Z}(t) = \begin{bmatrix} X(t) & Y(t) \end{bmatrix}^{\mathrm{T}}$ is the vector collecting the displacement of the degrees of freedom, $\boldsymbol{\tau} = \begin{bmatrix} 1 & 0 \end{bmatrix}^{\mathrm{T}}$ is the location vector and the transpose operation is denoted with the apex T. **M**, $\mathbf{C}_{\mathbf{lin}}$, and **K** are the mass matrix, the linearized damping matrix and the stiffness matrix, respectively, particularized as

$$\mathbf{M} = \begin{bmatrix} 1+\mu & \alpha\mu \\ \alpha & 1 \end{bmatrix}; \ \mathbf{C}_{lin} = \begin{bmatrix} 2\zeta_1\omega_1 & 0 \\ 0 & 2\zeta_2\omega_2 \end{bmatrix}; \ \mathbf{K} = \begin{bmatrix} \omega_1^2 & 0 \\ 0 & \omega_2^2 \end{bmatrix} \tag{3.8}$$

As a first attempt of the iterative procedure, $\sigma_{\dot{Y}}$ is easily evaluated by fixing an arbitrary value of ζ_2 (even equal to zero) as:

$$\sigma_{\dot{Y}}^2 = \int_0^\infty \omega^2 G_{YY}(\omega)\, d\omega \tag{3.9}$$

where $G_{YY}(\omega)$ is the one-sided Power Spectral Density function (PSD) of the fluid displacement, obtained by using the input-output relationship

$$\mathbf{G_{ZZ}}(\omega) = \begin{bmatrix} G_{XX}(\omega) & G_{XY}(\omega) \\ G_{YX}(\omega) & G_{YY}(\omega) \end{bmatrix} = \mathbf{H}(\omega)\boldsymbol{\tau}\boldsymbol{\tau}^{\mathrm{T}}\mathbf{H}(\omega)^{*\mathrm{T}} G_{\ddot{X}_g}(\omega) \tag{3.10}$$

in which * means complex conjugate, $G_{\ddot{X}_g}(\omega)$ is the one-sided PSD of the input and $\mathbf{H}(\omega)$ is the transfer function of the equivalent linear system, defined as follows:

$$\mathbf{H}(\omega) = \left[\mathbf{K} + i\omega\mathbf{C}_{lin} - \omega^2\mathbf{M}\right]^{-1} \tag{3.11}$$

i being the imaginary unit. A new attempt of ζ_2 is easily found by using Eq. (3.5) and by substituting $\sigma_{\dot{Y}}$ evaluated with Eq. (3.9), and so on. The procedure should converges rapidly to the actual value of ζ_2 and, by using other terms of the response PSD matrix $\mathbf{G_{ZZ}}(\omega)$, the complete response statistics of the response can be computed.

3.3 Direct pre-design procedure

The iterative procedure previously described is well established and represents a very reliable tool for evaluating the main dynamical characteristics of nonlinear systems; however the equivalent linear system is found through several numerical evaluations.

Aiming at providing a tool to promptly compute the equivalent damping ratio of TLCDs, the aforementioned iterative procedure cannot be pursued, and a different approach is needed.

To this aim, note that Eq. (3.5) provides a relationship between the equivalent damping ratio ζ_2 and the standard deviation of the fluid velocity $\sigma_{\dot{Y}}$. In order to find a simplified straight relationship between the input characterization $G_{\ddot{X}_g}(\omega)$ and the estimated value for ζ_2, a closed-form solution in terms of steady state response statistic $\sigma_{\dot{Y}}$ is proposed, as detailed in the following.

Specifically, modeling the input as a zero-mean stationary Gaussian white noise process, the Lyapunov equation of the evolution of the covariance matrix (Bryson and Ho, 1969) of the linear systems Eq. (3.7) can be used as:

$$\dot{\mathbf{\Sigma}}_{\mathbf{Q}}(t) = \mathbf{D}_s \mathbf{\Sigma}_{\mathbf{Q}}(t) + \mathbf{\Sigma}_{\mathbf{Q}}(t) \mathbf{D}_s^T + \mathbf{G}_s \mathbf{G}_s^T \pi G_0 \tag{3.12}$$

where $\mathbf{\Sigma}_{\mathbf{Q}}(t)$ is the covariance matrix in terms of the state vector coordinates $\mathbf{Q} = \begin{bmatrix} \mathbf{Z} & \dot{\mathbf{Z}} \end{bmatrix}^{\mathrm{T}}$, which can be written as

$$\mathbf{\Sigma_Q}(t)=\begin{bmatrix} \sigma_X^2 & \sigma_{XY}^2 & \sigma_{X\dot{X}}^2 & \sigma_{X\dot{Y}}^2 \\ & \sigma_Y^2 & \sigma_{Y\dot{X}}^2 & \sigma_{Y\dot{Y}}^2 \\ sym & & \sigma_{\dot{X}}^2 & \sigma_{\dot{X}\dot{Y}}^2 \\ & & & \sigma_{\dot{Y}}^2 \end{bmatrix} \tag{3.13}$$

G_0 is the one-sided white noise strength and $\mathbf{D}_s$ and $\mathbf{G}_s$ are defined as

$$\mathbf{D}_s=\begin{bmatrix} \mathbf{0} & \mathbf{I}_2 \\ -\mathbf{M}^{-1}\mathbf{K} & -\mathbf{M}^{-1}\mathbf{C}_{lin} \end{bmatrix};\ \mathbf{G}_s=\begin{bmatrix} \mathbf{0} \\ \mathbf{M}^{-1}\boldsymbol{\tau} \end{bmatrix} \tag{3.14}$$

where $\mathbf{I}_2$ is a 2x2 identity matrix.

The solution of Eq. (3.12) gives the full evolution of all response statistics. As above stated, we are interested only in the evaluation of the steady state response statistics, that can be achieved by equating to zero the right-hand side term of Eq. (3.12). This matrix equation provides a set of linear equations for the determination of all the nontrivial components of the response covariance matrix. By solving this set of equation the exact values of the steady state covariance matrix can be retrieved. In particular, after some algebra, the exact solution for the steady state variance of the main system displacement and fluid velocity can be expressed as

$$\sigma_X^2=\frac{\pi G_0}{4z_x\omega_1^3}\ ;\ \sigma_{\dot{Y}}^2=\frac{\pi G_0}{4z_y\omega_2} \tag{3.15 a, b}$$

in which the terms z_x and z_y have the following expression

$$z_x=\frac{N_z}{D_{zx}}\ ;\ z_y=\frac{N_z}{D_{zy}} \tag{3.16 a, b}$$

where

$$N_z = \zeta_1\zeta_2 + \zeta_2^2\left(4\zeta_1^2 + \alpha^2\mu\right)\nu + 2\zeta_1\zeta_2\left(2\zeta_1^2 + \alpha^2\mu + \left(2\zeta_2^2 - 1\right)\left(1+\mu\right)\right)\nu^2 + \zeta_1^2\left(\alpha^2\mu + 4\zeta_2^2\left(1+\mu\right)\right)\nu^3 + \zeta_1\zeta_2\left(1+\mu\right)^2\nu^4 \tag{3.17}$$

$$D_{zx} = \zeta_2\left(1+\mu-\alpha^2\mu\right)^2 + \zeta_1\left(\alpha^4\mu^2 + 4\zeta_2^2\left(1+\mu\right)^2\right)\nu + \zeta_2\left(1+\mu\right)^2\left(4\zeta_1^2 + 3\alpha^2\mu + \left(4\zeta_2^2 - 1\right)\left(1+\mu\right)\right)\nu^2 + \zeta_1\left(1+\mu\right)^2\left(\alpha^2\mu + 4\zeta_2^2\left(1+\mu\right)\right)\nu^3 + \zeta_2\left(1+\mu\right)^4\nu^4 \tag{3.18}$$

$$D_{zy} = \alpha^2\left(\zeta_1 + \zeta_2\left(1+\mu+4\zeta_1^2\right)\nu + 4\zeta_1^3\nu^2\right) \tag{3.19}$$

and the frequency ratio, namely $\left(\nu = \omega_2/\omega_1\right)$ has been introduced.

Obviously the obtained relations Eqs. (3.17 - 3.19) are cumbersome and cannot be used for practical design purposes. Aiming at an approximate evaluation of ζ_2, Eq. (3.16 b) may be expanded in Taylor's series with respect to ζ_2, retaining only the first two terms. Then, since the main system is assumed lightly damped, higher powers of ζ_1, namely ζ_1^2 and ζ_1^3, can be neglected obtaining:

$$z_y = \frac{\zeta_2 + 2\zeta_2\left[\alpha^2\mu - \left(1+\mu\right)\right]\nu^2}{\alpha^2} + \frac{\alpha^2\zeta_1\mu\nu^3 - \zeta_2\left(1+\mu\right)\left[\alpha^2\mu - \left(1+\mu\right)\right]\nu^4}{\alpha^2} \tag{3.20}$$

Moreover, the TLCD may be assumed perfectly tuned with the main system by letting $\nu = 1$. Introducing this assumption in Eq. (3.20) yields

$$z_y = \left(\zeta_1 + \gamma\zeta_2\right)\mu \tag{3.21}$$

in which the dimensionless parameter $\gamma = 1 - \mu + \mu/\alpha^2$ depends only on the geometry of the TLCD.

In this way the steady state variance of the fluid velocity $\sigma_{\dot{Y}}^2$ can be directly related to the white noise strength G_0 as

$$\sigma_{\dot{Y}}^2 = \frac{\pi G_0}{4\mu(\zeta_1 + \gamma\zeta_2)\omega_2} \tag{3.22}$$

Finally, a direct relationship that provides the equivalent damping ratio ζ_2 as a function of the input strength G_0 is obtained by eliminating $\sigma_{\dot{Y}}^2$ from Eqs. (3.3) and (3.22)

$$\zeta_2^2(\zeta_1 + \gamma\zeta_2) = \frac{G_0 c^2}{2\mu\nu^3\omega_1^3} \tag{3.23}$$

in which ω_2 has been replaced by $\nu\omega_1$.

The nonlinear algebraic Eq. (3.23) can be easily solved either in closed form or by numerical means in order to obtain a good estimate of ζ_2, useful for design purpose.

Specifically, considering that the cubic Eq. (3.23) lacks in its linear term and that, assuming realistic values of the system parameters included in Eq. (3.23), the polynomial discriminant Δ is greater than zero, then the proposed formulation provides only one real solution in terms of ζ_2 as

$$\zeta_2 = \frac{1}{3}\left[-a_2 + \frac{a_2^2}{\sqrt[3]{-a_2^3 + \frac{3}{2}\left(\sqrt{3\Delta} - 9a_0\right)}} + \sqrt[3]{-a_2^3 + \frac{3}{2}\left(\sqrt{3\Delta} - 9a_0\right)}\right] \tag{3.24}$$

where

$$a_0 = -\frac{G_0 c^2}{2\mu\nu^3\omega_1^3\gamma};\ a_2 = \frac{\zeta_1}{\gamma};\ \Delta = 4a_2^3 a_0 + 27a_0^2 \qquad \text{(3.25 a, b, c)}$$

Recalling the definitions of $\left(\omega_2^2 = 2g/L\right)$ and $\left(c = \xi/2L\right)$, a relationship that provides the value of the head loss factor ξ in terms of equivalent linear damping ratio ζ_2 is promptly found as

$$\xi = 4g\zeta_2 \frac{1}{\sqrt{G_0\omega_1}}\sqrt{\frac{2\mu\left(\zeta_1 + \gamma\zeta_2\right)}{\nu}} = \frac{\xi_0\left(\nu, \zeta_2\right)}{\sqrt{G_0\omega_1}} \qquad (3.26)$$

where

$$\xi_0\left(\nu, \zeta_2\right) = 4g\zeta_2\sqrt{\frac{2\mu\left(\zeta_1 + \gamma\zeta_2\right)}{\nu}} \qquad (3.27)$$

Although the approximate evaluation of the equivalent damping ratio has been derived for Gaussian white noise, its extension to non-white Gaussian processes characterized by a PSD function $G_{\ddot{X}_g}\left(\omega\right)$ can be easily achieved. In fact, for lightly damped structural systems, the response will be narrow-banded and there will be no significant differences if the term G_0 in Eq. (3.23) is replaced with $G_{\ddot{X}_g}\left(\omega_1\right)$.

In order to more strongly clarify the enhanced proposed procedure in comparison with the classical iterative one, in Fig. 3.1 a step-by-step flowchart comparing the two methods is provided.

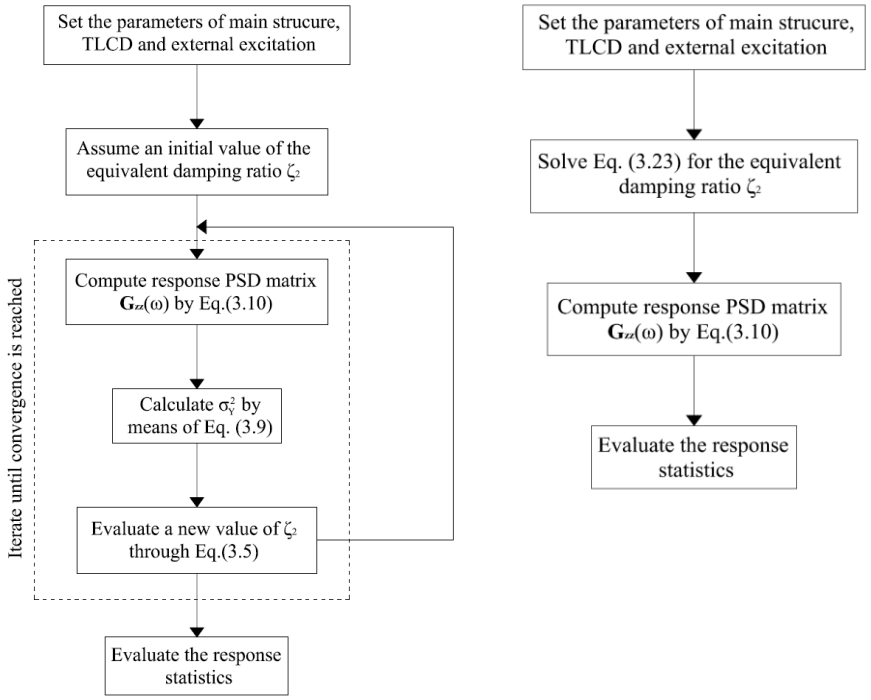

(a) (b)

Fig. 3.1 – Flowchart of the two methods: (a) classical iterative procedure; (b) proposed approach.

In the following section the approximate procedure here proposed will be validated through several numerical simulations in which the responses of two different structural systems equipped with TLCD, subjected to broadband noise and earthquake-type random loads, will be studied in detail.

3.4 Numerical analysis

In the present Section the direct proposed approach for the evaluation of the equivalent damping useful as pre-design tool is validated by means of numerical simulations.

The main system considered, hereinafter referred to as "*system 1*", relevant to buildings design and equipped with TLCD, is a flexible 75-story building used in Chang and Hsu (1998) and here adopted for TLCD design under random Gaussian broadband noise loading. The first mode properties of this building are $M = 4.61 \cdot 10^7 \; Ns^2/m$, $C = 1.04 \cdot 10^6 \; Ns/m$ (corresponding to $\zeta_1 = 1\%$) and $K = 5.83 \cdot 10^7 \; N/m$ (corresponding to $\omega_1 = 0.179 \cdot 2\pi \; rad/s$). The random Gaussian broadband noise is generated ensuring that the PSD can be considered constant in a frequency range from zero to the Nyquist frequency.

3.4.1 Exact solution versus approximate proposed solution for the steady state liquid velocity variance

In the previous section an approximate method to evaluate ζ_2 without iteration is introduced as pre-design tool. In order to prove the reliability of such a tool Fig. 3.2(a) shows the comparison among the values of ζ_2 estimated by means of the iterative procedure – Eqs. (3.9 – 3.11) - and

values obtained by numerically solving Eq. (3.23), for a wide range of the input strength G_0 acting on *system 1*.

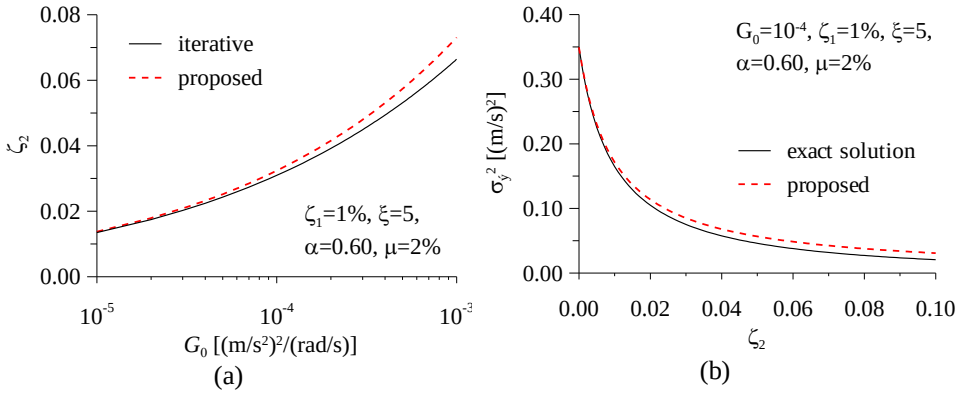

Fig. 3.2 – (a) Equivalent linear damping ratio versus input strength; (b) Fluid velocity steady state variance versus equivalent linear damping ratio.

As expected, the proposed formulation becomes less effective when the input strength G_0 increases. However, even for a high value of $G_0 = 10^{-3}\left(m/s^2\right)^2 \Big/ \left(rad/s\right)$ the error is always below 10%.

In Fig. 3.2(b) the exact values of variance $\sigma_{\dot{Y}}^2$, computed using Eq. (3.15 b), are compared with those computed through Eq. (3.22) for a wide range of the equivalent linear damping ratio ζ_2. The apparent good agreement between the two curves in Fig. 3.2(b) shows how the simplified formulation is able to correctly estimate the relationship between ζ_2 and $\sigma_{\dot{Y}}^2$. The maximum error for ζ_2 up to 0.05 is about 20%. However, as it will be demonstrated in the next section, the proposed method leads to an accurate estimate of main system displacements.

3.4.2 Results in time domain

The ability of the pre-design formulation to predict the system response in time domain is investigated. In this regard, results obtained considering *system 1* excited by a broadband Gaussian noise with a total duration of $20\,s$ (using $\xi = 5, \alpha = 0.6, \mu = 0.02$, and $\nu = 0.98$), are depicted in the following figures. In particular, main system and fluid displacements time histories are reported for nonlinear system Eq. (2.20) and equivalent linear system Eq. (3.1) in Figs. 3.3(a) and 3.3(b) respectively. It is evident the good match in time domain between the nonlinear and equivalent linear system responses, particularly for the main system case Fig. 3.3(a).

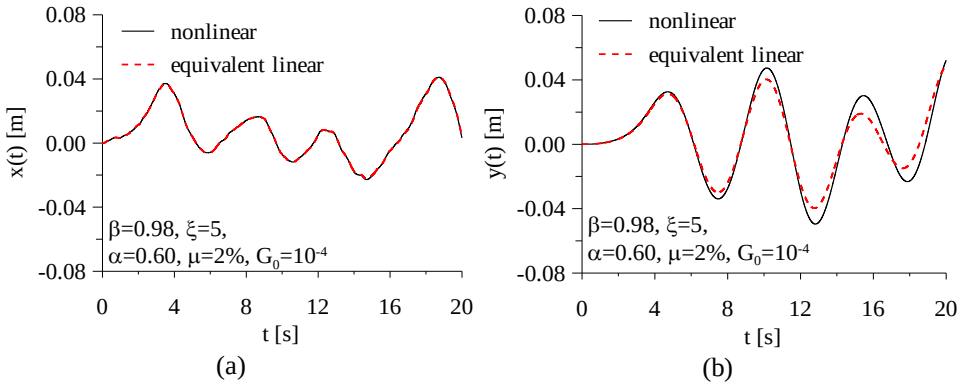

Fig. 3.3 – (a) Sample of main system displacement time history; (b) Sample of fluid displacement time history.

3.4.3 Results in terms of response variance

In this section comparison among response variances of *system 1*, considering the nonlinear system Eq. (2.20) and the equivalent linear system Eq. (3.1) with ζ_2 as in Eq. (3.23), is presented for various values of the input strength G_0.

Specifically, for the nonlinear systems in Eq. (2.20), the variances have been computed through MCS performed using for each analysis 2000 samples of ground accelerations and directly integrating the equation of motion; then response statistics in terms of steady state variances have been computed. Transient effects have been avoided by computing the response statistics in ergodicity. Thus, the initial conditions on the state variables of the response for the *k-th* sample function have been assumed as the state at the end of the *(k-1)-th* sample function of the response.

Further, steady state response variances of the equivalent linear system Eq. (3.1) have been then computed following the procedure reported in Eqs. (3.9 – 3.11).

The response statistics of the nonlinear system Eq. (2.20) and of the equivalent linear system Eq. (3.1) are then compared in Figs. 3.4. In particular, Fig. 3.4(a) shows the comparison in terms of the main system displacement variance σ_X^2, while Fig. 3.4(b) shows the comparison in terms of fluid displacement variance σ_Y^2.

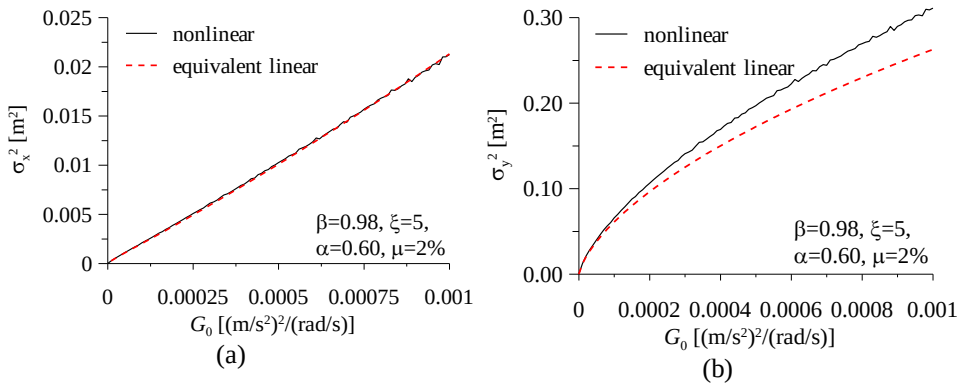

Fig. 3.4 – (a) Variance of main system displacement versus input strength; (b) Variance of fluid displacement versus input strength.

From a close observation of the latter figure, it appears that, since the nonlinear term in Eq. (2.20) involves the fluid velocity, the agreement between the fluid displacement variances σ_Y^2 is poor for increasing values of input strength. On the other hand, Fig. 3.4(a) shows that the main system displacement variances σ_X^2, predicted by the linearized system, are in a very good agreement with those obtained by the nonlinear system for a wide range of input strength, assessing the reliability of the proposed method.

3.5 Parametric analysis

In the present Section the pre-design tool is validated by means of a vast parametric numerical analysis.

Specifically, in previous Section 3.3 a pre-design value of ζ_2 has been derived assuming that ω_2 is practically coincident with ω_1 and that the main system is lightly damped.

In this section several numerical analyses will be carried out in order to investigate the effectiveness of the proposed formulation, when these assumptions are not fulfilled.

Two different main systems relevant to buildings design and equipped with TLCD will be used.

The first one, referred to as "*system 1*", is the 75-story building under random Gaussian broadband noise used in Chang and Hsu (1998) and in previous Section 3.4.

The second structural system (hereinafter referred to as "*system 2*") driven by non-white earthquake-type random loads, has the first mode properties $M = 4.61 \cdot 10^7\ Ns^2/m$, $C = 2.328 \cdot 10^6\ Ns/m$ (corresponding to $\zeta_1 = 1\%$) and $K = 2.904 \cdot 10^8\ N/m$ (corresponding to $\omega_1 = 0.401 \cdot 2\pi\ rad/s$).

The non-white earthquake-type loading is a Gaussian noise generated in such a way that the associated response spectrum (RS) is consistent with the one provided by a seismic code. For the sake of brevity, in the

present applications only results pertinent to the RS proposed by the Eurocode 8 with soil type C are reported, being the analyses conducted for other soil types always comparable. In Appendix B the characteristics of the non-white earthquake-type loading are reported.

It will be shown how variation in parameters like the structural damping ratio ζ_1, the mass ratio μ, the length ratio α, the presence of orifices (parameter ξ) and the input intensity, affects the proposed formulation.

The aim of this section is then to define the parameters range in which the proposed formulation is an efficient tool for structural design.

Therefore, a reference set of parameters has been selected, that is $\zeta_1 = 1\%, \mu = 2\%, \alpha = 0.60, \xi = 2, G_0 = 10^{-3}\left(m/s^2\right)^2 \Big/ \left(rad/s\right), a_g = 0.25g$ and, in turn, one of the parameters has been varied in a wide range.

In the following figures results in terms of normalized structural displacement variance $\sigma_X^2 / \sigma_{X_0}^2$ are reported, where $\sigma_{X_0}^2$ is the structural displacement variance of the uncontrolled system and σ_X^2 is computed according to Eq. (3.15 a) using the approximate proposed procedure. In particular, results obtained by MCS performed on the nonlinear system Eq. (2.20) (solid lines) are compared with those obtained by stochastic analyses on the equivalent linear system Eq. (3.3) (symbols) for frequency ratio $\nu = \omega_2 / \omega_1$ ranging from 0.80 to 1.20 and for both *system 1* and *system 2*.

3.5.1 Effect of structural damping

In Fig. 3.5 the effects of the variation of the structural damping ratio ζ_1 on the proposed formulation are shown for both systems. For all values of structural damping here considered, the normalized main displacement variance $\sigma_X^2/\sigma_{X_0}^2$ predicted by the approximate formulation are practically coincident with those computed by MCS when the tuning ratio ν is close to the unity, otherwise small deviations can be detected.

The maximum percentage differences for each value of ζ_1 in the range of ν of practical interest, i.e. $0.9 \le \nu \le 1$, are reported in Table 3.1 and Table 3.2 for both systems.

It is worth to note that in both *system 1* and *system 2* cases, the difference between the approximate formulation and the MCS results decreases when ζ_1 value increases.

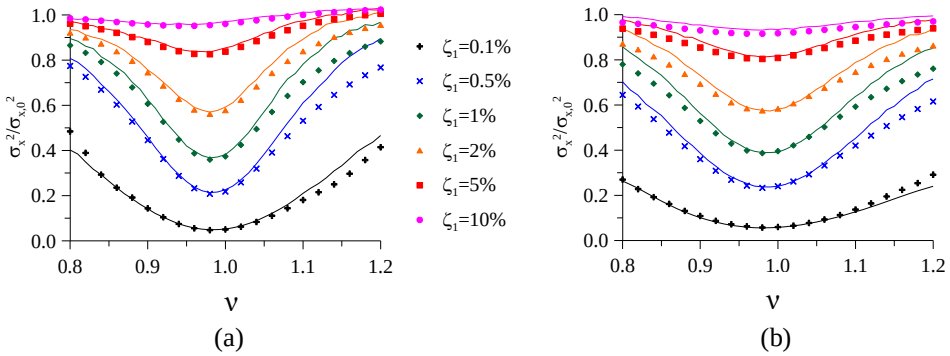

Fig. 3.5 – Main system normalized displacement variance: comparison between MCS (solid line) and the proposed formulation (symbols) for different values of the structural damping ζ_1: (a) *system 1*; (b) *system 2*.

Table 3.1 - Maximum percentage differences in terms of variances for ν ranging from 0.90 to 1.00 – *system 1*

ζ_1 (%)	% diff.	μ	% diff.	α	% diff.	ξ	% diff.	G_0	% diff.
0.1	3.75%	1.0%	3.94%	0.40	4.71%	1	3.30%	$5\cdot10^{-5}$	1.67%
0.5	3.62%	1.5%	4.03%	0.50	3.47%	2	3.39%	$1\cdot10^{-4}$	3.24%
1.0	3.39%	2.0%	3.39%	0.60	3.39%	5	2.31%	$5\cdot10^{-4}$	3.71%
2.0	2.51%	2.5%	3.08%	0.70	3.14%	10	5.91%	$1\cdot10^{-3}$	3.39%
5.0	1.90%	3.0%	2.90%	0.80	3.57%	20	8.51%	$5\cdot10^{-3}$	3.09%
10.0	1.10%	3.5%	2.80%	0.90	4.07%	50	11.00%	$1\cdot10^{-2}$	3.64%

Table 3.2 - Maximum percentage differences in terms of variances for ν ranging from 0.90 to 1.00 – *system 2*

ζ_1(%)	% diff.	μ	% diff.	α	% diff.	ξ	% diff.	a_g/g	% diff.
0.1	7.33%	1.0%	6.42%	0.40	7.03%	1	7.50%	0.05	7.82%
0.5	6.99%	1.5%	6.35%	0.50	6.70%	2	6.04%	0.10	7.40%
1.0	6.04%	2.0%	6.04%	0.60	6.04%	5	5.45%	0.15	7.36%
2.0	5.16%	2.5%	6.73%	0.70	5.70%	10	8.27%	0.20	6.95%
5.0	3.23%	3.0%	6.26%	0.80	5.35%	20	9.95%	0.25	6.04%
10.0	2.51%	3.5%	6.01%	0.90	5.35%	50	8.17%	0.30	5.23%

This behavior, apparently in contrast with one of the hypothesis of the approximate formulation, can be explained considering that when ζ_1 is very small the main structure behaves like a narrow band system, its response is more influenced by the tuning ratio and the linearized system response deviates from MCS results for non optimal values of ν (i.e. $\nu \approx 0.90$ and $\nu \approx 1.00$).

3.5.2 Effect of mass ratio

Figure 3.6 reports the effects of the variation of the mass ratio μ on the proposed formulation for both systems. Values of mass ratio from 1% to 3.5% have been considered and the normalized variance $\sigma_X^2 / \sigma_{X_0}^2$ determined by means of approximate formulation are very close to those computed by MCS on the nonlinear system for ν close to the unity. For other values of ν significant deviation can be observed, however, it is worth stressing that in the range of ν of practical interest, i.e. $0.9 \le \nu \le 1$, the maximum deviations are lower than 5% for *system 1* and lower than 10% for *system 2*, as reported in Table 3.1 and Table 3.2, respectively.

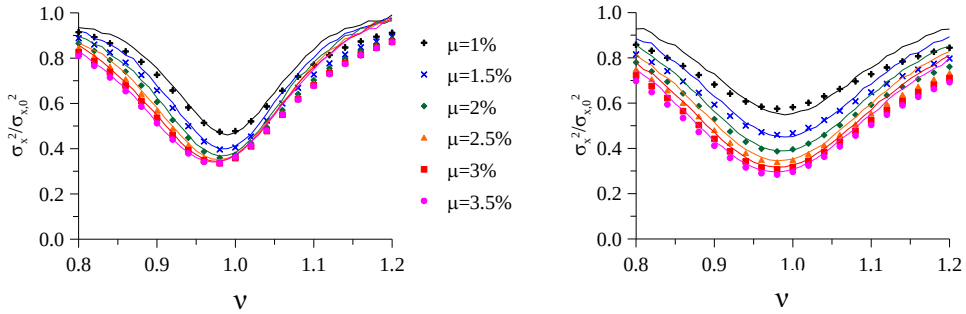

Fig. 3.6 – Main system normalized displacement variance: comparison between MCS (solid line) and the proposed formulation (symbols) for different values of the mass ratio μ : (a) *system 1*; (b) *system 2*.

3.5.3 Effect of length ratio

In Fig. 3.7 similar results obtained by varying the length ratio α from 0.40 to 0.90 are reported. It is shown that the proposed formulation is slightly affected by the variation of α for both systems.

The percentage differences between the normalized variance $\sigma_X^2 / \sigma_{X_0}^2$ obtained through the approximate formulation and by means of MCS on nonlinear system are very low for values of ν of practical interest and become larger when ν departs from unity, as reported in Table 3.1 and 3.2.

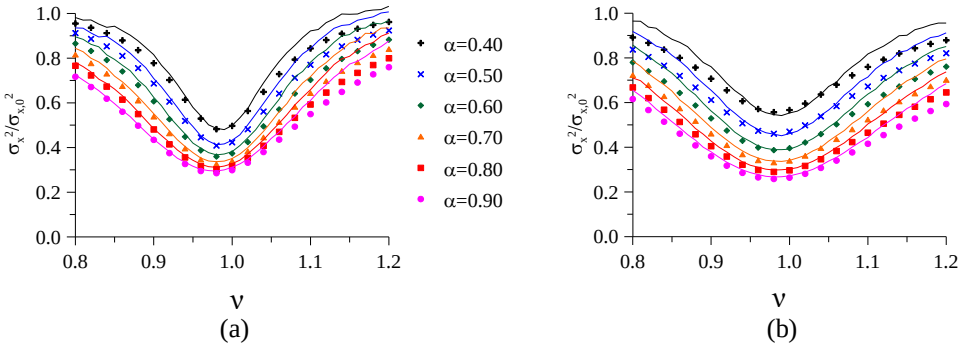

Fig. 3.7 – Main system normalized displacement variance: comparison between MCS (solid line) and the proposed formulation (symbols) for different values of the length ratio α : (a) *system 1*; (b) *system 2*

3.5.4 Effect of head loss coefficient

Figure 3.8 explains how the variation of the head loss coefficient ξ affects the proposed formulation. Varying ξ from 1 to 50 corresponding to orifice open ratio up to 80% (Wu et al., 2005), the normalized variance $\sigma_X^2 / \sigma_{X_0}^2$ has been evaluated by using the approximate formulation and by MCS on the nonlinear system for ν ranging from 0.80 to 1.20.

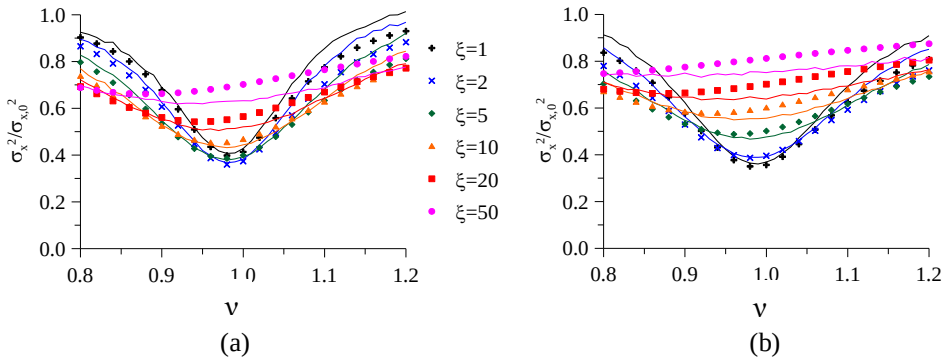

Fig. 3.8 – Main system normalized displacement variance: comparison between MCS (solid line) and the proposed formulation (symbols) for different values of the head loss coefficient ξ: (a) *system 1*; (b) *system 2*.

For values of ξ less than 10 (weak nonlinearity) and for ν close to the unity the result are in good agreement each other. If the nonlinear term increases (higher values of ξ) the accuracy of the results conducted by the SLT and approximations decreases and significant errors can be observed. Note that the maximum percentage errors are always lower than 11% and, if ξ is less than 10, the maximum percentage errors are lower than 6% for *system 1* and 8% for *system 2*, as reported in Table 3.1 and 3.2 respectively.

3.5.5 Effect of input intensity

Figure 3.9 reports the effects of the variation of the input intensity on the proposed formulation. For *system 1* driven by broadband Gaussian noise values of input strength G_0 ranging from $5 \cdot 10^{-5}$ to $1 \cdot 10^{-2} \left(m/s^2\right)^2 / \left(rad/s\right)$ have been considered, while for *system 2*, driven by earthquake-type loading, values of peak ground accelerations a_g ranging from 0.05g to 0.30g have been taken into account.

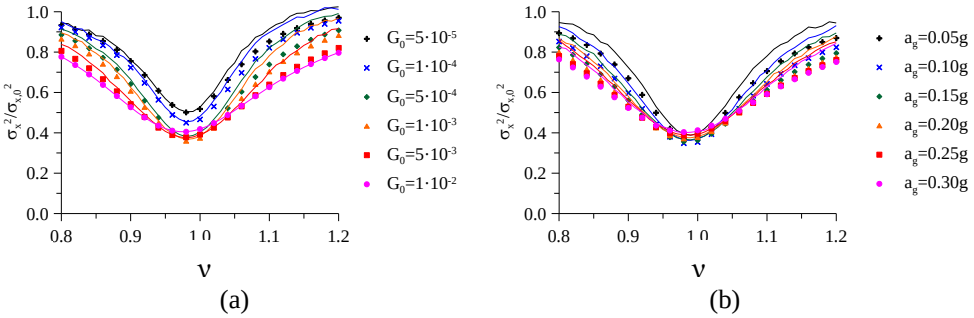

Fig. 3.9 – Main system normalized displacement variance: comparison between MCS (solid line) and the proposed formulation (symbols) for different values of input intensity: (a) *system 1*; (b) *system 2*.

Comparison between the normalized variances $\sigma_X^2 / \sigma_{X_0}^2$, determined by means of approximate formulation and those computed by MCS, shows that no significant deviation can be observed in the whole range of the input intensity. In the range of ν of practical interest, i.e. $0.9 \le \nu \le 1$ the maximum percentage differences are lower than 4% for broadband Gaussian noise and lower than 8% for earthquake-type loading, as shown in Tables 3.1 and 3.2 respectively.

In conclusion, in the present section some numerical simulations have been carried out in order to assess the robustness of the assumptions on which the approximate formulation is based. Moreover, the performed parametric analysis showed that the response variance computed by the proposed approximated formulation does not exhibit substantial deviation from the actual values (those obtained through the MCS on nonlinear system) in the parameters range of practical interest.

3.6 Determination of the optimal design parameters

In order to show the effectiveness of the proposed simplified procedure for practical use, in the present Section an analysis on the optimal choice of the TLCD design parameters has been developed. In particular it will be shown that the optimal design of the TLCD can be effectively performed using the proposed approximate formulation.

Because of the nonlinearity in equation of motion Eq. (2.20), a closed-form solution for the optimal values of the TLCD parameters is difficult to achieve and numerical methods have to be used. However, there is no need for an optimization procedure that involves all four parameters (namely the tuning ratio ν, the mass ratio μ, the length ratio α and the head loss coefficient ξ), since the mass ratio μ and the length ratio α are often limited by economical and structural constraints. In the optimization procedure here proposed, the optimum values of the tuning ratio ν and the head loss factor coefficient ξ are sought, while other parameters are assigned.

According to the approximate proposed formulation, Eq. (3.15 a) expresses the displacement variance of a 2-DOF linear system. The optimum values in terms of tuning ratio ν_{opt} and equivalent linear damping ratio $\zeta_{2,opt}$ can then be found by using a simple numeric minimization procedure on the smooth function $1/z_x$, with z_x given in Eq. (3.16 a). It is worth stressing that, at this stage, the optimal

parameters ν_{opt} and $\zeta_{2,opt}$ do not depend neither on the input intensity, since the system is linear, nor on the frequency of the main system, but only on the main system damping ratio ζ_1, and on the non-dimensional TLCD parameters μ and α. As a consequence, the parameter $\xi_0\left(\nu_{opt},\zeta_{2,opt}\right)$ in Eq. (3.27) also depends only on ζ_1, μ and α.

Once ν_{opt} and $\zeta_{2,opt}$ have been found, the corresponding value in terms of TLCD optimal head loss coefficient ξ_{opt} is easily obtained by Eq. (3.26) as

$$\xi_{opt}=\frac{\xi_0\left(\nu_{opt},\zeta_{2,opt}\right)}{\sqrt{G_0\omega_1}} \tag{3.28}$$

In the following some numerical results have been reported. Firstly, a comparison with the optimal values obtained in literature has been performed. With reference to the previously defined structural *system 1*, and accordingly to Wu and Chang(2006), the input strength of the white noise ground motion is set as $G_0=2\cdot 3.6373\cdot 10^{-6}\left(m/s^2\right)^2/\left(rad/s\right)$, while the mass ratio and the length ratio are $\mu=0.0298$ and $\alpha=0.774$, respectively. In Table 3.3 the parameters obtained for three cases of main structural damping: $\zeta_1=1\%$, $\zeta_1=5\%$ and $\zeta_1=10\%$, respectively have been reported in terms of optimal tuning ratio ν_{opt}, optimal head loss factor ξ_{opt}, and performance control index ε. The performance control index has been defined as $\varepsilon=\sigma_X^2/\sigma_{X_0}^2$, namely the normalized mean

square value of the structural response $X(t)$ with respect to the main structural response $X_0(t)$.

Table 3.3 - Comparison of optimum parameters with Chang (1999) and Wu and Chang (2006)

	tuning ratio		ξ_{opt}	ε
	ν_{opt}	err %		
Chang (1999)	0.973	-0.05	63.324	0.256
Wu and Chang (2006)	0.969	-	63.235	0.255
Proposed approach	0.969	0.01	65.390	0.255
	ν_{opt}		ξ_{opt}	ε
Chang (1999)	0.973	2.21	95.402	0.710
Wu and Chang (2006)	0.952	-	94.571	0.705
Proposed approach	0.952	-0.03	83.527	0.705
	ν_{opt}		ξ_{opt}	ε
Chang (1999)	0.973	5.53	133.937	0.889
Wu and Chang (2006)	0.922	-	130.683	0.879
Proposed approach	0.922	-0.03	106.370	0.879

It has to be stressed that the values provided by Chang (1999) are derived in absence of structural damping ($\zeta_1 = 0$), while results in Wu and Chang (2006) have been obtained by means of extensive numerical iterative procedures, similar to that reported in Fig. 3.1. In Table 3.3 are also reported the percentage differences between the herein obtained values and the ones reported in Wu and Chang (2006) in terms of optimal tuning ratio ν_{opt}.

As shown, the optimal values obtained by the proposed approach in terms of tuning ratio ν_{opt} are in a very good agreement with results from literature.

Note that by using the proposed definition of the equivalent linear damping an impressive reduction in computational effort is achieved. In fact, if a classical procedure is used to define the equivalent linear system, a time-consuming iterative scheme has to be set up. Conversely, following the here proposed approach, the evaluation of the optimal values can be obtained by means of a numerical minimization of a smooth function, without any iteration, thus resulting in a very significant reduction in computational effort.

The main advantage of the proposed approach lies in the evaluation of the optimal values in terms of tuning ratio ν_{opt} and equivalent linear damping ratio $\zeta_{2,opt}$ of an equivalent linear system.

Such parameters are suitable to be used to create design charts in which optimal values can be easily determined. In order to propose an effective tool for pre-designing TLCD devices, the charts depicted in this section report optimal values directly in terms of $\xi_0\left(\nu_{opt},\zeta_{2,opt}\right)$, taking full advantage of Eqs. (3.27) and (3.28). The design charts, reported in Figs. 3.10 and 3.11, have been evaluated for $\alpha = 0.60$. Clearly, it is possible to create other design charts for different values of α. In particular, the chart depicted in Fig. 3.10 illustrates the optimal tuning ratio ν_{opt} and the parameter ξ_0 in abscissa and ordinate, respectively, while in the chart depicted in Fig. 3.11 the optimal tuning ratio ν_{opt} and the performance control index ε are reported in abscissa and ordinate, respectively. In both design charts some curves for several different

values of damping ratio ζ_1 (black solid lines) and of mass ratio μ (dashed red lines) are also reported.

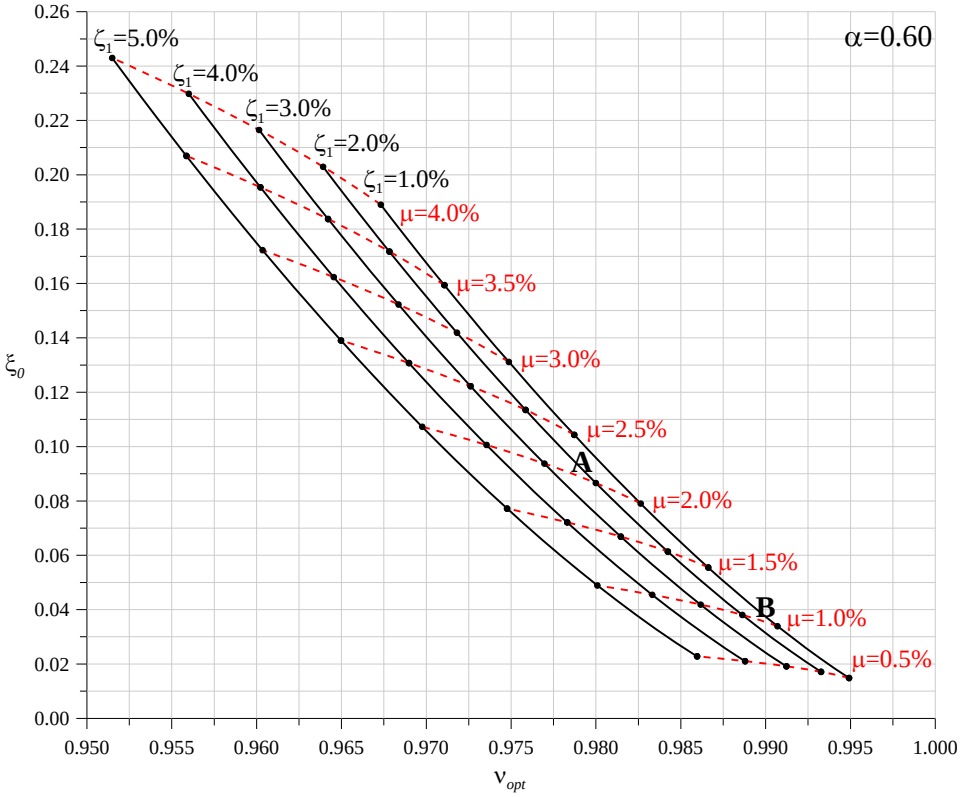

Fig. 3.10 –Optimal design chart in terms of ν_{opt} and ξ_0 for different values of damping ratio ζ_1 and mass ratio μ.

The use of the proposed design chart is illustrated in the following. Suppose that the damping ratio of the main system is $\zeta_1 = 2\%$ and the mass ratio is set as $\mu = 2\%$ for structural constraints, thus identifying the point **A** in FIgs. 3.10 and 3.11. The design charts provide the optimal parameters $\nu_{opt} = 0.980$ and $\xi_0 = 0.086$ (from Fig. 3.10) and the

corresponding performance control index $\varepsilon = 0.56$ (from Fig. 3.11). Obviously, from Eq. (3.26) the optimal head loss factor ξ_{opt} can be easily evaluated.

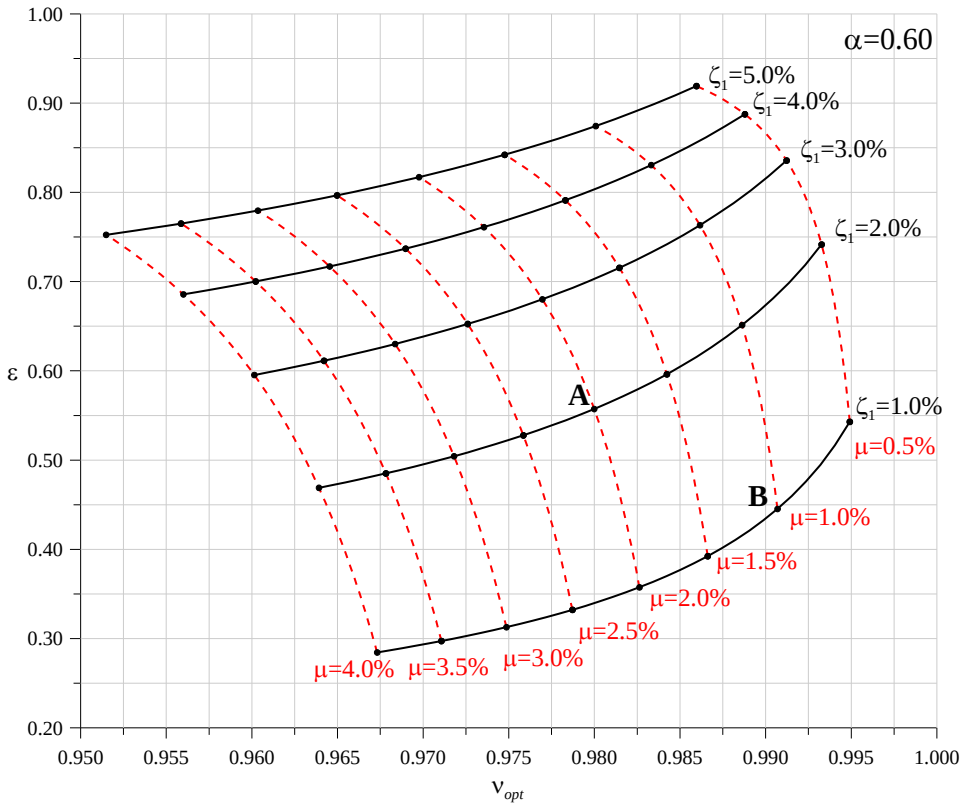

Fig. 3.11 –Optimal design chart in terms of ν_{opt} and ε for different values of damping ratio ζ_1 and mass ratio μ.

Furthermore, the herein proposed design charts can be used to properly choose the design parameters of a TLCD. Suppose that the damping ratio of the main system is $\zeta_1 = 1\%$ and that a target performance control index $\varepsilon = 0.45$ is desired. These parameters identify

the point **B** in the design chart in Fig. 3.11 and, from the chart in Fig. 3.10, the optimal design parameters $\nu_{opt} = 0.9906$ and $\xi_0 = 0.034$ may be evaluated and the optimal head loss factor ξ_{opt} can be evaluated again by Eq. (3.26).

At a design stage, in order to evaluate optimal parameters ν_{opt} and ξ_{opt} a value of the intensity of the input has to be estimated. This could be achieved by the following steps: a) according to the specific seismic code, the expected earthquake loading may be defined in terms of spectral acceleration response spectrum; b) seismic acceleration may be modeled by a zero-mean stationary Gaussian process $\ddot{X}_g$, fully characterized by its PSD function $G_{\ddot{X}_g}(\omega)$, coherent with the assigned response spectrum; c) in case of lightly damped system the evaluation of the input intensity may be easily obtained as $G_{\ddot{X}_g}(\omega_1)$.

To show the accuracy of the proposed procedure also in the case of a system under earthquake type of loading, the aforementioned procedure has been applied to *system 2* described in Section 3.5.

Specifically, in this case evaluation of optimal tuning parameters has been performed comparing results from the proposed approach with those obtained by MCS. With reference to structural *system 2*, in Table 3.4 tuning ratio ν_{opt} and optimum head loss coefficient ξ_{opt}, have been computed for both nonlinear formulation Eq. (2.20) and equivalent linear system Eq. (3.1) in which ζ_2 is computed via the proposed approximate formulation, while other parameters have been set as $\mu = 3\%$ and

$\alpha = 0.6$. In case of nonlinear systems the displacement variance σ_X^2 has been computed through MCS, while for equivalent linear systems Eqs.(3.7) to (3.11) have been used.

In Table 3.4 the performance control index $\varepsilon = \mathrm{E}[X^2]/\mathrm{E}[X_0^2]$ has been reported, as well. These results have been obtained for different values of input intensities. For the sake of shortness, in the present applications only results obtained by the RS proposed by the Eurocode 8 with soil type C are reported, but the analyses for other soil types or other inputs always give comparable results. In Appendix B the PSD function coherent with RS provided in Eurocode 8 has been fully defined. For all intensities of the input the optimal parameters of TLCD obtained by the proposed approximate procedure are in very good agreement with those obtained by MCS.

Table 3.4 - Optimum TLCD parameters for *system 2.*

	Equivalent linear			Nonlinear		
a_g/g	ν_{opt}	ξ_{opt}	ε	ν_{opt}	ξ_{opt}	ε
0.05	0.9813	6.5076	0.2982	0.9835	7.3511	0.3106
0.10	0.9813	3.2880	0.2983	0.9808	3.8263	0.3108
0.15	0.9808	2.1743	0.2983	0.9823	2.4849	0.3104
0.20	0.9811	1.6257	0.2983	0.9800	1.8479	0.3104
0.25	0.9810	1.3014	0.2983	0.9825	1.3219	0.3105
0.30	0.9810	1.0860	0.2983	0.9806	1.1684	0.3104

As stated before, optimal tuning parameters depend also on the main system damping ratio. Unfortunately, the estimation of ζ_1 is often affected by significant uncertainties. In Table 3.5 the percentage

differences in the evaluation of optimal parameters and performance control index are reported with respect to the errors in the evaluation of ζ_1 of ±10%. It is worth stressing that, uncertainties in ζ_1 cause very small deviation in the optimal tuning parameters, while the errors in performance control index determination are higher.

Table 3.5 - Deviations in optimal parameters and performance control index for errors in the evaluation of ζ_1 of ±10%.

		tuning ratio		normalized head loss factor		performance control index	
	ζ_1	ν_{opt}	err %	ξ_0	err %	ε	err %
	-10%	0.9829	0.03	0.0763	-0.91	0.3308	-7.44
1%	-	0.9826	-	0.0770	-	0.3574	-
	+10%	0.9824	-0.02	0.0777	0.91	0.3826	7.05
	-10%	0.9806	0.06	0.0826	-1.67	0.5250	-5.78
2%	-	0.9800	-	0.0840	-	0.5572	-
	+10%	0.9794	-0.06	0.0853	1.55	0.5864	5.24
	-10%	0.9717	0.20	0.0996	-2.83	0.7914	-3.13
5%	-	0.9698	-	0.1025	-	0.8170	-
	+10%	0.9677	-0.22	0.1053	2.73	0.8387	2.66

Furthermore, it is worth stressing that the optimal parameters obtained from these design charts are fully reliable, although they are determined by means of an approximate approach. In fact, in the parameters range of practical interest results from the proposed formulation are in very good agreement with those obtained by MCS performed on the nonlinear equations, as it has been already shown in the previous sections and in Table 3.1.

3.7 Experimental investigation

Once the proposed direct pre-design formulation has been extensively numerically investigated, in this Section numerical results previously obtained are validated through an experimental campaign on a small scale shear-type model built in the Laboratory of Experimental Dynamic at University of Palermo.

Specifically, in order to experimentally validate the pre-design proposed formulation for the equivalent linear damping estimation, a small-scale SDOF shear-type frame (main system), composed by two steel columns and two nylon rigid plates as base and floor respectively, has been built. Further, TLCD-controlled system has been realized with a U–shaped Plexiglas® cylinder tube rigidly connected to the upper plate of the main system.

To examine the effects of the mass ratio μ on the proposed formulation, three different configurations of TLCDs with same horizontal liquid length b, but different cross sectional area *A* have been considered. In particular, since in (Chang and Hsu, 1998) the mass ratio $\mu = 2.9\,\%$ for a 75 stories skyscraper has been used as benchmark problem, and many papers from then on have considered that value (see for example(Wu and Chang, 2006)) in order to compare the optimized parameter, Configuration #1 and #2 have been chosen so as their mass ratio values perfectly include the one considered in(Chang and Hsu, 1998). Furthermore, as described in Section 3.4, differences among the

simplified proposed formulation and the Monte Carlo Simulation (MCS) results increase when the value of the mass ratio increases. This behavior has led to investigate Configuration #3, which indeed takes into account a higher mass ratio not relevant for practical application.

It is worth noting that, since the proposed simplified formulation in Eq. (3.23) has been derived considering the input modeled as a zero-mean stationary Gaussian white noise process, the experimental campaign has been accomplished considering a broadband noise at the base, which is practically the same as considering a white noise excitation. However, as demonstrated in Section 3.4 through an extensive parametric investigation, satisfactory results may also be obtained considering non-white earthquake random loads with Response Spectra coherent with building codes.

3.7.1 Main systems

Note that, since the main system has to take into account the dead weight of the TLCDs tube, three small-scale SDOF shear-type frames with the three empty TLCD devices on the upper plate, have been used as three main systems configurations.

In Figs. 3.12(a-c) pictures of the three main systems configurations are shown while in Figs. 3.12(d- f) schematic drawings of the structures with the corresponding dimensions are depicted.

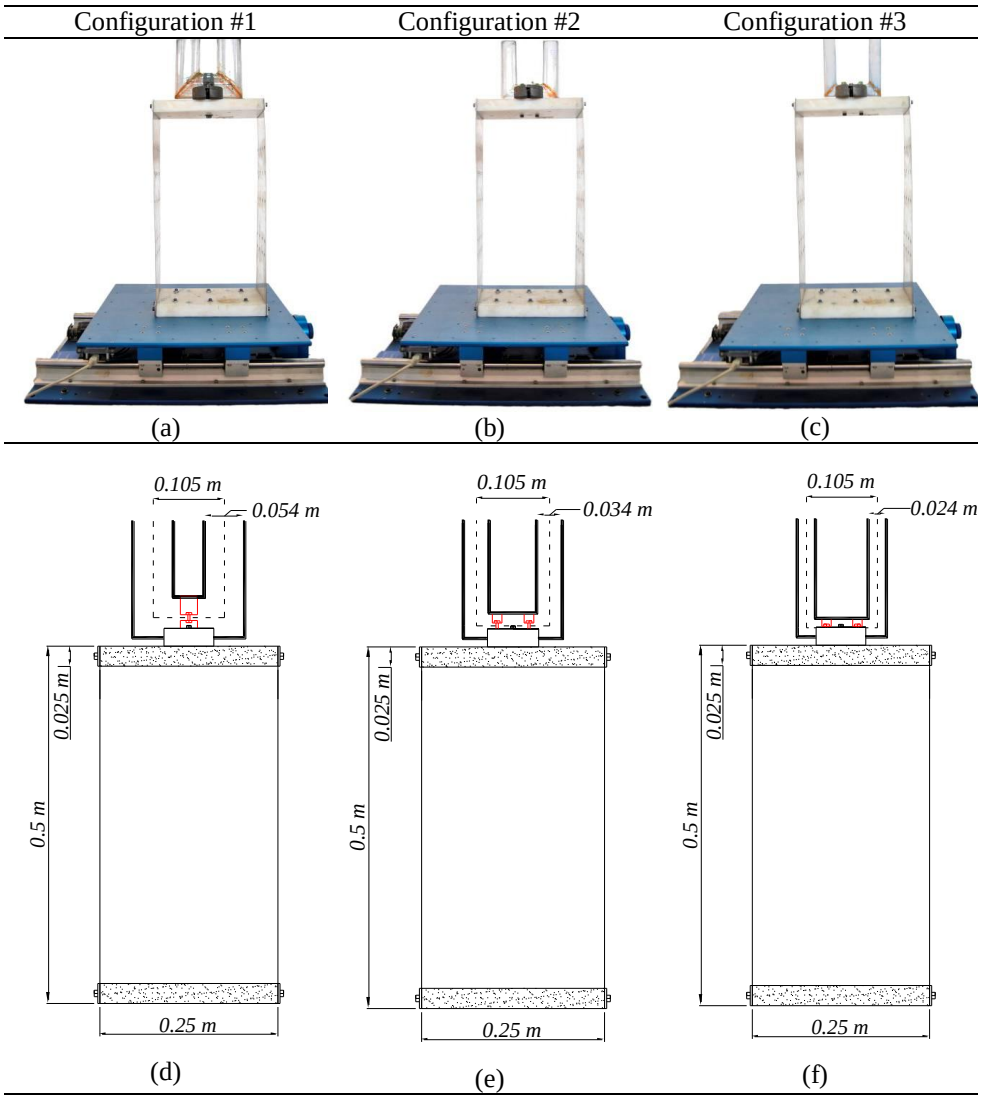

Fig. 3.12 – Experimental setup of the main systems; (a) - (c) picture of the three SDOF structures configurations; (d) - (f) main systems dimensions.

In order to experimentally identify dynamic parameters of the three main systems configurations, the three SDOF structures have been excited at the base through a shaking table model Quanser Shake Table II which provides the displacement controlled ground motion (Figs. 3.13(a-

c)). The acceleration responses at the base and at the storey of the systems have been acquired using Miniature DeltaTron Accelerometers Brüel&Kjær – Type 4507-002B piezoelectric accelerometers. In order to condition and amplify voltage signals coming from accelerometers before being acquired and saved, a conditioning amplifiers, the PCB model 481A amplifier, has been used.

Voltage signals have been generated by means of a National Instruments NI-PCI-MIO-16XE-10 and have been digitalized and acquired by means of a National Instruments NI-PCI-4472 Analogical-Digital (A-D) Acquisition Board and then processed using a self-developed signal processing software in LabView and Matlab environment.

Details on the various devices and systems employed for the experimental set-up are further described in Appendix A, while Fig. 3.13 shows an outline of the experimental set-up.

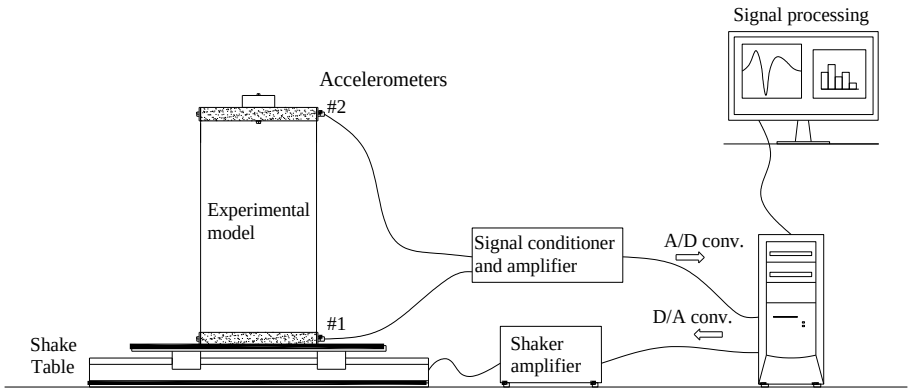

Fig. 3.13 – Acquisition system for Shake Table test.

Ten samples of broadband noise, in the range 0.5÷10 Hz, each having duration of 40 s and a sampling frequency of 1 kHz, have been generated and used as ground acceleration. For each sample the accelerations have been recorded and the mean Frequency Response Function (FRF) was computed (Maia and Silva, 1997).

Finally, once obtained the FRFs for each configuration, dynamic parameters were identified by using some well-known parameter extraction techniques (Ewins, 1984, Maia and Silva, 1997) such as Rational Fractional Polynomial method (Richardson and Formenti, 1982), genetic algorithm (Levin and Lieven, 1998) and particle-swarm optimization method (Kennedy and Eberhar, 1995).

All these techniques provide similar estimations of the parameters that are reported in Table 3.6.

Table 3.6 - Main systems dynamic parameters.

	Configuration #1	Configuration #2	Configuration #3
M	4.503 *kg*	4.267 *kg*	4.215 *kg*
C	0.0906 *N s/m*	0.1195 *N s/m*	0.1375 *N s/m*
K	455.72 *N/m*	458.86 *N/m*	466.48 *N/m*
ζ_1	0.001	0.0027	0.0031
ω_1	10.06 *rad/s*	10.37 *rad/s*	10.52 *rad/s*

In Figs. 3.14(a, c, e) comparisons among experimental and numerical mean FRFs are depicted for the three main systems configurations.

In order to assess the reliability of the identified parameters, a numerical-experimental comparison has also been made for the three configurations of main systems, as reported in Figs. 3.14(b, d, f). In this

pictures the relative acceleration time histories recorded at top mass location are compared with those computed by the theoretical model defined by Eq. (2.8) setting as parameters those reported in Table 3.6.

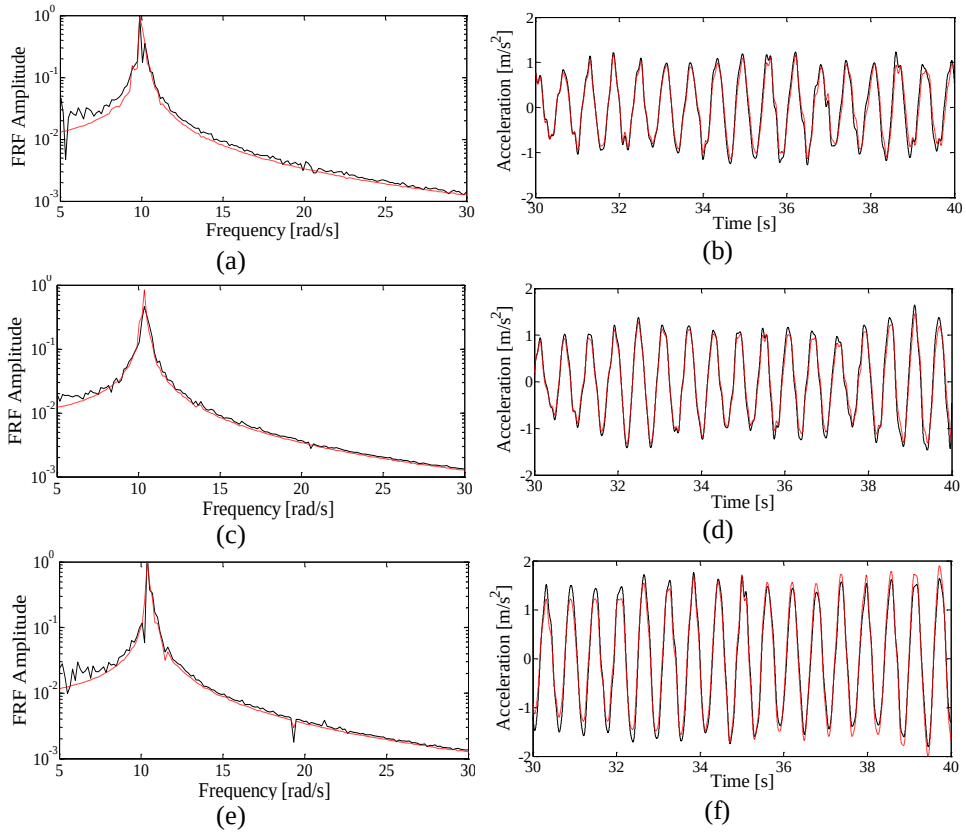

Fig. 3.14 – Experimental (black solid line) and numerical (red dashed line) comparison of mean FRFs (a ,c, e) and relative accelerations (b, d, f) of the main systems: (a, b) Configuration #1; (c, d) Configuration #2; (e, f) Configuration #3.

3.7.2 TLCD devices

As previously stated, to examine the effects of the mass ratio μ on the proposed formulation, three different groups of TLCDs have been considered. In this regard three different diameters d have been used for the three TLCDs configurations, while centerlines of the vertical branches are at the same distance b each other for all the TLCDs. The tube has been filled with water ($\rho = 1000\,kg/m^3$), reaching different levels h from the centerline of the base tube for tuning each TLCD with the main system.

In Figs. 3.15(a)-(c) pictures of the three TLCD devices are shown while in Figs. 3.15(d)-(f) schematic drawings of the TLCDs with the corresponding dimensions are depicted.

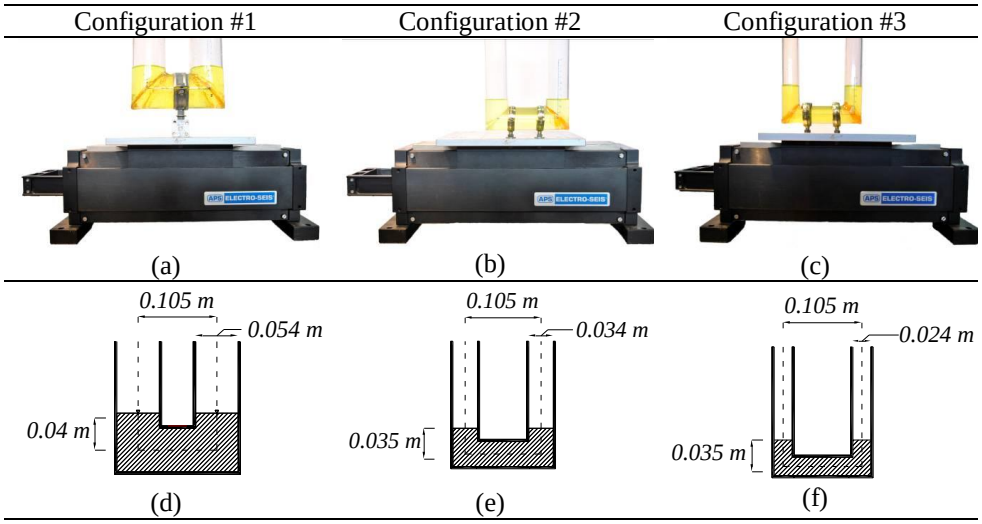

Fig. 3.15 – TLCD devices; (a) - (c) picture of the three TLCDs configurations; (d) - (f) TLCDs dimensions.

In order to experimentally identify dynamic parameters of the three TLCDs configurations, the U-shaped tubes filled with water to a level $h = 4\,cm$ for Configuration #1 and $h = 3.5\,cm$ for Configuration #2 and #3, have been rigidly connected and excited at the base through a APS Dynamic–Model 133 shake table (Figs. 3.15(a)-(c)).

An accelerometer on the table itself has been used to acquire the input signal while a simple video camera model Canon IXUS 100IS has been used to record the TLCD water free surface displacements.

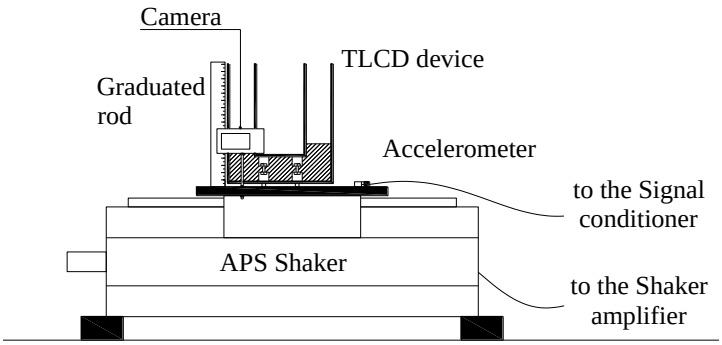

Fig. 3.16 – Acquisition system for TLCDs test.

As shown in Fig. 3.16, the camera was rigidly connected through a screw to the plate of the shaker to create a moving reference frame, integral with the TLCD devices. The screw was moved up or down until a suitable position was reached so that the camera focuses only on the left column liquid during its entire motion, to record the free water surface displacement only.

Dynamic parameters of the TLCD devices have been identified by exciting the U-shaped tubes with broadband noise in the range 0.5÷10 Hz through the APS shaker. For each TLCD device 20 samples of broadband

noise with a duration time of 25 s have been generated and used as ground acceleration. For each sample, the acceleration at ground and the liquid displacement were recorded through the accelerometer and the video camera respectively. Each video was recorded at 30 fps (corresponding to a sampling frequency of 30 Hz) and high-definition full-frame images of 1280 x 720 pixels were acquired and transferred to the computer.

In order to determine the free water surface displacements for each analyzed configuration, an image processing method in MATLAB environment was used.

(a) (b) (c)

Fig. 3.17 – Image processing; (a) extracted frame from the video; (b) binary image; (c) image with the determined pixel position (black point on the water interface).

Specifically, each frame in the RGB color space (Fig. 3.17(a)), is converted into the equivalent hue, saturation and value (HSV) image, and these components are then extracted. Once assigned and applied suitable low and high thresholds value to the HSV image components (to filter out unnecessary color and additional noises) these are converted into binary images, which have intensity values of 0 (corresponding to black color) or 1 (corresponding to white color), and then combined together to obtain a binary image in which the water is colored in white and the rest of the image is black (Fig. 3.17(b)). This binary image is used to identify

the free water surface in the left column of the TLCD, and the pixel position corresponding to the passage from the black to the white color of a chosen point at the centre of the TLCD column, is determined in the analyzed frame (point A in Fig. 3.17(c)).

Once the pixel positions have been acquired for all frames, conversion to displacement in meters has been made with a calculated scale factor, determined though the graduated rod rigidly connected to the plate of the shaker (Fig. 3.16). In this way the free water surface displacement time histories has been obtained from the videos and samples of the extracted time histories for the three TLCDs configuration are depicted in Fig. 3.18. Finally the mean Frequency Response Function (FRF) has been computed to identify the natural frequency of the liquid ω_2 while the head loss coefficient ξ was computed by minimizing the error between the measured FRFs of the liquid displacement and those from Eq. (2.4) considering as input the recorded accelerations. The identified TLCDs parameters are detailed in Table 3.7.

Table 3.7 - TLCD configurations parameters.

	Configuration #1	Configuration # 2	Configuration # 3
d	0.054 m	0.034 m	0.024 m
A	$2.29 \cdot 10^{-3}$ m^2	$9.08 \cdot 10^{-4}$ m^2	$4.52 \cdot 10^{-4}$ m^2
b	0.105 m	0.105 m	0.105 m
h	0.04 m	0.035 m	0.035 m
L	0.185 m	0.175 m	0.175 m
m_{TLCD}	0.4380 kg	0.1614 kg	0.0815 kg
ω_2	11.97 rad/s	11.81 rad/s	11.81 rad/s
ξ	6	7	7
c	16.21 m^{-1}	18.92 m^{-1}	20 m^{-1}
μ	9.7 %	3.8 %	1.9 %
α	0.57	0.6	0.6

In order to assess the reliability of the identified parameters, for each TLCD configuration numerical-experimental comparison of mean FRFs and of time history liquid displacements are depicted in Fig. 3.18.

As shown for each TLCD configuration the numerical results match very well the corresponding experimental results, in time domain and in frequency domain as well.

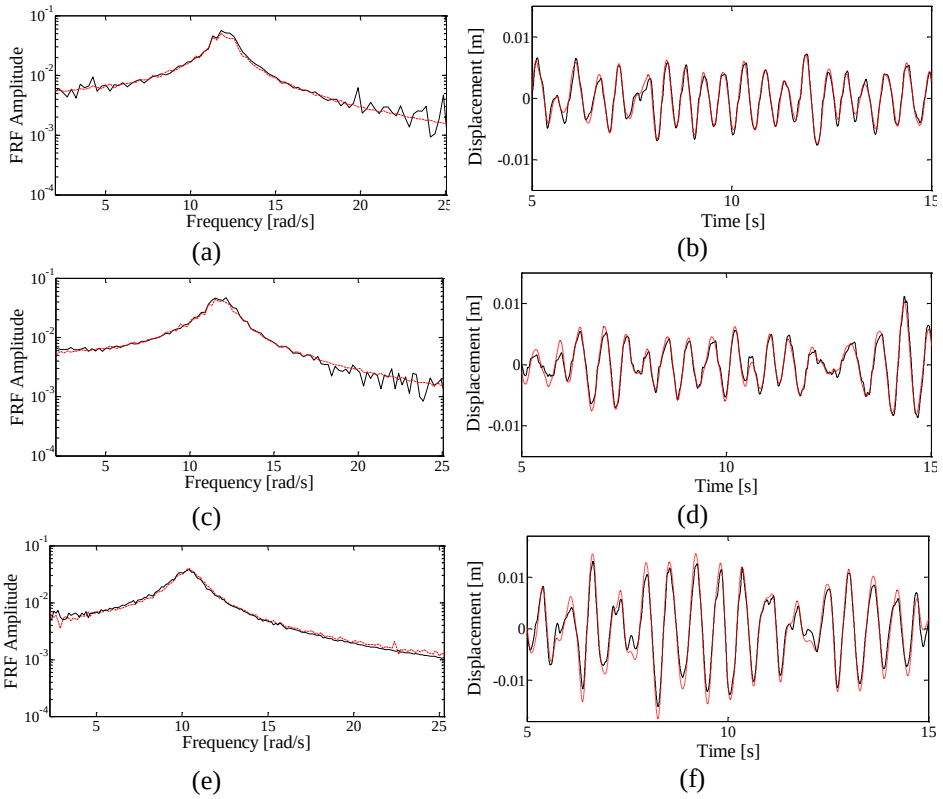

Fig. 3.18 – Experimental (black solid line) and numerical (red dashed line) comparison of mean FRF (a ,c, e) and liquid displacement time histories (b, d, f): (a, b) Configuration #1; (c, d) Configuration #2; (e, f) Configuration #3

3.7.3 TLCD controlled systems

In order to validate the reliability of the identified dynamic parameters of the main systems and TLCD devices (Tables 3.6 and 3.7), also for the three TLCD controlled systems, the three structures have been excited, with the same base excitation used for the main systems, through the shaking table model Quanser Shake Table II. In this regard in Figs. 3.19(a-c) pictures of the three TLCD controlled systems configurations are shown while in Figs. 3.19(d-f) schematic drawings of the three TLCDs configurations with the corresponding dimensions are reported.

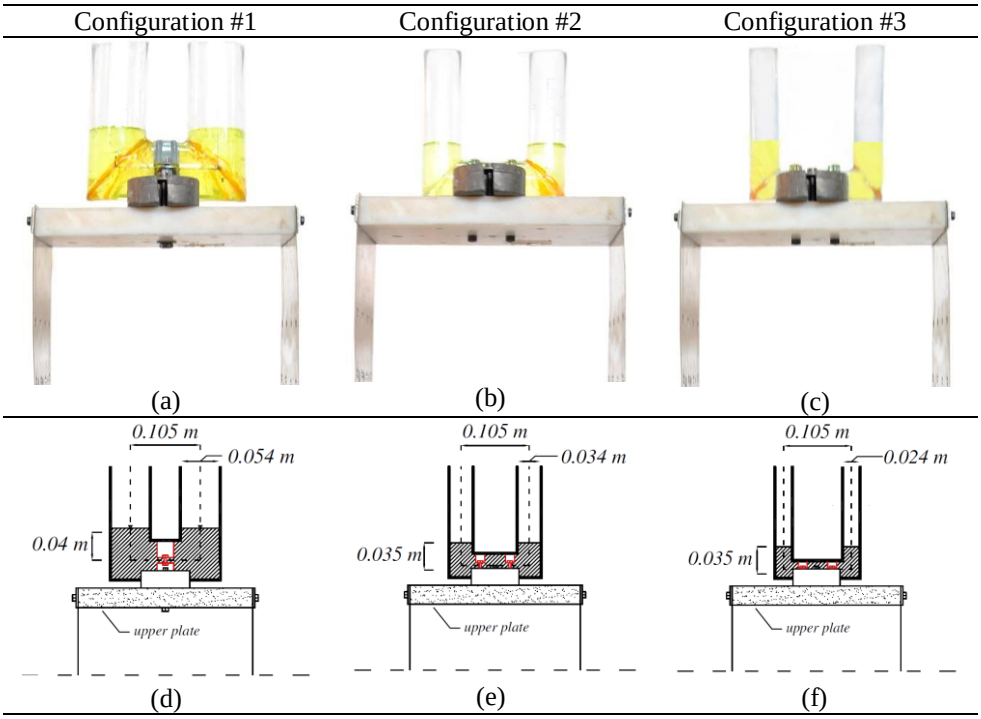

Fig. 3.19 – Experimental setup of the controlled system; (a) - (c) picture of the three controlled structures; (d) - (f) controlled systems dimensions.

A numerical-experimental comparison has been made for the three TLCD-controlled systems configurations, as reported in Fig. 3.20(a- c). In these pictures the relative acceleration time histories recorded at top mass location are compared with those computed by the numerical model defined by Eq. (2.20) and parameters in Tables 3.6 and 3.7.

The very good agreement between the numerical and experimental curves shows that the dynamical parameters have been correctly identified.

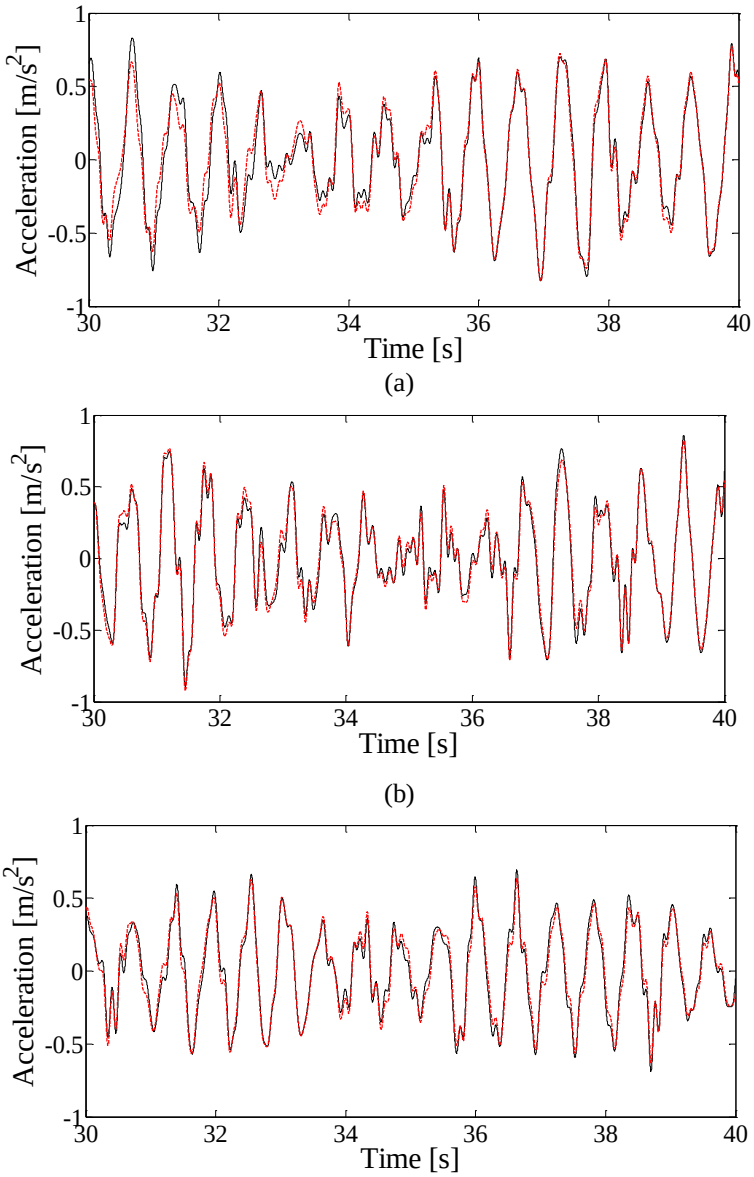

Fig. 3.20 – Comparison between experimental (black solid line) and numerical (red dashed line) data in time domain for the TLCD controlled systems: (a) Configuration #1; (b) Configuration #2; (c) Configuration #3.

3.7.4 Experimental validation of the proposed formulation

Once the main systems and TLCD-controlled systems have been identified, the proposed direct pre-design formula Eq. (3.23) has been validated in terms of statistics by the experimental procedure outlined in the following.

Experimental campaign has been developed to assess the validity of the formula for the three different values of mass ratio μ, characterizing the aforementioned three systems configurations. The three configurations of the main system and of the TLCD-controlled system have been subjected to a broadband noises in the range 0.5÷10 Hz. For each configuration 10 samples of broadband noise, with duration of 40 seconds, have been generated and the accelerations at the ground and at the top mass have been recorded.

The statistics of experimental response accelerations in terms of variance have been computed and then compared with the variances obtained by solving numerically the nonlinear system Eq. (2.20) and the linearized one Eq. (3.1) with ζ_2 obtained through Eq. (3.23). In the numerical simulations the recorded ground accelerations have been used as base accelerations $\ddot{X}_g$.

In Fig. 3.21 comparison among variances $\sigma^2_{\ddot{X}}$ of accelerations for main systems (green crosses and green dots) and TLCD-controlled system (red rhombi, red squares and red triangles) at the different levels of mass ratio μ is depicted.

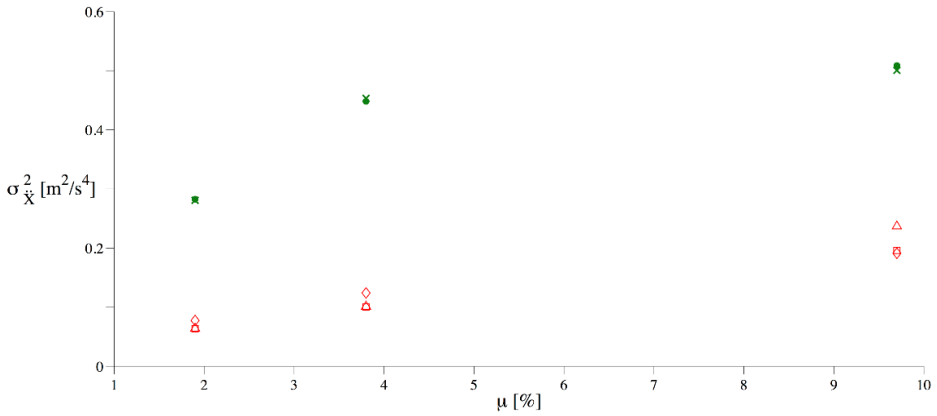

Fig. 3.21 – Experimental validation in term of variances. Variances of the main system (green) and TLCD-controlled system (red). Crosses and squares indicate numerical results (Eq. (2.8) for main system, Eq. (2.20) for TLCD-controlled system respectively), triangles stand for equivalent linear system (Eq. (3.1)), dots and rhombi stand for experimental results (main system and TLCD-controlled system respectively).

As shown, experimental results (red rhombi) are in a good agreement with the numerical ones (red squares) for all the values of mass ratio analyzed while results of the direct proposed procedure (red triangles) deviates from the experimental results at increasing values of the mass ratio, as also demonstrated in (Di Matteo et al., 2014).

Further experimental campaign to assess the validity of the formula at different values of the input strength G_0 has been done. Both Configurations #1 of the main system (Fig. 3.12(a)) and TLCD-controlled system (Fig. 3.19(a)) have been subjected to six increasing levels of input strength, by taking advantage of the capability of the shaking table to perfectly reproduce any displacement time history. For each level 50 samples of broadband noise, with duration of 50 seconds,

have been generated and the accelerations at the ground and at the top mass have been recorded.

The statistics of both input and response accelerations in terms of variance have been computed and then compared with the variances obtained by solving numerically Eqs. (2.20) and (3.1). In the numerical simulations the recorded ground accelerations have been used as base accelerations $\ddot{X}_g$.

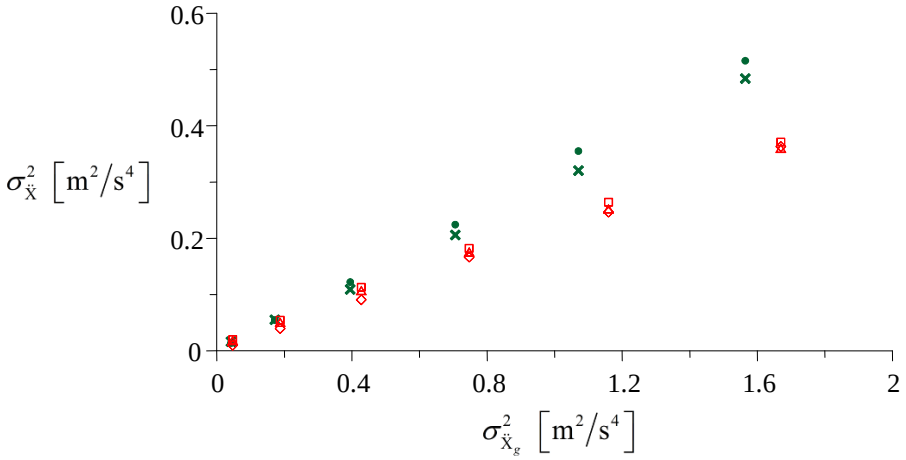

Fig. 3.22 - Experimental validation in term of variances. Variances of the main system (green) and TLCD-controlled system (red). Crosses and squares indicate numerical results (Eq. (2.8) for main system, Eq. (2.20) for TLCD-controlled system respectively), triangles stand for equivalent linear system (Eq. (3.1)), dots and rhombi stand for experimental results (main system and TLCD-controlled system respectively).

In Fig. 3.22 comparison among variances of accelerations $\sigma^2_{\ddot{X}}$ for main system (green crosses and green dots) and TLCD-controlled system (red rhombi, red squares and red triangles) versus the input variance $\sigma^2_{\ddot{X}_g}$ is shown.

The equivalent linear system (red triangles) obtained by using the proposed formulation follows very closely the trends of both experimental statistics and numerical results by using the nonlinear equation, showing that no significant deviation may be observed in the analyzed range of input intensity, as also highlighted in (Di Matteo et al., 2014). Further, in order to completely estimate the approximation induced by the SLT, in Fig. 3.23 relative acceleration time histories recorded at top mass location (experimental data) are compared with those computed by both the numerical nonlinear model defined by Eq. (2.20) and the equivalent linear system Eq. (3.1). In these evaluations the parameters reported in Tables 3.6 and 3.7 are used.

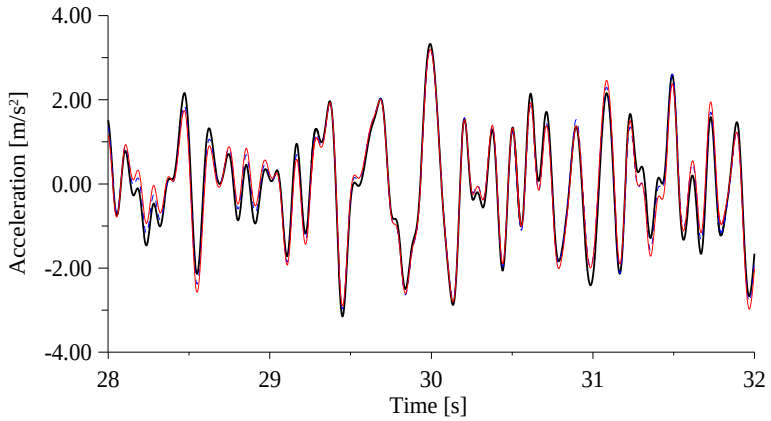

Fig. 3.23 - Comparison among experimental (bold line), nonlinear system (solid line) and numerical equivalent linear system (dashed line) data in time domain.

Once again, the curves corresponding to the nonlinear system and the equivalent linear system are practically coincident, thus proving the reliability of the proposed formulation in predicting structural responses, even in experimental field.

Chapter 4

Innovative modeling of TLCD motion: a fractional derivative perspective

4.1 Introduction

In this Chapter a different formulation for the liquid motion within a TLCD device is developed, based on the mathematical tool of fractional calculus.

As shown in Section 4.2, although the increasing use of these devices for structural vibration control, existing model does not always lead to accurate prediction of the liquid motion. In fact, for some TLCD geometrical configurations of engineering interest, the classical equation of motion, derived in previous Chapter 2, may not accurately describe the real liquid motion within the device. A refined model can be then necessary for accurate simulation of the behavior of TLCD systems.

In this regard, it will be demonstrated in Section 4.3 how correctly including the first linear liquid sloshing mode, through the equivalent mechanical analogy well established in literature, produces numerical results that highly match the corresponding experimental ones.

Furthermore, in Section 4.4 a different mathematical formulation of the equation of motion of the TLCD liquid displacement is proposed,

taking advantage of fractional operators and their properties. Specifically, since the apparent effect of sloshing is the deviation of the natural frequency from the theoretical one, a fractional differential equation of motion is proposed to model the liquid vertical displacements within the TLCD device. The latter choice is supported by the fact that the introduction a fractional derivative of order β alters simultaneously both the resonant frequency and the degree of damping of the system.

In Section 4.5 the proposed formulation will be extended to deal with structures controlled through TLCD devices.

Finally in Section 4.6 it will be shown, through an extensive experimental analysis, how the proposed model can accurately describe both liquid surface and structural displacements. Specifically, experimental validation of the predicted behavior is fully developed in frequency and time domain, focusing only on TLCDs without orifices, so that the characteristics associated with TLCD geometry could only be investigated.

4.2 Motivations and background

Since their first appearance in 1989 in the work by Sakai et al. (1989), TLCD devices received growing attention among researchers who deal with structural control.

Although TLCDs have been studied extensively in literature, most researches (Gao et al, 1997; Chang and Hsu, 1998; Chang, 1999; Yalla and Kareem, 2000; Wu et al., 2009) are mainly focused on the determination of their optimal design parameters through stochastic linearization technique. Experimental studies on these devices were first conducted by Sakai et al. (1989), but since then few researches have experimentally assessed the validity of the classical formulation developed in (Sakai et al; 1989), comparing predicted TLCD characteristics with the corresponding experimental values.

In this regard, one of the first and main contributions is the work of Hitchcock et al. (1997), where an extensive experimental investigation on the features of different TLCDs configuration is presented. As stated in the aforementioned study, TLCDs characteristics were found to be dependent on their geometrical configurations. In particular, it was pointed out for the first time that, increasing the area ratio $\tilde{\nu}$ between the TLCD vertical column cross-sectional area (A_v) and the horizontal column cross-sectional area (A_h), can increase substantially discrepancies among experimental and numerical natural frequencies. These discrepancies were ascribed to the amplified flow separation at the

corners for the larger area ratio, which was not considered in the classical theoretical model (Sakai et al., 1989). Since then, it seems that the engineering community has ignored those results, and no attempt has been made to derive different formulations leading to numerical results closer to the experimental ones, up to the study of Chaiviriyawong et al. (2007). As in fact highlighted in that paper, most previous researches focused on TLCDs with a small ratio of transition zone between the vertical and horizontal portion (corner-to-corner width *w* (see Fig. 4.1)) to horizontal length. This configuration is well described by classical formulation, but it is not generally appealing for structures, since space constraints often limit TLCD horizontal length.

Experimental evidences presented in (Chaiviriyawong et al., 2007) perfectly agree with those in (Hitchcock et al., 1997) showing how, in case of TLCD with large transition zones, poor agreement between numerical results based on the classical formulation in existence and experimental values is obtained. In this case, the variation in liquid velocity in the relatively large transition zone between the vertical columns and the horizontal part cannot be ignored.

A numerical potential-flow method, known as numerical panel method, has been then applied to predict the real liquid displacement in TLCDs. However, due to its complexity it is not suitable for engineering purposes; further, since the effect of liquid viscosity has not been considered, discrepancies between predicted natural frequencies and those experimentally obtained still exist in some cases.

Note that flow separation in large transition zone is not the only source of differences between theoretical and experimental results. As in

fact pointed out in the extensive experimental study of Wu et al. (2005), when broadband noise excitation tests are performed, significant sloshing behavior on the liquid surface may be clearly observed. However, since the liquid displacement is generally measured at the center of the cross-section, it is believed that such a motion may be neglected.

More recently, Konar and Gosh (2013) have studied the effects of the sloshing phenomenon on the control performance of TLCDs. In this case, however, the equations of motion of sloshing and vertical liquid displacement are not derived considering their simultaneous and coupled effect, which may lead to uncorrected prediction of the real behavior.

4.3 Equation of motion with sloshing

Consider a TLCD device excited at the base with an acceleration $\ddot{x}_g(t)$, as shown in Fig. 4.1. The vertical and the horizontal column cross-sectional areas are A_v and A_h, respectively.

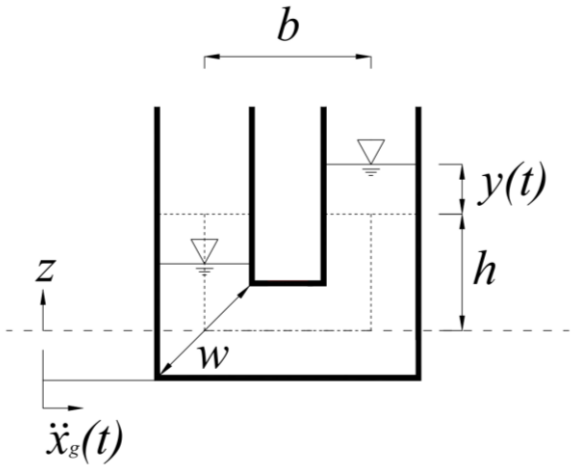

Fig. 4.1 - TLCD device.

As previously reported, for this system Eqs. (2.4) and (2.6) are widely used in literature to model the motion of the liquid inside the TLCD. However, in some recent works it has been experimentally seen that discrepancies between experimental and theoretical frequencies given by Eq. (2.6) arise (Hitchcock et al., 1997; Di Matteo et al., 2012), reflecting differences between experimental and numerical results in time domain as well.

Aforementioned discrepancies may be caused by several phenomena, which are not considered in the classical formulation Eq. (2.4), such as variation of the liquid velocity in case of large transition zones between vertical and horizontal part, vortices and separation in the flow induced by liquid viscosity, sloshing effects of the liquid in the vertical columns (Wu et al., 2005; Konar and Ghosh, 2013) and sharp edge effects in case of sharp corners (Lee et al., 2012)

Sloshing modes, for example, are clearly visible in experimental tests, as shown in Fig. 4.2. In this picture the movement of the water surface, corresponding to the first sloshing mode, in the left column of the TLCD during a test, performed at the Laboratory of Experimental Dynamics at University of Palermo, is depicted.

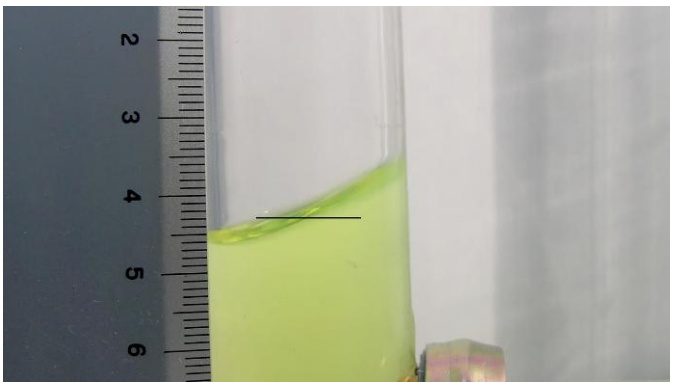

Fig. 4.2 - First sloshing mode of the TLCD during a test.

A first attempt to include the sloshing phenomenon has been presented in (Konar and Gosh, 2013), but in this case the equations of motion of sloshing and liquid displacement have not been derived considering the simultaneous effect of sloshing and liquid vertical motion.

Here the equation of motion of the liquid displacement is derived by taking into account this simultaneous effect. In particular, the fundamental sloshing mode of vibration in the two vertical columns is modeled by an equivalent mechanical model, as described in Ibrahim (2005), consisting of spring-mass-dashpot systems (see Fig. 4.3) with spring stiffness *k* in series with dashpots with damping coefficient *c*.

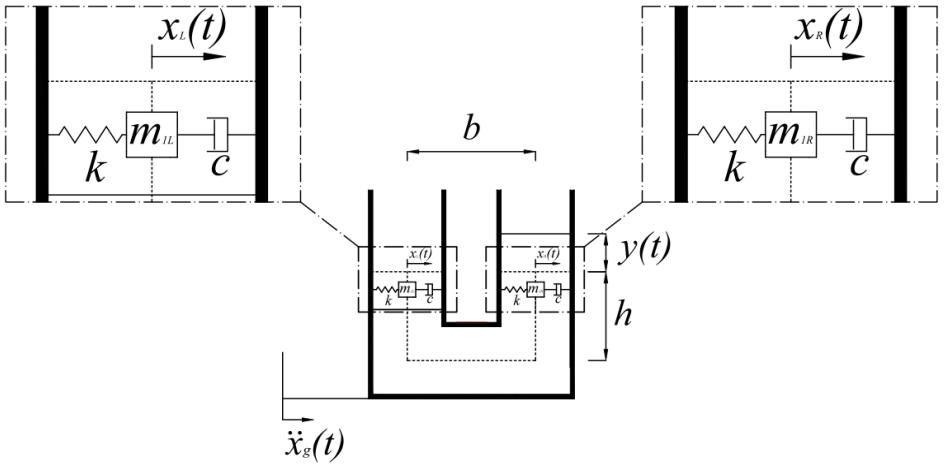

Fig. 4.3 - TLCD with equivalent mechanical model of sloshing.

Consider m_L and m_R as the total liquid masses of the left and right vertical column respectively, m_{1L} and m_{1R} as the equivalent masses of the first sloshing mode in the two vertical columns, and m_{0L} and m_{0R} the remaining liquid masses in the left and right part.

Similarly to the equivalent mechanical model used for sloshing in rigid containers (Ibrahim, 2005), but considering that, in the case of TLCD, fluid in the vertical columns moves in $y(t)$ direction, it is

assumed that m_{0L} and m_{0R} are associated to the vertical liquid displacement $y(t)$ as well. On the other hand m_{1L} and m_{1R} are associated to the displacement coordinates $x_L(t)$ and $x_R(t)$ of the equivalent linear mechanical systems representing the sloshing effect of the first mode (Ibrahim, 2005) of liquid surface in the left and right vertical columns of the TLCD respectively (Fig. 4.3).

As the left and the right vertical columns of the TLCD are geometrically identical and subjected to same base motion, then $x_L(t) = x_R(t) = x(t)$.

The equivalent model should satisfy the following conditions on the fluid total mass

$$m_L = \rho A_v (h - y) = m_{0L} + m_{1L} \tag{4.1 a}$$

$$m_R = \rho A_v (h + y) = m_{0R} + m_{1R} \tag{4.1 b}$$

Representing the masses m_{0L} and m_{0R} as a certain rate $\bar{p}$ of the total liquid masses m_L and m_R, from Eqs. (4.1) it can be derived that

$$m_{0L} = \bar{p}\, m_L = \bar{p}\, \rho A_v (h - y) \tag{4.2 a}$$

$$m_{0R} = \bar{p}\, m_R = \bar{p}\, \rho A_v (h + y) \tag{4.2 b}$$

$$m_{1L} = (1 - \bar{p}) m_L = (1 - \bar{p}) \rho A_v (h - y) \tag{4.2 c}$$

$$m_{1R} = (1 - \bar{p}) m_R = (1 - \bar{p}) \rho A_v (h + y) \tag{4.2 d}$$

With these assumptions, the total kinetic and potential energy can be written as

$$T = \bar{p}\rho A_v h\left(\dot{y}^2 + \dot{x}_g^2\right) + \left(1-\bar{p}\right)\rho A_v h\left(\dot{x} + \dot{x}_g\right)^2 + \frac{1}{2}\rho A_h b\left(\tilde{\nu}\dot{y} + \dot{x}_g\right)^2 \tag{4.3}$$

$$U = \rho A_v g\left(h^2 + y^2\right) + kx^2 \tag{4.4}$$

Using the energy principles, the equation of motion of the liquid displacement $y(t)$ can be derived from the Lagrange equation:

$$\frac{\partial}{\partial t}\left[\frac{\partial\left(T-U\right)}{\partial \dot{y}}\right] - \frac{\partial\left(T-U\right)}{\partial y} = Q_y \tag{4.5}$$

where Q_y is the total non-conservative force in the direction of $y(t)$, related to the head loss, as reported in Chapter 2.

Substitution of Eq.(4.3) and (4.4) in Eq.(4.5), leads to equation of motion of the liquid in the TLCD, associated to the vertical liquid displacement $y(t)$, considering the simultaneous effect of the first liquid sloshing mode

$$\ddot{y}(t) + \frac{1}{2}\frac{\xi}{\tilde{L}_e}\tilde{\nu}\left|\dot{y}(t)\right|\dot{y}(t) + \tilde{\omega}_2^2 y(t) = -\frac{b}{\tilde{L}_e}\ddot{x}_g(t) \tag{4.6}$$

where $\tilde{L}_e = 2\bar{p}h + \tilde{\nu}b$ can be defined as the sloshing induced effective liquid length, $\tilde{\nu}$ is the area ratio of the vertical column to the horizontal column of the TLCD $\left(\tilde{\nu} = A_v / A_h\right)$, and

$$\tilde{\omega}_2 = \sqrt{\frac{2g}{\tilde{L}_e}} \tag{4.7}$$

is the corresponding modified natural frequency of vertical liquid oscillation inside the tube.

Thus, it has been demonstrated that correctly including in the equation of motion the first linear sloshing mode dynamics, a variation of the natural frequency, experimentally seen in recent studies (Chaiviriyawong et al., 2007; Di Matteo et al., 2012; Lee et al., 2012), could be justified, leading to the modified natural frequency as in Eq. (4.7).

It is worth noting that the parameter $\bar{p}$, as the head loss coefficient ξ, may be experimentally identified. However, unlike the head loss coefficient for which many experimental tests are needed, $\bar{p}$ is easily obtained from Eq. (4.7) once the experimental natural frequency of liquid, say ω_{exp}, is identified.

4.4 Proposed model with fractional derivative

As highlighted in the previous Section, Eq. (4.6) is a nonlinear differential equation depending on two unknown parameters, namely $\bar{p}$ and ξ, which both have to be experimentally identified if differences between experimental and numerical results obtained with Eq. (2.4) emerge. For this reason at this stage it cannot be considered as a valid improvement of Eq. (2.4), until a correct prediction of the values of $\bar{p}$ depending on the TLCD parameters will be derived.

However, further enhancements may be observed if a fractional derivative term is introduced in Eq. (2.4) replacing the nonlinear damping term. This leads to the following proposed equation for modeling the liquid motion of TLCD

$$\ddot{y}(t)+\frac{1}{2}\frac{C_\beta}{L}\left({}_0^C D_t^\beta y(t)\right)+\omega_2^2 y(t)=-\frac{b}{L}\ddot{x}_g(t) \tag{4.8}$$

where C_β is a constant that can be viewed as the fractional damping coefficient and $\left({}_0^C D_t^\beta y(t)\right)$ is a force represented by an β-order left Caputo fractional derivative, expressed as (Podlubny, 1999)

$${}_0^C D_t^\beta y(t)=\frac{1}{\Gamma(1-\beta)}\int_0^t (t-\tau)^\beta \frac{d}{d\tau}y(\tau)\,d\tau, \quad 0<\beta<1 \tag{4.9}$$

being $\Gamma(\bullet)$ the Euler-Gamma function.

Note that, Eq. (4.8) depends on the theoretical natural frequency ω_2 given by Eq. (2.5) and, since it contains only linear terms, it is now a linear fractional differential equation that governs the motion of the liquid inside the TLCD.

Resorting to the Fourier transform property of fractional derivatives, that is

$$\mathscr{F}\left({}_0^C D_t^\beta y(t)\right) = (i\omega)^\beta \, \mathscr{F}\left(y(t)\right) \tag{4.10}$$

the liquid displacement Frequency Response Function (FRF) $\left(H_y(\omega) = Y(\omega) / \ddot{X}_g(\omega)\right)$ may be easily obtained from Eq. (4.8) as

$$H_y(\omega) = \frac{-\frac{b}{L}}{-\omega^2 + \frac{1}{2}\frac{C_\beta}{L}(i\omega)^\beta + \omega_2^2} \tag{4.11}$$

This theoretical model was proposed on the basis of several considerations:

i. As well established in literature (Wu et al., 2009; Di Matteo et al., 2014), the nonlinear behavior of the TLCD system may be effectively described considering the equivalent linear model, since the system is weakly nonlinear and stochastic linearization technique works very well both in frequency and time domain;
ii. As demonstrated in(Di Paola et al., 2012, Failla and Pirrotta, 2012), the fractional operator may be discretized in a set of Maxwell half-oscillator, leading to a mechanical representation analogous to the equivalent mechanical model of sloshing;

iii. As pointed out in (Spanos and Evangelatos, 2010), the fractional derivative may alter simultaneously both the resonant frequency and the degree of damping of the system.

On this solid ground, introducing this proposed formulation the cited effects of sloshing, turbulence and flow separation, that could modify the theoretical natural frequency, contemporary with viscous interaction and hydrodynamic head losses, that represent the damping effects, are naturally taken into account.

As far as the numerical solution of Eq. (4.8) is concerned, numerical results of the proposed formulation can be obtained implementing the Newmark method having discretized fractional derivative via Grunwald-Letnikov (GL) as detailed in (Failla and Pirrotta, 2012).

In particular, considering a quiescent system at $t = 0$ and subdividing the time interval $[0, t_f]$ into equally-spaced steps Δt, the fractional derivative Eq. (4.9) at time instant $t_i = i\Delta t$ may be approximated with the following GL series expansion

$$ {}_0^C D_t^\beta y(t_i) = \lim_{\Delta t \to 0} \Delta t^{-\beta} \sum_{k=0}^{i} GL_k \, y(t_i - k\Delta t) \tag{4.12} $$

where GL_k are coefficients to be computed in the recursive form as

$$ GL_k = \frac{k - \beta - 1}{k} GL_{k-1}, \quad GL_0 = 1 \tag{4.13} $$

Substituting Eq. (4.12) into Eq. (4.8), the equation of motion of the fractional system at the time instant $t_i = i\Delta t$ can be rewritten as

$$\ddot{y}(t_i)+\frac{1}{2}\frac{C_\beta}{L}\Delta t^{-\beta}\sum_{k=0}^{i}GL_k\, y(t_i-k\Delta t)+\omega_2^2 y(t_i)=-\frac{b}{L}\ddot{x}_g(t_i) \tag{4.14}$$

In this form, Eq. (4.14) can be solved with a classical Newmark method, as described in (Failla and Pirrotta, 2012).

Observe that Eq. (4.8) does represent a valid improvement of the classical model in Eq. (2.4). The proposed Eq. (4.8) is in fact a linear differential equation, albeit of fractional order. The corresponding FRF can be then found directly as in Eq. (4.11). Thus, even if two parameters (C_β and β) are still involved in the model, they can be efficiently found from experimental FRFs as it will be shown in the following section.

On the contrary, Eq. (4.6) is a nonlinear differential equation, and determination of the unknown parameters ($\bar{p}$ and ξ) from experimental data, may be a rather daunting task. Further, it is worth noting that even Eq. (2.4) is a nonlinear differential equation, in which at least one parameter (ξ) has to be determined through experimental tests. No reliable relations, in fact, exist in literature linking TLCD geometric parameters to the head loss coefficient.

4.5 Proposed model for TLCD controlled structures

In previous Section 4.4 attention was focused on the modeling of the liquid motion inside the device only.

To extend those results for TLCD controlled systems, proceeding as in Section 4.4, the nonlinear damping term in Eq. (2.20) can be replaced with a Caputo fractional derivative term, leading to the alternative equations of motion in the form

$$\begin{cases} (1+\mu)\ddot{x}(t)+\alpha\mu\ddot{y}(t)+2\zeta_1\omega_1\dot{x}(t)+\omega_1^2 x(t)=-(1+\mu)\ddot{x}_g(t) \\ \alpha\ddot{x}(t)+\ddot{y}(t)+\dfrac{1}{2}\dfrac{C_\beta}{L}\left({}_0^C D_t^\beta y(t)\right)+\omega_2^2 y(t)=-\alpha\ddot{x}_g(t) \end{cases} \quad (4.15\text{ a,b})$$

Note that Eq. (4.15) is now a system of linear coupled differential equations, the second of which is of fractional order.

Further, Fourier transforming Eqs. (4.15) and taking into account Eq. (4.10) yields

$$\begin{cases} X(\omega)\left[-\omega^2(1+\mu)+2i\omega\zeta_1\omega_1+\omega_1^2\right]-\omega^2\alpha\mu Y(\omega)=-(1+\mu)\ddot{X}_g(\omega) \\ -\omega^2\alpha X(\omega)+Y(\omega)\left[-\omega^2+(i\omega)^\beta\dfrac{C_\beta}{2L}+\omega_2^2\right]=-\alpha\ddot{X}_g(\omega) \end{cases} \quad (4.16\text{ a,b})$$

Thus, the structural displacement FRF $\left(H_x(\omega)=X(\omega)/\ddot{X}_g(\omega)\right)$ can be written as

$$H_x(\omega)=\frac{1+\mu+\dfrac{\omega^2\alpha^2\mu}{B(\omega)}}{(1+\mu)\omega^2+\dfrac{\omega^4\alpha^2\mu}{B(\omega)}-2i\omega\zeta_1\omega_1-\omega_1^2} \tag{4.17}$$

while the liquid vertical motion FRF $\left(\tilde{H}_y(\omega)=Y(\omega)/\ddot{X}_g(\omega)\right)$ is

$$\tilde{H}_y(\omega)=\frac{\alpha}{B(\omega)}\left[\frac{2\omega\zeta_1\omega_1+\omega_1^2}{(1+\mu)\omega^2+\dfrac{\omega^4\alpha^2\mu}{B(\omega)}-2i\omega\zeta_1\omega_1-\omega_1^2}\right] \tag{4.18}$$

where

$$B(\omega)=-\omega^2+\frac{1}{2}\frac{C_\beta}{L}(i\omega)^\beta+\omega_2^2 \tag{4.19}$$

It is worth stressing that, if the main structural parameters ζ_1 and ω_1 are known, Eq. (4.17) can be used to identify the two unknown parameters C_β and β, through a best fitting on the experimentally evaluated structural displacement FRF. This procedure will be clearly shown in the following sections.

As far as the numerical solution of Eq. (4.15) is concerned, considering a quiescent system at $(t=0)$ and subdividing the time interval $\left[0, t_f\right]$ into equally-spaced steps Δt, the fractional derivative in Eqs. (4.15) can be approximated with the following GL series expansion as in Eq. (4.12)

Therefore, the equation of motion for the proposed fractional model at the time instant t_i can be rewritten as

$$\begin{cases} (1+\mu)\ddot{x}(t_i)+\alpha\mu\ddot{y}(t_i)+2\zeta_1\omega_1\dot{x}(t_i)+\omega_1^2 x(t_i)=-(1+\mu)\ddot{x}_g(t_i) \\ \alpha\ddot{x}(t_i)+\ddot{y}(t_i)+\dfrac{1}{2}\dfrac{C_\beta}{L}\Delta t^{-\beta}\sum_{k=0}^{i}GL_k\, y(t_i-k\Delta t)+\omega_2^2 y(t_i)=-\alpha\ddot{x}_g(t_i) \end{cases} \tag{4.20}$$

Specifying Eq. (4.20) for the following time instant t_{i+1} and subtracting from Eq. (4.20), yields

$$\begin{cases} (1+\mu)\Delta\ddot{x}+\alpha\mu\,\Delta\ddot{y}+2\zeta_1\omega_1\Delta\dot{x}+\omega_1^2\Delta x=-(1+\mu)\Delta\ddot{x}_g \\ \alpha\,\Delta\ddot{x}+\Delta\ddot{y}+\dfrac{1}{2}\dfrac{C_\beta}{L}\Delta t^{-\beta}GL_0\Delta y+\omega_2^2\Delta y=-\alpha\Delta\ddot{x}_g-\dfrac{1}{2}\dfrac{C_\beta}{L}\Delta t^{-\beta}P_i \end{cases} \tag{4.21}$$

where $\left(\Delta x=x(t_{i+1})-x(t_i)\right)$, $\left(\Delta y=y(t_{i+1})-y(t_i)\right)$,

$\left(\Delta\ddot{x}_g=\ddot{x}_g(t_{i+1})-\ddot{x}_g(t_i)\right)$ and

$$P_i=\sum_{k=1}^{i}GL_k\left[y(t_{i+1}-k\Delta t)-y(t_i-k\Delta t)\right]+GL_{i+1}\,y(0) \tag{4.22}$$

The term P_i can be then considered as a pseudo-force, depending on the liquid displacement until the time instant t_i.

Rewriting Eq. (4.21) in compact matrix form, yields

$$\tilde{\mathbf{M}}\,\Delta\ddot{\mathbf{Z}}+\tilde{\mathbf{C}}\,\Delta\dot{\mathbf{Z}}+\tilde{\mathbf{K}}\,\Delta\mathbf{Z}=-\tilde{\mathbf{A}}\,\Delta\ddot{x}_g-\tilde{\mathbf{B}} \tag{4.23}$$

where

$$\Delta\mathbf{Z}=\begin{bmatrix}\Delta x\\ \Delta y\end{bmatrix} \tag{4.24}$$

$$\tilde{\mathbf{M}}=\begin{bmatrix}1+\mu & \alpha\mu\\ \alpha & 1\end{bmatrix} \tag{4.25}$$

$$\tilde{\mathbf{C}} = \begin{bmatrix} 2\zeta_1\omega_1 & 0 \\ 0 & 0 \end{bmatrix} \tag{4.26}$$

$$\tilde{\mathbf{K}} = \begin{bmatrix} \omega_1^2 & 0 \\ 0 & a_\beta \end{bmatrix} \tag{4.27}$$

$$\tilde{\mathbf{A}} = \begin{bmatrix} 1+\mu \\ \alpha \end{bmatrix} \tag{4.28}$$

$$\tilde{\mathbf{B}} = \begin{bmatrix} 0 \\ \frac{1}{2}\frac{C_\beta}{L}\Delta t^{-\beta} P_i \end{bmatrix} \tag{4.29}$$

$$a_\beta = \omega_2^2 + \frac{1}{2}\frac{C_\beta}{L}\Delta t^{-\beta} G L_0 \tag{4.30}$$

In this way a classical Newmark scheme can be applied to find the numerical solution of the differential Eq. (4.23). Specifically, applying the constant average acceleration method the following relations hold true

$$\Delta\dot{\mathbf{Z}} = \frac{\Delta t}{2}\left[\ddot{\mathbf{Z}}(t_i) + \ddot{\mathbf{Z}}(t_{i+1})\right] \tag{4.31}$$

$$\Delta\mathbf{Z} = \Delta t\,\dot{\mathbf{Z}}(t_i) + \frac{\Delta t^2}{4}\left[\ddot{\mathbf{Z}}(t_i) + \ddot{\mathbf{Z}}(t_{i+1})\right] \tag{4.32}$$

in which $\mathbf{Z}(t_i)$ is the state variables vector

$$\mathbf{Z}(t_i) = \begin{bmatrix} x(t_i) \\ y(t_i) \end{bmatrix} \tag{4.33}$$

Substituting Eqs. (4.31) and (4.32) into Eq. (4.23) and manipulating, yields

$$\ddot{\mathbf{Z}}\left(t_{i+1}\right)=\boldsymbol{\theta}^{-1}\left\{\left[\tilde{\mathbf{M}}-\frac{\Delta t}{2}\tilde{\mathbf{C}}-\frac{\Delta t^{2}}{4}\tilde{\mathbf{K}}\right]\ddot{\mathbf{Z}}\left(t_{i}\right)-\Delta t\,\tilde{\mathbf{K}}\,\dot{\mathbf{Z}}-\mathbf{A}\,\Delta\ddot{x}_{g}-\tilde{\mathbf{B}}\right\} \tag{4.34}$$

where

$$\boldsymbol{\theta}=\tilde{\mathbf{M}}+\frac{\Delta t}{2}\tilde{\mathbf{C}}+\frac{\Delta t^{2}}{4}\tilde{\mathbf{K}} \tag{4.35}$$

Clearly, once obtained the response acceleration vector $\ddot{\mathbf{Z}}\left(t_{i+1}\right)$ from Eq. (4.34), velocity and displacement responses can be determined through Eqs. (4.31) and (4.32).

4.6 Experimental investigation

In this Section the proposed formulations for the TLCD device and TLCD controlled structures are validated through an experimental campaign on a small scale model built in the Laboratory of Experimental Dynamic at University of Palermo.

Since a vast experimental campaign has been accomplished to validate the proposed formulations for both the device only and the TLCD controlled systems, here results will be analyzed separately.

Specifically, results obtained from the proposed fractional formulation Eq. (4.8) on the TLCD device only will be analyzed in Section 4.6.1, while results for the extension to the case of TLCD controlled structures Eq. (4.15) will be analyzed in Section 4.6.2.

4.6.1 TLCD devices

To experimentally validate the proposed linear fractional formulation Eq. (4.8), TLCD systems have been realized with U–shaped Plexiglas® cylinder tubes in the Laboratory of Experimental Dynamic at University of Palermo.

It is worth noting that in (Chaiviriyawong et al., 2007) three different configurations of TLCD have been studied varying the ratio between the corner to corner width *w* (see Fig. 4.1) and the horizontal liquid length *b*.

To aim at reproducing analogous results obtained in (Chaiviriyawong et al., 2007), so as to further validate the proposed formulation, three TLCDs configurations have been tested, which were characterized by the same corner to corner width to horizontal length ratios considered in (Chaiviriyawong et al., 2007). In particular, three sets of TLCD devices with same horizontal liquid length *b*, but three different diameters *d* have been used. Moreover, tubes have been filled with water reaching two different liquid levels *h* from the centerline of the base tube, for each one of the three sets of TLCD devices. Thus two different values of natural frequency for each set have been obtained.

In Fig. 4.4(a-c, g-i), pictures of the six TLCD device configurations are shown while in Fig. 4.4(d-f, l-n) schematic drawings of the TLCDs with the corresponding dimensions are depicted.

The six TLCD configurations have been rigidly connected and excited at the base through an APS Dynamic–Model 133 shake table, which provides the ground motion (Fig. 4.4(a-c, g-i)). In particular, the input signals have been acquired using an accelerometer on the table itself, the Miniature DeltaTron Accelerometers Brüel&Kjær – Type 4507-002B piezoelectric accelerometer. Further, in order to condition and amplify voltage signals coming from accelerometer before being acquired and saved, a PCB conditioning amplifier was used (model 481A).

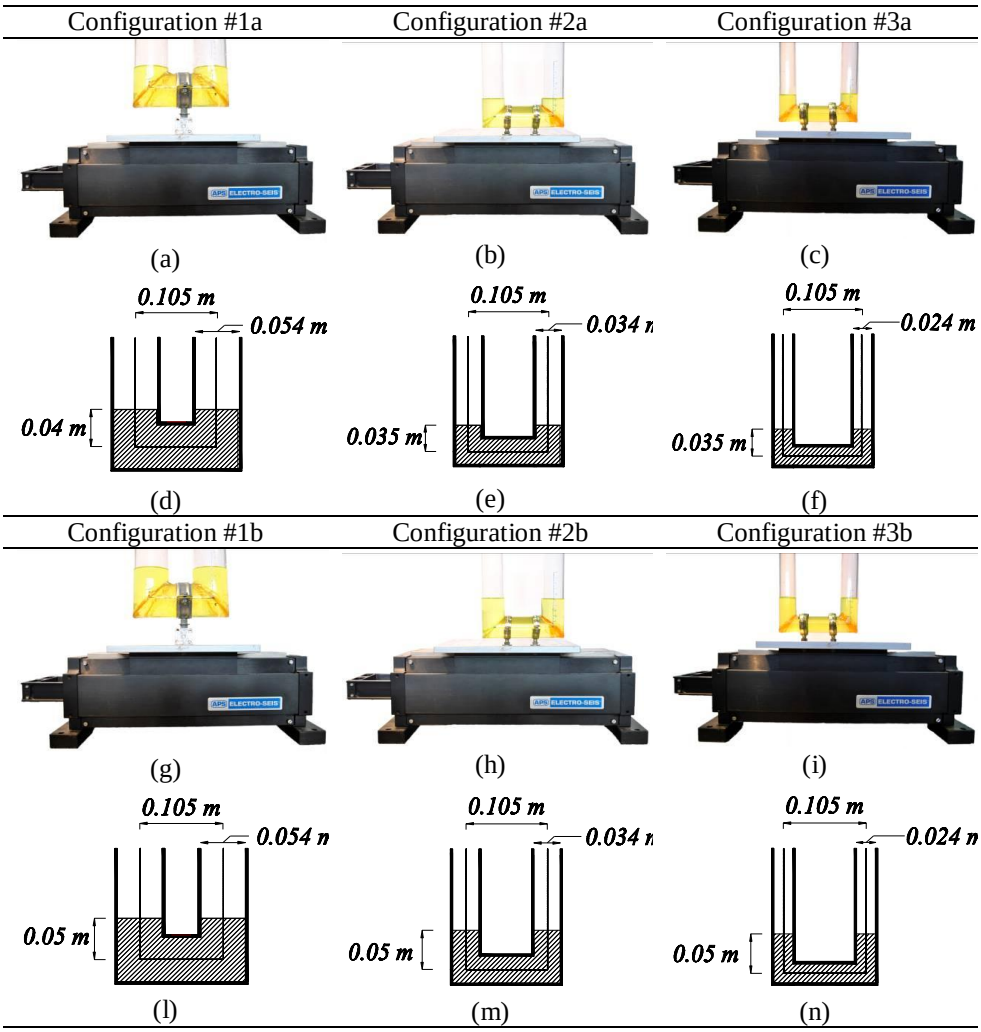

Fig. 4.4 - TLCD devices;(a) – (c), (l) – (n) pictures of the six TLCD configurations; (d) – (f), (g) – (i) TLCD dimensions.

Voltage signals have been generated by means of a National Instruments NI-PCI-MIO-16XE-10, and digitalized and acquired by means of a National Instruments NI-PCI-4472 Analogical-Digital (A-D) Acquisition Board and then processed using signal processing software in LabView and MATLAB environments.

During the motion, a video camera (model Canon IXUS 100IS) was used to record the TLCD water free surface displacements.

In Fig. 4.5, a schematic view of the acquisition system is depicted.

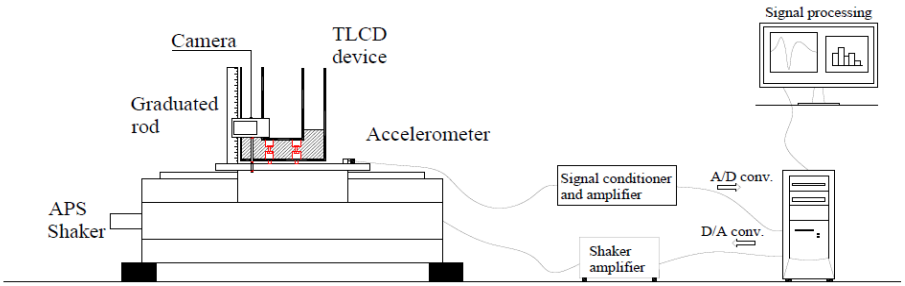

Fig. 4.5 - Acquisition system for TLCDs test.

As shown, the camera was rigidly connected through a screw to the shaker plate to create a moving reference frame, integral with the TLCD devices. To record the free water surface displacement only, the screw was moved up or down until a suitable position was reached so that the camera focuses only on the left column liquid during its entire motion.

Broadband noise in the range 0.5÷10 Hz, supplied through the APS shaker, was used as input signal both to identify the TLCD devices dynamic parameters, and to validate the proposed formulation as well. For each TLCD device, 20 samples of broadband noise, with a duration time of 25 s and sampling frequency of 1 kHz, have been generated and used as ground acceleration. For each sample, the acceleration at ground and the liquid displacement were recorded through the accelerometer and the video camera respectively. Each video was recorded at 30 fps (corresponding to a sampling frequency of 30 Hz) and high-definition

full-frame images of 1280 x 720 pixels were acquired and transferred to the computer.

In order to determine the free water surface displacements for each analyzed configuration, an image processing procedure in MATLAB environment was developed.

In particular, each frame in the RGB color space (Fig. 4.6(a)), has been converted into the equivalent hue, saturation and value (HSV) image. These components are then extracted. Once assigned and applied suitable low and high threshold values to the HSV image components (to filter out unnecessary color and additional noises) these have been converted into binary images, which have intensity values of 0 (corresponding to black color) or 1 (corresponding to white color), and then combined together to obtain a binary image in which the water is colored in white and the rest of the image in black (Fig. 4.6(b)). This binary image has been used to identify the free water surface in the left column of the TLCD, and the pixel position corresponding to the passage from the black to the white color of a chosen point at the centre of the TLCD column, has been determined in the analyzed frame (point A in Fig. 4.6(c)).

(a) (b) (c)

Fig. 4.6 - Image processing; (a) extracted frame from the video; (b) binary image; (c) image with the determined pixel position (black dot on the water interface).

Once the pixel positions have been acquired for all frames, conversion to displacement in meters has been made with a calculated scale factor, determined though the graduated rod rigidly connected to the shaker plate (Fig. 4.5). In this way the free water surface displacement time histories have been obtained from the videos, and the averaged Frequency Response Function (FRF) for each TLCD configuration has been computed.

4.6.1.1 Experimental results versus numerical results: classical formulation vis-à-vis equation of motion with sloshing

Once the FRFs have been obtained, experimental natural frequency $\omega_{\exp}$ has been directly identified from the corresponding FRF for each TLCD configuration, while the head loss coefficient ξ has been computed by minimizing the error between the measured FRFs of the liquid displacement and that from Eq. (2.4) having considered as input the recorded accelerations. The geometric and identified TLCD parameters, for each configuration, are detailed in Tables 4.1 and 4.2.

Table 4.1 - TLCD configurations parameters for Configurations #a.

	Configuration #1a	Configuration # 2a	Configuration # 3a
d	0.054 m	0.034 m	0.024 m
A	$2.29\cdot10^{-3}$ m^2	$9.08\cdot10^{-4}$ m^2	$4.52\cdot10^{-4}$ m^2
b	0.105 m	0.105 m	0.105 m
w	0.076	0.048	0.034
h	0.04 m	0.035 m	0.035 m
L	0.185 m	0.175 m	0.175 m
ω_2	10.29 *rad/s*	10.59 *rad/s*	10.59 *rad/s*
$\omega_{\exp}$	11.97 *rad/s*	11.81 *rad/s*	11.56 *rad/s*
ξ	6	8	15

Table 4.2 - TLCD configurations parameters for Configurations #b.

	Configuration #1b	Configuration # 2b	Configuration # 3b
d	0.054 m	0.034 m	0.024 m
A	$2.29 \cdot 10^{-3}$ m^2	$9.08 \cdot 10^{-4}$ m^2	$4.52 \cdot 10^{-4}$ m^2
b	0.105 m	0.105 m	0.105 m
w	0.076	0.048	0.034
h	0.05 m	0.05 m	0.05 m
L	0.205 m	0.205 m	0.205 m
ω_2	9.78 *rad/s*	9.78 *rad/s*	9.78 *rad/s*
ω_{exp}	11.31 *rad/s*	10.81 *rad/s*	10.56 *rad/s*
ξ	6	8	15

To assess the reliability of the identified parameters, for each TLCD configuration numerical-experimental comparison of liquid displacement time histories are depicted in Figs. 4.7-4.12. In these pictures numerical time histories liquid displacements are contrasted with the experimental ones; in particular the recorded free water surface displacements are compared with those computed with the classical theoretical model defined by Eq. (2.4) (say classical numerical results) and those obtained with the theoretical model defined by Eq.(4.6) (say numerical sloshing-vertical motion results) in which the real experimental natural frequency is involved, setting those reported in Table 4.1 as parameters. It is worth noting that classical numerical results and sloshing-vertical motion results have been obtained with a *4th*–order Runge-Kutta method, considering as input the recorded accelerations.

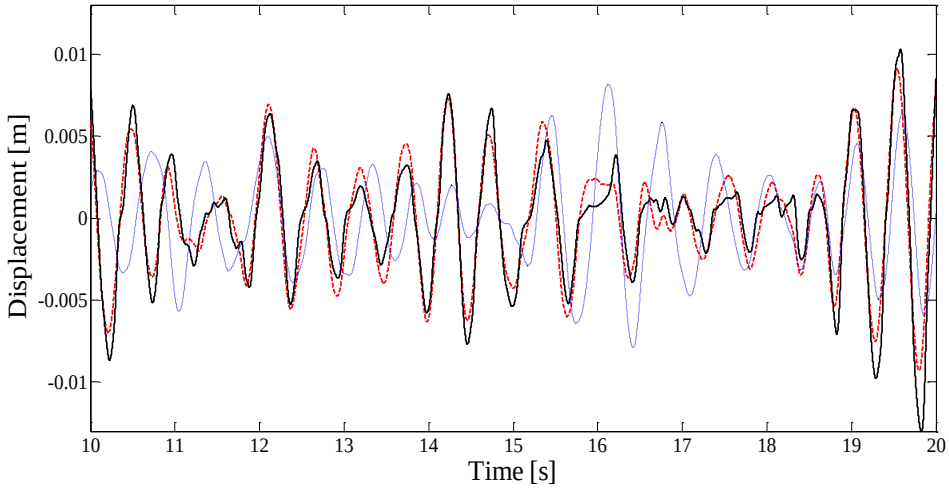

Fig. 4.7 - Comparison of liquid displacement time histories for Configuration #1a: Experimental results (black solid line), classical numerical results (blue dotted line) and numerical sloshing-vertical motion results (red dashed line).

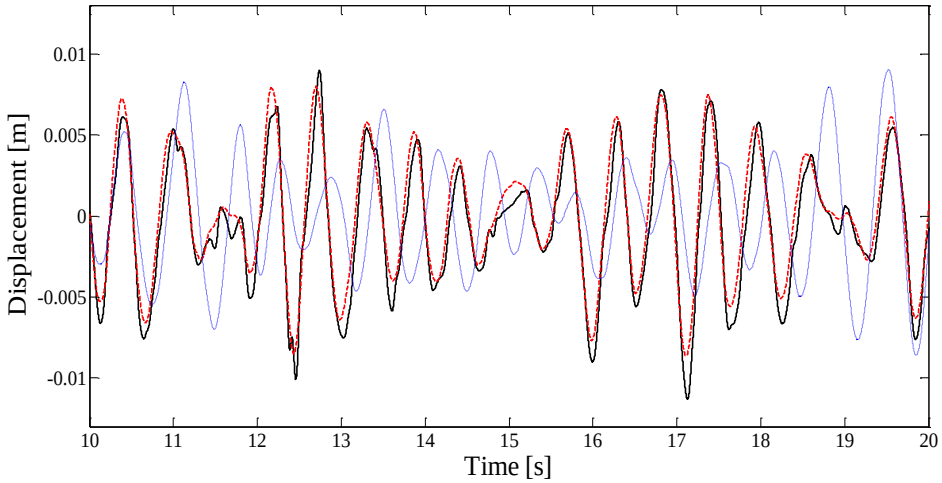

Fig. 4.8 - Comparison of liquid displacement time histories for Configuration #1b: Experimental results (black solid line), classical numerical results (blue dotted line) and numerical sloshing-vertical motion results (red dashed line).

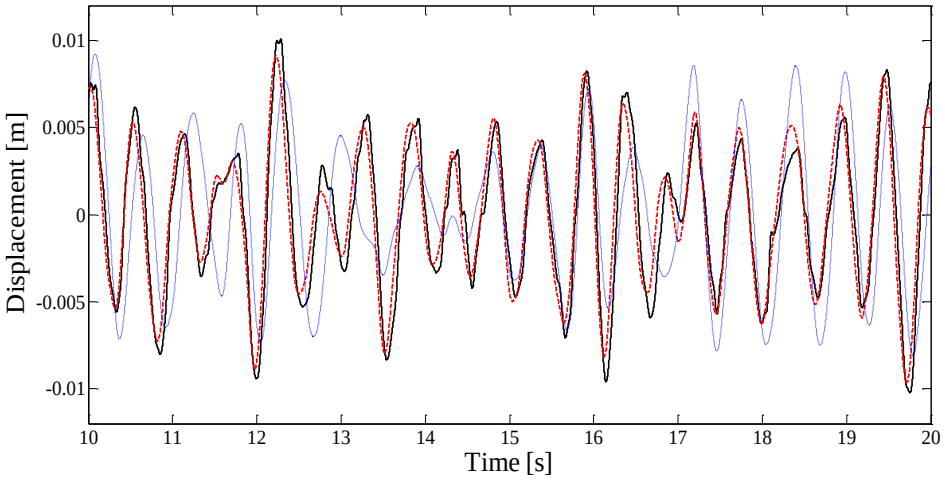

Fig. 4.9 - Comparison of liquid displacement time histories for Configuration #2a: Experimental results (black solid line), classical numerical results (blue dotted line) and numerical sloshing-vertical motion results (red dashed line).

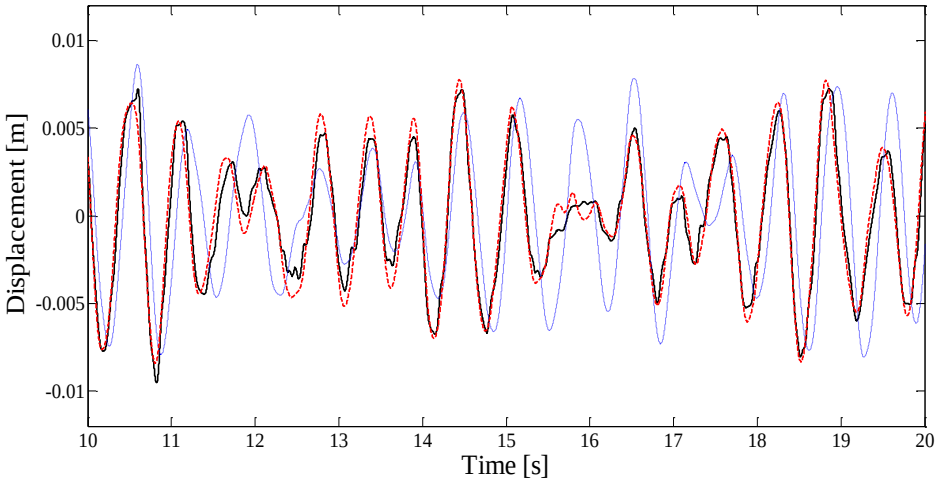

Fig. 4.10 - Comparison of liquid displacement time histories for Configuration #2b: Experimental results (black solid line), classical numerical results (blue dotted line) and numerical sloshing-vertical motion results (red dashed line).

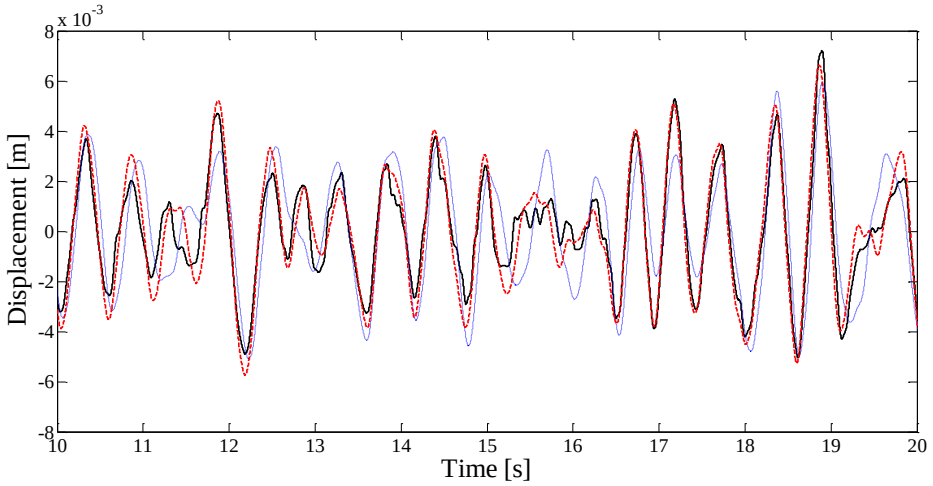

Fig. 4.11 - Comparison of liquid displacement time histories for Configuration #3a: Experimental results (black solid line), classical numerical results (blue dotted line) and numerical sloshing-vertical motion results (red dashed line).

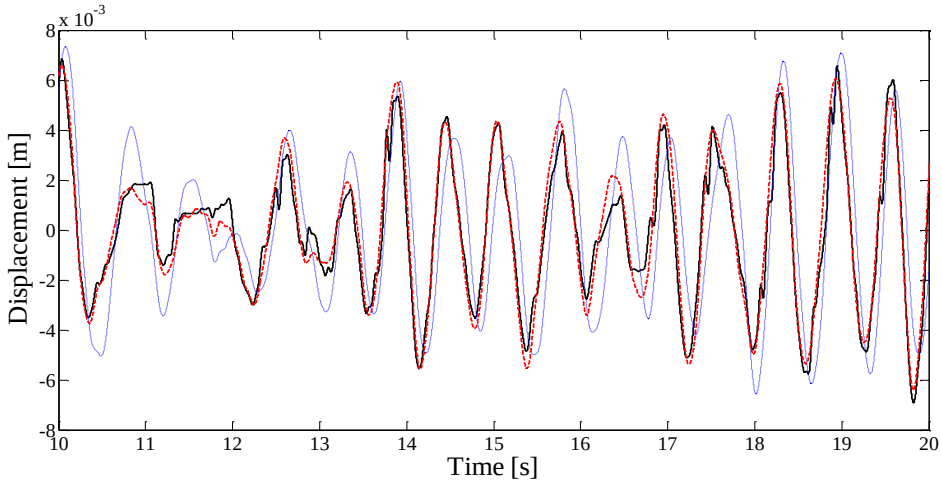

Fig. 4.12 - Comparison of liquid displacement time histories for Configuration #3b: Experimental results (black solid line), classical numerical results (blue dotted line) and numerical sloshing-vertical motion results (red dashed line).

As shown for each TLCD configuration, sloshing-vertical motion time histories match very well the corresponding experimental results. On the other hand, classical numerical results from Eq. (2.4) are rather different from the experimental ones, and the difference grows at increasing levels of the corner to corner width *w* to horizontal length ratio, as expected and detailed in aforementioned (Chaiviriyawong et al., 2007).

4.6.1.2 Experimental results versus numerical results: classical formulation vis-à-vis proposed fractional formulation

In order to evaluate the TLCD parameters of the theoretical proposed model (β and C_β) in Eq. (4.8), the nonlinear least square curve fitting method using MATLAB has been applied to fit the experimental data of the FRFs with Eq. (4.11). The identified TLCD parameters, for each configuration, are detailed in Table 4.3.

Table 4.3 - Fractional TLCD parameters

	Conf.#1a	Conf. #1b	Conf. #2a	Conf.#2b	Conf. #3a	Conf. #3b
β	0.2	0.21	0.3	0.41	0.6	0.63
C_β	8.58	7.41	4.58	3.59	2.17	2.06

To prove the validity of the aforementioned proposed fractional formulation, for each TLCD configuration numerical-experimental comparisons of liquid displacement time histories are depicted in Figs. 4.13-4.18. In these pictures the recorded free water surface displacements are compared with those computed with the proposed model defined by Eq. (4.8), setting those reported in Table 4.1-4.3 as parameters. It is

worth noting that numerical results of proposed formulation (Eq.(4.8)) have been obtained implementing the Newmark method having discretized fractional derivative via Grunwald-Letnikov (GL) as detailed in Section 4.4.

As shown for each TLCD configuration, time domain numerical results obtained considering the proposed model closely match the corresponding experimental results.

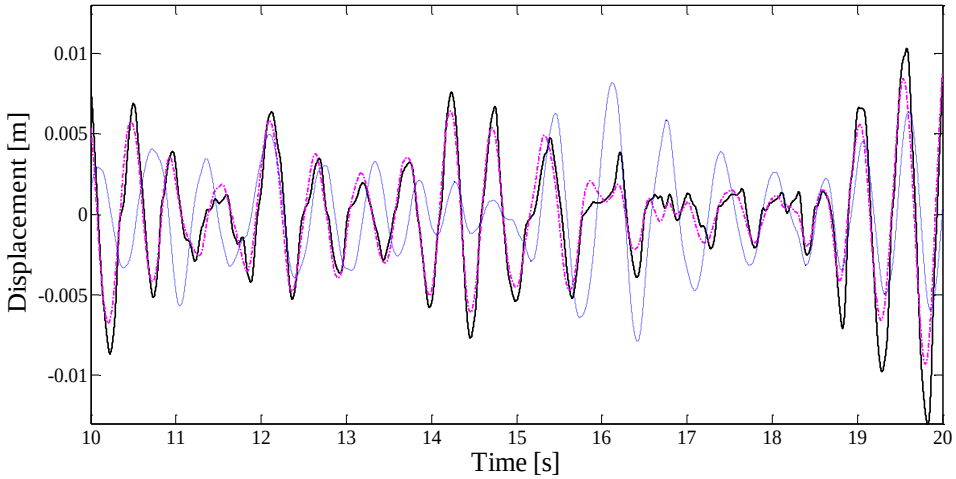

Fig. 4.13 - Comparison of liquid displacement time histories for Configuration #1a: Experimental results (black solid line), classical numerical results (blue dotted line) and proposed model results (magenta dash-dot line).

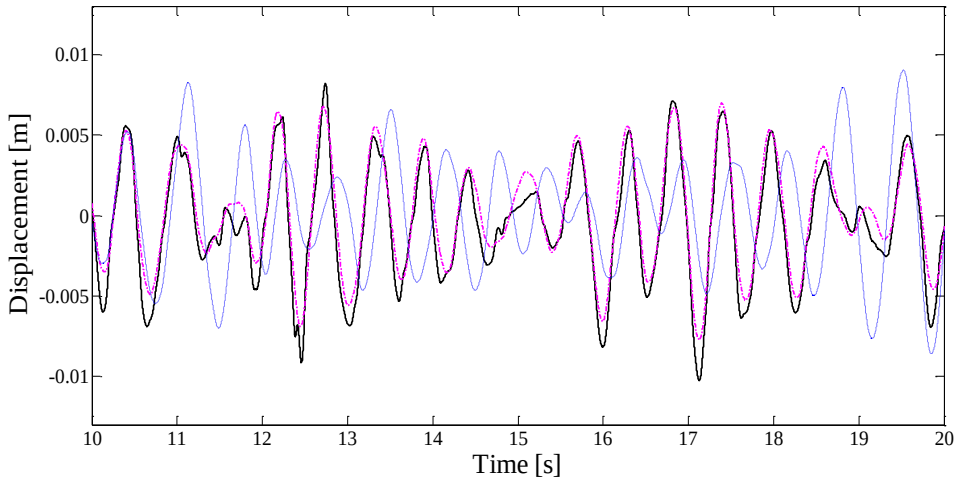

Fig. 4.14 - Comparison of liquid displacement time histories for Configuration #1b: Experimental results (black solid line), classical numerical results (blue dotted line) and proposed model results (magenta dash-dot line).

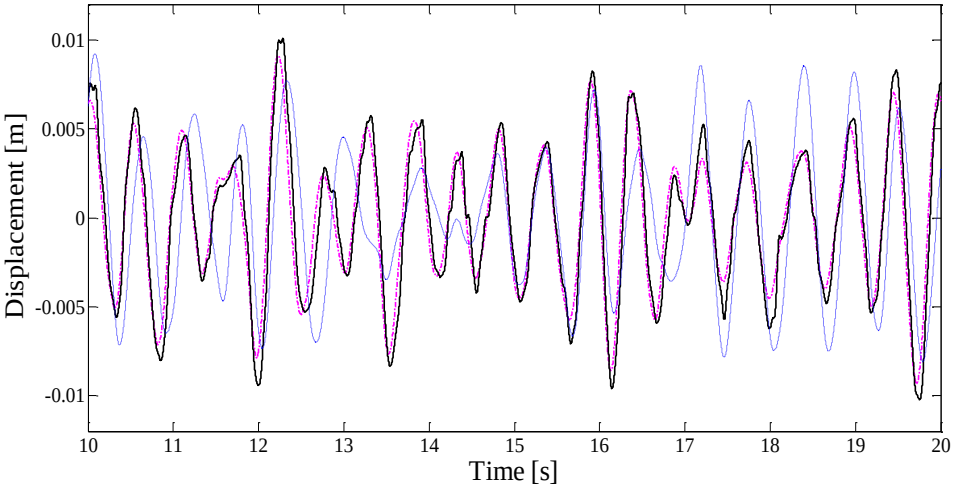

Fig. 4.15 - Comparison of liquid displacement time histories for Configuration #2a: Experimental results (black solid line), classical numerical results (blue dotted line) and proposed model results (magenta dash-dot line).

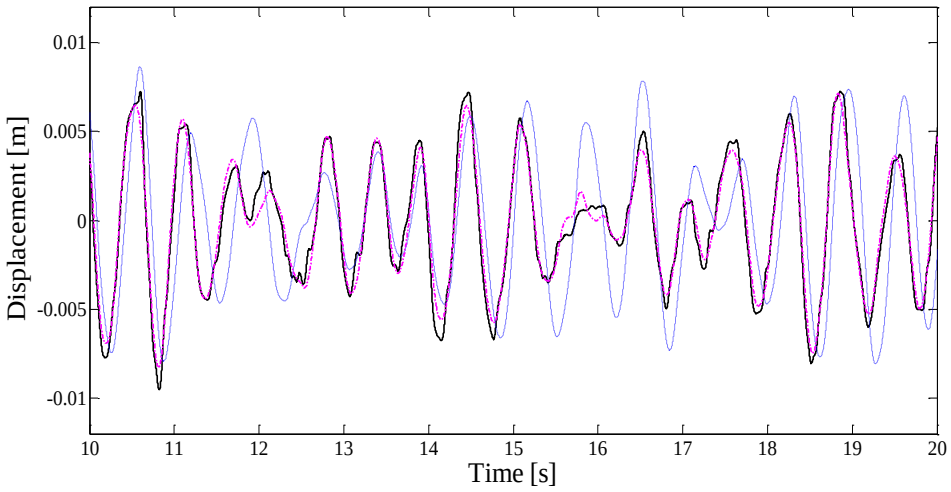

Fig. 4.16 - Comparison of liquid displacement time histories for Configuration #2b: Experimental results (black solid line), classical numerical results (blue dotted line) and proposed model results (magenta dash-dot line).

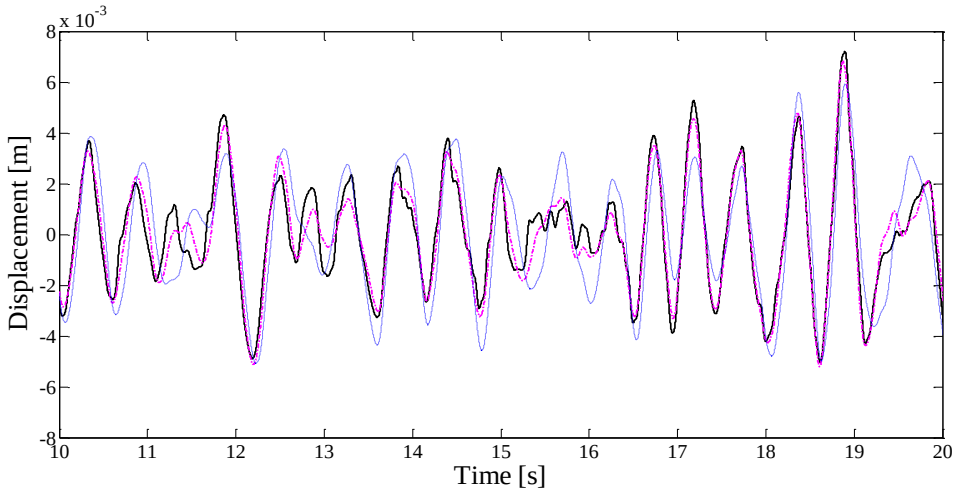

Fig. 4.17 - Comparison of liquid displacement time histories for Configuration #3a: Experimental results (black solid line), classical numerical results (blue dotted line) and proposed model results (magenta dash-dot line).

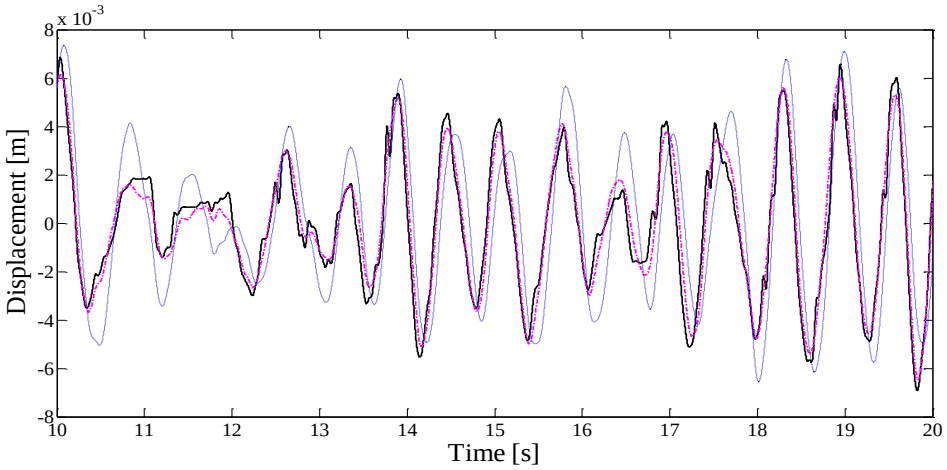

Fig. 4.18 - Comparison of liquid displacement time histories for Configuration #3b: Experimental results (black solid line), classical numerical results (blue dotted line) and proposed model results (magenta dash-dot line).

Further in Figs. 4.19 and 4.20, comparison among experimental, numerical sloshing-vertical motion and proposed model liquid displacement time histories and FRF are depicted, having chosen Configuration #3b case for sake's space only.

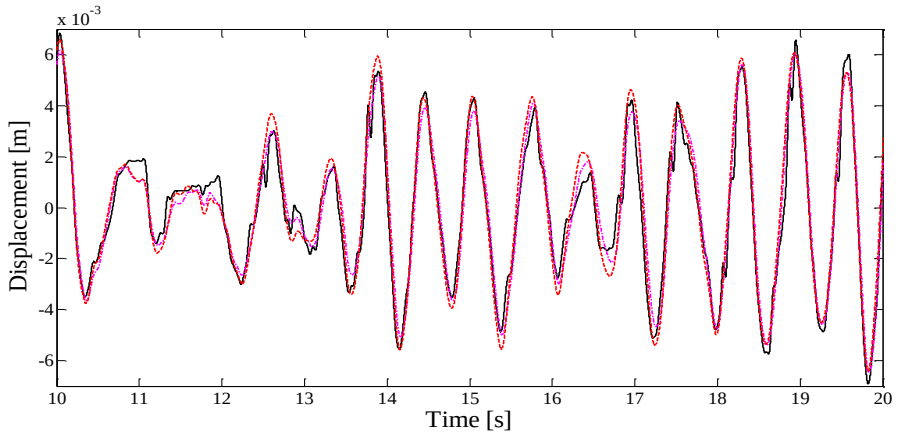

Fig. 4.19 - Comparison of liquid displacement time histories for Configuration #3b: Experimental results(black solid line), numerical sloshing-vertical motion results (red dashed line) and proposed model results (magenta dash-dot line).

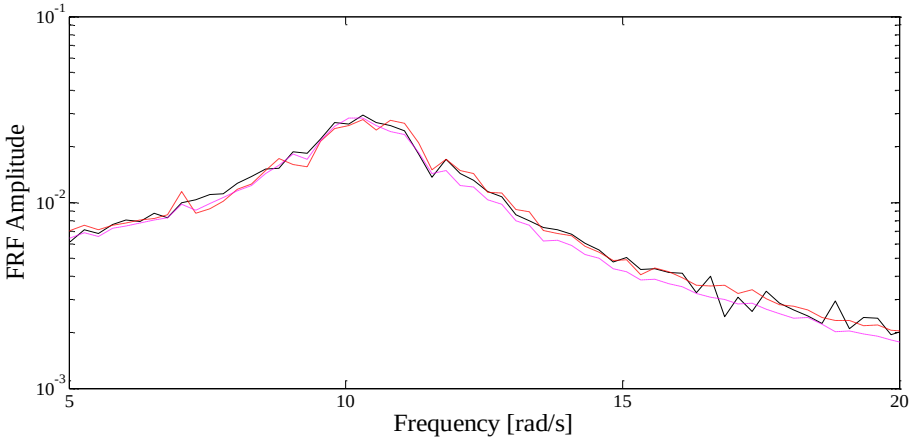

Fig. 4.20 - Comparison of liquid displacement mean FRF for Configuration #3b Experimental results (black solid line), numerical sloshing-vertical motion results (red dashed line) and proposed model results (magenta dash-dot line).

As it can be observed in Fig. 4.20, the curves are practically coincident in frequency domain, assessing that proposed model results are also very satisfactory in frequency domain. Note that in (Di Matteo et al., 2014b and 2015) analogous figures of liquid displacement FRF are reported for other configurations, showing the same order of accuracy of the proposed model in the frequency domain. Further, from a closer observation of Fig. 4.19, the proposed model time history appears to be slightly more accurate in predicting the experimental behavior, than the sloshing-vertical motion one.

4.6.1.3 Discrepancy evaluation and concluding remarks

In order to better evaluate the differences among experimental and numerical results, a properly percentage discrepancy index has been defined as

$$\varepsilon_i = \frac{\int_{t_i}^{t_f} \left[y_i^{th}(t) - y_i^{ex}(t) \right]^2 dt}{\int_{t_i}^{t_f} y_i^{ex}(t)^2 dt} \tag{4.36}$$

where $[t_i–t_f]$ is the observation window, $y_i(t)$ denotes the liquid displacement of the *i*-sample, while the apexes *th* and *ex* stand for numerical and experimentally measured, respectively.

Therefore, the discrepancy index between numerical and experimental time histories, for the various analyzed TLCD configurations, and for the three theoretical formulations, has been computed for each sample. In Fig. 4.21 the index ε_i for the twenty samples of Configuration #3b is reported.

Moreover to get an overview of all results, the mean error for each formulation has been computed, as reported in Table 4.4, where e_c stands for the mean discrepancy index of the classical formulation, e_s stands for the mean discrepancy index of the sloshing formulation and e_p stands for the discrepancy index of the proposed formulation.

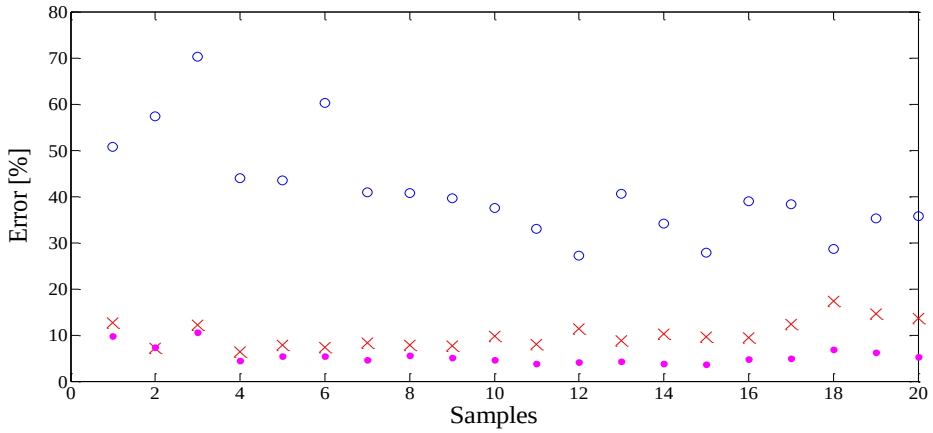

Fig. 4.21 - Values of the percentage discrepancy index ε_i for the twenty samples: comparison among classical numerical results (blue circles), numerical sloshing-vertical motion results (red crosses) and proposed model results (magenta dots) for Configuration #3b.

Table 4.4 - Mean value of the discrepancy index.

	Conf.#1a	Conf.#1b	Conf. #2a	Conf.#2b	Conf. #3a	Conf. #3b
e_c	136.89%	154.20%	81.22%	93.28%	28.82%	41.22%
e_s	12.19%	14.27%	13.07%	11.64%	13.52%	10.11%
e_p	11.68%	11.57%	11.62%	5.51%	6.72%	5.51%

As shown in Table 4.4, mean discrepancy indexes obtained considering the proposed fractional formulation are always smaller than those obtained from the other two formulations, thus proving that this fractional differential equation of motion can captures the real motion of the TLCD free water surface.

As in fact pointed out in Wu et al. (2009), considering a broadband noise, the TLCD free water surface experiences a sloshing motion together with the predicted vertical motion. Such additive sloshing effect may lead to deviation of the measured liquid frequency from the

theoretical one. The fractional damping term, introduced in the equation of motion, is able to recover excellently the different frequency.

Moreover, in literature so far, it has been pointed out that the bigger the ratio between the corner-to-corner width *w* and the horizontal length *b*, the more the classical formulation deviates from experimental results (Hitchcock et al., 1997). This fundamental behavior has been confirmed from findings here introduced. In fact from Configuration #1 (where classical formulation is not reliable) to Configuration #3, classical formulation results tend to match the corresponding experimental ones, with increasing accuracy, while the other two formulations always lead to reliable results.

4.6.2 TLCD controlled systems

Once the proposed fractional formulation has been validated for the TLCD device only, the behavior of TLCD controlled structures has been analyzed.

To this end, firstly an experimental campaign on a small scale SDOF shear-type frame has been carried out to determine main system parameters. Pertinent results are presented in Section 4.6.2.1.

Secondly, experimental tests on the corresponding TLCD controlled systems have been performed to validate the proposed fractional formulation. Pertinent numerical vis-à-vis experimental results are shown in Section 4.6.2.2.

4.6.2.1 Main systems parameters identification

In order to experimentally validate the proposed linear fractional formulation for TLCD controlled systems in Eq. (4.15), the same three main system configurations used in Section 3.7.1 have been employed. In Figs. 4.22(a-c) pictures of the three main systems configurations are shown while in Figs. 4.22(d-f) schematic drawings of the structures with the corresponding dimensions are depicted.

To experimentally identify dynamic parameters of the three main systems configurations, the three SDOF structures have been excited at the base through a shaking table model Quanser Shake Table II which provided the displacement controlled ground motion (Figs. 4.22(a-c)). The acceleration responses at the base and at the storey of the systems have been acquired using Miniature DeltaTron Accelerometers Brüel&Kjær – Type 4507-002B piezoelectric accelerometers.

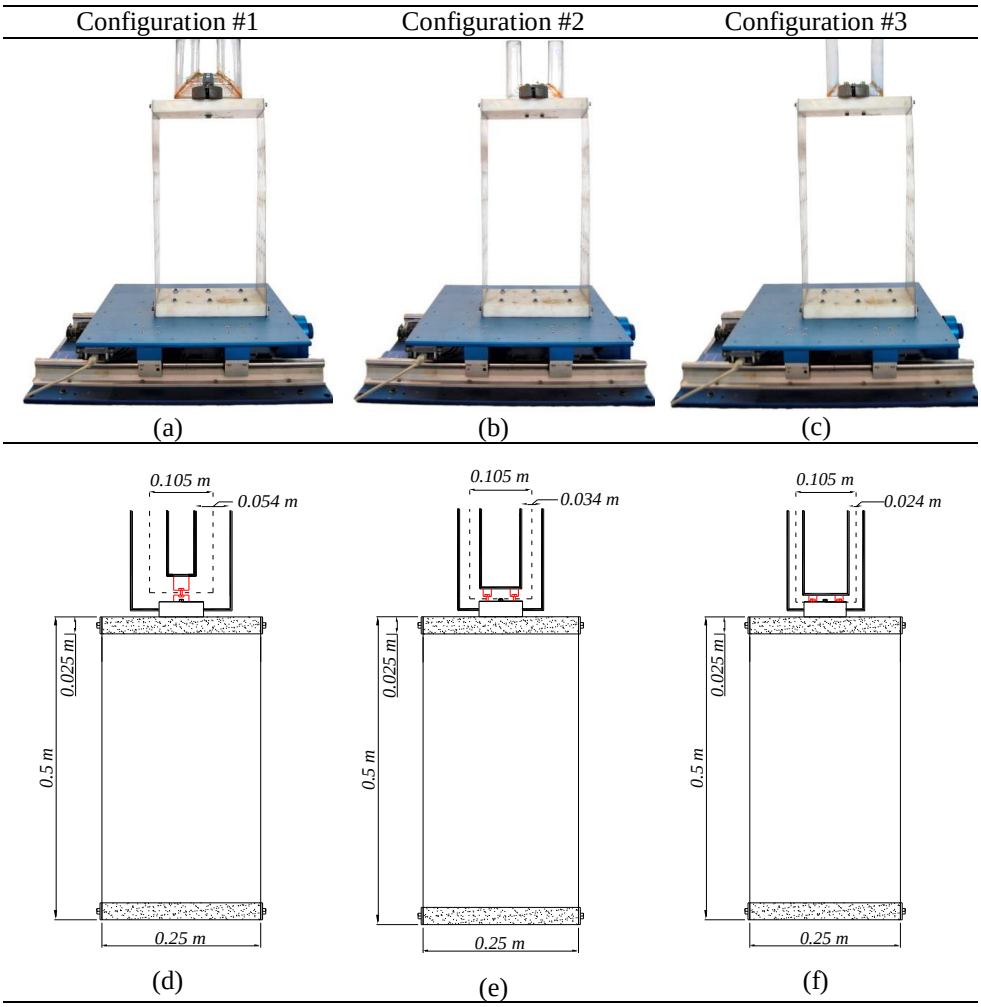

Fig. 4.22 – Experimental setup of the main systems; (a) - (c) picture of the three SDOF structures configurations; (d) - (f) main systems dimensions.

Signals coming from the accelerometers have been acquired trough a NI PXIe-1082 DAQ device, equipped with a high-performance 16-channels NI PXIe-4497 board. Finally the entire system has been controlled via a self-developed signal processing software in LabVIEW environment. In Fig. 4.23 the principal devices used for the shake table

tests are presented, while details on the various devices and systems employed for the experimental set-up are described in Appendix A.

Fig. 4.23 – Acquisition devices for shake table tests.

Ten samples of broadband noise, in the range 0.5÷10 Hz, each having duration of 60 s and a sampling frequency of 1 kHz, have been generated and used as ground acceleration. For each sample the accelerations have been recorded and the mean FRF was computed (Ewins, 1984).

Once obtained the sought FRFs, dynamic parameters have been identified for each configuration using well-known techniques such as half-power bandwidth method and Rational Fractional Polynomial method. All these techniques leaded to similar results of the systems dynamic parameters, which are reported in Table 4.5.

In order to assess the reliability of the identified parameters, experimental vis-à-vis numerical mean FRFs are depicted in Fig. 4.24 for the three main systems configurations. The perfect agreement between numerical and experimental results demonstrates the accuracy of the identified parameters in Table 4.5.

Table 4.5 - Main systems dynamic parameters.

	Configuration #1	Configuration #2	Configuration #3
M	4.486 *kg*	4.226 *kg*	4.208 *kg*
ζ_1	0.005	0.0032	0.0037
ω_1	9.10 *rad/s*	9.54 *rad/s*	9.65 *rad/s*

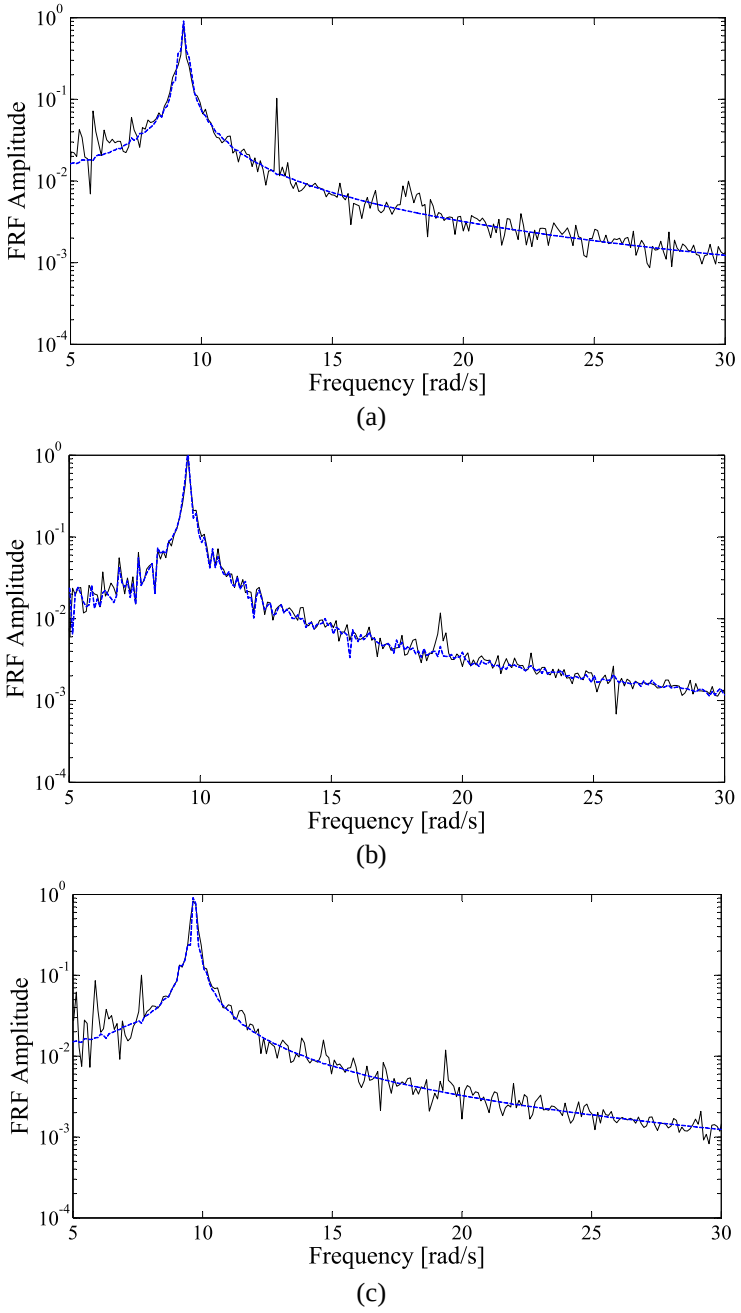

Fig. 4.24 - Comparison between experimental (black solid line) and numerical (blue dashed line) displacement FRFs: (a) Configuration #1; (b) Configuration #2; (c) Configuration #3.

4.6.2.2 TLCD controlled systems parameters

Once main systems and TLCD devices parameters have been identified (see Tables 4.1-4.5), the validity of the proposed theoretical fractional model Eqs. (4.15) has been proved through several experimental tests on three TLCD controlled systems configurations, as outlined in the following.

In this regard three configurations of TLCDs controlled systems have been analyzed. Specifically, Configurations #b parameters (see Table 4.2) of TLCDs devices have been used. Thus, just the diameter *d* of the TLCD devices has been varied for each configuration, keeping constant the horizontal length *b* and the liquid height *h* (Fig. 4.4(g-n)).

Pictures of the three systems configurations are shown in Figs. 4.25(a-b) while in Figs. 4.25(c-d) their schematic drawings are reported with the corresponding dimensions.

The three configurations have been excited at the base with the Quanser Shake Table II, through broadband noises in the range 0.5-10 Hz and duration of 60 s. Specifically 10 samples of broadband noise with variance equal to 0.0025 m^2/s^4 for each configuration have been generated, accelerations at the ground and at the upper plate have been recorded and the three mean FRFs have been computed.

As previously done for the TLCD devices only, once the three mean FRFs of the TLCD controlled structures have been obtained, a best fitting procedure has been applied to identify TLCD parameters for the theoretical fractional model (β and C_β). Therefore a nonlinear least

square curve fitting method using MATLAB, has been applied to fit the two mean experimental FRFs with the corresponding theoretical ones given in Eq. (4.17). Identified parameters are reported in Table 4.6 for the three configurations analyzed.

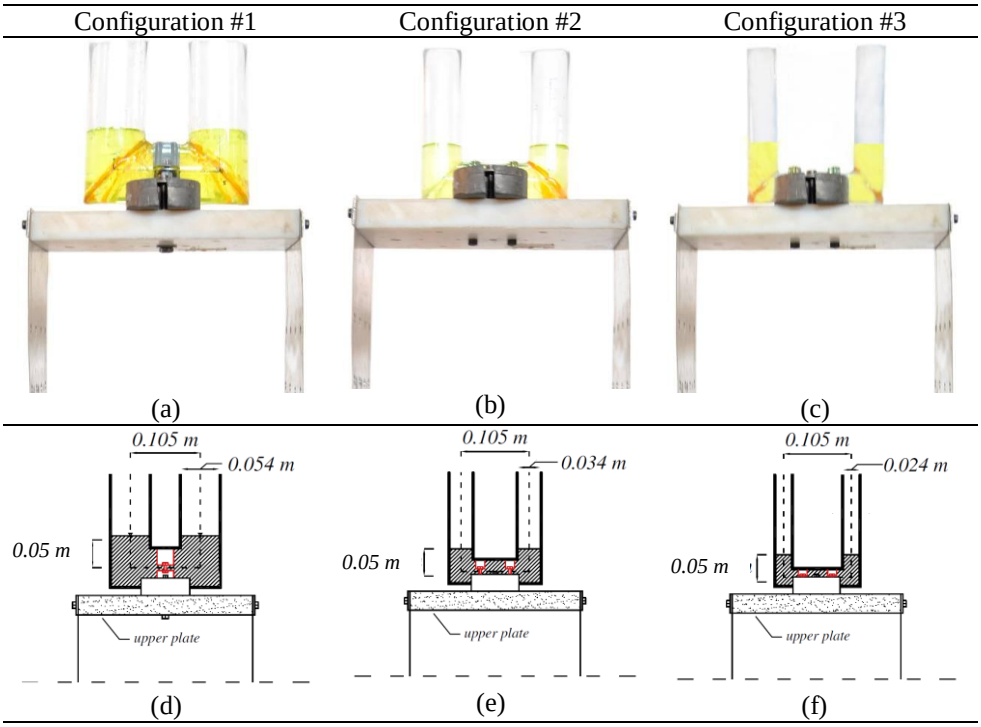

Fig. 4.25 – Experimental setup of the controlled system; (a) - (c) picture of the three controlled structures; (d) - (f) controlled systems dimensions.

It is worth noting that, rather remarkably, identified values of β and C_β are very close to those obtained using the TLCD devices only and reported in Table 4.3, thus further proving the correctness of the procedure outlined.

Table 4.6 - Fractional TLCD parameters

	Configuration #1	Configuration #2	Configuration #3
β	0.155	0.41	0.63
C_β	9.92	3.59	2.06

To assess the validity of the proposed theoretical fractional model in Eqs. (4.15), numerical-experimental comparison of mean FRFs and relative structural accelerations are depicted in Figs. 4.26-4.31 for each TLCD controlled system configuration. Specifically in Figs. 4.26-4.28 the recorded relative upper plate accelerations are compared with those computed with Eq. (2.20) (say classical nonlinear formulation results) and those obtained numerically integrating Eq. (4.15) (say proposed fractional formulation results) using as parameters those reported in Tables 4.5-4.6.

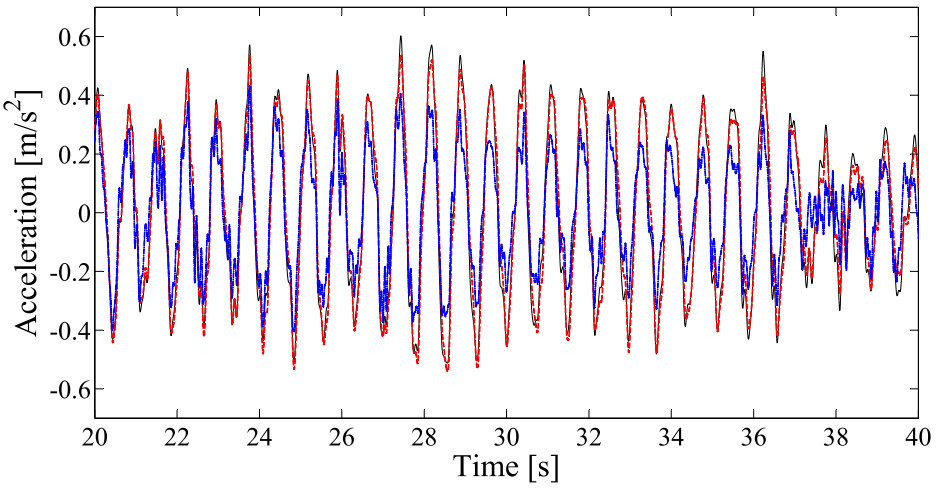

Fig. 4.26 - Comparison of structural acceleration time histories for Configuration #1: Experimental results (black solid line), classical numerical results (blue dash-dot line) and proposed fractional model results (red dashed line).

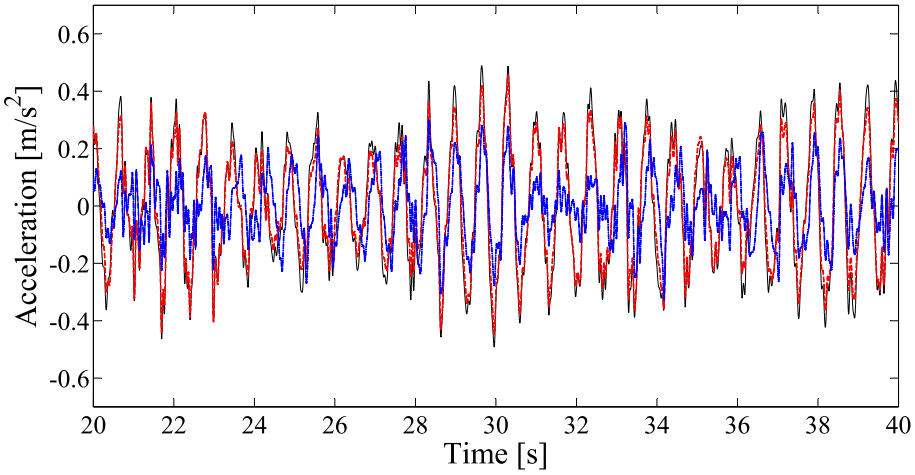

Fig. 4.27 - Comparison of structural acceleration time histories for Configuration #2: Experimental results (black solid line), classical numerical results (blue dash-dot line) and proposed fractional model results (red dashed line).

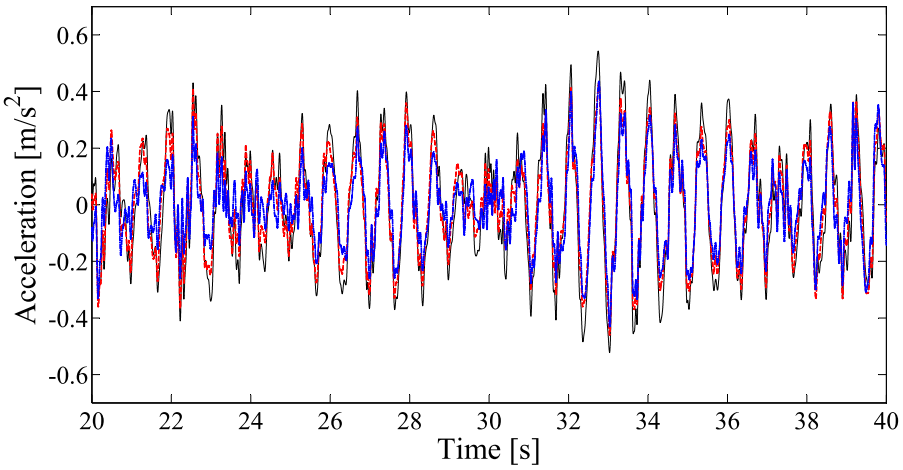

Fig. 4.28 - Comparison of structural acceleration time histories for Configuration #3: Experimental results (black solid line), classical numerical results (blue dash-dot line) and proposed fractional model results (red dashed line).

Further in Figs. 4.29-4.31 the corresponding experimental and numerical mean FRFs are depicted. In all cases, the recorded accelerations have been used as input. It is worth noting that numerical classical results have been obtained with a 4th-order Runge-Kutta method, whereas numerical solution of Eqs. (4.15) have been performed implementing a Newmark method through a discretization of the Caputo fractional derivative (Spanos and Evangelatos, 2010; Failla and Pirrotta, 2012), as detailed in previous Section 4.5.

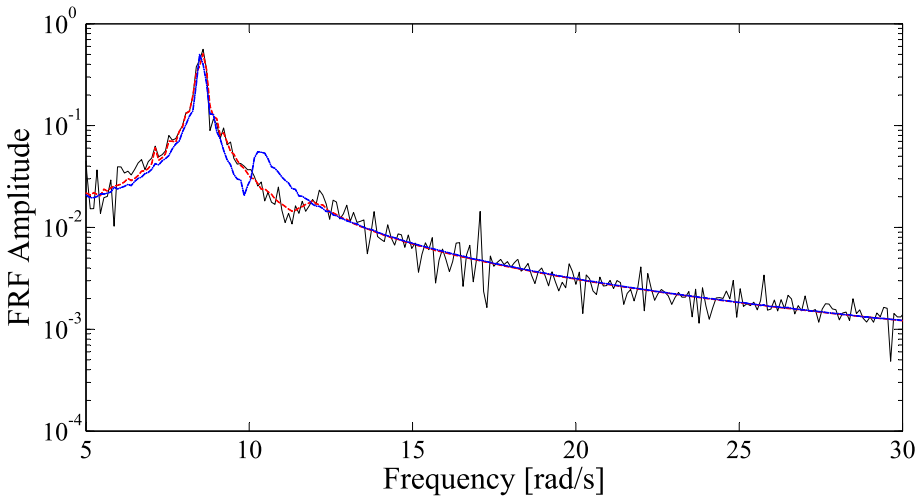

Fig. 4.29 - Comparison of structural displacement mean FRF for Configuration #1 Experimental results (black solid line), numerical classical results (blue dash-dot line) and proposed fractional model results (red dashed line).

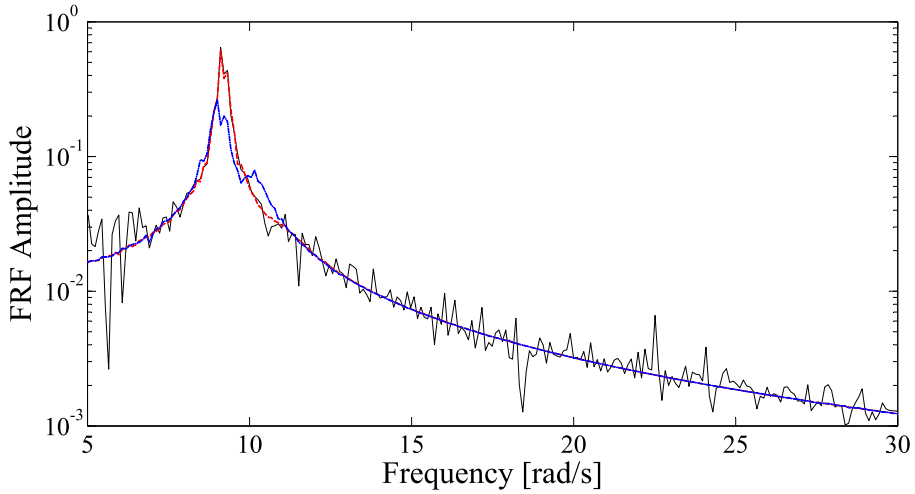

Fig. 4.30 - Comparison of structural displacement mean FRF for Configuration #2 Experimental results (black solid line), numerical classical results (blue dash-dot line) and proposed fractional model results (red dashed line).

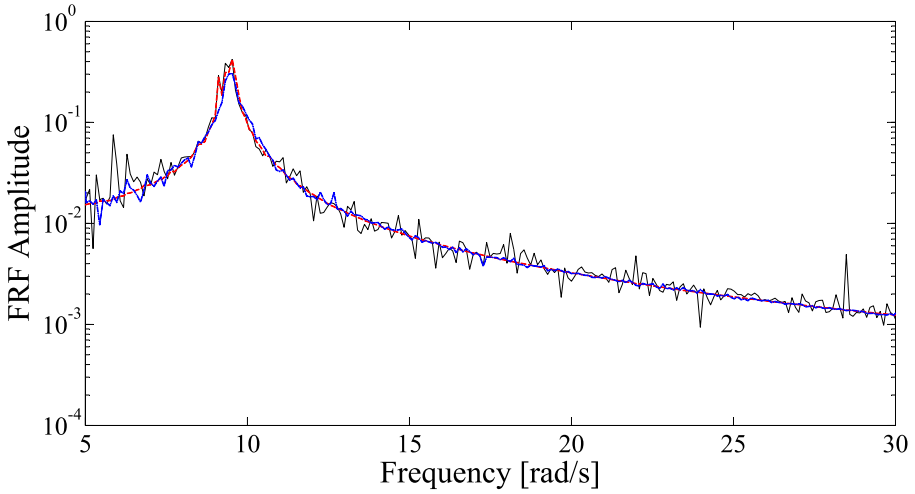

Fig. 4.31 - Comparison of structural displacement mean FRF for Configuration #3 Experimental results (black solid line), numerical classical results (blue dash-dot line) and proposed fractional model results (red dashed line).

As shown for each configuration, proposed fractional model results closely match the corresponding experimental ones both in time and in frequency domain. On the other hand, due to the discrepancies between theoretical liquid natural frequency ω_2 and the experimentally identified one $\omega_{\exp}$, numerical classical results are rather different from experimental data.

4.6.2.3 Discrepancy evaluation

In order to better evaluate the differences among experimental and numerical results, a properly percentage index has been introduced as

$$\varepsilon_i = \frac{\int_{t_i}^{t_f} \left[\ddot{x}_i^{th}(t) - \ddot{x}_i^{ex}(t) \right]^2 dt}{\int_{t_i}^{t_f} \ddot{x}_i^{ex}(t)^2 \, dt} \tag{4.37}$$

where $\left[t_i - t_f \right]$ is the observation window, $\ddot{x}_i(t)$ denotes the relative structural accelerations of the *i*-sample, while the apexes *th* and *ex* stand for numerical and experimentally measured, respectively. Clearly, as shown in Eq. (4.37), the greater the value of ε_i the higher the discrepancy is. Therefore, values of the index in Eq. (4.37) for the three analyzed TLCD controlled systems configurations have been computed for each sample considering both classical nonlinear formulation results (Eq. (2.20)) and proposed fractional formulation results (Eq. (4.15)). Figs. 4.32-4.34 show the trend of the discrepancy index ε_i for the 10 samples of Configurations #1-#3.

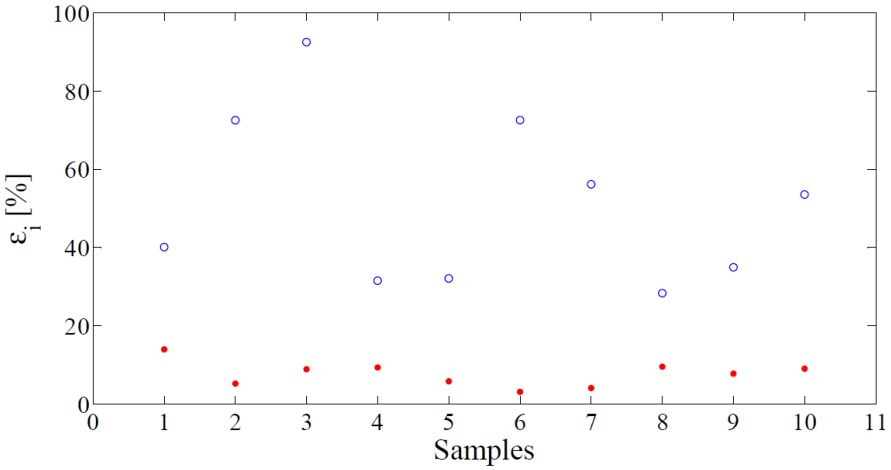

Fig. 4.32 - Values of the percentage discrepancy index ε_i for the ten samples: comparison among classical numerical results (blue circles) and proposed fractional model results (red dots) for Configuration #1.

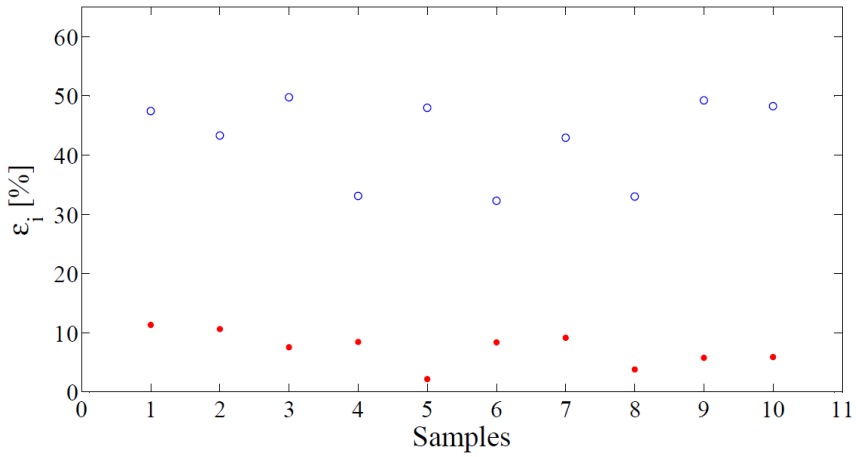

Fig. 4.33 - Values of the percentage discrepancy index ε_i for the ten samples: comparison among classical numerical results (blue circles) and proposed fractional model results (red dots) for Configuration #2.

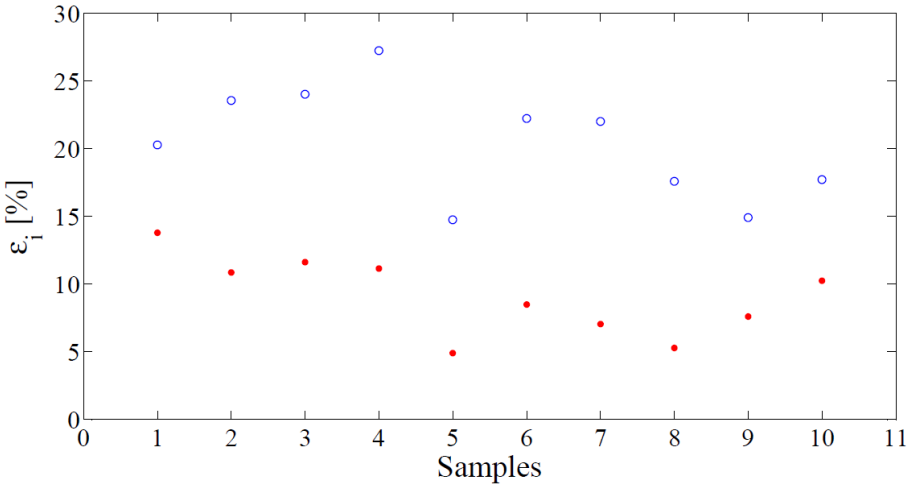

Fig. 4.34 - Values of the percentage discrepancy index ε_i for the ten samples: comparison among classical numerical results (blue circles) and proposed fractional model results (red dots) for Configuration #3.

Further, to get an overview of these results, the mean discrepancies for each model has been computed as reported in Table 4.7, where e_c stands for the mean discrepancy of the classical model and e_p stands for mean discrepancy of the proposed fractional formulation.

Table 4.7 - Mean value of the discrepancy index.

	Configuration #1	Configuration #2	Configuration #3
e_c	51.42%	42.72%	20.42%
e_p	7.69%	7.12%	9.09%

As shown in Table 4.7, mean discrepancies obtained considering the proposed formulation are always smaller than those obtained from the classical one, thus proving that Eq. (4.15) can captures the real motion of TLCD controlled structures.

Further, the statistics of experimental response accelerations in terms of variance have been computed and then compared with the variances obtained by solving numerically the nonlinear system Eq. (2.20) and the proposed fractional formulation. Eq. (4.15). In the numerical simulations the recorded ground accelerations have been used as base accelerations.

In Fig. 4.35 comparison among variances $\sigma^2_{\ddot{X}}$ of accelerations for main systems and TLCD-controlled system for the different levels of mass ratio μ is depicted.

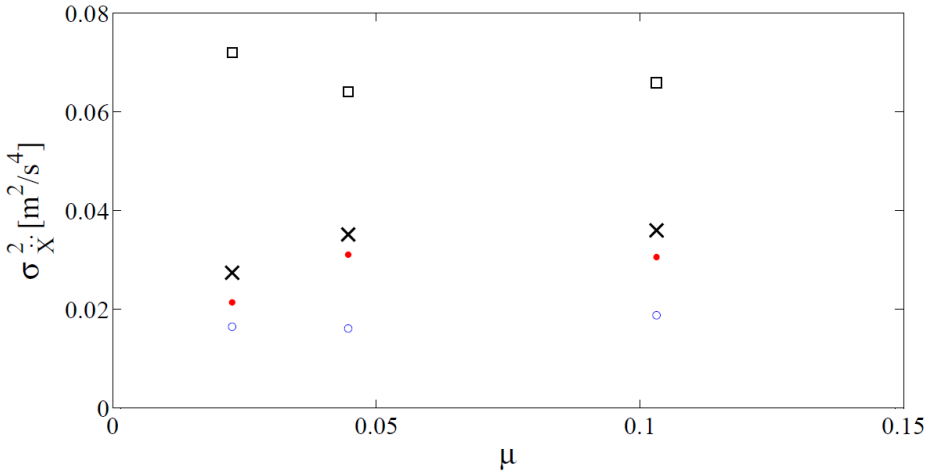

Fig. 4.35 – Experimental validation in term of variances for different mass ratios μ. Experimental variances of the main system (black squares) and TLCD-controlled system (black crosses). Classical numerical results (blue circles) and proposed fractional model results (red dots).

As shown, experimental results (black dots) are in a good agreement with the numerical fractional formulation ones (red stars) for all the values of mass ratio analyzed, while results of the classical formulation (blue crosses) deviates from the corresponding experimental results.

4.6.2.4 Variation of parameters to input strength

Since classical formulation for TLCD controlled structures Eq. (2.20) is a nonlinear equation of motion, a natural question arises regarding the behavior of the system at different levels of the input strength. Therefore, experimental campaign to assess the validity of the proposed linear fractional formulation at different values of the input strength has also been carried out.

Both Configurations #2 of the main system (Fig. 4.22(b)) and TLCD-controlled system (Fig. 4.25(b)) have been subjected to three increasing levels of input strength, by taking advantage of the capability of the shaking table to perfectly reproduce any displacement time history. For each level 10 samples of broadband noise, with duration of 60 seconds, have been generated and the accelerations at the ground and at the top mass have been recorded.

The statistics of both input and response accelerations in terms of variance have been computed and then compared with the variances obtained by solving numerically Eqs. (2.20) and (4.15).

In the numerical simulations the recorded ground accelerations have been used as base accelerations $\ddot{x}_g$, while already identified parameters in Tables 4.1 and 4.5-4.6 have been considered.

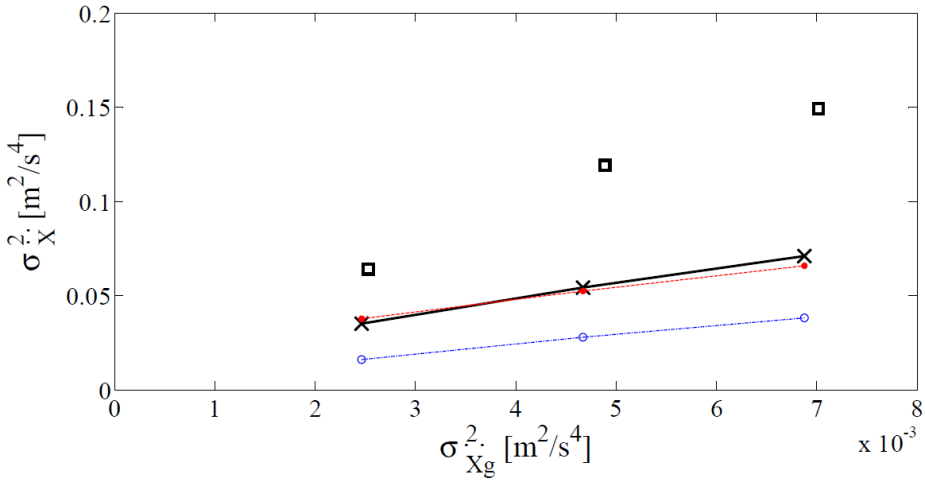

Fig. 4.35 - Experimental validation in term of variances for values of the input intensity. Experimental variances of the main system (black squares) and TLCD-controlled system (black crosses). Classical numerical results (blue circles) and proposed fractional model results (red dots)

In Fig. 4.35 comparison among variances of accelerations $\sigma^2_{\ddot{X}}$ for main system (black squares) and TLCD-controlled system versus the input variance $\sigma^2_{\ddot{X}_g}$ is shown.

As can be seen, numerical results obtained from the proposed fractional formulation (red dots) follow closely the corresponding experimental results (black crosses) for each input strength. On the other hand, numerical results obtained from the classical formulation (blue circles) are rather different, and discrepancies increase for greater values of the input strength.

It is worth noting that, for the numerical simulation of the proposed fractional formulation, identified parameters reported in the second column of Table 4.6 have been used. As stated in previous Section 4.6.2.2, those parameters have been obtained considering an input

strength of $\sigma^2_{\ddot{X}_g} = 0.0025 m^2/s^4$. Therefore the same parameters identified for one input strength $\sigma^2_{\ddot{X}_g}$ resulted to be suitable to determine the structural variances of accelerations $\sigma^2_{\ddot{X}}$ also for greater values of $\sigma^2_{\ddot{X}_g}$, thus further proving the validity of the proposed linear fractional formulation, even at increasing level of the input strength.

Chapter 5

Stochastic analysis of TLCDs: a Wiener Path Integral (WPI) approach

5.1 Introduction

Limitations pertaining to available information and the interpretation of prevalent mechanisms, as well as inherent uncertainty in critical engineering problems, have necessitated the study of systems with stochastic parameters and input. In this context, a stochastic approach constitutes a rational basis for system analysis and sustainable design.

Nevertheless, complex nonlinear and hysteretic behavior observed in many systems renders such a stochastic analysis a persistent challenge. In this regard, theoretical research in the field of stochastic dynamics has already led to seminal advancements (e.g. see Soong and Grigoriu (1993), Li and Chen (2009)). For instance, Monte Carlo simulation (MCS) techniques (e.g. Rubinsteinand Kroese (2007), Muscolino et al. (2003)) have been among the most versatile tools for determining the response statistics of arbitrary stochastic systems, and alternative efficient approximate analytical and numerical solution techniques (e.g. see Spanos and Kougioumtzoglou (2012), Kougioumtzoglou and Spanos (2013), Ricciardi (2007)) have been also developed.

In this context, it is noted that most of the researches in the field of stochastic dynamics, deal with the analysis of systems with different kind and degrees of nonlinearity.

However, in previous Chapter 4 a different mathematical operator, namely the fractional derivative, has been used to model the motion of the liquid in TLCD device. It is noted that in recent year there has been an increasing interest among researchers on the mathematical tool of fractional calculus, and a growing number of real applications in which fractional operators have been used (Sabatier et al. (2007), Hilfer (2000)).

Since classical techniques developed for the analysis of nonlinear stochastic systems cannot be used directly for systems endowed with fractional derivative elements, there is still a need for developing efficient approximate analytical and/or numerical solution techniques for these kind of systems.

In this regard, one of the promising frameworks relates to the concept of the Wiener Path Integral (WPI). It is noted that although the WPI has been well established in the field of theoretical physics, the engineering community has ignored its potential as a powerful uncertainty quantification tool. The concept of path integral was introduced by Wiener (1921, 1930) and was reinvented in a different form by Feynman (1948) to reformulate quantum mechanics. A detailed treatment of path integrals, especially of the Feynman path integral and its applications in physics, can be found in a number of books such as the one by Chaichian and Demichev (2001) and Kleinert (2009). Recently, an approximate analytical WPI technique for addressing certain stochastic engineering dynamics problems was developed by Kougioumtzoglou and Spanos

(2012). The technique is based on a variational principle formulation in conjunction with a stochastic averaging/linearization treatment of the nonlinear equation of motion. In this regard, relying on the concept of the most probable trajectory an approximate expression was derived for the non-stationary response probability density function (PDF). Further, the aforementioned technique was extended by Kougioumtzoglou and Spanos (2014) to treat multi-degree-of-freedom (MDOF) systems and hysteretic nonlinearities. The enhanced technique circumvents approximations associated with the stochastic averaging/linearization treatment of the previous development.

On this base, in this Chapter this novel technique is further investigated, showing its reliability also for the efficient determination of the response PDF of nonlinear MDOF systems, and systems with fractional derivative elements.

Specifically, in Section 5.2 the basic concepts of the WPI are introduced, its application for nonlinear SDOF systems under Gaussian white noise is discussed, and several numerical examples are developed to show the accuracy of the method.

In Section 5.3 the application of the WPI for the analysis of nonlinear MDOF system is presented, and a novel formulation for an efficient evaluation of the nonstationary response PDF of such systems is proposed. Several numerical examples have been reported to assess the reliability of this proposed procedure. Further the case of the 2 degree-of-freedom TLCD controlled structure is considered in the last part of the Chapter (Section 5.5), assessing the accuracy of the outlined technique also with the corresponding experimentally obtained PDFs.

Finally, in Section 5.4 the WPI technique is extended to the case of nonlinear systems comprising fractional derivatives elements. Several numerical examples are presented to show the reliability of the proposed procedure, including the case of the proposed fractional formulation for the TLCD device, developed in previous Section 4.4. Finally, The case of the 2 degree-of-freedom TLCD controlled structure is considered, assessing the accuracy of the outlined procedure also with the corresponding experimentally obtained PDFs.

5.2 WPI for nonlinear systems under Gaussian white noise

In this Section an overview of the Wiener Path Integral technique for nonlinear SDOF systems will be presented for sake of clarity.

Specifically, in Section 5.2.1 few basic concepts regarding the simpler case of a half-oscillator under Gaussian white noise will be provided, together with a brief background on Markov processes and the associated Chapman-Kolmogorov and Fokker-Planck equations.

On this base, in Sections 5.2.2 and 5.2.3 the WPI will be introduced, and further extended to the case of nonlinear SDOF systems in Section 5.2.4. Finally, in Section 5.2.5 the implementation of the procedure will be discussed and two numerical examples will be presented to demonstrate the reliability of the procedure.

5.2.1 Nonlinear half oscillator under Gaussian white noise

Let a nonlinear system under a zero-mean Gaussian white noise $W(t)$ be given in the form

$$\begin{cases} \dot{X}(t) = f(X,t) + g(X,t)W(t) \\ X(0) = X_0 \end{cases} \tag{5.1}$$

where $f(X,t)$ and $g(X,t)$ are nonlinear functions of the response process $X(t)$ and X_0 is the initial condition which may be either deterministic or a random variable with assigned PDF.

Further, as far as the Gaussian white noise is concerned, it can be characterized by its correlation function given as

$$E\left[W(t_1)W(t_2)\right] = q\,\delta\left(t_{1-t_2}\right) \tag{5.2}$$

where $E[\bullet]$ is the ensemble average, q is the strength of the white noise and $\delta(\bullet)$ is the Dirac's delta function.

Equation (5.1) may in turn be converted into an Itô type stochastic differential equation, that is the increment $dX(t)$ of the response can be written in the form

$$dX(t) = f(X,t)dt + g(X,t)dB(t) \tag{5.3}$$

in which $B(t)$ is the so-called normal Brownian motion process, i.e. a zero-mean process with independent increments, $B(0)=0$ with probability one and whose increment $dB(t)$ possesses characteristic function (CF) given by

$$\phi_{dB}(\theta) = E\left[\exp(i\theta)\,dB(t)\right] = \exp\left(-\frac{q}{2}\theta^2 dt\right) \tag{5.4}$$

where i is the imaginary unit. Form this equation it may be recognized that $dB(t)$ is of order $(dt)^{1/2}$ since its variance $E\left[dB(t)^2\right] = qdt$ and higher order moments are exactly zero.

Considering that $W(t)$ is a zero-th order memory Markov process, from Eq. (5.1) it immediately follows that the response process $X(t)$ is Markovian too, hence the so-called Chapman-Kolmogorv (CK) equation holds true, that is

$$p_X\left(x_f, t_i+\tau\right) = \int_{-\infty}^{\infty} p_X\left(x_f, t_i+\tau \mid x_i, t_i\right) p_X\left(x_i, t_i\right) dx_i \tag{5.5}$$

which is valid for every value of τ.

Equation (5.5) clearly states that to evaluate the PDF $p_X\left(x_f, t_i+\tau\right)$ of the response process $X(t)$ at the time $(t_i+\tau)$, when the PDF of $X(t)$ at earlier time t_i is already known, it is only necessary to determine the so-called Transition Probability Density Function (TPDF) $p_X\left(x_f, t_i+\tau \mid x_i, t_i\right)$ at the same time instant, for an assigned (deterministic) initial condition x_i at earlier time t_i.

Note that, in the case of normal white noise input the TPDF in Eq. (5.5) follows a Gaussian distribution for small τ (short time Gaussian approximation) (Risken, 1996), given as

$$p_X\left(x_f, t_i+\tau \mid x_i, t_i\right) = \frac{1}{\sqrt{2\pi q \tau g\left(x_f, t_i+\tau\right)^2}} \exp\left[-\frac{\left(x_f - x_i - f\left(x_f, t_i+\tau\right)\tau\right)^2}{2q\tau g\left(x_f, t_i+\tau\right)}\right] \tag{5.6}$$

Therefore Eq. (5.6) together with Eq. (5.5) leads to the evolution of the response PDF of the process $X(t)$ in short time steps τ.

Further it has been shown in (Dekker, 1976) that Eqs. (5.5) and (5.6) when $\tau \to 0$ lead, in exact manner, to the equation

$$\frac{\partial}{\partial t} p_X(x,t) = -\frac{\partial}{\partial x}\left[f(x,t)\, p_X(x,t)\right] + \frac{q}{2}\frac{\partial^2}{\partial x^2}\left[g(x,t)\, p_X(x,t)\right] \tag{5.7}$$

which is the well-know Fokker-Planck (FP) equation, ruling the evolution of the response PDF of the process $X(t)$.

5.2.2 Probability density functional and the Wiener Path Integral

It is worth noting that Eq. (5.6) has been the starting point for the development of numerical path integral solution approaches which essentially constitute a discrete version of the CK equation Eq. (5.5). The basic characteristic of the approaches is that the evolution of the PDF is computed in short time steps. It was Wehner and Wolfer (1983a, 1983b, 1987) who first developed certain numerical aspects of the approach and established it as a robust numerical tool. Related advancements include the work by Naess and Moe (2000) and Di Paola and Santoro (2008) who extended the approach to deal with Poisson white noise excitation.

A characteristic of this numerical approach is the great accuracy achieved at the tails of the computed PDF, indicating its suitability also for reliability analysis (e.g. Bucher and Di Paola, 2015).

Note that the fact that the PDF is computed in short time steps can be regarded as a major shortcoming of the approach making it computationally inefficient.

In general, the transition PDF $p_X\left(x_f, t_f \mid x_i, t_i\right)$ denotes the probability of a transition from a point x_i in state space at time t_i to a

point x_f in state space at time t_f where $t_f > t_i$. Adopting the notation of Chachian and Demichev (2001), let $C\left\{x_i, t_i; x_f, t_f\right\}$ denote the set of trajectories starting at point $x\left(t_i\right) = x_i$ and having the end point $x\left(t_f\right) = x_f$.

Clearly to obtain the transition PDF that the particle starting at point $x\left(t_i\right) = x_i$ ends up at point $x\left(t_f\right) = x_f$, the probabilities over the set $C\left\{x_i, t_i; x_f, t_f\right\}$ of all the trajectories which have common starting and ending points must be summed in an appropriate way. This is done by utilizing the WPI, which formally denotes the summation over a set of trajectories which are assumed to be continuous.

The WPI can be realized as a functional integral over the space of all possible paths. It possesses a probability distribution on the path space as its integrand, which is denoted by $W\left[x(t)\right]$ and is called probability density functional. In this sense, the transition PDF is given by

$$p_X\left(x_f, t_f \mid x_i, t_i\right) = \int_{\{x_i, t_i\}}^{\{x_f, t_f\}} W\left[x(t)\right]\left[dx(t)\right] \tag{5.8}$$

The method to describe a stochastic process, as that ruled by Eq. (5.1), by its probability density functional was first considered by Wiener (1930) for the process with $f\left(X,t\right) = 0$ and $g\left(X,t\right) = 1$. In this case the WPI (Eq. (5.8)) can be evaluated directly from its definition (e.g. Chaichian and Demichev (2001)) and thus, an analytical solution is possible. Subsequent generalizations were made by Onsager and

Machlup (1953) who considered processes with a linear form of $f(X,t)$ and a constant $g(X,t)$. In this regard Tisza and Manning (1957) expressed the probability density functional of this oscillator in the form

$$W[x(t)][dx(t)] = \bar{C}\exp\left[-\int_{t_i}^{t_f} OM(x,\dot{x})dt\right][dx(t)] \tag{5.9}$$

where $\bar{C}$ is a normalization constant; and $OM(x,\dot{x})$ is the Onsager-Machlup (O-M) function. It is noted that several research efforts towards determining the O-M function for a stochastic process with general nonlinear form of $f(X,t)$ and $g(X,t)$ resulted in controversial results in the 1970s. Nevertheless, most papers converged towards the results found in Stratonovich (1971). In this regard, the probability density functional for processes with general $f(X,t)$ and $g(X,t)$ is given by

$$W[x(t)][dx(t)] = \bar{C}\exp\left[-\int_{t_i}^{t_f} OM(x,\dot{x})dt\right]\left[\frac{dx(t)}{g(x,t)}\right] \tag{5.10}$$

where

$$OM(x,\dot{x}) = \frac{1}{2}\left[\left(\frac{\dot{x}}{g(x,t)} - b(x)\right)^2 + g(x,t)b'(x)\right] \tag{5.11}$$

and

$$b(x) = \frac{f(x,t) - \frac{1}{2}g'(x,t)g(x,t)}{g(x,t)} \tag{5.12}$$

in which (‘) denotes differentiation with respect to the variable x.

5.2.3 Lagrangian formulation and variational principle for the most probable path

It can be readily seen that even if the O-M function Eq. (5.11) is constructed, the analytical solution of the WPI in Eq. (5.8) is at least a rather daunting, if not impossible, procedure. Thus, to circumvent the aforementioned challenge, several research efforts have focused on developing approximate techniques for determining the transition PDF $p_X\left(x_f, t_f \mid x_i, t_i\right)$. In this regard, researchers have adopted a Lagrangian formulation and have interpreted the O-M function as a Lagrangian function for determining the most probable path, namely the most probable trajectory that connects the points $x\left(t_i\right)=x_i$ and $x\left(t_f\right)=x_f$. In this manner, a variational principle can lead to the associated Euler-Lagrange equations, whose solution is the most probable process realization (Graham, 1977).

Note that the solution to the variational formulation is required to be twice differentiable. This is not the case for the sample paths of systems with nonlinear function $g\left(X, t\right)$ (e.g., Grigoriu 2002). Thus, in these cases, the O–M function cannot be defined as a Lagrangian. Instead, the O–M function can be defined as the Lagrangian giving the most probable tube if one seeks the probability that a path lies within a certain region (e.g. tube) along a differentiable function (see Durr and Bach (1978) and Kougioumtzoglou and Spanos (2012) for relevant discussions).

On the other hand, for the quite general class of processes with nonlinear function $f(X,t)$ and $g(X,t)=\bar{c}$, where $\bar{c}$ is a constant, the O-M function can be defined as a Lagrangian function. In this case then

$$W\left[x(t)\right]\left[dx(t)\right]=\bar{C}\,\exp\left[-\int_{t_i}^{t_f}\mathscr{L}(x,\dot{x})dt\right]\left[dx(t)\right] \tag{5.13}$$

with

$$\mathscr{L}(x,\dot{x})=\frac{1}{2}\left[\left(\frac{\dot{x}-f(x)}{\bar{c}}\right)^2+f'(x)\right] \tag{5.14}$$

while Eq. (5.8) provides the transition PDF.

It is noted that the O-M function has been substituted by the Lagrangian $\mathscr{L}(x,\dot{x})$ in Eq. (5.13) to provide a variational principle compatible solution technique. The basic concept of the variational technique (e.g. Chachian and Demichev 2001) suggests that the largest contribution to the WPI of Eq. (5.8) comes from the trajectory for which the integral in the exponential in Eq. (5.13) becomes as small as possible. Calculus of variations (e.g. Ewing 1985) dictates that this trajectory is subjected to the condition

$$\delta\int_{t_i}^{t_f}\mathscr{L}(x_c,\dot{x}_c)dt=0 \tag{5.15}$$

which leads to the Euler-Lagrange (E-L) equation

$$\frac{\partial\mathscr{L}}{\partial x_c}-\frac{\partial}{\partial t}\frac{\partial\mathscr{L}}{\partial\dot{x}_c}=0,\ x_c(t_i)=x_i,\ x_c(t_f)=x_f \tag{5.16}$$

where $x_c(t)$ represents the most probable trajectory. Further, solving the boundary value problem of Eq. (5.16) yields a solution for the transition PDF of the process $x_c(t)$ (e.g. Chachian and Demichev 2001) in the form

$$p_X\left(x_f, t_f \mid x_i, t_i\right) = \varphi\left(t_f - t_i\right) \exp\left[-\int_{t_i}^{t_f} \mathscr{L}\left(x_c, \dot{x}_c\right) dt\right] \tag{5.17}$$

Note that for fixed time points t_i and t_f the function $\varphi\left(t_f - t_i\right)$ can be determined by applying the normalization condition

$$\int_{-\infty}^{\infty} p_X\left(x_f, t_f \mid x_i, t_i\right) dx_f = 1 \tag{5.18}$$

This formulation yields the most probable path of a diffusion process, namely the trajectory which determines the most probable sample paths of the process. The concept of the most probable path can be viewed as something equivalent to the fact that the most probable value of a random variable is the one corresponding to the maximum value of the PDF.

5.2.4 Lagrangian formulation for the most probable path of SDOF systems

In previous sections, the simple case of a half-oscillator has been considered to introduce the WPI technique. In the ensuing analysis, based on the work of Kougioumtzoglou and Spanos (2014) the analytical WPI-based technique is extended and generalized to account for nonlinear SDOF and for MDOF systems. The enhanced technique builds on the early research paper by Onsager and Machlup (1953) and on some recent research work by Taniguchi and Cohen (2008), where they generalized the original approach by Onsager and Machlup (1953) to systems with kinetic energy. In this manner, they considered explicitly the inertial effects of particles. In this regard, consider the nonlinear oscillator in the form

$$\ddot{x}+2\zeta\omega_0\dot{x}+\omega_0^2 x+f\left(x,\dot{x}\right)=w(t) \tag{5.19}$$

where $f\left(x,\dot{x}\right)$ represents a nonlinear function which depends on the instantaneous values of x and $\dot{x}$, ζ in the damping ratio, ω_0 is the natural frequency of oscillator; and $w(t)$ represents a Gaussian, zero-mean white noise process possessing a power spectrum S_0.

The probability density functional for the white noise process $w(t)$ is given by (e.g. Chaichian and Demichev (2001), Taniguchi and Cohen (2008))

$$W\left[w(t)\right]=\bar{C}\,\exp\left[-\int_{t_i}^{t_f}\frac{1}{2}\frac{w^2(t)}{2\pi S_0}dt\right] \tag{5.20}$$

Following the approach suggested in Kougioumtzoglou and Spanos (2014), substituting Eq. (5.19) into Eq. (5.20) and interpreting the probability density functional $W\left[w(t)\right]$ as the probability density functional $W\left[x(t)\right]$ for x yields

$$W\left[w(t)\right]=\bar{C}\,\exp\left[-\int_{t_i}^{t_f}\frac{1}{2}\frac{\left(\ddot{x}+2\zeta\omega_0\dot{x}+\omega_0^2x+f\left(x,\dot{x}\right)\right)^2}{2\pi S_0}dt\right] \tag{5.21}$$

Thus the corresponding Lagrangian function is given by

$$\mathscr{L}\left(x,\dot{x},\ddot{x}\right)=\frac{1}{2}\frac{\left(\ddot{x}+2\zeta\omega_0\dot{x}+\omega_0^2x+f\left(x,\dot{x}\right)\right)^2}{2\pi S_0} \tag{5.22}$$

According to the variational principle of Eq. (5.15) the sample path which contributes most to the associated WPI satisfies the equation

$$\delta\int_{t_i}^{t_f}\mathscr{L}\left(x_c,\dot{x}_c,\ddot{x}_c\right)dt=0 \tag{5.23}$$

which leads to the E-L equation

$$\frac{\partial\mathscr{L}}{\partial x_c}-\frac{\partial}{\partial t}\frac{\partial\mathscr{L}}{\partial\dot{x}_c}+\frac{\partial^2}{\partial t^2}\frac{\partial\mathscr{L}}{\partial\ddot{x}_c}=0 \tag{5.24}$$

with the four boundary conditions

$$x_c\left(t_i\right)=x_i,\,\dot{x}_c\left(t_i\right)=\dot{x}_i,\,x_c\left(t_f\right)=x_f,\,\dot{x}_c\left(t_f\right)=\dot{x}_f \tag{5.25}$$

where $x_c\left(t\right)$ represents the most probable trajectory.

Next, solving Eq. (5.24) together with Eq. (5.25) yields a solution for the transition PDF $p\left(x_f,\dot{x}_f,t_f \mid x_i,\dot{x}_i,t_i\right)$ (e.g. Chachian and Demichev 2001) in the form

$$p\left(x_f,\dot{x}_f,t_f \mid x_i,\dot{x}_i,t_i\right)=\varphi\left(t_f-t_i\right)\exp\left[-\int_{t_i}^{t_f}\mathscr{L}\left(x_c,\dot{x}_c,\ddot{x}_c\right)dt\right] \tag{5.26}$$

where, for fixed time points t_i and t_f the function $\varphi\left(t_f-t_i\right)$ can be determined by applying the normalization condition

$$\int_{-\infty}^{\infty}\int_{-\infty}^{\infty}p\left(x_f,\dot{x}_f,t_f \mid x_i,\dot{x}_i,t_i\right)dx_f\,d\dot{x}_f=1 \tag{5.27}$$

5.2.5 Mechanization of the procedure and numerical applications

In this Section the mechanization of the WPI technique is outlined and the versatility and the accuracy of the technique is assessed via numerical examples. In this regard, two nonlinear oscillators are considered. In the following, the initial time instant $\left(t_i=0\right)$ is used, whereas zero initial conditions are assumed, that is $x_c\left(0\right)=x_i=0$ and $\dot{x}_c\left(0\right)=\dot{x}_i=0$. To apply the WPI technique for the given boundary conditions $x_c\left(0\right)=0,\dot{x}_c\left(0\right)=0,x_c\left(t_f\right)=x_f,\dot{x}_c\left(t_f\right)=\dot{x}_f$, the most probable path $x_c\left(t\right)$ is determined by solving numerically the boundary value problem Eq. (5.24). Specifically, for a given final time instant t_f and a given final boundary conditions $\left(x_f,\dot{x}_f\right)$, Eq. (5.24) yields a single path $x_c\left(t\right)$.

Further, substituting the determined most probable path $x_c(t)$, in the Lagrangian function of Eq. (5.22), a single point of the system response PDF is given through Eq. (5.26). In this regard, if an effective domain of values for the system joint response PDF is considered (i.e. $x_{u,f} \in \left[x_{f,min}, x_{f,max}\right]$ and $\dot{x}_{q,f} \in \left[\dot{x}_{f,min}, \dot{x}_{f,max}\right]$), discretized so that

$$x_{u,f} = x_{f,min} + (u-1)\Delta x_f, \quad (u = 1,\ldots,s) \tag{5.28}$$

with

$$\Delta x_f = \left(x_{f,max} - x_{f,min}\right)/(s-1) \tag{5.29}$$

and

$$\dot{x}_{q,f} = \dot{x}_{f,min} + (q-1)\Delta \dot{x}_f, \quad (q = 1,\ldots,r) \tag{5.30}$$

with $\Delta \dot{x}_f = \left(\dot{x}_{f,max} - \dot{x}_{f,min}\right)/(r-1)$, the system response joint PDF at time instant t_f can be determined by solving the boundary value problem of Eq. (5.24) for each and every combination of $x_{u,f}$ and $\dot{x}_{q,f}$ ($s \times r$ times in total).

In Fig. 5.1 a schematic representation of the WPI procedure is outlined. Obviously, in the general case where no analytical solution exists for the system of ordinary differential equations (Eqs. (5.24-5.25)) the determination of the system response PDF can be computationally demanding. Nevertheless, to obtain reliable response PDF estimates for instance via a Monte Carlo Simulation (MCS), especially in the tails of the PDF where samples occur with low probability, the number *N* of excitation realizations to be produced and of subsequent numerical

integrations of Eq. (5.19) must be large $\left(N \approx 10^6\right)$. Further, the values of *s* and *r* can be reduced substantially if a priori knowledge related to the PDF shape characteristics is available (e.g. for an adequately smooth PDF shape).

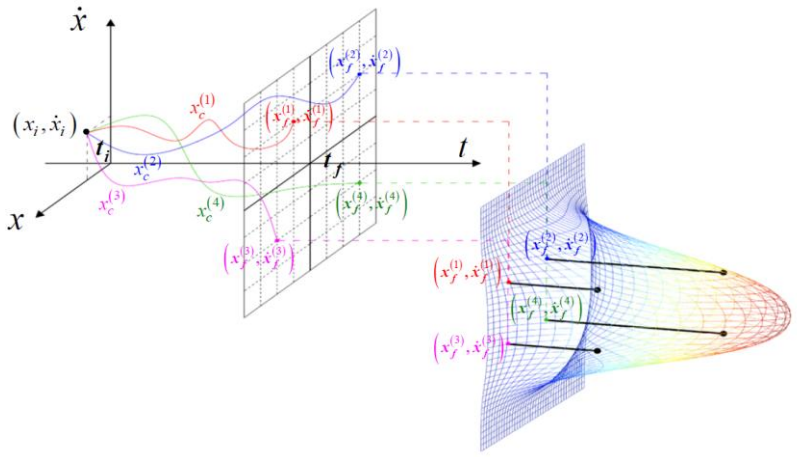

Fig. 5.1 - Schematic representation of the WPI procedure.

5.2.5.1 Duffing nonlinear system

As far as the numerical examples are concerned, firstly the case of a Duffing nonlinear oscillator is considered. The associated equation of motion is

$$\ddot{x} + \beta\dot{x} + k_0 x + \varepsilon x^3 = w(t) \tag{5.31}$$

where ε represents the magnitude of the nonlinearity. Considering Eq. (5.22) the Lagrangian associated to Eq. (5.31) becomes

$$\mathscr{L}\left(x, \dot{x}, \ddot{x}\right) = \frac{1}{2}\frac{\left(\ddot{x} + \beta\dot{x} + k_0 x + \varepsilon x^3\right)^2}{2\pi S_0} \tag{5.32}$$

whereas Eq. (5.24) yields the corresponding E-L as

$$\frac{d^4 x_c}{dt^4} + \left(2k_0 + 6\varepsilon x_c^2 - \beta^2\right)\ddot{x}_c + \left(6\varepsilon \dot{x}_c^2 + k_0^2\right)x_c + 3\varepsilon^2 x_c^5 + 4k_0 \varepsilon x_c^3 = 0 \tag{5.33}$$

along with the four boundary conditions.

To assess the reliability of the proposed technique, comparisons are made between the response PDF determined by the described WPI technique and the exact stationary PDF, which is know in closed form for the Duffing nonlinear oscillator in Eq. (5.31) as (e.g., Lin (1967))

$$p_{st}\left(x, \dot{x}\right) = \tilde{C} \exp\left[-\frac{\beta}{\pi S_0}\left(\frac{k_0 x^2}{2} + \frac{\varepsilon x^4}{4} + \frac{\dot{x}^2}{2}\right)\right] \tag{5.34}$$

where $\tilde{C}$ is a constant to be determined applying the normalization condition. In Fig. 5.2 the exact steady-state PDF is compared with the solution of the WPI considering $\left(s = r = 100\right)$. Comparison demonstrates a satisfactory level of accuracy.

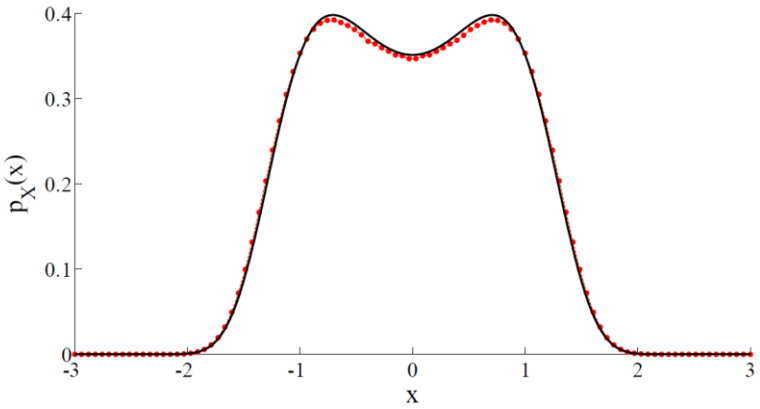

Fig. 5.2 - Marginal displacement response PDF for the Duffing oscillator with $\beta = 1, k_0 = -0.5, \varepsilon = 1, S_0 = 1/2\pi$ at *t=6s*: black solid line - exact steady state solution; red dot line - WPI solution.

5.3 Proposed efficient WPI for nonlinear MDOF systems

In previous Section 5.2 the WPI technique has been introduced and derived for the case of a nonlinear SDOF system. Numerical examples in Section 5.2.5 have shown the reliability and accuracy of the procedure, even for highly nonlinear systems.

Here, in Section 5.3.1, the WPI technique is further extended to deal with nonlinear MDOF systems, as more clearly detailed in Kougioumtzoglou and Spanos (2014). As shown, in this case the derived procedure can be computationally demanding. For this reason, in Section 5.3.2, a novel efficient WPI technique for the response determination of nonlinear MDOF systems will be proposed. In Section 5.3.3, numerical examples will show the accuracy and enhanced efficiency of the proposed procedure.

5.3.1 Numerical implementation for MDOF systems and computational cost

As far as the stochastic response determination of nonlinear MDOF systems is concerned, the WPI technique outlined in previous Section 5.2 can be further generalized for the case of MDOF systems. To this aim, consider a *m*-degree-of-freedom (*m*-DOF) nonlinear system

$$\mathbf{M}\ddot{\mathbf{x}}+\mathbf{C}\dot{\mathbf{x}}+\mathbf{K}\mathbf{x}+\mathbf{g}\left(\mathbf{x},\dot{\mathbf{x}}\right)=\mathbf{f}\left(t\right) \tag{5.35}$$

where $\mathbf{x}$ is a $m\times 1$ displacement vector $\mathbf{x}^T=\left[x_1\ldots x_m\right]$, $\mathbf{M}$, $\mathbf{C}$ and $\mathbf{K}$ denote the $m\times m$ mass, damping and stiffness matrices, respectively, and $\mathbf{g}\left(\mathbf{x},\dot{\mathbf{x}}\right)$ is an arbitrary nonlinear vector function. Further, $\mathbf{f}\left(t\right)$ is a white noise stochastic excitation vector process possessing a power spectrum matrix $\mathbf{S_f}$ of the form

$$\mathbf{S_f}=\begin{bmatrix} S_0 & \cdots & 0 \\ \vdots & \ddots & \vdots \\ 0 & \cdots & S_0 \end{bmatrix} \tag{5.36}$$

In a similar manner as in Eq. (5.22) the Lagrangian for the MDOF system of Eq. (5.35) becomes

$$\mathscr{L}\left(\mathbf{x},\dot{\mathbf{x}},\ddot{\mathbf{x}}\right)=\frac{1}{2}\left(\mathbf{M}\ddot{\mathbf{x}}+\mathbf{C}\dot{\mathbf{x}}+\mathbf{K}\mathbf{x}+\mathbf{g}\left(\mathbf{x},\dot{\mathbf{x}}\right)\right)^{\mathbf{T}}\mathbf{B}^{\mathbf{-1}}\left(\mathbf{M}\ddot{\mathbf{x}}+\mathbf{C}\dot{\mathbf{x}}+\mathbf{K}\mathbf{x}+\mathbf{g}\left(\mathbf{x},\dot{\mathbf{x}}\right)\right) \tag{5.37}$$

where

$$\mathbf{B}=\begin{bmatrix} 2\pi S_0 & \cdots & 0 \\ \vdots & \ddots & \vdots \\ 0 & \cdots & 2\pi S_0 \end{bmatrix} \tag{5.38}$$

Next, the variational principle of Eq. (5.23) becomes

$$\delta\int_{t_i}^{t_f}\mathscr{L}\left(\mathbf{x}_c,\dot{\mathbf{x}}_c,\ddot{\mathbf{x}}_c\right)dt=0 \tag{5.39}$$

which yields the system of E-L equations

$$\begin{aligned}
&\frac{\partial \mathscr{L}}{\partial x_{c,1}} - \frac{\partial}{\partial t}\frac{\partial \mathscr{L}}{\partial \dot{x}_{c,1}} + \frac{\partial^2}{\partial t^2}\frac{\partial \mathscr{L}}{\partial \ddot{x}_{c,1}} = 0 \\
&\qquad\vdots \\
&\frac{\partial \mathscr{L}}{\partial x_{c,m}} - \frac{\partial}{\partial t}\frac{\partial \mathscr{L}}{\partial \dot{x}_{c,m}} + \frac{\partial^2}{\partial t^2}\frac{\partial \mathscr{L}}{\partial \ddot{x}_{c,m}} = 0
\end{aligned} \tag{5.40}$$

together with the $4\times m$ boundary conditions

$$\begin{aligned}
&x_{c,1}(t_i) = x_{1,i},\ \dot{x}_{c,1}(t_i) = \dot{x}_{1,i},\ x_{c,1}(t_f) = x_{1,f},\ \dot{x}_{c,1}(t_f) = \dot{x}_{1,f} \\
&\qquad\vdots \\
&x_{c,m}(t_i) = x_{m,i},\ \dot{x}_{c,m}(t_i) = \dot{x}_{m,i},\ x_{c,m}(t_f) = x_{m,f},\ \dot{x}_{c,m}(t_f) = \dot{x}_{m,f}
\end{aligned} \tag{5.41}$$

Next, solving Eqs. (5.40-5.41) yields the transition PDF $p(\mathbf{x}_f, \dot{\mathbf{x}}_f, t_f \,|\, \mathbf{x}_i, \dot{\mathbf{x}}_i, t_i)$ in the form

$$p(\mathbf{x}_f, \dot{\mathbf{x}}_f, t_f \,|\, \mathbf{x}_i, \dot{\mathbf{x}}_i, t_i) = \varphi(t_f - t_i)\exp\left[-\int_{t_i}^{t_f} \mathscr{L}(\mathbf{x}_c, \dot{\mathbf{x}}_c, \ddot{\mathbf{x}}_c)\,dt\right] \tag{5.42}$$

where $\mathbf{x}_c^T = \left[x_{c,1} \ldots x_{c,m}\right]$ represents the most probable trajectory (m-dimensional). Note that for fixed time points t_i and t_f the function $\varphi(t_f - t_i)$ can be determined by appropriate normalization of the form

$$\int_{-\infty}^{\infty} \ldots \int_{-\infty}^{\infty} p(\mathbf{x}_f, \dot{\mathbf{x}}_f, t_f \,|\, \mathbf{x}_i, \dot{\mathbf{x}}_i, t_i)\, dx_{1,f}\, d\dot{x}_{1,f} \ldots dx_{m,f}\, d\dot{x}_{m,f} = 1 \tag{5.43}$$

It is worth pointing out that for linear systems, i.e. $\mathbf{g}(\mathbf{x}, \dot{\mathbf{x}}) = 0$, the boundary value problem (BVP) of Eqs. (5.40-5.41) can be solved analytically yielding an explicit closed-form expression for the most

probable path $\mathbf{x}_c$. In this regard, substituting $\mathbf{x}_c$ into Eq. (5.42) the transition PDF becomes a multi-dimensional Gaussian PDF of the form

$$p_{G_{lin}}\left(\mathbf{y}_f, t_f \,|\, \mathbf{y}_i, t_i\right) = \frac{(2\pi)^{-m}}{\sqrt{|\mathbf{S}_{lin}|}} \exp\left(-\frac{1}{2}\left(\mathbf{y}_f - \boldsymbol{\mu}_{y,lin}\right)^T \mathbf{S}_{lin}^{-1}\left(\mathbf{y}_f - \boldsymbol{\mu}_{y,lin}\right)\right) \quad (5.44)$$

where $\mathbf{y}_f$ denotes the state space vector

$$\mathbf{y}_f = (x_{1,f}\, \dot{x}_{1,f} \ldots x_{m,f}\, \dot{x}_{m,f})^T \quad (5.45)$$

and $\mathbf{S}_{lin}$ and $\boldsymbol{\mu}_{y,lin}$ are the covariance matrix and the mean response vector for the state space vector, respectively.
Clearly, for $\mathbf{y}_i = 0$ yields $\boldsymbol{\mu}_{y,lin} = 0$.

Unfortunately, for the case of nonlinear systems, i.e. $\mathbf{g}(\mathbf{x}, \dot{\mathbf{x}}) \neq 0$, the BVP of Eqs. (5.40-5.41) cannot, in general, be solved analytically; thus, a numerical solution technique needs to be implemented. In this regard, for a given time instant t_f and a given vector value $\left(\mathbf{x}_f, \dot{\mathbf{x}}_f\right)$ numerical solution of Eqs. (5.40-5.41) yields a single point of the response PDF via Eq. (5.42).

As shown in Section 5.2.5, ordinarily an effective domain of values is assumed for the response PDF $p\left(\mathbf{x}_f, \dot{\mathbf{x}}_f, t_f \,|\, \mathbf{x}_i, \dot{\mathbf{x}}_i, t_i\right)$; that is, for the *j*-th components $x_{j,f}$ of $\mathbf{x}_f$ and $\dot{x}_{j,f}$ of $\dot{\mathbf{x}}_f$ it is assumed that $x_{j,f}^{(k)} \in \left[x_{j,f}^{(\min)}, x_{j,f}^{(\max)}\right]$, $x_{j,f}^{(k)} = x_{j,f}^{(\min)} + (k-1)\Delta x_{j,f}, (k = 1, \ldots, n)$ with $\Delta x_{j,f} = \left(x_{j,f}^{(\max)} - x_{j,f}^{(\min)}\right) \Big/ (n-1)$ and $\dot{x}_{j,f}^{(k)} \in \left[\dot{x}_{j,f}^{(\min)}, \dot{x}_{j,f}^{(\max)}\right]$,

$\dot{x}_{j,f}^{(k)} = \dot{x}_{j,f}^{(\min)} + (k-1)\Delta\dot{x}_{j,f}$, $(k=1,\ldots,n)$ with $\Delta\dot{x}_{j,f} = \left(\dot{x}_{j,f}^{(\max)} - \dot{x}_{j,f}^{(\min)}\right) \Big/ (n-1)$, respectively. It can be readily seen that in the general case where no analytical solution exists for the system of ordinary differential equations (Eqs. (5.40-5.41)) the determination of the system response PDF can be computationally demanding. Specifically, for an *m*-DOF system the number of BVPs of the form of Eqs. (5.40-5.41) to be solved is n^{2m}. Note that based on numerical examples a value of $n=30$ has been deemed adequate for determining the system response PDF with reasonable accuracy in most cases. Clearly, this value is indicative as well as problem dependent. For instance, a higher value of n is expected to be used for highly non-smooth/non-Gaussian system response PDFs.

Overall, for low-dimensional problems the proposed technique can be significantly more efficient than MCS. For instance, for the case of SDOF systems, and utilizing the value $n=30$ the related computational cost corresponds to the numerical solution of $n^2=900$ BVPs of the form of Eqs. (5.24-5.25). Alternatively, to obtain reliable response PDF estimates via MCS, especially in the tails of the PDF where samples occur with low probability, the number N of excitation realizations to be produced and of subsequent numerical integrations of Eq. (5.35) needs to be quite large $N \approx 10^6$. Further, the determination of the system response PDF at a specific time instant t_f via the WPI technique is accomplished without the need to advance the solution in short time steps as it is required by the existing alternative numerical path integral solution

schemes that rely on a discrete version of the Chapman-Kolmogorov equation. Thus, the computationally expensive multi-dimensional convolution integral that needs to be evaluated at every time step is circumvented.

5.3.2 Proposed efficient MDOF system response PDF determination

The standard implementation of WPI technique as discussed in Section 5.3.1 proves to be computationally cumbersome for MDOF systems. However, combining the WPI solution framework with appropriately chosen expansions for approximating the system response PDF can dramatically decrease the associated computational cost.

In general, the joint non-Gaussian transition PDF for the system of Eq.(5.35) can be approximated by

$$p_{NG}\left(\mathbf{y}_f, t_f \mid \mathbf{y}_i, t_i\right) = \sum_{j_1=0}^{\infty}\sum_{j_2=0}^{\infty}\cdots\sum_{j_{2m}=0}^{\infty} c_{j_1 j_2 \ldots j_{2m}} \frac{\partial^{j_T} p_{G,nonlin}\left(\mathbf{y}_f, t_f \mid \mathbf{y}_i, t_i\right)}{\partial y_{1,f}^{j_1} \partial y_{2,f}^{j_2} \ldots \partial y_{2m,f}^{j_{2m}}} \qquad (5.46)$$

where $j_T = j_1 + j_2 + \ldots + j_{2m}$. The function $p_{G,nonlin}\left(\mathbf{y}_f, t_f \mid \mathbf{y}_i, t_i\right)$ is a joint Gaussian distribution of the form of Eq. (5.44). The difference is that the covariance matrix and the mean response vector of $p_{G,nonlin}$ denoted as $\mathbf{S}_{nonlin}$ and $\boldsymbol{\mu}_{y,nonlin}$ respectively, correspond to the response state vector of the nonlinear system of Eq. (5.35). Further, Eq. (5.46) can take various specific forms depending on the expansion chosen, such as Gram-Charlier and Edgeworth expansions; see Beaman and Hedrick

(1981), Crandall (1985), Spanos and Donley (1991, 1992), Lee (1995), Muscolino et al. (1997), Ricciardi (2007) for some indicative references.

Nevertheless, ordinarily utilized expansions such as the Gram-Charlier and the Edgeworth ones can lead to unacceptable estimates of the PDF, since the positive-definite property of the PDF is not always guaranteed. Thus, to avoid negative PDF estimate values, the joint non-Gaussian transition PDF of the system in Eq. (5.35) can be approximated as

$$p_{NG}\left(\mathbf{y}_f, t_f \,|\, \mathbf{y}_i, t_i\right) = \exp\left[\mu_{\mathbf{y}_f}\left(\mathbf{y}_f, t_f\right)\right] \tag{5.47}$$

where $\mu_{\mathbf{y}_f}\left(\mathbf{y}_f, t_f\right)$ is a polynomial of degree *l* for the *2m* variables $\mathbf{y}_f$. In other words, the polynomial function $\mu_{\mathbf{y}_f}\left(\mathbf{y}_f, t_f\right)$ approximates the joint non-Gaussian log-PDF (e.g. Er 1998; Di Paola and Sofi 2002).

In this regard, the polynomial corresponding to the *m*-DOF system of Eq.(5.35) can be written in the compact form

$$\mu_{\mathbf{y}_f}\left(\mathbf{y}_f, t_f\right) = \sum_{k=0}^{l}\sum_{j_1=0}^{k}\sum_{j_2=0}^{k-j_1}\cdots\sum_{j_{2m}=0}^{k-\left(j_1+\cdots+j_{2m-1}\right)} c_{i_P}\left(t_f\right) x_{1,f}^{k-\sum_{i=1}^{2m-1} j_i}\dot{x}_{1,f}^{j_{2m-1}}\cdots x_{m,f}^{j_2}\dot{x}_{m,f}^{j_1} \tag{5.48}$$

where *l* is the chosen degree of the polynomial; and $c_{i_P}\left(t_f\right)$ denotes the unknown coefficients with $i_p = \left\{1,\ldots,N_p\right\}$, where N_p is the total number of unknown coefficients.

In particular, for an *l*-degree polynomial and *2m* state variables, N_p can be obtained as

$$N_P = \sum_{k=0}^{l} \binom{k+2m-1}{2m-1} = \frac{(2m+l)!}{l!2m!} \tag{5.49}$$

Note that the unknowns to be determined in the expansion of Eq.(5.48) are only the N_p coefficients $c_{i_P}\left(t_f\right)$. In the following, an efficient determination technique based on the "localization" properties of the WPI is developed.

Specifically, for a number $\tilde{N}$ of points corresponding to an effective domain of values of the response state vector $\mathbf{y}_f$ the BVP of Eqs. (5.40-5.41) is solved numerically; thus, $\tilde{N}$ points of the joint response PDF $p_{NG}\left(\mathbf{y}_f, t_f \,|\, \mathbf{y}_i, t_i\right)$ are determined via Eq. (5.42), considering $\varphi\left(t_f - t_i\right) = 1$. Next, utilizing Eqs. (5.47) and (5.48) a linear system of $\tilde{N}$ algebraic equations for the N_p unknown coefficients $c_{i_P}\left(t_f\right)$ can be formed; that is,

$$\mathbf{Ac} = \ln\left[\mathbf{b}\right] \tag{5.50}$$

where $\mathbf{c}$ is the $N_p \times 1$ vector of the unknowns $c_{i_P}\left(t_f\right)$; $\mathbf{b}$ is the $\tilde{N} \times 1$ vector of the joint response PDF $p_{NG}\left(\mathbf{y}_f, t_f \,|\, \mathbf{y}_i, t_i\right)$ values as determined by numerically solving Eqs. (5.40-5.42) for $\tilde{N}$ PDF domain points; and $\mathbf{A}$ is the $\tilde{N} \times N_p$ matrix of the PDF effective domain values $x_{1,f}^{k-\sum_{i=1}^{2m-1} j_i} \dot{x}_{1,f}^{j_{2m-1}} \cdots x_{m,f}^{j_2} \dot{x}_{m,f}^{j_1}$.

Clearly, if $\tilde{N} > N_p$ the linear system of algebraic equations of Eq.(5.50) is over-determined, whereas if $\tilde{N} = N_p$ the number of unknowns is equal to the number of available equations. Further, solving the linear system of Eq. (5.50) yields the N_p unknown coefficients $c_{i_p}\left(t_f\right)$ to be used in Eq. (5.47). Finally, applying the normalization condition as in Eq. (5.43) to the joint response PDF $p_{NG}\left(\mathbf{y}_f, t_f \,|\, \mathbf{y}_i, t_i\right)$ in Eq. (5.43), yields the joint non-Gaussian transition PDF for the system response of Eq. (5.35).

To emphasize the efficiency of the aforementioned implementation, consider the case of a 2-DOF system $\left(2m = 4\right)$ and a fourth-order polynomial $\left(l = 4\right)$. Note the degree of the polynomial is sufficient, in general, to approximate the non-Gaussian form the response PDF of a wide range of nonlinear systems of engineering interest. For this case, the total number of unknown coefficients is $N_p = 70$ which means that the number of BVPs to be solved is, at least, $\tilde{N} = N_p = 70$. In comparison with the standard implementation of the WPI where $n^{2m} = 810000$ BVPs need to be solved for a value of $n = 30$, the herein proposed technique appears thousands of times more efficient computationally than the standard implementation of the WPI technique.

More generally, for relatively greater values of the DOF of the system *m*, the proposed implementation yields $\tilde{N} = N_p \approx \left(2m\right)^l / l!$, which is a power law function of *m*. On the other hand the standard implementation

of the WPI yields n^{2m} BVPs to be solved, which is an exponential function of *m*. Since an exponential function diverges to infinity much faster than a power law function, the proposed implementation of the WPI is always more computationally efficient than its standard implementation, and the efficiency grows almost exponentially as the number of DOF *m* grow.

5.3.3 Numerical examples

In this section the reliability and efficacy of the proposed technique are demonstrated by various numerical examples. These include nonlinear systems with a bimodal response PDF as well as MDOF nonlinear systems of engineering interest. The initial conditions assumed are $\mathbf{x}_c(0)=\mathbf{x}_i=0$ and $\dot{\mathbf{x}}_c(0)=\dot{\mathbf{x}}_i=0$. The most probable path $\mathbf{x}_c$ is determined by numerically solving the BVP of Eq. (5.40) in conjunction with the boundary conditions Eq. (5.41). Specifically, following the procedure described in the previous Section 5.3.2, the N_p coefficients $c_{i_P}(t_f)$ are obtained by solving $\tilde{N}$ BVPs, whereas the joint non-Gaussian transition PDF for the system of Eq. (5.35) is determined through Eq. (5.47). Note that all the numerical results presented in this section have been obtained considering $\tilde{N}=N_p$.

Clearly, as highlighted in section 5.3.2 the proposed technique is hundreds orders of magnitude faster than both the standard WPI technique and the MCS, which requires solving Eq. (5.35) numerically

millions of time to derive a reliable response PDF estimate. Further, note that the value of N_p can be reduced substantially if a priori knowledge of the PDF shape characteristics is available (e.g., for an adequately smooth PDF shape). In fact, not all of the N_p terms of the polynomial expansion in Eq. (5.48) would be generally necessary to adequately estimate the system response PDF.

5.3.3.1 Duffing nonlinear SDOF system

Firstly, for sake of simplicity in order to show how to apply the proposed efficient WPI procedure, a SDOF Duffing nonlinear oscillator is considered.

$$\ddot{x}+\beta\dot{x}+k_0 x+\varepsilon x^3 = w(t) \tag{5.51}$$

where ε is a constant describing the magnitude of the nonlinearity. The associated Lagrangian function of Eq. (5.51) is already given in Eq.(5.29), whereas the corresponding E-L equation is given in Eq. (5.30).

Figure 5.3 shows plotted nonstationary marginal displacement response PDFs corresponding to various time instants. These have been obtained considering a fourth order polynomial in Eq. (5.48), and by integrating the corresponding joint PDF in Eq. (5.47) over the velocity domain. Note that for the fourth order polynomial $(l=4)$ of this SDOF system $(2m=2)$, the number of coefficients $c_{i_P}(t_f)$ in Eq.(5.48) is $(N_p=15)$; and thus, the polynomial can be written as

$$\mu_{x_f,\dot{x}_f}\left(x_f,\dot{x}_f,t_f\right)=c_1+c_2x_f+c_3\dot{x}_f+c_4x_f^2+c_5x_f\dot{x}_f+c_6\dot{x}_f^2+\cdots+c_{15}\dot{x}_f^4 \quad (5.52)$$

Comparisons with the exact marginal stationary response displacement PDF, obtained by integrating Eq. (5.32), and pertinent MCS results, demonstrating a high level of accuracy.

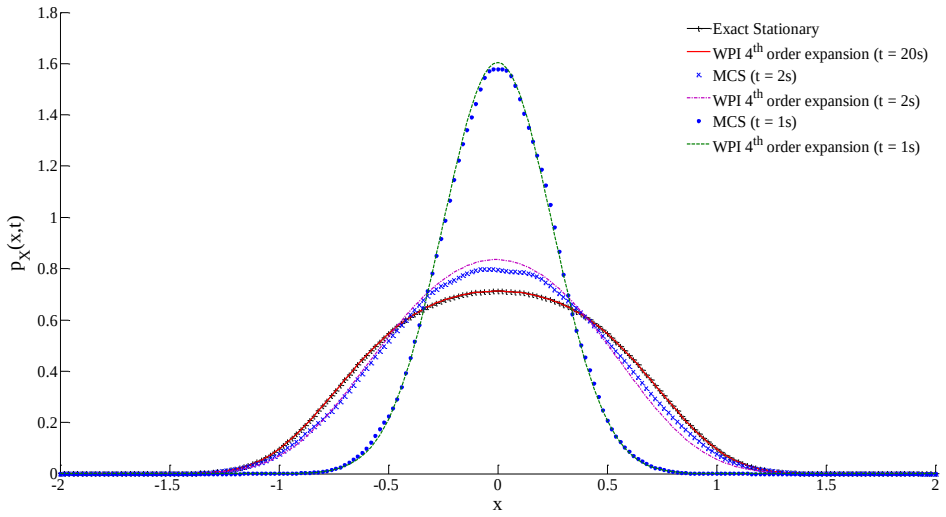

Fig. 5.3 - Marginal response displacement PDF $p(x,t)$ for the Duffing oscillator with $\beta=1, k_0=0.3,\ \varepsilon=1$ and $S_0=1/2\pi$ via the developed technique; comparison with MCS data (20000 samples) and exact marginal stationary distribution.

The reliability of developed approximate technique is further assessed by considering a Duffing bimodal oscillator, obtained by utilizing a negative term k_0. Figure 5.4 shows the plotted nonstationary marginal displacement response PDF, for various time instants. These have been obtained by considering a fourth order polynomial as in Eq. (5.52). Comparisons with pertinent Monte Carlo simulations demonstrate a

satisfactory level of accuracy obtained with the proposed approximate technique.

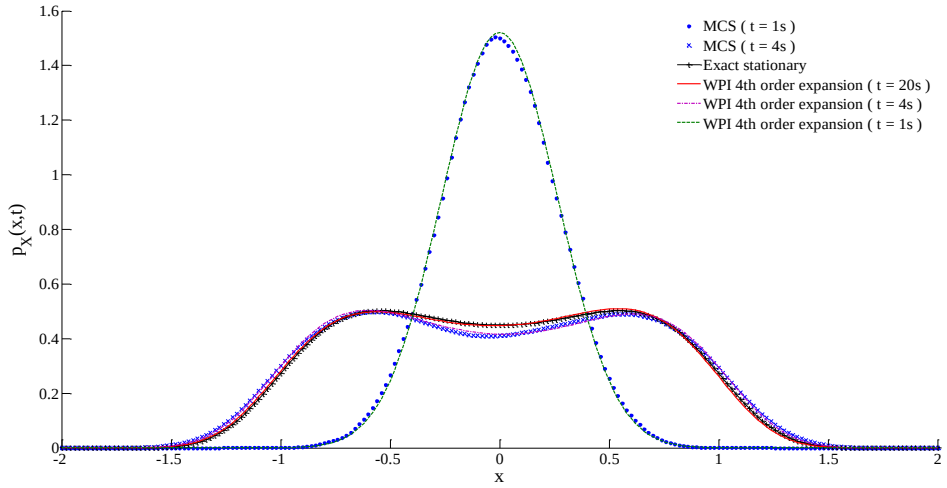

Fig. 5.4 - Marginal response displacement PDF $p(x,t)$ for the bimodal Duffing oscillator with $\beta=1, k_0=-0.3$, $\varepsilon=1$ and $S_0=1/2\pi$ via the developed technique; comparison with MCS data (40000 samples) and exact marginal stationary distribution.

5.3.3.2 MDOF nonlinear system

The case of a 2-DOF system endowed with a Duffing nonlinearity is considered next. By introducing the coordinate transformations

$$y_1 = x_1;\ y_2 = x_2 - x_1 \tag{5.53}$$

Eq. (5.35) becomes

$$\mathbf{M}\ddot{\mathbf{y}} + \mathbf{C}\dot{\mathbf{y}} + \mathbf{K}\mathbf{y} + \mathbf{g}(\mathbf{y}) = \mathbf{f}(t) \tag{5.54}$$

where

$$\mathbf{M}=\begin{bmatrix}1 & 0\\ 1 & 1\end{bmatrix} \tag{5.55}$$

$$\mathbf{C}=\begin{bmatrix}c & -c\\ 0 & c\end{bmatrix} \tag{5.56}$$

and

$$\mathbf{K}=\begin{bmatrix}k & -k\\ 0 & k\end{bmatrix} \tag{5.57}$$

Further the nonlinear vector $\mathbf{g}(\mathbf{y})$ of Eq. (5.54) takes the form

$$\mathbf{g}(\mathbf{y})=\begin{pmatrix}0\\ \varepsilon k\, y_2^3\end{pmatrix} \tag{5.58}$$

where ε is a constant defining the magnitude of the nonlinearity. The associated Lagrangian of Eq. (5.54) takes the form

$$\mathscr{L}(\mathbf{y},\dot{\mathbf{y}},\ddot{\mathbf{y}})=\frac{1}{2}\frac{\left(\ddot{y}_1+c\dot{y}_1+ky_1-ky_2-c\dot{y}_2\right)^2+\left(\ddot{y}_2+c\dot{y}_2+ky_2+\ddot{y}_1+\varepsilon k y_2^3\right)^2}{2\pi S_0} \tag{5.59}$$

Next, substituting Eq. (5.59) into Eq. (5.40) an manipulating yields

$$\begin{aligned}
&2\frac{d^4y_{1,c}}{dt^4}+\frac{d^4y_{2,c}}{dt^4}+\left(2k-c^2\right)\ddot{y}_{1,c}+k^2y_{1,c}\\
&+c^2\ddot{y}_{2,c}-k^2y_{2,c}+6k\varepsilon y_{2,c}\dot{y}_{2,c}^2+3k\varepsilon y_{2,c}^2\ddot{y}_{2,c}=0,\\
&\frac{d^4y_{2,c}}{dt^4}+\frac{d^4y_{1,c}}{dt^4}+\left(2k-2c^2\right)\ddot{y}_{2,c}+2k^2y_{2,c}+c^2\ddot{y}_{1,c}-k^2y_{1,c}\\
&+k^2\varepsilon y_{2,c}^2\left(4y_{2,c}+3\varepsilon y_{2,c}^3\right)+6k\varepsilon y_{2,c}\dot{y}_{2,c}^2+3k\varepsilon y_{2,c}^2\ddot{y}_{1,c}+6k\varepsilon y_{2,c}^2\ddot{y}_{2,c}=0
\end{aligned} \tag{5.60}$$

together with the 4×2 boundary conditions

$$\begin{aligned} &x_{c,1}(t_i)=x_{1,i},\dot{x}_{c,1}(t_i)=\dot{x}_{1,i},x_{c,1}(t_f)=x_{1,f},\dot{x}_{c,1}(t_f)=\dot{x}_{1,f},\\ &x_{c,2}(t_i)=x_{2,i},\dot{x}_{c,2}(t_i)=\dot{x}_{2,i},x_{c,2}(t_f)=x_{2,f},\dot{x}_{c,2}(t_f)=\dot{x}_{2,f}. \end{aligned} \tag{5.61}$$

To assess the reliability of the technique, comparisons are made between the nonstationary response displacement PDFs of the nonlinear 2-DOF system $(k=1,c=0.1,S_0=1/2\pi,\varepsilon=0.1)$ determined by the WPI technique together with a fourth order expansion of the polynomial in Eq.(5.48), and data obtained via MCS (30000 samples). Specifically, for a fourth order polynomial $(l=4)$ corresponding to this 2-DOF system $(2m=4)$, the number of coefficients $c_{i_p}(t_f)$ in Eq.(5.48) is $(N_p=70)$. Thus, only 70 BVPs of the form of Eq. (5.40) are numerically solved for determining the N_p coefficients through Eq. (5.50). Note that in Kougioumtzoglou and Spanos (2014), where the same example was considered, 15^4 BVPs were solved to obtain the PDFs of the response processes via the ordinarily used implementation of the WPI technique. Figures 5.5 and 5.6 show the plotted nonstationary marginal response displacement PDFs $p(y_1,t)$ and $p(y_2,t)$, respectively. As shown in these figures, comparisons with MCS data demonstrate a satisfactory degree of accuracy for the determined response PDFs.

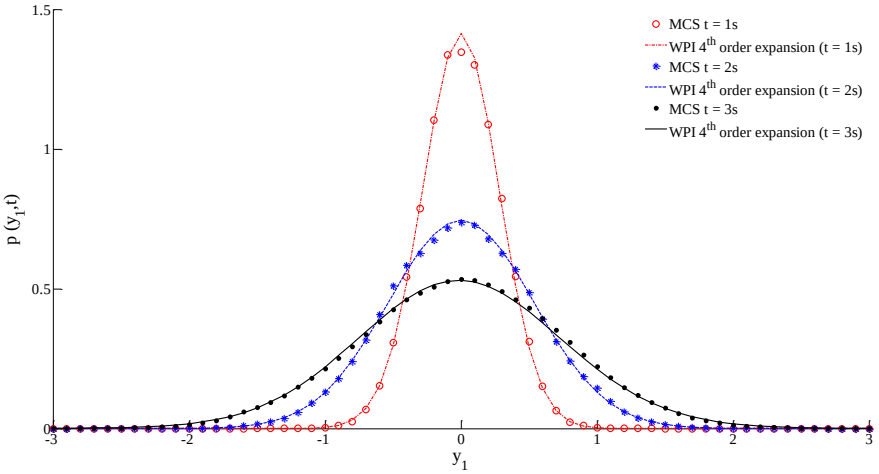

Fig. 5.5 - Marginal response displacement PDF $p(y_1,t)$ for 2-DOF nonlinear building structure with $k=1, c=0.1,\ \varepsilon=0.1$ and $S_0=1/2\pi$ via the developed technique; comparison with MCS data (30000 samples).

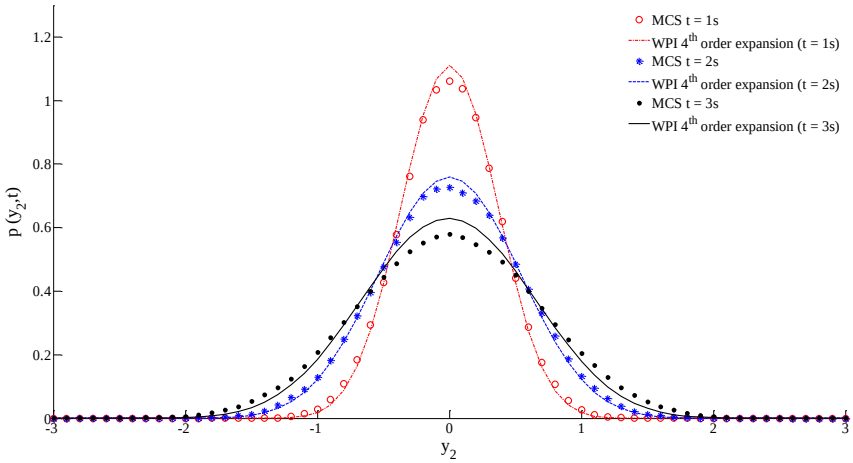

Fig. 5.6 - Marginal response displacement PDF $p(y_2,t)$ for 2-DOF nonlinear building structure with $k=1, c=0.1,\ \varepsilon=0.1$ and $S_0=1/2\pi$ via the developed technique; comparison with MCS data (30000 samples).

5.4 Extension of the WPI for nonlinear systems endowed with fractional derivative elements

The WPI technique, introduced in Section 5.2 and extended to the case of MDOF systems in Section 5.3, proved to be an interesting tool which allowed for an efficient determination of the nonstationary response PDF of nonlinear systems under Gaussian white noise.

As demonstrated in previous Chapter 4, the motion of a TLCD device and TLCD controlled structures can be accurately described through linear differential equations of fractional order, as in Eqs. (4.8) and (4.15). Obviously applications of fractional derivatives in structural and mechanical engineering are not limited only to the case of TLCD systems. On the contrary, fractional calculus has been successfully applied in diverse fields such as viscoelasticity and rheology, control theory, bioengineering, image and signal processing, random walk models (Sabatier et al. (2007) and Hilfer (2000)) and vibration control or seismic isolation (Makris and Constantinou (1991, 1992) and Koh and Kelly (1990)).

Clearly, due to uncertainties for instance related to input forcing functions, analysis of systems with fractional derivative terms under stochastic excitations represent an interesting open topic.

In this context, existing approaches for the stochastic response evaluation of linear and nonlinear oscillators endowed with fractional derivative elements resort either to stochastic averaging (Huang and Jin

(2009), Chen and Zhu (2011)) or to statistical linearization (Spanos and Evaangelatos, 2010) or to a simplification of the original SDOF system by an increase of the system dimension (Di Paola et al. (2012), Failla and Pirrotta (2012)). These techniques exhibit various degrees of approximation or limitations, due to the characteristics of the fractional operators and the complex nonlinear behavior observed in many systems which renders such a stochastic analysis a persistent challenge. Thus, there is still a need for an efficient and accurate procedure for the stochastic response determination of these systems.

Considering the advantages introduced with the WPI, it can be of interest to extend this technique also for systems with fractional derivative elements.

In this regard, in Sections 5.4.1 and 5.4.2 the WPI technique will be further generalized to treat linear and nonlinear systems endowed with fractional derivatives terms subjected to stochastic excitation. Further, numerical applications will show that the herein developed WPI technique may offer a desirable alternative for determining the non-stationary response PDF of linear and nonlinear oscillators efficiently and with a satisfactory degree of accuracy.

5.4.1 Problem formulation

In the following the analytical WPI based technique, described in Section 5.2.4 (see also Kougioumtzoglou and Spanos (2014)) is extended and generalized to account for linear and nonlinear SDOF systems endowed with fractional derivatives elements. In this regard, consider a nonlinear oscillator whose motion is governed by the differential equation

$$\ddot{x}(t)+C_{\beta}\left({}_{t_i}^{C}D_t^{\beta}x\right)(t)+\omega_0^2x(t)+f\left(x(t),{}_{t_i}^{C}D_t^{\beta}x(t)\right)=w(t) \tag{5.62}$$

where a dot over a variable denotes differentiation with respect to time; $\left({}_{t_i}^{C}D_t^{\beta}x\right)(t)$ is a force governed by a β-order left Caputo fractional derivative defined as (Podlubny (1999))

$${}_{t_i}^{C}D_t^{\beta}x(t)=\frac{1}{\Gamma(n-\beta)}\int_{t_i}^{t}(t-\tau)^{n-\beta-1}\frac{d^n}{d\tau^n}x(\tau)d\tau,\ \ n-1<\beta<n \tag{5.63}$$

ω_0 is the natural frequency; C_{β} is a constant which can be viewed as a damping coefficient if $\beta=1$, or as a stiffness coefficient if $\beta=0$; $f\left(x(t),{}_{t_i}^{C}D_t^{\beta}x(t)\right)$ represents a non-linear function depending on the instantaneous values of $x(t)$ and $\left({}_{t_i}^{C}D_t^{\beta}x\right)(t)$; and $w(t)$ is a zero mean Gaussian white noise process of power spectral density S_0. Note that Eq.(5.62) reduces to the equation of motion of a conventional (non-fractional) nonlinear oscillator (Kougioumtzoglou and Spanos (2014)) when β approaches one.

In order to apply the WPI to this kind of systems, following the approach proposed in Kougioumtzoglou and Spanos (2014), Eq. (5.62) is substituted into Eq. (5.21) and the probability density functional $W\left[w(t)\right]$ for $w(t)$ is interpreted as the probability density functional $W\left[x(t)\right]$ for $x(t)$. This yields

$$W\left[x(t)\right]=\bar{C}\exp\left[-\int_{t_i}^{t_f}\frac{1}{2}\frac{\left(\ddot{x}+C_\beta\left({}_{t_i}^{C}D_t^\beta x\right)+\omega_0^2 x+f\left(x,{}_{t_i}^{C}D_t^\beta x\right)\right)^2}{2\pi S_0}dt\right] \tag{5.64}$$

Next, resorting to the Lagrangian formulation for the most probable path introduced in Section 5.2.3, for the oscillator of Eq. (5.62), the corresponding Lagrangian function can be defined as

$$\mathscr{L}\left(x,{}_{t_i}^{C}D_t^\beta x,\ddot{x}\right)=\frac{1}{2}\frac{\left(\ddot{x}+C_\beta\left({}_{t_i}^{C}D_t^\beta x\right)+\omega_0^2 x+f\left(x,{}_{t_i}^{C}D_t^\beta x\right)\right)^2}{2\pi S_0} \tag{5.65}$$

Adopting next the variational formulation followed in Kougioumtzoglou and Spanos (2014) the largest contribution to the Wiener path integral comes from the trajectory for which the integral in the exponential becomes as small as possible. Variational calculus rules (Ewing (1985)) dictate that this trajectory with fixed end points satisfies the extremality condition

$$\delta\int_{t_i}^{t_f}\mathscr{L}\left(x_c,{}_{t_i}^{C}D_t^\beta x_c,\ddot{x}_c\right)dt=0 \tag{5.66}$$

where $x_c(t)$ denotes the most probable trajectory. In the ensuing analysis, the variational problem defined in Eq. (5.66) is coined fractional

variational problem (FVP), since Eq. (5.66) contains a β-order left Caputo fractional derivative. This yields a corresponding Euler-Lagrange (E-L) equation of the form

$$\frac{\partial \mathscr{L}}{\partial x_c} + {}_t D_{t_f}^{\beta} \frac{\partial \mathscr{L}}{\partial {}_0^C D_t^{\beta} x_c} + \frac{\partial^2}{\partial t^2} \frac{\partial \mathscr{L}}{\partial \ddot{x}_c} = 0 \tag{5.67}$$

with the four boundary condition $x_c(t_i) = 0, \dot{x}_c(t_i) = 0$, $x_c(t_f) = x_f, \dot{x}_c(t_f) = \dot{x}_f$. Note that although Eq. (5.62) contains Caputo fractional derivatives only, the fractional E-L Eq. (5.67) contains right Riemann-Liouville fractional derivatives of the form

$${}_t D_{t_f}^{\beta} f(t) = \frac{1}{\Gamma(n-\beta)} \frac{d^n}{dt^n} \int_t^{t_f} (t-\tau)^{n-\beta-1} f(\tau) d\tau, \quad n-1 < \beta < n, \tag{5.68}$$

as well (see Appendix C for details). Further, solution of the fractional Euler-Lagrange Eq. (5.67) yields a closed form expression for the transition PDF $p(x_f, \dot{x}_f, t_f \mid x_i, \dot{x}_i, t_i)$; that is,

$$p(x_f, \dot{x}_f, t_f \mid x_i, \dot{x}_i, t_i) = \varphi(t_f - t_i) exp\left[-\int_{t_i}^{t_f} \mathscr{L}\left(x_c, {}_{t_i}^C D_t^{\beta} x_c, \ddot{x}_c\right) dt \right] \tag{5.69}$$

Note that for fixed time points t_i and t_f the function $\varphi(t_f - t_i)$ can be determined by merely applying the normalization condition

$$\int_{-\infty}^{\infty} \int_{-\infty}^{\infty} p(x_f, \dot{x}_f, t_f \mid x_i, \dot{x}_i, t_i) dx_f \, d\dot{x}_f = 1 \tag{5.70}$$

5.4.2 The fractional variational problem (FVP)

It is worth stressing that the FVP of Eq. (5.66) is a special case of the following general class of FVPs which contain several functions $y_j(t)(j=1,\ldots,m)$, and positive fractional order derivatives $\alpha_k \in \mathbb{R}^+$; that is,

$$\begin{aligned} &Min(Max)\ J[y_1,\ldots,y_m] = \\ &= \int_{t_i}^{t_f} \mathcal{F}\left(t, y_1,\ldots,y_m, {}_{t_i}^{C}D_t^{\beta_1} y_1,\ldots, {}_{t_i}^{C}D_t^{\beta_1} y_m,\ldots, {}_{t_i}^{C}D_t^{\beta_n} y_1,\ldots, {}_{t_i}^{C}D_t^{\beta_n} y_m\right) dt \end{aligned} \tag{5.71}$$

$$\begin{aligned} &y_j(t_i) = y_{ji} \qquad y_j(t_f) = y_{jf}, \\ &\dot{y}_j(t_i) = \dot{y}_{ji} \qquad \dot{y}_j(t_f) = \dot{y}_{jf}, \\ &\vdots \\ &\frac{d^{n-1}y_j(t_i)}{dt^{n-1}} = \frac{d^{n-1}y_{ji}}{dt^{n-1}} \qquad \frac{d^{n-1}y_j(t_f)}{dt^{n-1}} = \frac{d^{n-1}y_{jf}}{dt^{n-1}} \end{aligned} \tag{5.72}$$

where $1 \le j \le m,\ k-1 \le \beta_k \le k,\ k = 1,\ldots,n \in \mathbb{Z}^+$ and the function $\mathcal{F}$ is continuously differentiable with respect to all its arguments. The involved fractional derivatives are defined in the Caputo sense with ${}_{t_i}^{C}D_t^{\beta_k} y(t) = \dfrac{d^k y(t)}{dt^k}$, if $\beta_k = k$.

According to a well-established result in calculus of variations (Agrawal (2002), Malinowska and Torres (2010)), the corresponding Euler-Lagrange equations for the above defined FVP of Eq. (5.72) are

$$\frac{\partial \mathcal{F}}{\partial y_j} + \sum_{k=1}^{n} {}_t D_{t_f}^{\beta_k} \frac{\partial \mathcal{F}}{\partial {}_{t_i}^{C} D_t^{\beta_k} y_j} = 0, \quad 1 \le j \le m \tag{5.73}$$

which should satisfy the boundary conditions of Eq. (5.72). Note that the right Riemann-Liouville fractional derivatives $\left({}_{t_i} D_t^{\beta_k} \right)$ appear in the fractional differential Eq. (5.73), even though they do not appear in the functional $J\left[y_1, \ldots, y_m \right]$. In Appendix C, a detailed derivation of the Euler-Lagrange Eq. (5.73) is presented. Also, note that if $\beta_k = k, \left(k = 1, \ldots, n \right)$, the terms ${}_{t_i}^{C} D_t^{\beta_k} y_j(t)$ are replaced with $\partial^k y_j / \partial t^k$ and the operators $\left({}_{t_i} D_t^{\beta_k} \right)$ are replaced with $(-1)^k \left(\partial^k / \partial t^k \right)$; thus, in this case Eq. (5.73) reduces to the standard Euler–Lagrange equations

$$\frac{\partial \mathcal{F}}{\partial y_j} + \sum_{k=1}^{n} (-1)^k \frac{\partial^k}{\partial t^k} \frac{\partial \mathcal{F}}{\partial y_j^{(k)}} = 0, \quad 1 \le j \le m \tag{5.74}$$

where $y_j^{(k)} = \dfrac{\partial^k y_j(t)}{\partial t^k}$. It follows that a necessary condition for $J\left[y_1, \ldots, y_m \right]$ to have an extremum for the given functions $y_j(t) \left(j = 1, \ldots, m \right)$ is that $y_j(t)$ satisfy the E-L equations (5.73) and the boundary conditions (5.72). The fact that Eq. (5.82) combines right Riemann-Liouville fractional derivatives with left Caputo fractional derivatives increases the difficulty of finding an exact solution. Thus, several numerical methods have been developed in the literature to address the FVP of Eq. (5.73). In the ensuing analysis a general direct solution approach (Ritz method) is utilized building on earlier work by

Lotfi and Yousefi (2013). Readers are referred to (Lofti and Yousefi, 2013) for further details regarding the convergence of the adopted technique.

5.4.2.1 General FVP solution technique

Obviously, the E-L Eq. (5.73) has its own theoretical and methodological, albeit somewhat cumbersome, merit. However, as shown in Lotfi and Yousefi (2013), it is possible to solve directly the FVP of Eq. (5.71) and (5.72) without resorting to the E-L Eq. (5.73) by making use of the shifted Legendre polynomials and the Hermite interpolating polynomials. Specifically, the Legendre polynomials are orthogonal polynomials in the interval $[-1,1]$, which can be defined by the well-known Rodrigues' formula

$$L_p(x)=\frac{1}{2^p\,p!}+\frac{d^p}{dx^p}\left[\left(x^2-1\right)^p\right],\quad p=1,2,\ldots \tag{5.75}$$

or, by utilizing the recurrence formula

$$L_{p+1}(x)=\frac{2p+1}{p+1}xL_p(x)-\frac{p}{p+1}L_{p-1}(x),\quad p=1,2,\ldots \tag{5.76}$$

where $L_0(x)=1, L_1(x)=x$ and $L_p(x)$ is the Legendre polynomial of order p.

Further, since the functional $J[y_1,\ldots,y_m]$ of Eq. (5.71) is defined in the interval $[t_i,t_f]$ together with the constraints of Eq. (5.72), approximate solutions of the FVP can be expressed as a combination of

shifted Legendre polynomials, orthogonal in the interval $\left[t_i, t_f\right]$, and Hermite interpolating polynomials which respect the boundary conditions of Eq. (5.72). In particular, considering the change of variable $x = \dfrac{2t - t_i - t_f}{t_f - t_i}$, the shifted Legendre polynomial $P_{p+1}(t)$ of order $p+1$, which is defined in the interval $\left[t_i, t_f\right]$, can be evaluated via the recurrence formula

$$P_{p+1}(t) = \frac{2p+1}{p+1}\left(\frac{2t - t_i - t_f}{t_f - t_i}\right)P_p(t) - \frac{p}{p+1}P_{p-1}(t), \quad p = 1, 2, \ldots \tag{5.77}$$

where $P_0(t) = 1$ and $P_1(t) = \dfrac{2t - t_i - t_f}{t_f - t_i}$. Furthermore, the coefficients a_k, $0 \le k \le n-1$, of the Hermite interpolating polynomial $H_j(t)$, $1 \le j \le m$, of the form

$$H_j(t) = \sum_{k=0}^{2n-1} a_k t^k \tag{5.78}$$

can be determined so that

$$\begin{aligned}
&H_j(t_i) = y_{ji} \qquad H_j(t_f) = y_{jf}, \\
&\dot{H}_j(t_i) = \dot{y}_{ji} \qquad \dot{H}_j(t_f) = \dot{y}_{jf}, \\
&\vdots \\
&\frac{d^{n-1}H_j(t_i)}{dt^{n-1}} = \frac{d^{n-1}y_{ji}}{dt^{n-1}} \qquad \frac{d^{n-1}H_j(t_f)}{dt^{n-1}} = \frac{d^{n-1}y_{jf}}{dt^{n-1}}
\end{aligned} \tag{5.79}$$

Finally, let $\tilde{y}_j(t)$ denote polynomials of the form

$$\tilde{y}_j(t) = \sum_{l=0}^{h-1} c_{l,j} (t-t_i)^n \left(t-t_f\right)^n P_l(t) + H_j(t) \tag{5.80}$$

where $P_l(t)$ is the shifted Legendre polynomial of order l orthogonal in the interval $\left[t_i, t_f\right]$, $H_j(t)$ is the Hermite interpolating polynomial, $h \in \mathbb{Z}^+$, $c_{l,j} \in \mathbb{R}$, $n \in \mathbb{Z}^+$, with $1 \le j \le m, -1 \le \beta_k \le k, (k = 1, \ldots, n)$.

In this regard, it is possible to determine an approximate solution $\tilde{y}_j(t), (j = 1, \ldots, m)$ of the FVP Eq. (5.71) and (5.72) by simply determining the coefficients $c_{l,j}$. Substituting next Eq. (5.80) into Eq.(5.71) yields

$$\begin{aligned} &J\left[c_{0,1}, \ldots, c_{h,1}, \ldots, c_{0,m}, \ldots, c_{h,m}\right] = \\ &= \int_{t_i}^{t_f} \mathcal{F}\left(t, \tilde{y}_1, \ldots, \tilde{y}_m, {}_{t_i}^{C}D_t^{\beta_1}\tilde{y}_1, \ldots, {}_{t_i}^{C}D_t^{\beta_1}\tilde{y}_m, \ldots, {}_{t_i}^{C}D_t^{\beta_n}\tilde{y}_1, \ldots, {}_{t_i}^{C}D_t^{\beta_n}\tilde{y}_m\right) dt \end{aligned} \tag{5.81}$$

Note that Eq. (5.81) is now a function of the unknowns $c_{l,j}$ $(l = 0, \ldots, h), (j = 1, \ldots, m)$. In this manner, the FVP of Eqs. (5.71) and (5.72) can be solved approximately by directly optimizing the function $J\left[c_{0,1}, \ldots, c_{h,1}, \ldots, c_{0,m}, \ldots, c_{h,m}\right]$ to determine the coefficients $c_{l,j}$. Specifically, according to differential calculus rules, a necessary condition for determining the minimum (or the maximum) of function $J[\bullet]$ is the existence of the system of equations

$$\frac{\partial J\left[c_{l,j}\right]}{\partial c_{l,j}} = 0, \quad l = 0, \ldots, h, \; j = 1, \ldots, m \tag{5.82}$$

The solution of Eq. (5.91) yields the values of the coefficients $c_{l,j}$; thus, the polynomials $\tilde{y}_j(t),(j=1,\ldots,m)$ which approximate the solution of the original FVP of Eq. (5.71) and (5.72) are determined.

Note that for the specific special case of Eq. (5.66) only one function of a single variable is involved; thus, it follows that $(j=m=1)$ and the approximate function of Eq. (5.81) degenerates to

$$J[c_0,\ldots,c_h]=\int_{t_i}^{t_f}\mathcal{F}\left(t,\tilde{y},{}_{t_i}^{C}D_t^{\beta_1}\tilde{y},\ldots,{}_{t_i}^{C}D_t^{\beta_n}\tilde{y}\right)dt \tag{5.83}$$

which is an algebraic function of the unknowns $c_l,(l=0,\ldots,h)$. The corresponding approximate polynomial solution Eq. (5.83) becomes

$$\tilde{y}(t)=\sum_{l=0}^{h-1}c_l\,(t-t_i)^n\left(t-t_f\right)^n P_l(t)+H(t) \tag{5.84}$$

where only one interpolating polynomial $H(t)$ has to be determined for every group of boundary value conditions considered. Based on the aforementioned developments, a simple scheme for the direct solution of the FVP of Eq. (5.66) takes the form:

Step 1. Find the value of the maximum order derivative and the corresponding maximum order integer derivative *n* in Eq.(5.65);

Step 2. For the considered *2n* boundary conditions, find the Hermite interpolating polynomial of degree *2n-1*;

Step 3. Choose a suitable number *h* of shifted Legendre polynomials for the approximating polynomial of Eq. (5.84);

Step 4. Solve the system of *h* algebraic equations (5.82) and find the *h* coefficients $c_l, (l = 0,\ldots,h-1)$;

Step 5. Substitute the computed coefficients c_l in Eq. (5.84) to determine the approximate polynomial solution $\tilde{y}(t)$ of the FVP of Eq. (5.66).

5.4.3 Numerical results

In this section, the versatility and the accuracy of the proposed technique is assessed via numerical examples. Specifically, the linear oscillator with fractional derivatives elements (System 1) and the Duffing nonlinear oscillator with fractional derivatives elements (System 2) are considered.

In the following, the initial time instant $(t_i = 0)$ is used, whereas zero initial conditions are assumed (initially at rest). To apply the developed WPI technique for the given boundary conditions $x_c(0) = 0, \dot{x}_c(0) = 0$ and $x_c(t_f) = x_f, \dot{x}_c(t_f) = \dot{x}_f$, the most probable path $x_c(t)$ is determined by solving the FVP of Eq. (5.66) according to the methodology developed in Section 5.4.2. In this regard, $x_c(t)$ is approximated by the polynomial $\tilde{y}(t)$ after solving the system of *h* algebraic equations Eq. (5.82) to determine the *h* coefficients

$c_l, (l=0,\ldots,h-1)$. Further, substituting the determined most probable path $x_c(t)=\tilde{y}(t)$, for a given final time instant t_f and given boundary conditions $\left(x_f, \dot{x}_f\right)$, in the Lagrangian function of Eq. (5.69), a single point of the system response PDF is given. In this regard, if an effective domain of values for the system joint response PDF is considered (i.e. $x_{u,f} \in \left[x_{f,\min}, x_{f,\max}\right]$ and $\dot{x}_{q,f} \in \left[\dot{x}_{f,\min}, \dot{x}_{f,\max}\right]$) discretized so that $x_{u,f} = x_{f,\min} + (u-1)\Delta x_f$, $(u=1,\ldots,s)$ with $\Delta x_f = \left(x_{f,\max} - x_{f,\min}\right)/(s-1)$ and $\dot{x}_{q,f} = \dot{x}_{f,\min} + (q-1)\Delta \dot{x}_f$, $(q=1,\ldots,r)$ with $\Delta \dot{x}_f = \left(\dot{x}_{f,\max} - \dot{x}_{f,\min}\right)/(r-1)$, the system response joint PDF at time instant t_f can be determined by solving the FVP of Eq.(5.66) for each and every combination of $x_{u,f}$ and $\dot{x}_{q,f}$ ($s \times r$ times in total). As far as the selection of the number *h* is concerned, it is noted that the value of this parameter strongly depends on the specific problem under consideration. In this regard, in general, a greater value of *h* might be required for determining the solution of the FVP for greater values of the final time instant t_f. Also, a greater value of *h* might be required when strong nonlinearities are considered in the kernel of the functional Eq. (5.83). Obviously, a greater value of *h* leads to enhanced accuracy, at the expense, however, of higher computational cost. Readers may refer to the following numerical examples for potential candidate values of the parameter *h*. Further, as a rule of thumb for choosing an appropriate value for the parameter *h*, steps 1-5 of previous Section 5.4.2.1 can be

performed for just one pair of values $x_{u,f}$ and $\dot{x}_{q,f}$ by utilizing various values for *h*. For an increasing value of the parameter *h*, a good indication that the specific value of *h* is a reasonable one is when no considerable difference is noted anymore in the form of the most probable path.

To further elucidate the mechanics of the technique, Fig. 5.7 provides a step-by-step flowchart for the method.

To demonstrate the accuracy of the developed technique, the WPI based determined response PDF for System 1 is compared with the corresponding Gaussian distribution, whereas the WPI based determined response PDF for System 2 is compared with the corresponding Monte Carlo simulation based estimated response PDF. Specifically, for the Monte Carlo simulations of System 2 the linear acceleration method (Failla and Pirrotta (2012)) is utilized to integrate numerically the nonlinear fractional differential equations of motion.

It is worth noting that one of the significant advantages of the developed technique is the determination of the system non-stationary response PDF at a time instant t_f without the need to evaluate the PDF at all the past time instants as it is required for the existing alternative numerical path integral solution schemes.

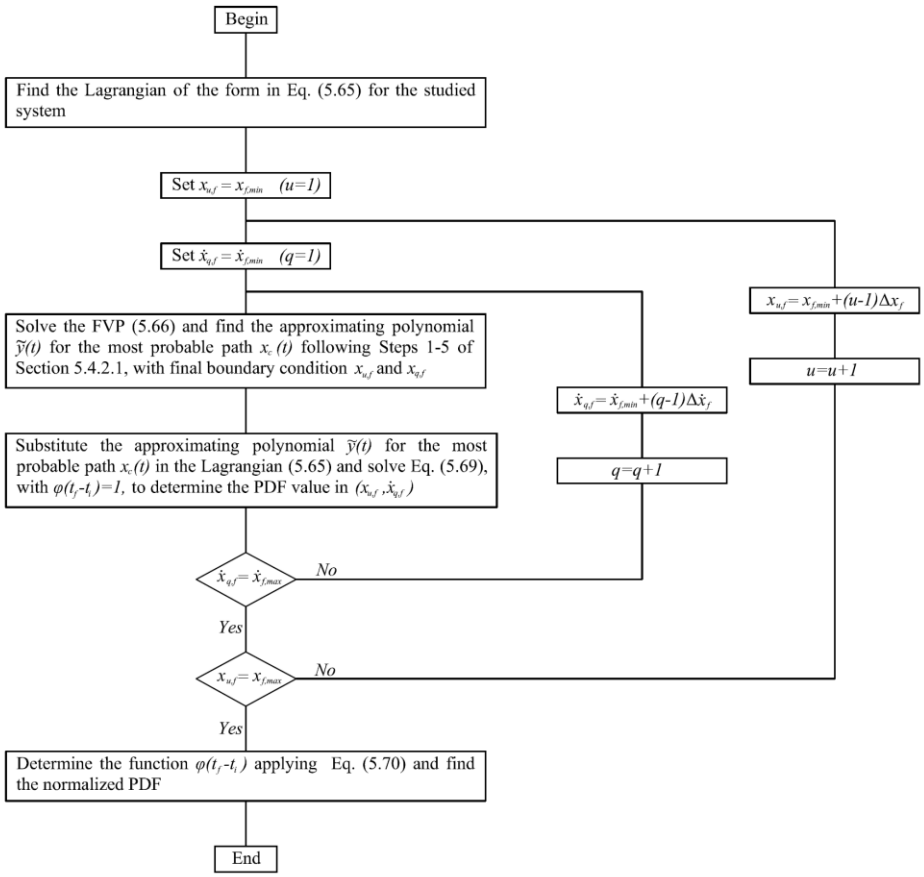

Fig. 5.7 - Flowchart of the algorithm.

5.4.3.1 The TLCD case: SDOF linear oscillator with fractional derivatives elements

Consider firstly a linear SDOF oscillator with fractional derivatives elements (System 1) whose motion is governed by the differential equation

$$\ddot{x} + C_\beta \left({}_0^C D_t^\beta x \right) + \omega_2^2 x = w(t) \tag{5.85}$$

Clearly, this may represent also the equation of motion of the TLCD device, given in Eq. (4.8), for the liquid displacement only.

According to the developed technique, substituting Eq. (5.854) into Eq.(5.20), the probability density functional $W\left[w(t)\right]$ for $w(t)$ is interpreted as the probability density functional $W\left[x(t)\right]$ for $x(t)$. This yields

$$W\left[x(t)\right] = \bar{C} \exp\left[-\int_{t_i}^{t_f} \frac{1}{2} \frac{\left(\ddot{x} + C_\beta \left({}_{t_i}^C D_t^\beta x \right) + \omega_2^2 x \right)^2}{2\pi S_0} dt \right] \tag{5.86}$$

Note that the associated Lagrangian function becomes

$$\mathscr{L}\left(x, {}_0^C D_t^\beta x, \ddot{x} \right) = \frac{1}{2} \frac{\left(\ddot{x} + C_\beta \left({}_0^C D_t^\beta x \right) + \omega_2^2 x \right)^2}{2\pi S_0} \tag{5.87}$$

whereas the corresponding E-L Eq. (5.67) takes the form

$$\frac{\partial \mathscr{L}}{\partial x} + {}_t D_{t_f}^\beta \frac{\partial \mathscr{L}}{\partial {}_0^C D_t^\beta x} + \frac{\partial^2}{\partial t^2} \frac{\partial \mathscr{L}}{\partial \ddot{x}} = 0 \tag{5.88}$$

In Eq. (5.88) ${}_{t}D_{t_f}^{\beta}$ denotes the β-order Riemann-Liouville right fractional derivative. Manipulating Eq. (5.887) yields

$$\begin{aligned}&\frac{d^4x_c}{dt^4}+2\omega_2^2\,\ddot{x}_c+C_\beta\,\omega_2^2\,{}_0^C D_t^\beta x_c+\omega_2^4\,x_c+C_\beta\,{}_0^C D_t^{\beta+2}x_c\\&+C_\beta\,\omega_2^2\,{}_tD_{t_f}^\beta x_c+C_\beta\,{}_tD_{t_f}^\beta\ddot{x}_c+C_\beta^2\,{}_tD_{t_f}^\beta\left({}_0^C D_t^\beta x_c\right)=0\end{aligned}\tag{5.89}$$

together with the corresponding boundary conditions $x_c(0)=0,\dot{x}_c(0)=0$ and $x_c(t_f)=x_f,\dot{x}_c(t_f)=\dot{x}_f$. This fourth order fractional differential equation Eq. (5.88) involves the right Riemann-Liouville operator with the left Caputo fractional derivative, with no obvious exact analytical solution. Thus, the FVP of Eq. (5.66) is solved directly without using Eq. (5.88), via the approach detailed in previous Section 5.4.2.1. In this regard, an effective domain of values for the joint response PDF $x_{u,f}\in[-0.5,0.5]$ and $\dot{x}_{q,f}\in[-3,3]$ is chosen. Further, the parameters values $\beta=0.41, C_\beta=3.59, \omega_2=10.81\frac{rad}{s}, S_0=\frac{1}{2\pi}$ have been considered (experimentally obtained in Chapter 4 for Configuration#2b), whereas $(h=7)$ Legendre polynomials orthogonal in the interval $[0,t_f]$ have been used in Eq. (5.84) for determining the approximate solution $\tilde{y}(t)$ of the most probable path $x_c(t)$.

In Fig. 5.8 solution of the FVP considering 5, 7 and 10 Legendre polynomials, for the boundary conditions $x_c(0)=0,\dot{x}_c(0)=0$ and $x_c(10)=-2.9,\dot{x}_c(10)=-3$, is plotted. It can be readily seen that the

solution of the boundary value problem considering 7 and 10 Legendre polynomials, respectively, is of similar satisfactory accuracy, whereas using 5 Legendre polynomials results in decreased accuracy and considerable deviation from the 7 and 10 Legendre polynomials cases. Further, the determined joint response PDF is plotted in Fig. 5.9.

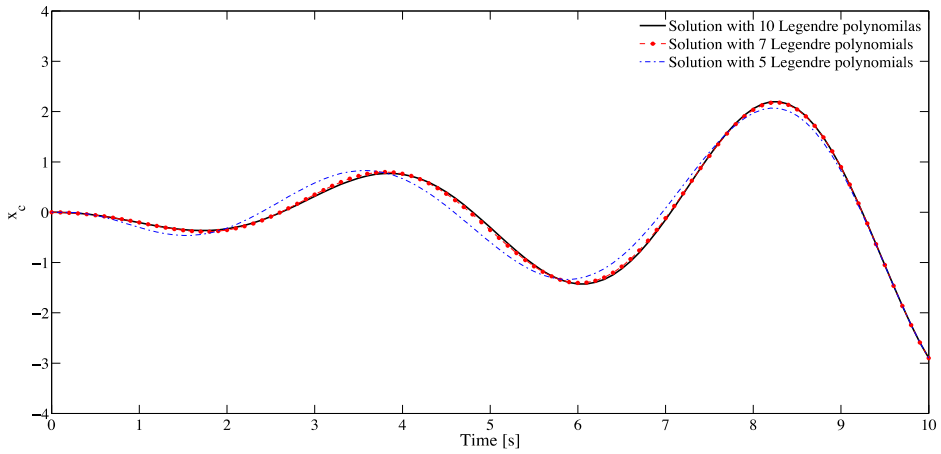

Fig. 5.8 - Comparison of the solution of the boundary value problem for $x_C(10) = -2.9, \dot{x}_C(10) = -3$.

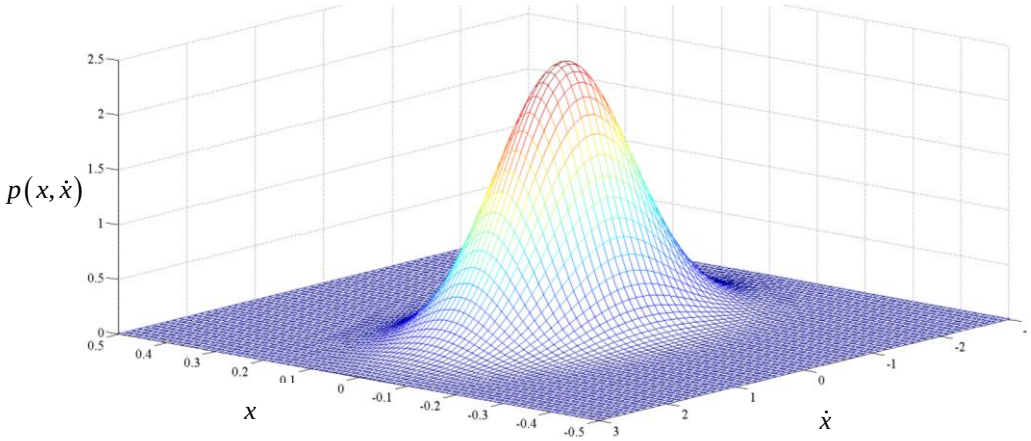

Fig. 5.9 - Response PDF in the given domain $x_{u,f} \in [-3,3]$ and $\dot{x}_{q,f} \in [-3,3]$.

Since System 1 is linear and subjected to a Gaussian process, the response is Gaussian too; thus, it is possible to compare the response PDF of the oscillator with the corresponding Gaussian distribution with the same variance. In this regard, the variance of the linear oscillator is determined by employing the following input-output spectral relationship in the frequency domain (Spanos and Evangelatos (2010))

$$\sigma_X^2 = \int_{-\infty}^{\infty} \frac{S_0}{\left| -\omega^2 + \omega_2^2 + C_\beta (i\omega)^\beta \right|^2} d\omega \tag{5.90}$$

In Fig. 5.10, the marginal stationary displacement response PDF, obtained by integrating the PDF over the velocity domain, is compared with the corresponding Gaussian distribution.

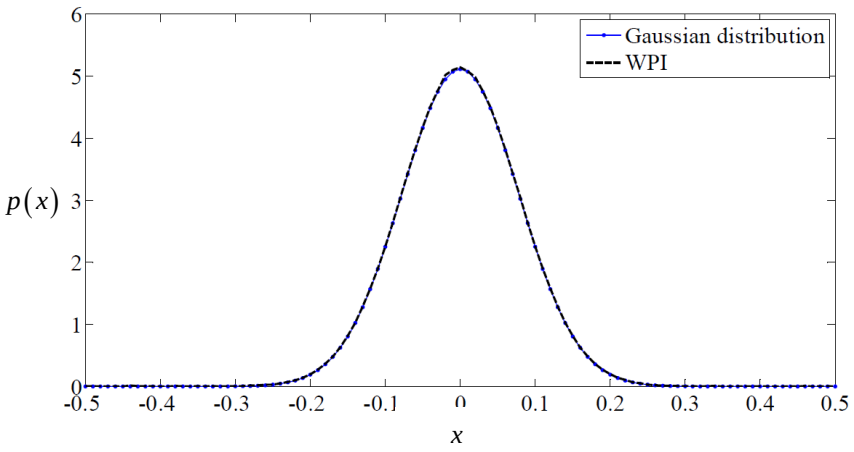

Fig. 5.10 - Marginal stationary displacement response PDF at $t_f = 10\,s$.

Fig. 5.10 shows a perfect correspondence between the Gaussian distribution and the response PDF obtained by the WPI technique, demonstrating the satisfactory accuracy of the proposed technique.

5.4.3.2 SDOF nonlinear Duffing oscillator with fractional derivatives elements

Consider next a Duffing nonlinear SDOF oscillator with fractional derivatives elements whose motion is governed by the differential equation

$$\ddot{x}+C_{\beta}\left({}_{0}^{C}D_{t}^{\beta}x\right)+\omega_{2}^{2}x+\varepsilon x^{3}=w(t) \tag{5.91}$$

According to the developed technique, substituting Eq. (5.91) into Eq.(5.20), the probability density functional $W\left[x(t)\right]$ for $x(t)$ becomes

$$W\left[x(t)\right]=C\exp\left[-\int_{t_i}^{t_f}\frac{1}{2}\frac{\left(\ddot{x}+C_{\beta}\left({}_{0}^{C}D_{t}^{\beta}x\right)+\omega_{2}^{2}x+\varepsilon x^{3}\right)^{2}}{2\pi S_{0}}dt\right] \tag{5.92}$$

Further, the associated Lagrangian function becomes

$$\mathscr{L}\left(x,{}_{0}^{C}D_{t}^{\beta}x,\ddot{x}\right)=\frac{1}{2}\frac{\left(\ddot{x}+C_{\beta}\left({}_{0}^{C}D_{t}^{\beta}x\right)+\omega_{2}^{2}x+\varepsilon x^{3}\right)^{2}}{2\pi S_{0}} \tag{5.93}$$

whereas the corresponding E-L Eq. (5.67) takes the form

$$\begin{aligned}&\frac{d^{4}x_{c}}{dt^{4}}+\left(2\omega_{2}^{2}+6\varepsilon {x_{c}}^{2}\right)\ddot{x}_{c}+\omega_{2}^{4}\,x_{c}+4\omega_{2}^{2}\varepsilon\,{x_{c}}^{3}+6\varepsilon x_{c}{\dot{x}_{c}}^{2}\\&+C_{\beta}\omega_{2}^{2}\,{}_{0}^{C}D_{t}^{\beta}x_{c}+C_{\beta}\,{}_{0}^{C}D_{t}^{\beta+2}x_{c}+C_{\beta}\,\omega_{2}^{2}\,{}_{t}D_{t_f}^{\beta}x_{c}+C_{\beta}\,{}_{t}D_{t_f}^{\beta}\ddot{x}_{c}\\&+{C_{\beta}}^{2}\,{}_{t}D_{t_f}^{\beta}\left({}_{0}^{C}D_{t}^{\beta}x_{c}\right)+3C_{\beta}\,\varepsilon\,{x_{c}}^{2}\,{}_{0}^{C}D_{t}^{\beta}x_{c}+C_{\beta}\,\varepsilon\,{}_{t}D_{t_f}^{\beta}{x_{c}}^{3}=0\end{aligned} \tag{5.94}$$

together with the corresponding boundary condition $x_{c}(0)=0,\dot{x}_{c}(0)=0$ and $x_{c}(t_{f})=x_{f},\dot{x}_{c}(t_{f})=\dot{x}_{f}$. Similarly to Eq. (5.89) this nonlinear

fourth order fractional differential equation involves the right Riemann-Liouville operator of left Caputo fractional derivative, and has no obvious exact analytical solution. Thus, the FVP of Eq. (5.66) is solved directly without using Eq. (5.94), via the approach detailed in Section 5.4.2.1. In this regard, an effective domain of values for the joint response amplitude PDF $x_{u,f} \in [-2,2]$ and $\dot{x}_{q,f} \in [-3,3]$ $(s = r = 41)$, is chosen. Further, the parameters values $\beta = 0.3, C_\beta = 1, \omega_2 = 1\frac{rad}{s}, \varepsilon = 1, S_0 = \frac{1}{2\pi}$ are considered, whereas $(h = 4)$ Legendre polynomials orthogonal in the interval $\left[0, t_f\right]$ are used in Eq. (5.84) for determining the approximate solution $\tilde{y}(t)$ of the most probable path $x_c(t)$.

In Fig. 5.11 solution of the FVP considering 3, 4 and 5 Legendre polynomials, for the boundary conditions $x_c(0) = 0, \dot{x}_c(0) = 0$ and $x_c(10) = -1.9, \dot{x}_c(10) = -3$, is plotted. It can be readily seen that the solution of the boundary value problem considering 4 and 5 Legendre polynomials, respectively, is of similar satisfactory accuracy, whereas using 3 Legendre polynomials results in decreased accuracy and considerable deviation from the 4 and 5 Legendre polynomials cases. Further, the determined joint response PDF is plotted in Fig. 5.12.

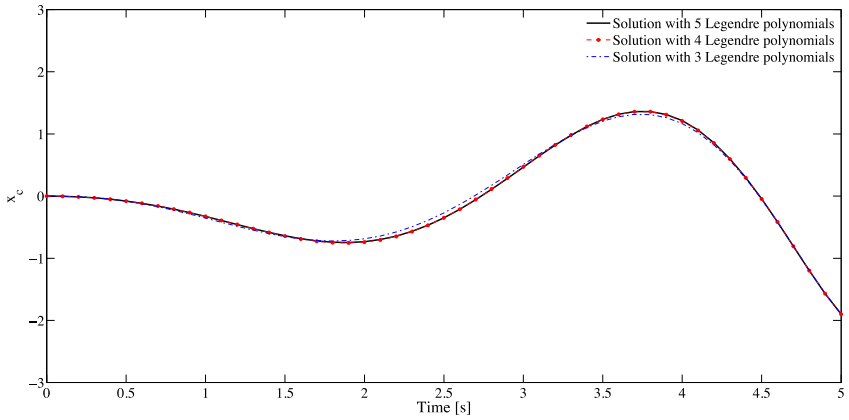

Fig. 5.11 - Comparison of the solution of the boundary value problem for $x_c(10) = -1.9, \dot{x}_c(10) = -3$.

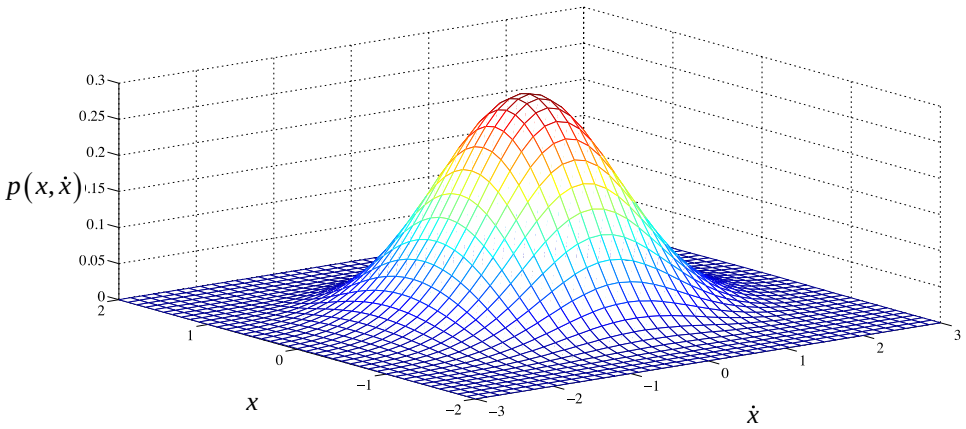

Fig. 5.12 - Response PDF in the given domain $x_{u,f} \in [-2,2]$ and $\dot{x}_{q,f} \in [-3,3]$.

To assess the accuracy of the proposed technique for the nonlinear case also, the non-stationary marginal displacement and velocity response PDFs, obtained by integrating the WPI technique based joint PDF over the displacement domain (Fig. 5.13) and the velocity domain (Fig. 5.14), respectively, are compared with the ones obtained via MCS

using 30000 samples and the corresponding Gaussian distribution $(\varepsilon = 0)$. Comparisons with the MCS data demonstrate a satisfactory level of accuracy even for this significant level of system nonlinearity (it can be seen that the response PDF for the Duffing system deviates significantly from the Gaussian one which corresponds to the linear system).

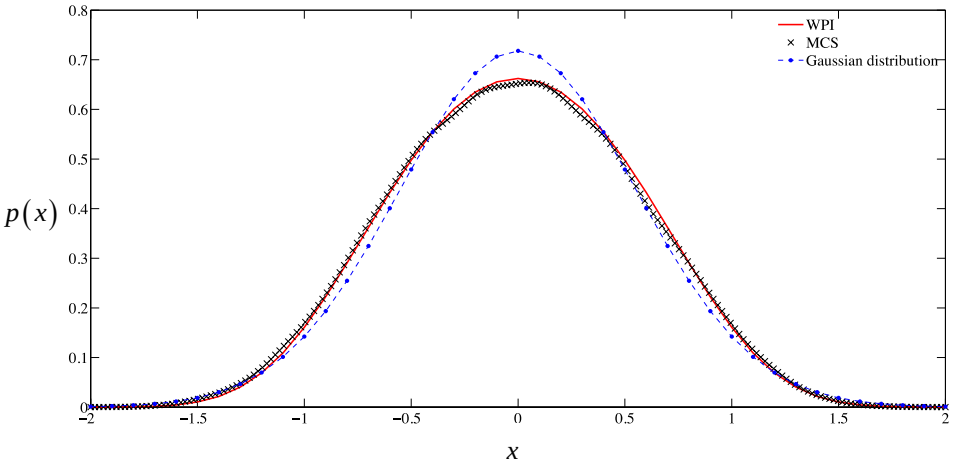

Fig. 5.13 - Marginal non-stationary displacement response PDF at $t_f = 5s$.

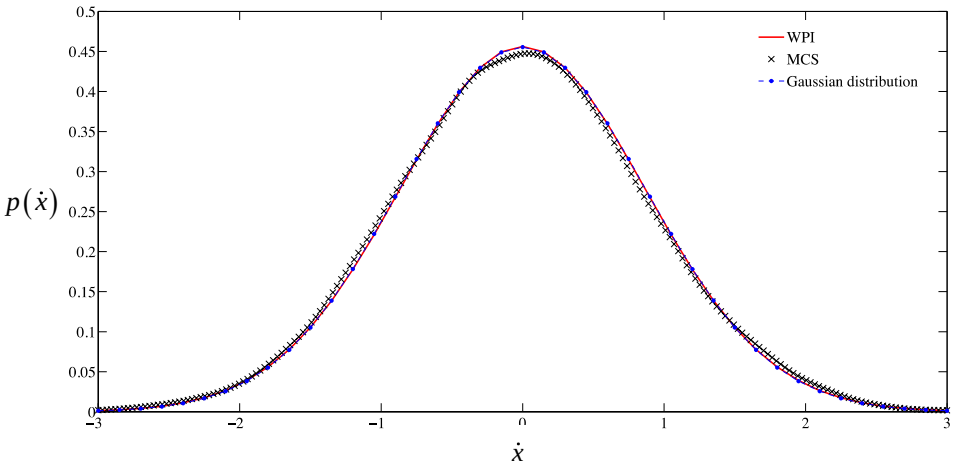

Fig. 5.14 - Marginal non-stationary velocity response PDF at $t_f = 5s$.

Regarding computational efficiency, for the chosen grid of 41x41 points in the PDF domain, the computational cost related to the developed technique was approximately 30% of that corresponding to the MCS estimates considering 30000 sample paths.

5.5 Experimental validation of the proposed efficient WPI on TLCD controlled structures

In this Section the proposed efficient WPI technique, developed in previous Section 5.3, is applied to the case of a TLCD controlled structure. Specifically, in order to further assess the reliability of the procedure, parameters of the TLCD controlled system Configuration #3 of Section 3.7.3, are here used. In this manner, the experimental PDFs will be compared with the ones obtained through the proposed efficient WPI technique.

Following Chapter 2 and 5.3.3, the equation of motion of the TLCD controlled system can be written as

$$\mathbf{M}\ddot{\mathbf{x}}+\mathbf{C}\dot{\mathbf{x}}+\mathbf{K}\mathbf{x}+\mathbf{g}\left(\dot{\mathbf{x}}\right)=\mathbf{f}\left(t\right) \tag{5.95}$$

where

$$\mathbf{M}=\begin{bmatrix} 1 & \dfrac{\alpha\mu}{1+\mu} \\ 1 & \dfrac{1}{\alpha} \end{bmatrix} \tag{5.96}$$

$$\mathbf{C}=\begin{bmatrix} \dfrac{2\zeta_1\omega_1}{1+\mu} & 0 \\ 0 & 0 \end{bmatrix} \tag{5.97}$$

$$\mathbf{K}=\begin{bmatrix} \dfrac{\omega_1^2}{1+\mu} & 0 \\ 0 & \dfrac{\omega_2^2}{\alpha} \end{bmatrix} \tag{5.98}$$

and

$$\mathbf{x}=\begin{pmatrix} x \\ y \end{pmatrix} \tag{5.99}$$

$x(t)$ and $y(t)$ being the structural and the liquid displacement respectively.

Further the nonlinear vector $\mathbf{g}(\dot{\mathbf{x}})$ of Eq. (5.95) takes the form

$$\mathbf{g}(\dot{\mathbf{x}})=\begin{pmatrix} 0 \\ \dfrac{\xi|\dot{y}|\dot{y}}{2\alpha L} \end{pmatrix} \tag{5.100}$$

where ξ is the head loss coefficient, μ is the mass ratio and $\alpha = b/L$. The associated Lagrangian of Eq. (5.95) takes the form

$$\begin{aligned} \mathscr{L}(\mathbf{x},\dot{\mathbf{x}},\ddot{\mathbf{x}}) = \frac{1}{16\pi S0}\Bigg[& \left(8\ddot{x}+\frac{16\zeta_1\omega_1}{1+\mu}\dot{x}+\frac{8\omega_1^2}{(1+\mu)}x+\frac{4\xi|\dot{y}|\dot{y}}{L\alpha}+\frac{8\omega_2^2}{\alpha}y\right)\ddot{x}+ \\ & +\left(\frac{16\alpha\zeta_1\mu\omega_1}{(1+\mu)^2}\dot{x}+\frac{8\omega_1^2\alpha\mu}{(1+\mu)^2}x+\left(\frac{4\alpha^2\mu^2}{(1+\mu)^2}+\frac{4}{\alpha^2}\right)\ddot{y}+\frac{4\xi|\dot{y}|\dot{y}}{L\alpha^2}+\frac{8\omega_2^2}{\alpha^2}y\right)\ddot{y}+ \\ & +\left(\frac{8}{\alpha}+\frac{8\alpha\mu}{1+\mu}\right)\ddot{x}\ddot{y}+\left(\frac{16\zeta_1^2\omega 1^2}{(1+\mu)^2}\dot{x}+\frac{16\omega_1^3\zeta_1}{(1+\mu)^2}x\right)\dot{x}+ \\ & +\frac{4\omega_2^2\xi|\dot{y}|\dot{y}}{L\alpha^2}y+\frac{\xi^2\dot{y}^4}{L^2\alpha^2}+\frac{4\omega_1^4x^2}{(1+\mu)^2}+\frac{4\omega_2^4y^2}{\alpha^2}\Bigg] \end{aligned} \tag{5.101}$$

which yields the system of E-L equations in the form

$$\begin{aligned}&\frac{\partial \mathscr{L}}{\partial x_{c,1}}-\frac{\partial}{\partial t}\frac{\partial \mathscr{L}}{\partial \dot{x}_{c,1}}+\frac{\partial^2}{\partial t^2}\frac{\partial \mathscr{L}}{\partial \ddot{x}_{c,1}}=0\\&\frac{\partial \mathscr{L}}{\partial x_{c,2}}-\frac{\partial}{\partial t}\frac{\partial \mathscr{L}}{\partial \dot{x}_{c,2}}+\frac{\partial^2}{\partial t^2}\frac{\partial \mathscr{L}}{\partial \ddot{x}_{c,2}}=0\end{aligned} \tag{5.102}$$

together with the 4×2 boundary conditions

$$\begin{aligned}&x_{c,1}(t_i)=x_{1,i},\dot{x}_{c,1}(t_i)=\dot{x}_{1,i},x_{c,1}(t_f)=x_{1,f},\dot{x}_{c,1}(t_f)=\dot{x}_{1,f},\\&x_{c,2}(t_i)=x_{2,i},\dot{x}_{c,2}(t_i)=\dot{x}_{2,i},x_{c,2}(t_f)=x_{2,f},\dot{x}_{c,2}(t_f)=\dot{x}_{2,f}.\end{aligned} \tag{5.103}$$

where $x_{c,1}(t)$ is the most probable path of $x(t)$ and $x_{c,2}(t)$ is the most probable path of $y(t)$.

As previously stated, to assess the reliability of the technique, comparisons are made among the stationary response displacement and velocity PDFs of the nonlinear 2-DOF system in Eq. (5.95) determined by the WPI technique together with a fourth order expansion of the polynomial in Eq. (5.48), and experimental data obtained on Configuration #3 in Section 3.7.3 (totally considering 50000 samples for the stationary case). In this regard, for a fourth order polynomial $(l=4)$ corresponding to this 2-DOF system $(2m=4)$, the number of coefficients $c_{i_P}(t_f)$ in Eq.(5.48) is $(N_p=70)$. Thus, only 70 BVPs of the form of Eq. (5.40) are numerically solved for determining the N_p coefficients through Eq. (5.50). Further, as far as the parameters of the system in Eq. (5.95) are concerned, the ones experimentally obtained in Section 3.7.3 on Configuration #3 are here used. For sake of clarity those parameters are here reported in Table 5.1.

Table 5.1 - Parameters of the model in Eq. (6.62).

	Configuration # 3
ω_1	10.52 *rad/s*
ζ_1	0.0031
L	0.175 *m*
ω_2	11.81 *rad/s*
ξ	7
μ	1.9 %
α	0.6

Figures 5.15 and 5.16 show the plotted stationary marginal structural response displacement and velocity PDFs $p(x)$ and $p(\dot{x})$, respectively. As shown in these figures, comparisons with experimental data demonstrate a satisfactory degree of accuracy for the determined response PDFs.

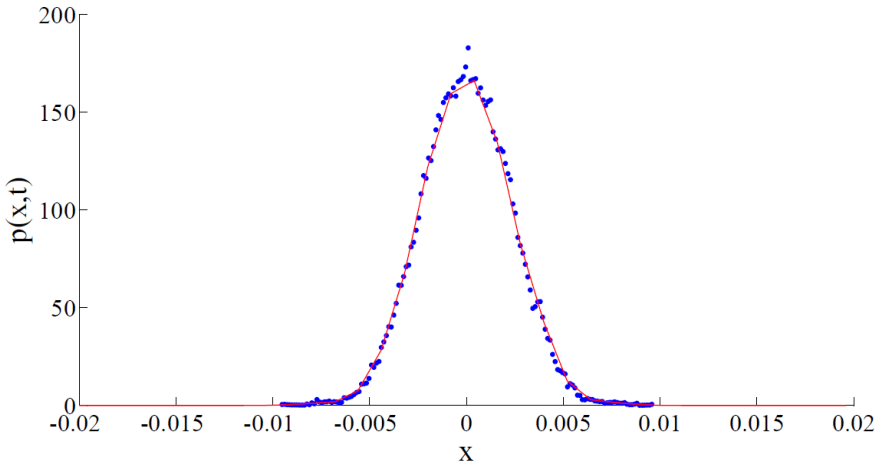

Fig. 5.15 - Marginal stationary response structural displacement PDF $p(x)$ for TLCD controlled structure: comparison among experimental data (blue dots) and the developed technique (red line).

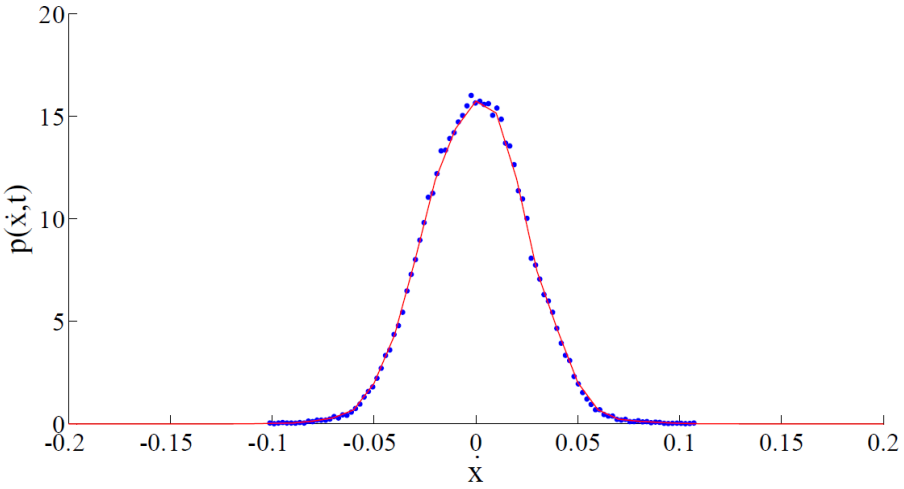

Fig. 5.16 - Marginal stationary response structural velocity PDF $p(\dot{x})$ for TLCD controlled structure: comparison among experimental data (blue dots) and the developed technique (red line).

Concluding Remarks

In this dissertation the Tuned Liquid Column Damper (TLCD), a passive vibration control device nowadays increasingly used, has been studied, and its effects on structural systems thoroughly investigated. Due to some of its inherent characteristics such as low costs, easy installation and tuning and lack of maintenance requirements, TLCD represents an appealing alternative to many other passive control devices, including the widely used Tuned Mass Damper (TMD). Hence, the growing interest on this device among researchers concerned with vibration control.

Beginning with a brief introduction on vibration control mechanism, firstly the most common passive vibration control systems have been presented, focusing specifically on the simple, yet remarkably interesting, case of the TMD.

Once the basic principles of vibration control have been addressed, the system object of this dissertation, namely the TLCD, has been introduced. In this regard, after a discussion on the pertinent literary review and a presentation on its real applications for buildings vibration control, the classical nonlinear governing equations ruling the TLCD controlled systems response have been derived. Further, existing approaches in literature for the optimal design of these dampers have been outlined, and results of a numerical/experimental investigation on the control performances of this system compared to the TMD case has been also reported. Results confirm that both vibration control devices

are able to adequately reduce structural vibrations, and TLCD performances are deemed comparable to TMD systems, if an appropriate choice of TLCD parameters is accomplished.

On this base, the optimal selection of the absorber parameters, namely tuning ratio and damping ratio, has been considered. Specifically, a direct procedure for the determination of optimal TLCD parameters has been introduced, considering the case of damped under random agencies. The proposed straightforward approximate formulation has been derived by means of statistical linearization techniques and under some assumptions pertaining the system. Moreover, the design formulation has been derived for stochastic loads that can be modeled as zero mean Gaussian white noise processes, but an extension to random processes which have Response Spectra coherent with building codes can be straightforwardly obtained. The analytical formulation consists in a smooth function of the main system displacement variance as a function of the approximated equivalent TLCD damping ratio. A parametric numerical analysis showed that the response statistics obtained by Monte Carlo simulations (MCS) on the actual nonlinear system are in good agreement with those obtained using the proposed formulation even when the underlying assumptions are removed. Results on a benchmark structure have been compared with literature results showing the reliability of the proposed formulation. It is worth noting that, by using the proposed definition of the equivalent linear damping, an impressive reduction in computational effort is achieved. In fact, if a classical procedure is used to define the equivalent linear system, a time-consuming iterative scheme has to be set up. Conversely, following the herein proposed approach, the evaluation

of the optimal values can be obtained by means of a numerical minimization of a smooth function, without any iteration, thus resulting in a very significant reduction in computational effort. From simple design it is apparent that the optimal tuning ratio, the optimal head loss coefficient and a performance control index can be easily computed once the main system structural parameters and the input intensity are provided, thus resulting in a very useful and ready-to-use design tool. Finally, the straightforward formulation has been validated by means of an experimental campaign on a small scale SDOF shear-type model built at the Laboratory of Experimental Dynamic of University of Palermo. The identification of the main linear system and of the TLCD parameters has been conducted and a very good agreement among experimental and numerical data has been achieved for three different configurations of the device. Results have shown that the responses obtained by the equivalent linear system via the proposed formulation are very close to those obtained by classical nonlinear one and by experimental results as well.

Next the analytical modeling of TLCDs has been investigated. Although the increasing use of these devices for structural vibration control, it has been shown that for some geometrical configuration of engineering interest, existing classical formulation does not always lead to accurate prediction of the liquid motion. In this regard, it has been demonstrated how correctly including the sloshing behavior of the liquid inside the TLCD container could greatly improve prediction of the real liquid surface displacements. Further it has been shown that the described effects which lead to discrepancies among theoretical and experimental findings, contemporary with the damping effects, may be taken into

account through the mathematical tools of fractional derivatives and related concepts. Therefore, an alternative formulation, based on fractional operators, has been proposed to model liquid vertical displacements in TLCD devices, and its extension to the case of TLCD controlled structures have been also derived. In order to fully validate the proposed formulation, experimental tests have been conducted in the Laboratory of Experimental Dynamic at University of Palermo, on various configurations of TLCD devices and TLCD controlled systems. Numerical results obtained with the proposed fractional formulation have been compared with the corresponding numerical ones computed with the classical model and pertinent experimental data. Results have shown that proposed fractional formulation can describe with great accuracy the real experimental behavior of the liquid and the response of TLCD controlled structures, notably improving the prediction of the real liquid surface displacements with respect to the classical nonlinear model used in literature. Further, since the resulting equations of motion are linear, albeit of fractional order, identification of involved parameters is extremely simpler than the classical nonlinear formulation.

Finally, in the last part of the dissertation, the stochastic analysis of TLCD systems, and TLCD controlled structures, under Gaussian white noise excitation is addressed through the promising novel framework of the Wiener Path Integral (WPI) technique. Although for low-dimensional systems the recently developed WPI technique can be significantly more efficient than MCS, its standard implementation proves to be computationally prohibitive for relatively high-dimensional MDOF systems. In this regard, a novel WPI technique implementation has been

developed by combining the localization capabilities of the classical WPI solution framework with an appropriately chosen expansion for approximating the system response PDF. It has been shown that the herein proposed implementation can drastically decrease the associated computational cost by several orders of magnitude. Clearly, for relatively high-dimensional systems, the proposed technique is several orders of magnitude faster than both the standard WPI technique and the MCS, which requires solving the equations of motion numerically thousands of times to derive a reliable response PDF estimate. Several numerical examples have been presented, whereas comparisons with pertinent MCS data have demonstrated the efficiency and reliability of the approach. The utility of this theoretical advanced tool for predicting the stochastic response of a TLCD-controlled structure has been stressed in the last part of the dissertation, where the case of the 2 degree-of-freedom TLCD controlled structure is considered, assessing the accuracy of the outlined procedure also with the corresponding experimentally obtained PDFs.

Moreover, with regard to the proposed fractional formulation for the motion of TLCD systems, it is worth stressing that the WPI technique has been extended for determining the non-stationary response PDF of linear and nonlinear systems endowed with fractional derivatives elements. A fractional variational principle, in conjunction with the concept of the most probable path related to the WPI, has yielded an approximate closed form solution for the system non-stationary joint response PDF. In this regard, note that the associated Euler-Lagrange fractional differential equations to be solved for the most probable path include both right Riemann-Liouville fractional derivatives and left Caputo fractional

derivatives. Therefore, determining an exact analytical solution is a rather daunting, if not impossible task. Here the problem has been circumvented by addressing directly the original fractional variational problem without resorting to the corresponding Euler-Lagrange equations. Specifically, utilizing shifted Legendre polynomials and Hermite interpolating polynomials has yielded a simple system of algebraic equations which must be solved for determining the most probable path. Thus, the system joint response PDF can be determined at a low computational cost. Several numerical examples have been presented to show the reliability of the proposed procedure, including the case of the TLCD device, and comparisons with pertinent MCS data have demonstrated a satisfactory degree of accuracy.

As far as future studies and possible suggested developments are concerned, the following points may be considered as possible improvements:

i. In the proposed fractional formulation for TLCD systems, the two involved parameters have been experimentally determined. This could be further refined, should it be possible to analytically relate these parameters to TLCD characteristics.

ii. Further investigations should be undertaken in order to consider also the influence of orifices in the U-shaped containers, on the behavior these dampers.

iii. The effect of more than one TLCD, and their optimal position in MDOF systems could be further analyzed.

iv. The extension of the WPI to non-Gaussian type of white noise excitation should be still developed.

Appendix A

The experimental setup

All the experimental tests reported throughout this dissertation in the previous chapters have been developed in the Laboratory of Experimental Dynamics at the Department of Civil, Environmental, Aerospace and Material Engineering of the University of Palermo. An overview of the instruments used for the experimental campaign is reported in this Appendix.

A.1 Excitation device: Shake Table

Shaking table model Quanser Shake Table II has been employed to provide the base excitation to the SDOF shear-type models.

The main devices used to run the shake table are depicted in Fig A.1. The entire setup is composed of a Universal Power Module (UPM) (see Fig. A.2), a data acquisition card (DAC) (see Fig. A.3), a PC running the WinCon control software and the Shake Table II itself (Fig. A.4).

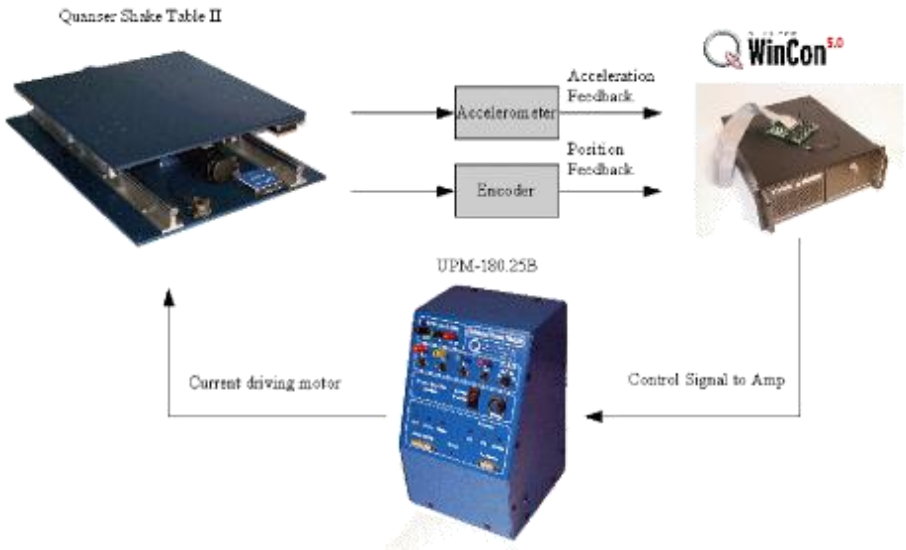

Fig. A.1 - Overview of the major systems components for the Quanser Shake Table II.

Consider for example the signal transitions between the system components when the user wishes the Shake Table II to track a sine wave and read the resulting acceleration.

Fig. A.2 - UPM front panel.

Fig. A.3 - Extended terminal board.

Fig. A.4 - Quanser Shake Table II.

Using WinCon on the PC, the user specifies the amplitude and frequency of the sine wave. The current needed to move the stage at the desired sine wave position is calculated in WinCon and sent through the analog output channel of the data acquisition board to the UPM device.

The power amplifier in the UPM amplifies the current and drives the motor. The table moves back and forth at the position and frequency of the commanded sine wave. The resulting displacement and acceleration of the stage are measured through the on-board encoder and accelerometer sensors. These devices are connected to the DAC board and their signal can be displayed and processed further in WinCon.

The top stage of the shake table is driven by a powerful motor that allow it to achieve an acceleration of 2.5 g when up to 7.5 kg of mass is mounted. The stage rides on two ground-hardened metal shafts using linear bearings which allows for smooth linear motions with low path deflection. When starting from the center position, the stage is able to move 7.62 cm (3 inches) on each side, therefore possessing a total displacement of 15.24 cm. In order to move the top platform, a robust ball-screw and motor assembly is used. The high-power 400 Watt motor is a 3-phase brushless DC actuator. The motor contains an embedded high-resolution encoder that allows for the position of the stage to be measured with an effective linear resolution of 3.10 μm. An analog accelerometer is mounted on the shake table platform in order to measure the accelerations of the stage directly, thus allowing for the control software to check step-by-step desired and effective displacements of the table. A complete list of the Shake Table II specifications is reported in Table A.1.

Table A.1 - Shake Table II specifications

Parameter	Parameter Description	SI Value	Units
R_m	Motor armature resistance	2.94	ohm
K_t	Motor current-torque constant	0.360	N.m/A
K_m	Motor back-emf constant	0.2034	V/(rad/s)
P_b	Ball-screw pitch	0.0127	m/rev
M_p	Preload mass	7.74	kg
$M_{l\ max}$	Maximum total load mass	15.0	kg
M_s	Mass of Shake Table II system	27.2	kg
	Dimension of top stage	0.46 ×0.46	m^2
	Dimension of bottom stage	0.61 ×0.46	m^2
	Height from bottom to top stage	12.4	cm
x_{max}	Maximum stroke position	76.2	mm
v_{max}	Maximum linear velocity of stage	664.9	mm/s
F_{max}	Maximum linear force of stage	708.7	N
a_{max}	Maximum linear acceleration of stage for 0 kg load	24.5	m/s^2
g_{max}	Maximum linear acceleration of stage for 0 kg load	2.50	g
K_{ENC}	Encoder sensitivity gain	3.1006	µm/count
K_{ACC}	Accelerometer sensitivity gain	-1	g/V
	Dynamic load capacity of ball nut	12000	N
	Life expectancy of ball nut at full load	6.35E+008	m
	Life expectancy of linear bearing	6.35E+006	m
	Load carrying capacity of linear bearings	131.5	kg

A.2 Accelerometers

In order to acquire structural responses in terms of acceleration, the principal type of accelerometer used was the Miniature DeltaTron Accelerimeter Bruel&Kjær-Type 4507-002. This type of device (Fig. A.5) presents high sensitivity, large frequency range and very small dimensions and weight.

Fig. A.5 - Miniature DeltaTron accelerometers Bruel&Kjær-Type 4507-002.

DeltaTron is a generic name for Bruel&Kjær accelerometers, identifying products that operate on a constant current power supply and give output signals in the form of voltage modulation on the power supply line. The built-in low noise preamplifiers are made using thick film technology. They comprise ASICs including a special reference voltage that ensures very stable bias voltage over the entire operating temperature range. The low output impedance means that one can connect long cables between the accelerometers and measurement equipment. Further specifications are reported in Table A.2.

Table A.2 - Miniature DeltaTron accelerometers Bruel&Kjær-Type 4507-002 specifications.

Housing material	ASTM Grade 2 titanium
Weight	4.8 g
Sensitivity (@a59.2 Hz)	100 mV/ms^{-2}
Resonance Frequency	18 kHz
Amplitude response ± 10%	from 0.4 Hz to 8400 Hz
Transverse Sensitivity	<5%
Transverse Resonance Frequency	>10 kHz
Ambient Temperature Range	-54 to +100°C
Max. Operational Acceleration (Peak)	5000 g

A.3 Conditioning Amplifiers

Charge and current signals coming from the accelerometers need to be conditioned and amplified before being acquired and saved. To this aim, the conditioning amplifier model Bruel&Kjær Nexus Range of Conditoning Amplifier-Type 2693A014 (Fig. A.6) has been used.

Fig. A.6 - Miniature DeltaTron accelerometers Bruel&Kjær-Type 4507-002.

This device is able to condition and amplify current signals coming from the above presented accelerometers. It is also able to filter and integrate acceleration signals into velocity and/or displacements signals.

A.4 Analogical-Digital (A-D) Acquisition Board

To acquire accelerometers signals a National Instrument NI-PCI-4472 Analogical-Digital (A-D) acquisition board has been used (Fig. A.7).

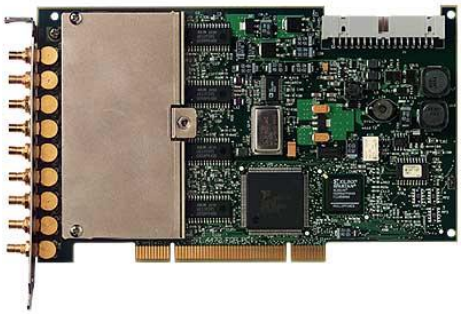

Fig. A.7 - National Instrument NI-PCI-4472 A-D acquisition board.

This is a 8-channel dynamic signal acquisition board with 24-bit resolution ADCs with 110 dB dynamic range, 8 simultaneously sampled analog inputs at up to 102.4 kS/s, ±10 V input range or ±31 V with SMB-120 cable, variable antialiasing filters and ability to synchronize multiple devices for higher channel count applications. Specifications are reported in Table A.3.

Table A.3 - National Instrument NI-PCI-4472 A-D acquisition board specifications.

Size	17.5 by 10.7 cm
Connectors	SMB male
Channels	8, simultaneously sampled
Resolution	24 bit
Sampling Frequency f_s	from 1.0 to 102.4 kS/s
Input signal Amplitude Range	±10 V (peak)
Anti aliasing Bandwidth	from 0 to 0.5465 f_s
Crosstalk (Channel Separation)	-90 dB
Operating Temperature	from 0 to 50 °C
Relative Umidity	from 10 to 90%

A.5 The NI PXI system

Recently acquired National Instruments NI PXIe-1082 DAQ device, equipped with a high-performance 16-channels NI PXIe-4497 board, has been used to acquire signals coming from the accelerometers for some of the latest experiments.

The entire systems can be considered as an all-in-one device able to acquire, condition and amplify voltage and charge signals. Further, since the same device is also equipped with a NI PXIe-4497 board digital-to-analog (D/A) converter, it has been used to generate the output voltage signals for the APS shake table, thus providing the base excitation.

Finally the entire system is controlled via a self-developed signal processing software in LabVIEW environment. Picture of the device is reported in Fig. A.8.

Fig. A.8 - National Instruments NI PXIe-1082 DAQ device.

A.6 Data acquisition software and procedure

Structure vibrations and table motion have been acquired in terms of acceleration. Acquisition sample frequency has been chosen equal to 1kHz in order to avoid sample aliasing (resulting Nyquist frequency for acquired data is 500 Hz, much higher that the highest model frequency).

Acceleration signals have been processed using self developed LabView software which allows real time processing. Post processing procedures includes:

- Anti bias and detrending functions, to eliminate non-zero mean in the digitized signals due to a current shift or to a bad conditioning in the analogical signal.
- High frequency filtering to exclude instrumental noise.
- Time windowing to avoid signal leakage. Leakage is a problem encountered when performing the Fourier Transform of a sampled data and consists of a spreading of the spectrum over a range of frequencies wider than the real ones. Hanning time windows have been used for steady periodic and random vibrations.
- Integration. Accelerations have been integrated twice by means of an appropriate high-pass filter to obtain velocities and displacements of the systems.

When necessary recorder signals have been filtered with an 8th order Butterworth filter, using cut-off frequencies from 0.5 to 15 Hz.

Acceleration signals have been then stored and used to perform system identifications procedures and time and frequency analysis, as shown in the previous chapters.

Appendix B

Power Spectral Density coherent with Response Spectra

In the present Appendix, the Power Spectral Density (PSD) function coherent with elastic Response Spectra (RS) for Eurocode 8 in piecewise analytical relationship is reported in order to use the concepts outlined in the Chapter 3 of the dissertation.

Equation (B.1) reports the analytic expression of elastic pseudo-acceleration Response Spectra prescribed by Eurocode:

$$S_a(T)=\begin{cases} a_g \cdot S\left[1+\dfrac{T}{T_B}\left(\eta \cdot 2.5-1\right)\right] & 0 \le T \le T_B \\ 2.5 \cdot a_g \cdot S \cdot \eta & T_B < T \le T_C \\ 2.5 \cdot a_g \cdot S \cdot \eta \left(\dfrac{T_C}{T}\right) & T_C < T \le T_D \\ 2.5 \cdot a_g \cdot S \cdot \eta \left(\dfrac{T_C T_D}{T^2}\right) & T > T_D \end{cases} \tag{B.1}$$

where T is the natural period, a_g is the peak ground acceleration, η is a factor depending on the structural damping ($\eta = 1$ for $\zeta = 5\%$), T_B, T_C and T_D are the period values that delimitate the various branches. In the applications of this paper RS for soil type C are used, and the parameters values are $T_B = 0.20$ s, $T_C = 0.60$ s, $T_D = 2.00$ s and $S = 1.15$. In Fig.

B.1(a) the RS is depicted. Analyses conducted for other soil types always give comparable results.

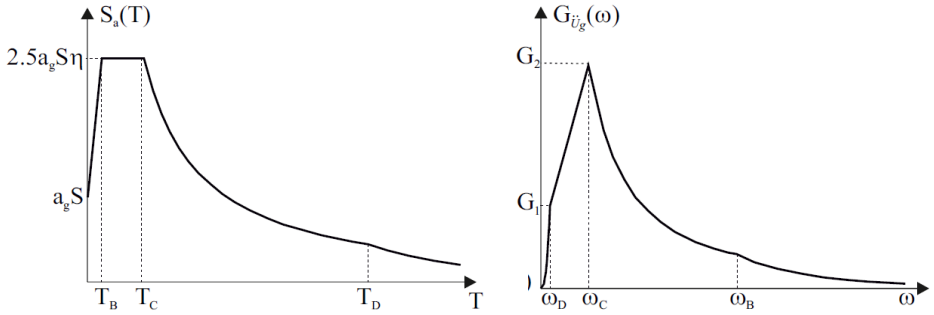

Fig. B.1 – (a) Pseudo-acceleration response spectra prescribed by Eurocode 8; (b) PSD compatible with Eurocode 8 response spectra.

Once the nominal duration of the earthquake Ts is selected, it is possible to evaluate a PSD function such as the mean maximum peak of the response acceleration, computed into the same window of the nominal duration of the earthquake, which gives the same results of the target RS. It has to be stressed that the PSD so obtained is only related to the ground acceleration and not to the superimposed structure, i.e. it is absolutely independent of the damping ratio either by yielding or by inherent nonlinearities present on the superimposed structure.

In order to do so, in literature several techniques are available and a simple analytical model (Navarra et al., 2013) that is derived from the numerical method reported in Cacciola et al. (2004) is here presented. It was recognized that the PSD functions compatible with Eurocode 8 RS have the shape reported in Fig. B.1(b). In (Navarra et al., 2013) the

analytical model reported in Eq. (B.2) is proposed, where G_1 and G_2 have the meaning illustrated in Fig. B.1(b).

$$G_{\ddot{U}_g}(\omega)=\begin{cases} G_1\left(\dfrac{\omega}{\omega_D}\right)^{e_1} & 0\le\omega\le\bar{\omega}_D \\ G_2\left(\dfrac{\omega}{\omega_C}\right)^{e_2} & \bar{\omega}_D<\omega\le\omega_C \\ G_2\left(\dfrac{\omega}{\omega_C}\right)^{e_3} & \omega_C<\omega\le\omega_B \\ G_2\left(\dfrac{\omega_B}{\omega_C}\right)^{e_3}\left(\dfrac{\omega}{\omega_B}\right)^{e_4} & \omega>\omega_B \end{cases} \tag{B.2}$$

The circular frequencies ω_i corresponding to the periods T_i in Eq. (B.1) and the parameter $\bar{\omega}_D$ are reported in Eq. (B.3)

$$\omega_i=\frac{2\pi}{T_i},\ i=B,C,D, \qquad \bar{\omega}_D=\left(\frac{G_2}{G_1}\frac{\omega_D^{e_1}}{\omega_C^{e_2}}\right)^{\frac{1}{e_1-e_2}} \tag{B.3}$$

According to the model presented in (Navarra et al., 2013) the values for the exponents e_i for Eurocode 8 are: $e_1=10/3$, $e_2=2/3$, $e_3=-4/3$ and $e_4=-8/3$, while $T_S=20$ s. In Table B.1 the values for G_1, G_2 and $\bar{\omega}_D$ for the RS in Eurocode 8 and soil-type C are reported for several values of the intensity parameter a_g. In this case the parameter $\bar{\omega}_D$=3.365 rad/s. Figure B.2 reports a comparison between the target RS provided by Eurocode 8 and the one obtained by means of a stochastic analysis of a SDOF system subjected to a Gaussian process with the PSD in Eq. (B.2), in terms of both pseudo-acceleration and displacements. In

every case the percentage difference is much below the allowed tolerance of 10%.

Table B.1 - Parameter values for the definition of the PSD compatible with Eurocode 8, soil C response spectra.

a_g/g	G_1 10^{-4} [(m/s²)²/(rad/s)]	G_2 10^{-4} [(m/s²)²/(rad/s)]
0.05	3.294	8.832
0.10	13.176	35.328
0.15	29.645	79.488
0.20	52.703	141.312
0.25	82.348	220.801
0.30	118.581	317.953

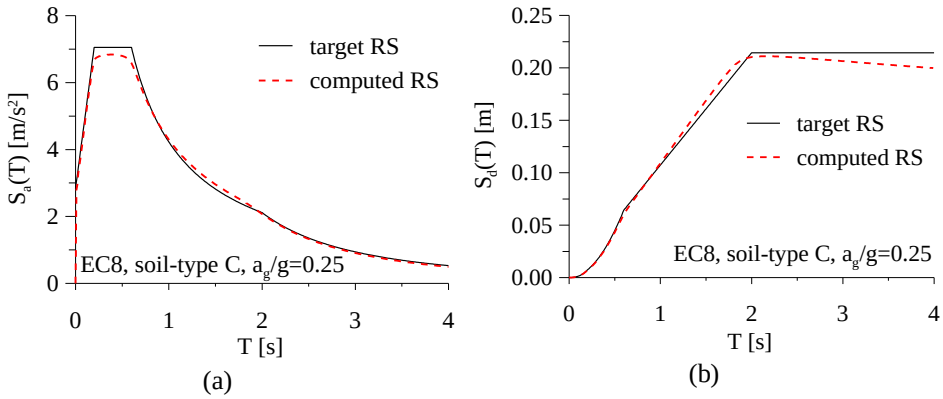

Fig. B.2 – (a) Comparison between target RS and the one obtained via compatible PSD; a) pseudo-acceleration response spectra; (b) displacement response spectra.

Appendix C

The fractional Euler-Lagrange Equation

In this Appendix the detailed derivation of the Euler-Lagrange equations for the FVPs In Chapter 5 is presented. The problem is formulated herein only in terms of β-order left Caputo fractional derivatives, defined as

$$ {}_{t_i}^{C}D_t^{\beta} x(t) = \frac{1}{\Gamma(n-\beta)} \int_{t_i}^{t} (t-\tau)^{n-\beta-1} \frac{d^n}{d\tau^n} x(\tau)\, d\tau, \;\; n-1 < \beta < n \tag{C.1} $$

As shown in Eq. (5.67), the right Riemann-Liouville fractional derivatives, defined as

$$ {}_{t}D_{t_f}^{\beta} f(t) = \frac{1}{\Gamma(n-\beta)} \frac{d^n}{dt^n} \int_{t}^{t_f} (t-\tau)^{n-\beta-1} f(\tau)\, d\tau, \;\; n-1 < \beta < n, \tag{C.2} $$

naturally occur in a problem of fractional calculus of variations, even though they do not appear in the functional. These derivatives will be denoted as the LCFD and the RRLFD, respectively. Next, utilizing the above definitions, let us consider the general class of FVPs which contain several functions $y_j(t)\,(j=1,\ldots,m)$, and multiple positive fractional order derivatives $\beta_k \in \mathbb{R}^+$; that is,

$$J\left[y_1,\ldots,y_m\right]=\int_{t_i}^{t_f}\mathcal{F}\left(t,y_1,\ldots,y_m,{}_{t_i}^{C}D_t^{\beta_1}y_1,\ldots,{}_{t_i}^{C}D_t^{\beta_1}y_m,\ldots,{}_{t_i}^{C}D_t^{\beta_n}y_1,\ldots,{}_{t_i}^{C}D_t^{\beta_n}y_m\right)dt \tag{C.3}$$

$$\begin{aligned}
&y_j\left(t_i\right)=y_{ji} \qquad y_j\left(t_f\right)=y_{jf},\\
&\dot{y}_j\left(t_i\right)=\dot{y}_{ji} \qquad \dot{y}_j\left(t_f\right)=\dot{y}_{jf},\\
&\vdots\\
&\frac{d^{n-1}y_j\left(t_i\right)}{dt^{n-1}}=\frac{d^{n-1}y_{ji}}{dt^{n-1}} \qquad \frac{d^{n-1}y_j\left(t_f\right)}{dt^{n-1}}=\frac{d^{n-1}y_{jf}}{dt^{n-1}}
\end{aligned} \tag{C.4}$$

where $1\le j\le m, k-1\le\beta_k\le k, k=1,\ldots,n\in\mathbb{Z}^+$, and the function $\mathcal{F}$ is continuously differentiable with respect to all its arguments. Note that in this case, all the boundary conditions (at the starting and ending point) are given.

Next, assume that $y_j^*(t)\left(j=1,\ldots,m\right)$ are the desired extremizers of $J\left[y_1,\ldots,y_m\right]$. Let $\varepsilon_j\in\mathbb{R}$ be a small parameter, and $\eta_j\left(t\right)$ an arbitrary admissible function; it is possible to define the following family of curves

$$y_j\left(t\right)=y_j^*\left(t\right)+\varepsilon_j\eta_j\left(t\right), \quad 1\le j\le m \tag{C.5}$$

which satisfy the boundary conditions (C.4); i.e. it is required that

$$\begin{aligned}
&\eta_j\left(t_i\right)=0 \qquad \eta_j\left(t_f\right)=0\\
&\dot{\eta}_j\left(t_i\right)=0 \qquad \dot{\eta}_j\left(t_f\right)=0\\
&\vdots\\
&\frac{d^{n-1}\eta_j\left(t_i\right)}{dt^{n-1}}=0 \qquad \frac{d^{n-1}\eta_j\left(t_f\right)}{dt^{n-1}}=0
\end{aligned} \tag{C.6}$$

Since fractional derivatives are linear operators, it follows that

$$ {}_{t_i}^{C}D_t^{\beta_k} y_j(t) = {}_{t_i}^{C}D_t^{\beta_k}\left(y_j^*(t)+\varepsilon_j\eta_j(t)\right) = {}_{t_i}^{C}D_t^{\beta_k} y_j^*(t)+\varepsilon_j\,{}_{t_i}^{C}D_t^{\beta_k}\eta_j(t) \tag{C.7} $$

Substituting Eqs. (C.5) and (C.7) into Eq. (C.3), yields

$$ J\left[\varepsilon_j\right] = \int_{t_i}^{t_f} \mathcal{F}\begin{pmatrix} t, y_1^*(t)+\varepsilon_1\eta_1(t),\ldots, \\ y_m^*(t)+\varepsilon_m\eta_m(t), {}_{t_i}^{C}D_t^{\beta_1} y_1^*(t)+{}_{t_i}^{C}D_t^{\beta_1}\varepsilon_1\eta_1(t),\ldots, \\ {}_{t_i}^{C}D_t^{\beta_1} y_m^*(t)+{}_{t_i}^{C}D_t^{\beta_1}\varepsilon_m\eta_m(t),\ldots, \\ {}_{t_i}^{C}D_t^{\beta_n} y_1^*(t)+{}_{t_i}^{C}D_t^{\beta_n}\varepsilon_1\eta_1(t),\ldots, \\ {}_{t_i}^{C}D_t^{\beta_n} y_m^*(t)+{}_{t_i}^{C}D_t^{\beta_n}\varepsilon_m\eta_m(t) \end{pmatrix} dt \tag{C.8} $$

A necessary condition for $J\left[y_1,\ldots,y_m\right]$ to have an extremum for $y_j(t)=y_j^*(t),\ (j=1,\ldots,m)$ is given by

$$ \left.\frac{\partial J\left[\varepsilon_j\right]}{\partial\varepsilon_j}\right|_{\varepsilon_j=0} = 0 \tag{C.9} $$

whereas this should be true for all admissible $\eta_j(t)$. Differentiating Eq. (C.8) with respect to ε_j and equating to zero, we obtain

$$ \begin{aligned} \frac{\partial J\left[\varepsilon_j\right]}{\partial\varepsilon_j} &= \int_{t_i}^{t_f}\left[\frac{\partial\mathcal{F}}{\partial y_j}\eta_j(t)+\frac{\partial\mathcal{F}}{\partial\,{}_{t_i}^{C}D_t^{\beta_1} y_j}\,{}_{t_i}^{C}D_t^{\beta_1}\eta_j(t)+\ldots+\frac{\partial\mathcal{F}}{\partial\,{}_{t_i}^{C}D_t^{\beta_n} y_j}\,{}_{t_i}^{C}D_t^{\beta_n}\eta_j(t)\right]dt = \\ &= \int_{t_i}^{t_f}\left[\frac{\partial\mathcal{F}}{\partial y_j}\eta_j(t)+\sum_{k=1}^{n}\frac{\partial\mathcal{F}}{\partial\,{}_{t_i}^{C}D_t^{\beta_k} y_j}\,{}_{t_i}^{C}D_t^{\beta_k}\eta_j(t)\right]dt = 0 \end{aligned} \tag{C.10} $$

Further, employing the formula for fractional integration by parts for left Caputo fractional derivatives, for $\beta_k\in\mathbb{R}^+$, see (Agrawal, 2007a,b; Almeida et al., 2011).

$$\int_{t_i}^{t_f} g(t)\,{}_{t_i}^{C}D_t^{\beta_k} f(t)\,dt = \sum_{l=0}^{n-1}\left[\frac{d^{n-1-l} f(t)}{dt^{n-1-l}}\,{}_{t}D_{t_f}^{\beta_k+l-n} g(t)\right]_{t=t_i}^{t=t_f} + \\ + \int_{t_i}^{t_f} f(t)\,{}_{t}D_{t_f}^{\beta_k} g(t)\,dt \tag{C.11}$$

the second integral of Eq. (C.10) can be written as

$$\int_{t_i}^{t_f} \sum_{k=1}^{n} \frac{\partial \mathcal{F}}{\partial\,{}_{t_i}^{C}D_t^{\beta_k} y_j}\,{}_{t_i}^{C}D_t^{\beta_k}\eta_j(t)\,dt = \sum_{l=0}^{n-1}\left[\frac{d^{n-1-l}\eta_j(t)}{dt^{n-1-l}} \sum_{k=1}^{n} {}_{t}D_{t_f}^{\beta_k+l-n} \frac{\partial \mathcal{F}}{\partial\,{}_{t_i}^{C}D_t^{\beta_k} y_j}\right]_{t=t_i}^{t=t_f} \\ + \int_{t_i}^{t_f} \eta_j(t) \sum_{k=1}^{n} {}_{t}D_{t_f}^{\beta_k} \frac{\partial \mathcal{F}}{\partial\,{}_{t_i}^{C}D_t^{\beta_k} y_j}\,dt \tag{C.12}$$

Since conditions of Eq. (C.6) are required, Eq. (C.12) reduces to

$$\int_{t_i}^{t_f} \sum_{k=1}^{n} \frac{\partial \mathcal{F}}{\partial\,{}_{t_i}^{C}D_t^{\beta_k} y_j}\,{}_{t_i}^{C}D_t^{\beta_k}\eta_j(t)\,dt = \int_{t_i}^{t_f} \eta_j(t) \sum_{k=1}^{n} {}_{t}D_{t_f}^{\beta_k} \frac{\partial \mathcal{F}}{\partial\,{}_{t_i}^{C}D_t^{\beta_k} y_j}\,dt \tag{C.13}$$

Substituting Eq. (C.13) into (C.10), we get

$$\int_{t_i}^{t_f} \left[\frac{\partial \mathcal{F}}{\partial y_j} + \sum_{k=1}^{n} {}_{t}D_{t_f}^{\beta_k} \frac{\partial \mathcal{F}}{\partial\,{}_{t_i}^{C}D_t^{\beta_k} y_j}\right] \eta_j(t)\,dt = 0 \tag{C.14}$$

Since $\eta_j(t)$ is arbitrary, by a fundamental lemma of the calculus of variations, it follows that

$$\frac{\partial \mathcal{F}}{\partial y_j} + \sum_{k=1}^{n} {}_{t}D_{t_f}^{\beta_k} \frac{\partial \mathcal{F}}{\partial\,{}_{t_i}^{C}D_t^{\beta_k} y_j} = 0, \qquad 1 \le j \le m, \tag{C.15}$$

Equation (C.15) is the desired Euler-Lagrange equation for the fractional variational problem (C.3).

References

Adam C., Heuer R., Pirrotta A., 2003, Experimental dynamic analysis of elastic-plastic shear frames with secondary structures, *Experimental Mechanics*, Vol. 43(2), 124-130.

Agrawal O.P, 2002, Formulation of Euler–Lagrange equations for fractional variational problems, *Journal of Mathematical Analysis and Applications*, Vol. 272, 368-379.

Agrawal O.P, 2007a, Generalized Euler-Lagrange equations and transversality conditions for FVPs in terms of the Caputo Derivative, *Journal of Vibration and Control*, Vol. 13, 1217-1237.

Agrawal O.P, 2007b, Fractional variational calculus in terms of Riesz fractional derivatives, *Journal of Physics A-Mathematical Theory*, Vol. 237, 6287-6303.

Almeida R., Torres D.F.M., 2011, Necessary and sufficient conditions for the fractional calculus of variations with Caputo derivatives, *Communications in Nonlinear Science and Numerical Simulation*, Vol. 16, 1490–1500.

Al-Saif K.A., Aldakkan K.A., Foda M.A., 2011, Modified liquid column damper for vibration control of structures, *International Journal of Mechanical Sciences*, Vol. 53(7), 505-512.

Balendra T., Wang C.M., Cheong H.F., 1995, Effectiveness of tuned liquid column dampers for vibration control of towers, *Engineering Structures*, Vol. 17(9), 668-675.

Balendra T., Wang C.M., Rakesh G., 1998, Vibration control of tapered buildings using TLCD, *Journal of Wind Engineering and Industrial Aerodinamics*, Vol. 77, 245-257.

Balendra T., Wang C.M., Rakesh G.., 1999, Effectiveness of TLCD on various structural systems, *Engineering Structures*, Vol. 21, 291-305.

Barone G., Navarra G., Pirrotta A., 2008, Probabilistic response of linear structures equipped with non-linear damper devices (PIS method), *Probabilistic Engineering Mechanics*, Vol 23, 125-133.

Battista R.C., Carvalho E.M.L, Souza R.D.A., 2008, Hybrid fluid dynamic control devices to attenuate slender structures oscillations, *Engineering Structures*, Vol. 30, 3513-3522.

Beaman J.J., Hedrick J.K., 1981, Improved Statistical Linearization for Analysis and Control of Nonlinear Stochastic Systems: Part I: An Extended Statistical Linearization Technique, *Journal of Dynamic Systems, Measurement, and Control*, Vol. 103(1), 14–21.

Bergman L.A., Mc Farland D.M., Hall J.K., Johnson E.A., Kareem A. 1989, Optimal Distribution of Tuned Mass Dampers in Wind Sensitive Structures, *Proceedings of 5th ICOSSAR*, New York.

Bryson A.E., Ho Y.C., 1969, Applied Optimal Control, *Ginne Company*, Waltham, MA, USA.

Bucher C., Di Paola M., 2015, Efficient solution of the First passage problem by Path Integration, *Probabilistic Engineering Mechanics*, Vol. 41, 121-128.

Cacciola P., Colajanni P., Muscolino G., 2004, Combination of Modal Responses Consistent with Seismic Input Representation, *Journal of Structural Engineering*, Vol. 130(1), 47-55.

Chaichian M., Demichev A., 2001, Path integrals in Physics, Vol. 1, *Institute of Physics Publishing*, London, UK.

Chaiviriyawong and Prachaseree, 2009, Applications of passive mass dampers for civil engineering structural control: a review, *Proceeding of the Sixth Regional Symposium on Infrastructure Development*, January, Bangkok, Thailand.

Chaiviriyawong P., Webster W. C., Pinkaew T., Lukkunaprasit P., 2007, Simulation of characteristics of tuned liquid column damper using a potential-flow method, *Engineering Structures*, Vol. 29, 132-144.

Chang C.C., 1999, Mass dampers and their optimal designs for building vibration control, *Engineering Structures*, Vol. 21, 454-463.

Chang C.C., Hsu C.T., 1998, Control performance of liquid column vibration absorbers, *Engineering Structures*, Vol. 20(7), 580-586.

Chang C.C., Hsu C.T., Swei S.M., 1998, Control of buildings using single and multiple tuned liquid column dampers. *Structural Engineering and Mechanics*, Vol. 6(1), 77-93.

Chen L., Zhu W., 2011, Stochastic jump and bifurcation of Duffing oscillator with fractional derivative damping under combined harmonic and white noise excitations, *International Journal of Non-Linear Mechanics*, Vol. 46, 1324-1329.

Chopra A.K., 1995, Dynamics of structures, *Prentice Hall*, Englewood Cliffs.

Ciampi V., 1991, Use of energy dissipating devices, based on yielding of steel, for earthquake protection of structures, *International Meeting on Earthquake Protection of Buildings*, 14/D-58/D, Ancona, Italy.

Clark A.J., 1988, Multiple Passive Tuned Mass Dampers for reducing earthquake induced building motion, *Proc. 9th World Conference Earthquake Eng*., May, Japan, 779-784.

Colwell S., Basu B., 2008, Experimental and Theoretical Investigations of Equivalent Viscous Damping of Structures with TLCD for Different Fluids, *Journal of Structural Engineering*, Vol. 134(1), 154-163.

Constantinou M.C., Soong T.T., Dargush G.F., 1998, Passive energy dissipation systems for structural design and retrofit. Monograph No.1. Buffalo (NY): Multidisciplinary Center for Earthquake Engineering Research.

Crandall S.H., 1985, Non-Gaussian Closure Techniques for Stationary Random Vibration, *International Journal of Non-Linear Mechanics*, Vol. 20, 1-8.

Debbarma R., Chakraborty S., Ghosh S. K., 2010, Optimum design of tuned liquid column dampers under stochastic earthquake load considering uncertain bounded system parameters, *International Journal of Mechanical Sciences*, Vol. 52, 1385-1393.

Dekker H., 1976, Time-local Gaussian processes, path integrals and nonequilibrium nonlinear diffusion, *Physica A*, Vol. 85(2), 363–373.

Den Hartog J.P., 1956, Mechanical Vibrations, *McGraw-Hill*, New York.

Di Matteo A., Lo Iacono F., Navarra G., Pirrotta A., 2012a, The control performance of TLCD and TMD: experimental investigation, *5th European Conference on Structural Control*, 18-20 June, Genoa, Italy

Di Matteo A., Lo Iacono F., Navarra G., Pirrotta A., 2012b, The TLCD Passive Control: Numerical Investigations Vs Experimental Results, *Proceedings ASME 2012-IMECE2012*, DOI: 10.1115/IMECE2012-86568, Houston, USA.

Di Matteo A., Lo Iacono F., Navarra G., Pirrotta A., 2014a, Direct evaluation of the equivalent linear damping for Tuned Liquid Column Damper systems in random vibration for pre-design purposes, *International Journal of Non-linear Mechanics*, Vol. 63, 19-30.

Di Matteo A., Lo Iacono F., Navarra G., Pirrotta A., 2014b, A novel mathematical model for TLCD: theoretical and experimental investigations, *Proceedings ASCE 2014-Second Int. Conf. Vulnerability Risk Anal. Manag. ICVRAM2014*, Liverpool, UK.

Di Matteo A., Lo Iacono F., Navarra G., Pirrotta A., 2015, Innovative modeling of tuned liquid column damper motion, *Communications in Nonlinear Science and Numerical Simulation*, Vol. 23, 229-244.

Di Paola M., Failla G., Pirrotta A., 2012, Stationary and non-stationary stochastic response of linear fractional viscoelastic systems, *Probabilistic Engineering Mechanics*, Vol. 28, 85-90.

Di Paola M., La Mendola L., Navarra G., 2007, Stochastic seismic analysis of structures with non-linear viscous dampers, *Journal of Structural Engineering*, Vol. 133(10), 1475-1478.

Di Paola M., Lo Iacono F., Navarra G., 2008, Amplification of interstory drift and velocity for the passive control of structural vibrations, *Proceedings of the 3rd International Conference on Smart Materials, Structures and Systems-Embodying Intelligence in Structures and Integrated Systems*, Vol. 56, 363-373.

Di Paola M., Navarra G., 2009, Stochastic seismic analysis of MDOF structures with non-linear viscous dampers, *Structural Control and Health Monitoring*, Vol. 16, 303-318.

Di Paola M., Santoro R., 2008, Path integral solution for non-linear system enforced by Poison White Noise, *Probabilistic Engineering Mechanics*, Vol. 23, 164-169.

Di Paola M., Sofi A., 2002, Approximate Solution of the Fokker-Planck-Kolmogorov Equation, *Probabilistic Engineering Mechanics*, Vol. 17(4), 369-384.

Durr D., Bach A., 1978, The Onsager–Machlup function as Lagrangian for the most probable path of a diffusion process, *Communications in Mathematical Physics*, Vol. 60, 153-170.

Er G.K., 2000, Exponential Closure Method for Some Randomly Excited Non-Linear Systems, *International Journal of Non-Linear Mechanics*, Vol. 35(1), 69-78.

Ewing G.M., 1985, Calculus of variations with applications, *Dover*, New York, USA.

Ewins D.J., 1984, Modal Testing: Theory and Practice, *Research Studies Press*, Taunton, Somerset, England.

Failla G., Pirrotta A., 2012, On the stochastic response of fractionally-damped Duffing oscillator, *Communications in Nonlinear Science and Numerical Simulation*, Vol. 17, 5131-5142.

Farshidianfar A. and Oliazadeh P., 2009, Closed form optimal solution of a tuned liquid column damper responding to earthquake, *World Academy of Science, Engineering and Technology*, Vol. 59, 159-164.

Feynman R.P., 1948, Space-time approach to non-relativistic quantum mechanics, *Review of Modern Physics*, Vol. 20, 367-387.

Frahm H., 1909, Device for damped vibrations of bodies, *U.S. Patent No. 989958*.

Fujino Y., Pacheco B.M., Chaiseri P., Sun L.M., 1988, Parametric studies on Tuned Liquid Damper (TLD) using circular containers by free oscillation experiments, *Structural Engineering/Earthquake Engineering*, Vol. 5(2), 381-391.

Fujino Y., Sun L.M., 1993, Vibration control by multiple tuned liquid dampers (MTLCDs), *Journal of Structural Engineering*, Vol. 119(12), 3482–3502.

Gao H., Kwok K.C.S, Samali, B., 1999, Characteristics of multiple tuned liquid column dampers in suppressing structural Vibration, *Engineering Structures*, Vol. 21, 316-331.

Gao H., Kwok K.C.S., 1997, Optimization of tuned liquid column dampers, *Engineering Structures,* Vol. 19(6,) 476-486.

Gosh A., Basu B., 2007, Alternative approach to optimal tuning parameter of liquid column damper for seismic applications, *Journal of Structural Engineering*, Vol. 133(12), 1848-1852.

Graham R., 1977, Path integral formulation of general diffusion processes, *Zeitschrift für Physik B*, Vol. 26, 281-290.

Grigoriu M., 2002, Stochastic calculus, applications in science and engineering, *Birkhäuser*, Boston, USA.

Hilfer R., 2000, Applications of Fractional Calculus to Physics, *World Scientific*, Singapore.

Hitchcock P.A., Kwok K.C.S., Watkins R.D., Samali B., 1997a, Characteristics of liquid column vibration absorbers (LCVA)–I, *Engineering Structures,* Vol. 19, No. 2, 126-134.

Hitchcock P.A., Kwok K.C.S., Watkins R.D., Samali B., 1997b, Characteristics of liquid column vibration absorbers (LCVA)–II, *Engineering Structures,* Vol. 19, No. 2, 135-144.

Hoang N., Fujino Y., Warnitchai P., 2008, Optimal tuned mass damper for seismic applications and practical design formulas, *Engineering Structures*, Vol. 30, 707-715.

Hochrainer M. J., 2005, Tuned liquid column damper for structural control, *Acta Mechanica*, Vol. 175, 57-76.

Hochrainer M. J., Ziegler F., 2006, Control of tall building vibrations by sealed tuned liquid column dampers, *Structural Control and Health Monitoring*, Vol. 13, 980–1002.

Housner G.W., Bergman L.A., Caughey T.K., Chassiakos A.G., Claus R.O., Masri S.F., Skelton R.E., Soong T.T., Spencer B.F. and Yao J.T.P., 1997, Structural control: Past, Present and Future, *Journal of Engineering Mechanics*, Vol. 123(9), 897–971.

Huang Z.L., Jin X.L., 2009, Response and stability of a SDOF strongly nonlinear stochastic system with light damping modeled by a fractional derivative, *Journal of Sound and Vibration*, Vol. 319, 1121-1135.

Ibrahim R.A., 2005, Liquid sloshing dynamics theory and applications, *Cambridge University Press*, New York, USA.

Ioi T.and Ikeda K., 1978, On the dynamic vibration damped absorber of the vibration system, *Bulletin of Japanase Society of Mechanical Engineering*, Vol. 21(151), 64-71.

Kareem A. and Sun W.J., 1987, Stochastic response of structures with fluid-containing appendages, *Journal of Sound and vibration*, Vol. 119, 389–408.

Kareem A., Kijewski T., Tamura Y., 1999, Mitigation of motions of tall buildings with specific examples of recent applications, *Wind and Structures*, Vol. 2, No. 3, 201-251.

Kennedy J.E., Eberhart R.C., 1995, Particle Swarm Optimization, *Proceedings of the IEEE International Conference on Neural Networks*, 942-1948.

Kleinert H., 2009, Path Integrals in Quantum Mechanics, Statistics, Polymer Physics, and Financial Markets, 5th ed., *World Scientific Publishing*, Singapore, China.

Koh C.G., Kelly L.M., 1990, Application of fractional derivatives to seismic analysis of base isolated models, *Earthquake Engineering and Structural Dynamics*, Vol. 9, 229-241.

Konar T., Ghosh A., 2013, Bimodal vibration control of seismically excited structures by the liquid column vibration absorbers, *Journal of Vibration and Control*, Vo. 19, 385-394.

Kougioumtzoglou I.A., Spanos P.D., 2012, An analytical Wiener path integral technique for non-stationary response determination of nonlinear oscillators, *Probabilistic Engineering Mechanics*, Vol. 28, 125-131.

Kougioumtzoglou I.A., Spanos P.D., 2013, Nonlinear MDOF system stochastic response determination via a dimension reduction approach, *Computers and Structures*, Vol 126, 135-148.

Kougioumtzoglou I.A., Spanos P.D., 2014, Non-stationary Stochastic Response Determination of Nonlinear Systems: A Wiener Path Integral Formalism, *Journal of Engineering Mechanics*, Vol. 140, p. 04014064.

Lee J., 1995, Improving the Equivalent Linearization Technique for Stochastic Duffing Oscillators, *Journal of Sound and Vibration*, Vol. 186(5), 846-855.

Lee S.H., Min K.W., Hwang J.S., Kim J., 2004, Evaluation of equivalent damping ratio of a structure with added dampers, *Engineering Structures*, Vol. 26(3), 335-346.

Lee S.K., Lee H.R., Min K.W., 2012, Experimental verification on nonlinear dynamic characteristic of a tuned liquid column damper subjected to various excitation amplitudes, *The Structural Design of Tall and Special Buildings*, Vol. 21(5), 374-388.

Levin R.I., Lieven N.A.J., 1998, Dynamic Finite Element Model Updating using Simulated Annealing and Genetic Algorithms, *Mechanical Systems and Signal Processing*, Vol. 12(1), 91-120.

Li J., Chen J., 2009, Stochastic Dynamics of structures, *John Wiley & Sons*, Singapore, China.

Lin Y.K., 1967, Probabilistic Theory of Structural Dynamics, *McGraw-Hill*, New York, USA.

Lotfi A., Yousefi S.A., 2013, A numerical technique for solving a class of fractional variational problems, *Journal of Computational and Applied Mathematics*, Vol. 237, 633-643.

Luft R.W., 1979, Optimal tuned mass dampers for buildings, *Journal of the Structural Division*, Vol. 105(12), 2766-2772.

Maia N.M.M., Silva J.M.M., 1997, Theoretical and experimental modal analysis, *Research Studies Press Ltd*, John Wiley & Sons, New York, USA.

Makris N., Constantinou M.C., 1991, Fractional-derivative Maxwell model for viscous dampers, *Journal of Structural Engineering*, Vol. 117, 2708-2724.

Makris N., Constantinou M.C., 1992, Spring-viscous damper systems for combined seismic and vibration isolation, *Earthquake Engineering and Structural Dynamics*, Vol. 21, 649-664.

Malinowska A.B., Torres D.F.M., 2010, The generalized natural boundary conditions for fractional variational problems in terms of the

Caputo derivative, *Computer and Mathematics with Applications*, Vol. 59, 3110-3116.

Martinez-Romero E., 1993, Experiences on the use of supplemental energy dissipators on building structures, *Earthquake Spectra*, Vol. 9(3), 581-625.

Min K.W., Kim J., Lee H.R., 2014, A design procedure of two way liquid dampers for attenuation of wind-induced responses of tall buildings, J*ournal of Wind Engineering and Industrial Aerodynamics*, Vol. 129, 22-30.

Modi V.J., Welt F., 1987, Vibration control using nutation dampers, *International Conference on Flow Induced Vibrations*, BHRA, London, 369-376.

Muscolino G. Pirrotta A., Ricciardi G., 1997, Non Gaussian closure technique for the analysis of R-FBI isolation systems, *Journal of Structural Control*, Vol. 4(1), 23-46.

Muscolino G., Ricciardi G., Cacciola P., 2003, Monte Carlo simulation in the stochastic analysis of non-linear systems under external stationary Poisson white noise input, *International Journal on Non-linear Mechanics*, Vol. 38, 1269-1283.

Muscolino G., Ricciardi G., Vasta M., 1997, Stationary and Non-Stationary Probability Density Function for Non-Linear Oscillators, *International Journal of Non-Linear Mechanics*, Vol. 32(6), 1051-1064.

Naeim F., Kelly J.M., 1999, Design of Seismic Isolated Structures: from Theory to Practice, *John Wiley & Sons*, New York.

Naess A., Moe V., 2000, Efficient path integration method for nonlinear dynamic systems, *Probabilistic Engineering Mechanics*, Vol. 15, 221-231.

Navarra G., Barone G., Lo Iacono F., 2013, Stochastic seismic analysis by using an analytical model of PSD consistent with Response

Spectra, *Proceedings of Vienna Congress on Recent Advances in Earthquake Engineering and Structural Dynamics*, Vienna, Austria.

Onsager L., Machlup S., 1953, Fluctuations and irreversible processes, *Physical Review*, Vol. 91, 1505-1515.

Palazzolo B., Petti L., 1999, Combined control strategy: based isolation and tuned mass damping, *ISET Journal of Earthquake Technology*, Vol. 36, 121-137.

Pall A.S., Pall R., 1996, Friction-dampers for seismic control of buildings "A Canadian experience", *11th World Conference on Earthquake Engineering*, paper No. 497, Acapulco, Mexico.

Perry C.L., Fierro E.A., Sedarat H., Scholl R.E., 1993, Seismic upgrade in San Francisco using energy dissipation devices, *Earthquake Spectra*, Vol. 9(3), 559-579.

Pirrotta A., 1996, Cascaded approach to study isolated structures, *European Earthquake Engineering*, Vol. 10(1), 14-20.

Pirrotta A., Ibrahim R.A., 1997, Experimental investigation of friction-base isolation, *Probabilistic Engineering Mechanics*, Vol. 12(3), 125-135.

Podlubny I., 1999, Fractional differential equations. An introduction to fractional derivatives, fractional differential equations, some methods of their solution and some of their applications, *Academic Press*, New York, USA.

Rana R., Soong T.T., 1998, Parametric study and simplified design of tuned mass dampers, *Engineering Structures*, Vol. 20(3), 193-204.

Ricciardi, G., 2007, A non-Gaussian stochastic linearization method, *Probabilistic Engineering Mechanics*, Vol. 22, 1-11.

Richardson M.H., Formenti D.L., 1982, Parameter estimation from frequency response measurements using rational fraction polynomials, *International Modal Analysis Conference IMAC I*, Orlando, Florida, 167-181.

Risken H., 1996, The Fokker Planck equation, *Springer*, Berlin.

Roberts J.B., Spanos P.D., 1990, Random Vibration and Statistical Linearization, *John Wiley & Sons*, New York, USA.

Rubinstein R.Y., Kroese D.P., 2007, Simulation and the Monte Carlo method, *John Wiley & Sons*, Hoboken.

Saaed T., Nikolakopoulos G., Jonasson J. and Hedlund H., 2015, A state-of-the-art review of structural control systems, *Journal of Vibration and Control*, Vol.21(5), 919-937.

Sabatier J., Agrawal O.P., Tenreiro Machado J.A., 2007, Advances in Fractional Calculus. Theoretical Developments and Applications in Physics and Engineering, *Springer*, Dordrecht.

Sadek F., Mohraz B., Lew H. S., 1998, Single and multiple tuned liquid column dampers for seismic applications, *Earthquake Engineering and Structural dynamics*, Vol. 27, 439-463.

Sakai F., Takaeda S., Tamaka T., 1991, Tuned Liquid Column Damper (TLCD) for cable-stayed bridges, *Proc. Speciality-Conference, Innovation in Cable-Stayed Bridges*, Fukuoka, Japan, 197-205.

Sakai F., Takeda S., Tamaki, T., 1989, Tuned liquid column damper-new type device for suppression of building vibrations, *Proceedings of the international conference on highrise buildings*, 926-931, Nanjing, China.

Samali B., Kwock K.C.S., 1995, Use of viscoelastic dampers in reducing wind and earthquake induced motion of building structures, *Engineering Structures*, Vol. 17(9), 639-654.

Sarkar A., Gudmestad O.T., 2013, Pendulum type liquid column damper (PLCD) for controlling vibrations of a structure-theoretical and experimental study, *Engineering Structures*, Vol. 49, 221-233.

Shum K.M., 2009, Closed form optimal solution of a tuned liquid column damper for suppressing harmonic vibration of structures, *Engineering Structures*, Vol. 31, 84-92.

Skinner R.I., Tyler R.G., Heine A.J., Robinson W.H., 1980, Hysteretic dampers for the protection of structures from earthquakes, *Bulletin New Zealand Society of Earthquake Engineering*, Vol. 13(1), 22-36.

Soong T.T., Constantinou M.C., 1994, Passive and Active Structural Vibration Control in Civil Engineering, *Springer*, NewYork, USA.

Soong T.T., Dargush G.F., 1997, Passive energy dissipation system in structural engineering, *John Wiley & Sons*, Chichester.

Soong T.T., Grigoriu M., 1993, Random Vibration of Mechanical and Structural Systems, *Prentice Hall*, New Jersey, USA.

Soong T.T., Spencer B.F., 2002, Supplementary energy dissipation: State-of-the-art and state-of-the-practice, *Engineering Structures*, Vol. 24, 243– 259.

Spanos P.D., 1981, Stochastic linearization in structural dynamics, *Applied Mechanics Review*, Vol. 34(1), 1-8.

Spanos P.D., Donley M.G., 1991, Equivalent Statistical Quadratization for Nonlinear Systems, *Journal of Engineering Mechanics*, Vol. 117(6), 1289-1310.

Spanos P.D., Donley M.G., 1992, Non-Linear Multi-Degree-of-Freedom System Random Vibration by Equivalent Statistical Quadratization, *International Journal of Non-Linear Mechanics*, Vol. 27(5), 735-748.

Spanos P.D., Evangelatos G.I., 2010, Response of a non-linear system with restoring forces governed by fractional derivatives-time domain simulation and statistical linearization solution, *Soil Dynamics and Earthquake Engineering*, Vol. 30, 811–821.

Spanos P.D., Kougioumtzoglou I.A., 2012, Harmonic wavelets based statistical linearization for response evolutionary power spectrum determination, *Probabilistic Engineering Mechanics*, Vol. 27, 57-68.

Spencer B.F., Nagarajaiah F., 2003, State of the art of structural control, *Journal of Structural Engineering*, Vol. 129, 845-856.

Stratonovich R.L., 1971, Selected Translations in Mathematical Statistics and Probability, Vol. 10, 273, *American Mathematical Society*, Providence, USA.

Symans M.D., Constantinou M.C., 1999, Semi-active control systems for seismic protection of structures: a state-of-the art review, *Engineering Structures*, Vol. 21, 469– 487.

Tamura Y,.Fujii K., Ohtsuki T., Wakahara T. and Koshaka R., 1995, Effectiveness of Tuned Liquid Column Dampers in tower-like structures, *Engineering Structures*, Vol. 17(9), 609-621.

Taniguchi T., Cohen E.G.D., 2008, Inertial effects in non-equilibrium work fluctuations by a path integral approach, *Journal of Statistical Physic*s, Vol. 130, 1-26.

Teramura A., Yoshida O., 1996, Development of vibration control system using U-shaped water tank, *Proceedings of the 11th World Conference on Earthquake Engineering*, Paper No. 1343.

Tisza L., Manning I., 1957, Fluctuations and irreversible processes. *Physical Review*, Vol. 105, 1695-1705.

Villaverde R., 1994, Seismic control of structures with damped resonant appendages, *Proceedings of the 1st World Conference on Structural Control*, 3-5 August, Los Angeles, California, USA.

Warburton G.B., 1982, Optimum absorber parameters for various combinations of response and excitation parameters. *Earthquake Engineering and Structural Dynamics*, Vol. 10, 381-401.

Warburton G.B., Ayorinde E.O., 1980, Optimum absorber parameters for simple system. *Earthquake Engineering and Structural Dynamics*, Vol. 8, 197-217.

Wehner M.F., Wolfer W.G., 1983a, Numerical evaluation of path integral solutions to Fokker-Planck equations, *Physical Review A*, Vol. 27(5), 2663–2670.

Wehner M.F., Wolfer W.G., 1983b, Numerical evaluation of path integral solutions to Fokker-Planck equations. II. Restricted stochastic processes, *Physical Review A*, Vol. 28(5), 3003–3011.

Wehner M.F., Wolfer W.G., 1987, Numerical evaluation of path integral solutions to Fokker-Planck equations. III. Time and functionally dependent coefficients, *Physical Review A*, Vol. 35(4), 1795–1801.

Wiener N., 1921, The average of an analytic functional, *Proceeding of the National Academy of Science*, Vol. 7, 253- 260.

Wiener N., 1930, Generalized harmonic analysis, *Acta Mathematica*, Vol. 55, 117-258.

Won A.Y.J., Pirest J.A., Harount M.A., 1996, Stochastic seismic performance evaluation of tuned liquid column dampers, *Earthquake Engineering and Structural Dynamics*, Vol. 25, 1259-1274.

Won A.Y.J., Pirest J.A., Harount M.A., 1997, Performance assessment of tuned liquid column dampers under random seismic loading, *International Journal of Non-Linear Mechanics*, Vol. 32(4), 745-758.

Wu J.C., Chang C.H., 2006, Design table of optimal parameters for tuned liquid column damper responding to earthquake, *Proceedings of the 4th International Conference on Earthquake Engineering*, Taipei, Taiwan.

Wu J.C., Chang C.H., Lin Y.Y., 2009, Optimal design of non-uniform tuned liquid column dampers in horizontal motion, *Journal of Sound and Vibration*, Vol. 326, 104–122.

Wu J.C., Shih M.H., Lin Y.Y., Shen Y.C., 2005, Design guidelines for tuned liquid column dampers for structures responding to wind, *Engineering Structures*, Vol. 27, 1893-1905.

Xu K. and Igusa T., 1992, Dynamic characteristics of multiple substructures with closely spaced frequencies, *Earthquake Engineering and Structural. Dynamics*, Vol. 21, 1059-1070.

Xu Y.L, Samali B, Kwok K.C.S., 1992, Control of Along-wind Response of Structures by Mass and Liquid Dampers, *Journal of Engineering Mechanics*, Vol. 118(1), 20-39.

Xue S.D., Ko J.M., Xu Y.L., 2000, Tuned liquid column damper for suppressing pitching motion of structures, *Engineering Structures*, Vol. 23, 1538–1551.

Yalla S., Kareem A., 2000, Optimum absorber parameters for tuned liquid column dampers, *Journal of Structural Engineering*, Vol. 126(8), 906-915.

Yamaguchi H. and Harnpornchai N., 1993, Fundamental characteristics of multiple tuned mass dampers for suppressing harmonically forced oscillations, *Earthquake Engineering and Structural. Dynamics*, Vol. 22, 51-62.

Ziegler F., 2007, The tuned liquid column damper as a cost-effective alternative for the mechanical damper in civil engineering structures, *International Journal of Acoustic and Vibration*, Vol. 12, 25–39.

Ziegler F., 2008, Special design of tuned liquid column-gas dampers for the control of spatial structural vibrations, *Acta Mechanica*, Vol. 201, 249-267.